Exploiting molecular vulnerabilities in genetically defined lung cancer models

Inaugural-Dissertation

zur

Erlangung des Doktorgrades

der Mathematisch-Naturwissenschaftlichen Fakultät

der Universität zu Köln

vorgelegt von
Hannah Lea Tumbrink
aus Höxter

Köln, 2022

Berichterstatter: Prof. Dr. Martin L. Sos

Prof. Dr. Ulrich Baumann

Prüfungsvorsitz: Prof. Dr. Kay Hofmann

Tag der mündlichen Prüfung: 15.02.2023

Danksagung

DANKE an alle die mit mir im Labor standen, mit denen ich kooperieren konnte, von denen ich Neues lernen durfte.

Danke **Martin,** dass ich meine Doktorarbeit bei dir im Labor anfertigen konnte und für die vielen wissenschaftlich interessanten Fragestellungen.

Ganz besonderer Dank geht an meine Betreuer/ Tutoren/ Prüfer **Roman** und **Prof. Dr. Ulrich Baumann** für den Input über die vielen Jahre hinweg bei den Projektbesprechungen, sowie an **Prof. Dr. Kay Hofmann** für die Übernahme des Prüfungsvorsitzes.

Ein besonders großer Dank geht an **Marcel**, der mich fast meine ganze Promotion begleitet hat, nur zu Ende ja leider zu DISCO wechseln musste. Danke fürs stetige Diskutieren/ Beraten/ Korrigieren – sei es Labor bezogen oder Privat. Die Zeit im Labor wäre nicht ansatzweise so erträglich, lustig und schön gewesen ohne dich. Beim Blumen gießen haben wir uns eine Zeit lang beide nicht viel genommen, aber ich glaube gute Gärtner sind wir beide nicht.

Carina was würde ich nur ohne deinen Input tun? Vielen Dank für die vielen wissenschaftlichen und auch kulturellen Diskussionen. Und natürlich danke, dass ich deinen MAC nutzen konnte, ohne den es nicht eine Histo Auswertung gäbe.

Fabi, ohne dich wären meine Mittagspausen definitiv kürzer gewesen. Nicht nur das Labor hat uns zu sehr, sehr guten Freunden werden lassen – danke fürs zuhören, verstehen und ausdiskutieren diverser Problematiken.

Ebenso möchte ich mich bei der ganzen **AG SOS/Thomas/Reinhardt/Brägelmann** bedanken, besonders bei **Alena**, **Lisa**, **Ayla**, **Laura, Katia**, **Johannes**, **Steffi**, **Davide**, **Jenny**, **Nicole**, **Ilona**, **Nina, Anna**, ….

Außerdem möchte ich mich bei meinen **Freunden** und meiner **Familie** bedanken, auch wenn Omas & Opas Satz: *„Wir würden deine Promotion so gerne noch erleben“* doch gewissen Druck ausgeübt hat. Ihr habt mich in meiner Arbeit stets bestärkt, meine guten und meine schlechten Launen ertragen und seid immer für mich da gewesen. Danke an **Mama & Papa**, **Oma & Opa** (ihr dürft gerne die 100 noch voll machen!), **Matthäus & Greta**, **PuM**, **Anna** und den ganzen Rest der Scharz-Tumbrink Sippschaft.

Index of Contents

List of Abbreviations

A-loop	activation loop
ALK	anaplastic lymphoma kinase
ALL	acute lymphoblastic leukemia
ASCL1	acheate-scute like 1
ATP	adenosine triphosphate
ATR	ataxia telangiectasia and rad3 related
BCL2	B-cell CLL/lymphoma 2
bHLHLZ	basic helix-loop-helix leucine zipper
BR	basic region
BTB	broad complex, tramtrack, and Bric-a-brac
CC3	cleaved caspase-3
CDKN2A	cyclin dependent kinase inhibitor 2A
CGRP	neuroendocrine calcitonin gene-related peptide
Chk1	checkpoint kinase 1
CMV	cytomegalovirus
CREBBP	cyclic adenosine monophosphate response element binding protein binding protein
DNA	deoxyribonucleic acid
E-box	enhancer-box
EGFR	epidermal growth factor receptor
FDA	food and drug administration
FGFR1	fibroblast growth factor receptor
GEMM	genetically engineered mouse models
GI_{50}	half-maximal growth inhibition

H&E	hematoxylin and eosin
HER2	human epidermal growth factor receptor 2
HGF	hepatocyte growth factor
HRAS	harvey rat sarcoma virus
ICH	immunohistochemistry
ICI	immune checkpoint inhibitors
JAK	janus kinase
KRAS	kirsten rat sarcoma virus
LCC	large cell carcinoma
LSL	lox-stop-lox
LUAD	lung adenocarcinoma
LUSC	squamous cell carcinoma
LZ	leucine zipper
MAP2K1	mitogen-activated protein kinase kinase 1
MAPK	mitogen-activated protein kinase
MAX	Myc-associated factor X
MB	MYC homology boxes
MIZ1	MYC-interacting zinc finger protein 1
MRI	magnetic resonance imaging
mTOR	mammalian target of rapamycin
NCAM	Neural cell adhesion molecule
NEUROD1	Neuronal differentiation 1
NK	natural killer
NLS	nuclear localization sequence
NOTCH1	neurogenic locus notch homolog protein 1
Npm1	nucleophosmin

NRAS	neuroblastoma ras viral oncogene homolog
NSCLC	non-small cell lung cancer
ORR	overall response rate
OS	overall survival
PD-1	programmed cell death protein 1
PD-L1	programmed death-ligand 1
PEST	proline-rich middle segment, glutamic acid, threonine and protein residues
PFS	progression free survival
PI3K	phosphatidylinositol-3-kinase
PKC	protein kinase C
POUF2F3	POU Class 2 Homeobox 3
POZ	poxvirus and zinc finger
PTEN	Phosphatase and tensin homolog
RB1	retinoblastoma protein
RET	rearranged during transfection
RNA	ribonucleic acid
RP	Rb1$^{fl/fl}$Trp53$^{fl/fl}$
RPM	Rb1$^{fl/fl}$Trp53$^{fl/fl}$Myc$^{LSL/LSL}$MIZ1
RPMM	Rb1$^{fl/fl}$Trp53$^{fl/fl}$Myc$^{LSL/LSL}$MIZ1$^{\Delta POZfl/fl}$
RT	room tempreture
RTK	receptor tyrosine kinases
SCLC	small cell lung cancer
STAT	signal transducer and activator of transcription
TAD	transactivation domain
TKI	tyrosine kinase inhibitor
Top	topoisomerase

TP53	tumor protein 53
TP73	tumor protein 73
WT	wild type
YAP1	yes-associated protein 1
ZF	zinc-finger

Summary

Lung cancer is the leading cause of cancer-related death worldwide, with approximately 1.8 million deaths in 2020. Based on histology, lung cancer is divided into non-small cell lung cancer (NSCLC) (85 %) and small cell lung cancer (SCLC) (15 %). The most common types of NSCLC are lung squamous cell carcinoma (LUSC), large-cell carcinoma (LCC), and lung adenocarcinoma (LUAD). LUAD, the largest subgroup of NSCLC, is characterized by genomic alterations in oncogenic driver genes such as *KRAS* or *EGFR*. Mutations in the kinase domain of EGFR result in aberrant signaling activation and subsequent cancer development. Tyrosine kinase inhibitors (TKIs) selectively target and inhibit mutant kinases, thereby killing oncogene-addicted cancer cells. The introduction of TKIs into clinical practice shifted NSCLC treatment from cytotoxic chemotherapy towards precision medicine, improving both survival and the quality of life during therapy. Patients with canonical EGFR mutations like the point-mutation L858R or exon 19 deletions mutations, which account for the majority of EGFR mutations, respond well to EGFR targeted TKIs. However, rare mutations like insertions in exon 20 insertions still represent challenging drug targets. αC-helix–β4-loop insertion mutations in exon 20 push the αC-helix into the active, inward position without altering the binding site for TKIs. This leaves the binding site for TKIs in kinases with exon 20ins mutations highly similar to wild type (WT) EGFR. Thus, the challenge in the development of exon 20 inhibitors is the design of wild type sparing small molecules. Here, we analyzed a novel small molecule EGFR inhibitor (LDC0496) targeting an emerging cleft in exon 20-mutated EGFR to achieve selectivity over the wild type. In contrast to classical EGFR TKIs, LDC0496 reduces the cellular viability of EGFR exon 20 mutated cells but spares wild type EGFR.

Targeted therapy inevitably results in the development of on- or off-target resistance. Drug-induced resistance mutations require the constant development of novel drugs targeting the diverse landscape of resistance mechanisms. We detected *BRAF* mutations in *EGFR*-driven lung cancer patients as a resistance mechanism to EGFR inhibitors. Notably, we also detected co-occurrence of *EGFR* and *BRAF* mutations before treatment start. Combination treatment of EGFR and mitogen-activated protein kinase kinase (MEK) inhibition displayed activity in *BRAF*- and *EGFR*-mutated xenograft studies, therefore providing a treatment strategy to overcome *BRAF* mutation as a resistance mechanism.

Compared to NSCLC, SCLC lacks druggable targets and the initial chemosensitive state rapidly turns into a chemoresistance state. SCLC is genetically defined by a biallelic loss of tumor suppressors *RB1* and *TP53* and alterations of *MYC* family members. The transcription factor MYC is a challenging target that cannot be directly targeted. Therefore, alternative strategies are needed, for example targeting its co-factors, such as the MYC-interacting zinc finger protein 1 (MIZ1). To study the complex interplay of Myc–Miz1 in SCLC, we developed a novel mouse model with a truncated Miz1, which is unable to stably bind chromatin (RPMM: Rb1$^{fl/fl}$Trp53$^{fl/fl}$Myc$^{LSL/LSL}$MIZ1$^{\Delta POZ fl/fl}$). Compared to Miz1 wild type the characterization of the novel mouse model revealed tumor-onset, localization, size and immune infiltration to be unaffected by the ablation of the Miz1-POZ domain, but mice with Miz1-ΔPOZ live longer, exhibit an increased number of apoptotic cells and are more sensitive towards chemotherapy. We found that truncated Miz1 alter SCLC tumorigenesis towards a less aggressive phenotype and prolongs the chemosensitive state. Our study highlights alternative strategies to define novel vulnerabilities and options to overcome chemoresistance.

Zusammenfassung

Lungenkrebs ist weltweit die häufigste Ursache für krebsbedingte Todesfälle, mit etwa 1,8 Millionen Todesfällen im Jahr 2020. Auf der Grundlage der Histologie wird Lungenkrebs in nicht-kleinzelligen Lungenkrebs (NSCLC) (85 %) und kleinzelligen Lungenkrebs (SCLC) (15 %) unterteilt. Die häufigsten Arten von NSCLC sind das Plattenepithelkarzinom der Lunge (LUSC), das großzellige Karzinom (LCC) sowie das Adenokarzinom der Lunge (LUAD). Die größte Untergruppe des nicht-kleinzelligen Lungenkarzinoms, LUAD, ist durch gnomische Veränderungen in *KRAS* oder *EGFR* und andere onkogene Faktoren gekennzeichnet. EGFR Mutationen in der Kinasedomäne führen zu einer abnormen Aktivierung und damit zur Entstehung von Krebs. Tyrosinkinase-Inhibitoren (TKI) adressieren selektiv mutierte Kinasen und hemmen sie, wodurch sie onkogenabhängige Krebszellen abtöten. Mit der Einführung der TKIs in die klinische Praxis verlagerte sich die Behandlung des NSCLS von der zytotoxischen Chemotherapie hin zur Präzisionsmedizin, was sowohl die Überlebensrate als auch die Lebensqualität während der Therapie verbesserte. Patienten mit kanonischen EGFR-Mutationen wie der Punktmutation L858R oder Exon 19-Deletionsmutationen, die die Mehrheit der EGFR-Mutationen ausmachen, sprechen gut auf klassische EGFR-TKIs an. Seltene Mutationen wie Insertionen in Exon 20 stellen jedoch nach wie vor schwierige Zielmoleküle für Medikamente dar. α*C*-helix–β4-Schleifen-Insertionsmutationen in Exon 20 verschieben die α*C*-Helix in die aktive, nach Innen gerichtete Position, ohne die Bindungsstelle für TKIs zu verändern. Dadurch ist die Bindungsstelle für TKIs in Kinasen mit Exon-20ins-Mutationen dem Wildtyp des EGFR sehr ähnlich. Die Herausforderung bei der Entwicklung von Exon-20-Inhibitoren besteht daher darin, niedermolekulare Moleküle zu entwickeln, die den Wildtyp schonen. Wir haben einen neuartigen niedermolekularen Inhibitor mit einem Rest entwickelt, der auf eine entstehende Lücke im Exon 20 mutierten EGFR abzielt, um Selektivität gegenüber dem Wildtyp zu erreichen. Im Gegensatz zu klassischen TKIs reduziert der neuartige Inhibitor (LDC0496) die zelluläre Viabilität von EGFR Exon 20 mutierten Zellen, verschont aber EGFR Wildtyp.

Eine zielgerichtete Therapie führt unweigerlich zur Entwicklung einer *On-* oder *Off*-Target-Resistenzen. Medikamenteninduzierte Resistenzmutationen erfordern die ständige Entwicklung neuer Medikamente, die auf die vielfältigen Resistenzmechanismen abzielen. Wir haben *BRAF*-Mutationen bei EGFR-getriebenen Lungenkrebspatienten als

Resistenzmechanismus gegen EGFR-Inhibitoren entdeckt. Überraschenderweise konnten wir auch das gleichzeitige Auftreten von EGFR- und BRAF-Mutationen vor Beginn der Behandlung feststellen. Die Kombinationstherapie aus EGFR- und Mitogen-aktivierter Proteinkinase-Kinase-Kinase (MEK) zeigte in *BRAF*- und *EGFR*-mutierten Xenograft-Studien eine gute Wirkung und bietet somit eine Behandlungsstrategie zur Überwindung der BRAF-Mutation als Resistenzmechanismus.

Im Vergleich zum NSCLC fehlt es dem SCLC an Zielmolekülen und der anfänglich chemosensitive Zustand wandelt sich rasch in einen chemoresistenten Zustand. SCLC ist genetisch durch einen Verlust der Tumorsuppressoren *RB1* und *TP53* sowie durch Veränderungen von Mitgliedern der *MYC*-Familie definiert. Der Transkriptionsfaktor MYC ist ein schwer zu adressierendes Zielmolekül, und Ansätze, die direkt MYC adressieren, bleiben schwierig. Daher sind alternative Strategien erforderlich, die beispielsweise auf seine Kofaktoren abzielen, wie das MYC-interagierende Zinkfingerprotein 1 (MIZ1). Um das komplexe Zusammenspiel von Myc-Miz1 bei SCLC zu untersuchen, haben wir ein neues Mausmodell mit einem verkürzten Miz1 entwickelt, das nicht in der Lage ist, Chromatin stabil zu binden (RPMM: $\mathrm{Rb1}^{fl/fl}\mathrm{Trp53}^{fl/fl}\mathrm{Myc}^{LSL/LSL}\mathrm{MIZ1}^{\Delta POZfl/fl}$). Im Vergleich zum Miz1-Wildtyp zeigte die Charakterisierung des neuen Mausmodells, dass Tumorausbruch, -lokalisierung, -größe und Immuninfiltration durch die Ablation der Miz1-POZ-Domäne nicht beeinflusst werden. Im Vergleich zum Miz1-Wildtyp leben Mäuse mit Miz1-ΔPOZ länger, weisen eine erhöhte Anzahl apoptotischer Zellen auf und sind empfindlicher gegenüber Chemotherapie. Wir fanden heraus, dass verkürztes Miz1 die SCLC-Tumorgenese in Richtung eines weniger aggressiven Phänotyps lenkt und den chemosensitiven Zustand verlängert. Unsere Studie zeigt alternative Strategien auf, um neue Schwachstellen und Möglichkeiten zur Überwindung der Chemoresistenz zu definieren.

1 Introduction

1.1 Lung cancer

For several decades, lung cancer is still the leading cause of cancer-related death worldwide with, 2 million new cases and 1.76 million deaths per year (18 % of total cancer deaths)[1-3]. The 5-year survival rate is approximately 19 % for all lung cancer cases but varies immensely within lung cancer subtypes[4,5]. Compared with other cancer types, only minor improvements in the 5-year survival rates have been archived in the last years. Especially the usually late stage at the time of diagnosis, proves to be complicated. While tobacco smoking is the most critical risk factor for lung cancer, approximately 20 % of all patients diagnosed with lung cancer are never-smokers. The proportion is higher in females and the number rises up to 80 % if only female patients with Asian backgrounds are considered[1,6,7]. Reduced smoking rates in high-income countries concomitantly reduced the incidence of lung cancer. However, in low-income countries with limited access to health care and few public health initiatives against smoking, lung cancer cases continue to increase[3].

Lung cancer is histologically divided into non-small cell lung cancer (NSCLC) and small cell lung cancer (SCLC) (**Figure 1**)[8]. NSCLC represents the majority of all cases accounting for 85 %, and is further subdivided into lung adenocarcinoma (LUAD) (~40 %), squamous cell carcinoma (LUSC) (~25-30 %), and large cell carcinoma (LCC) (~10-15 %). SCLC represents the remaining 15 % of lung cancer cases.

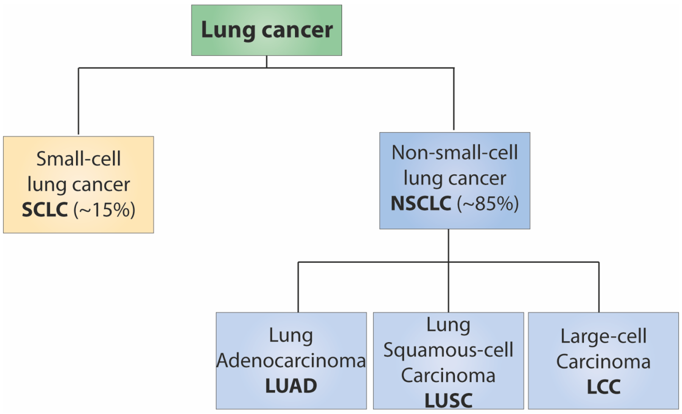

Figure 1: Classification of lung cancer. Lung cancer is subdivided into small-cell lung cancer (~15%) and non-small cell lung cancer (~85). NSCLC is further subdivided into lung adenocarcinoma, lung squamous-cell carcinoma and large-cell carcinoma. Adapted from Gridelli et al.[8].

Depending on the subtype, the 5-year overall survival rate is higher in NSCLC (23 %) and dramatically lower in SCLC (6 %)[4,5]. The current clinical treatment of SCLC and NCSLC depends on the stage at diagnosis and on the lung cancer subtype. Early-stage NSCLC and SCLC cases can undergo surgery, whereas advanced stage cases are mainly treated using radio- and chemotherapy, immunotherapy, and targeted therapy. Most patients are at an advanced stage at the time of diagnosis, where current treatment options are limited. In early 2000s, gefitinib[9,10], a small molecule tyrosine kinase inhibitor (TKI), and the subsequent discovery of epidermal growth factor receptor (*EGFR*) mutations as the driver in a subset of LUAD fundamentally changed the treatment options for those patients from unspecific treatments towards precision medicine[11]. It was also the starting point for developing multiple generations of TKIs targeting relevant driver mutations in lung adenocarcinoma[12]. In sharp contrast to NSCLC, advances in the development of novel drugs for SCLC patients were minimal, and the standard of care is still chemotherapy, with the recent addition of immune checkpoint inhibitors (ICI)[13].

1.2 EGFR-mutant lung adenocarcinoma

Non-small cell lung cancer is a heterogeneous disease. LUAD represents the majority of cases accounting for approximately 40 % of all NSCLC cases[8]. The understanding of its complex biology is indispensable for developing novel drugs. The identification of driver oncogenes and the concomitant development of specific drugs changed the treatment from cytotoxic therapy to targeted therapy.

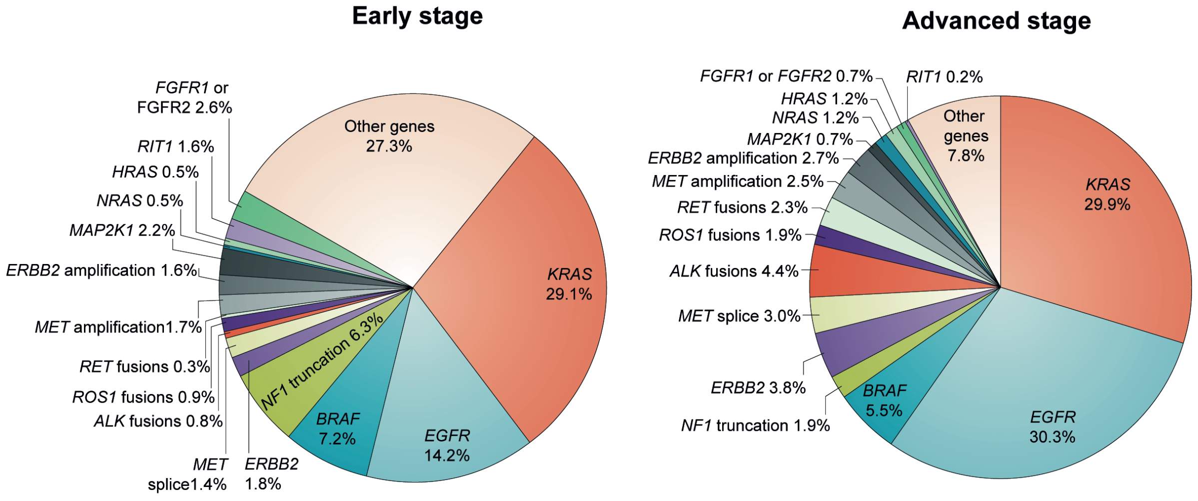

Figure 2: Oncogenic driver alterations in early stage and advanced or metastatic lung adenocarcinoma. Early stage: Data combined from the PanCancer Atlas cohort of The Cancer Genome Atlas (TCGA)[14-16] and cohorts reported from Imielinski et al.[17] and Kadara et al.[18] (n=741). Oncogenic drivers in advanced or metastatic based on data from the Memorial Sloan Kettering Cancer Center[19] and Foundation Medicine[20] (n=5262). Modified from Skoulidis et al.[21].

The most common genomic alterations that drive LUAD occur in *KRAS*, *EGFR*, *BRAF*, *NF1*, *HER2*, *MET*, *ALK*, *ROS1*, *RET*, *MAP2K1*, *NRAS*, *HRAS*, *RIT*, *FGFR1,* and *FGFR2* (**Figure 2**). About ~30 % of all metastatic or advanced stage LUAD cases are driven by mutations in the *EGFR* gene[19,21]. EGFR is a member of the ERBB receptor tyrosine kinase family that also includes HER2 (*ERBB2*), HER3 (*ERBB3*) and HER4 (*ERBB4*). EGFR is a single-chain, transmembrane protein composed of an extracellular ligand binding domain, a transmembrane domain, a juxtamembrane domain, and an intracellular segment harboring the highly conserved kinase domain, and a regulatory *C*-terminal phosphorylation region (**Figure 3**). The kinase domain contains two subdomains – the N-lobe consisting of five β-sheets, one αC helix, and the C-lobe with the highly flexible activation loop (A-loop). The two subdomains are connected via the hinge region and, a deep cleft of these two lobes forms the binding pocket for adenosine triphosphate (ATP). The activation and inactivation of the catalytic domain is regulated by three conserved structure elements: Asp-Phe-Gly (DFG) motif, alpha-C helix and the A-loop. In the active kinase, the αC helix is twisted inwards (αC in) and the aspartate of the DFG motive points to the ATP-binding site (DFG-in), thereby stabilizing the ATP complex. In the inactive state, the A-loop is closed and the αC helix is in an outwards position (αC out) as well as the DFG motif (DFG-out)[22,23]. Under normal physiological conditions, the activation of ERBB receptors is controlled by the spatial and temporal expression of their ligands. Ligand binding induces the formation of receptor homo- and heterodimers, resulting in the phosphorylation of a tyrosine residue in the C-terminal tail[24]. This phosphorylated tyrosine serves as a docking site for further signaling molecules and thereby activates intracellular downstream signaling pathways like MAPK, PI3K/AKT/mTOR, PKC and JAK/STAT (**Figure 3a**)[25]. The activation of these signaling cascades leads, e.g., to proliferation, migration, and differentiation. Oncogenic mutations in the kinase domain constitutively activate EGFR resulting in deregulated signaling, oncogenic transformation and cancer development[26]. The classical, activating *EGFR* mutations are a point mutation in Exon 21 (L858R, 41 %) and the deletion mutation in exon 19 (45 %)[21,27] (**Figure 4**).

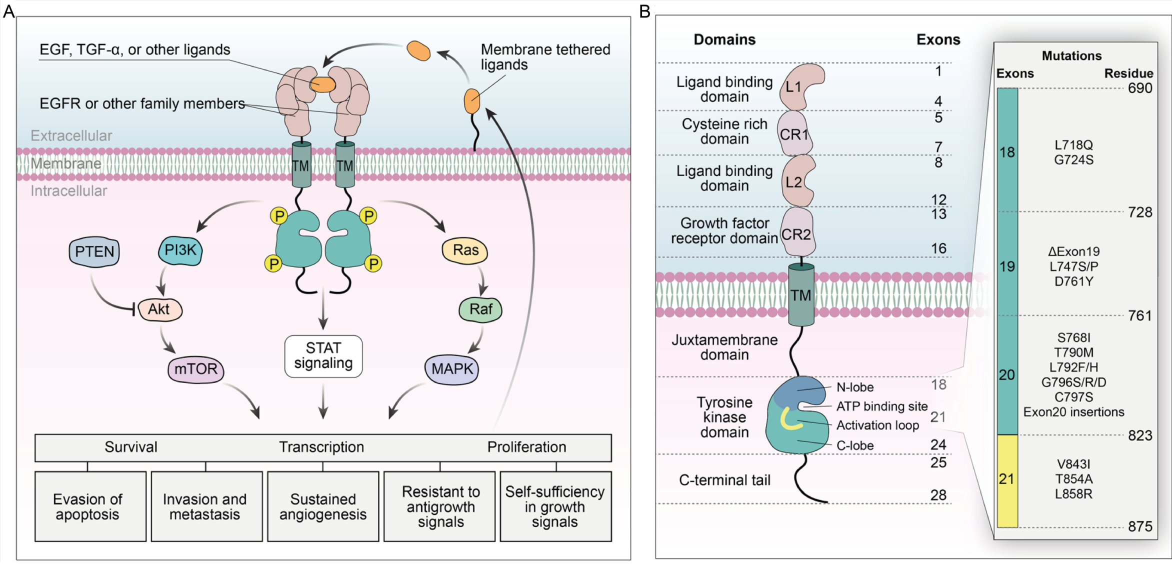

Figure 3: Structure and function of EGFR. A) Schematic activation and signaling pathways of EGFR. B) Detailed extra- and intracellular domains of EGFR. Mutations occurring in the kinase domain are highlighted on the right. Modified from Shi et al.[25].

Not only activating mutation in oncogenes but also receptor and/or ligand overexpression can lead to “oncogene addiction”, in which the growth and survival of the cell becomes dependent on the activation of the specific signaling pathway. Since oncogene addiction can be exploited by inhibition of the activated pathway, it can be considered as the “Achilles’ heel” of the cancer[28]. Small-molecule tyrosine kinase inhibitors (TKIs) were developed to specifically target oncogenic kinase signaling and thereby inhibit the survival signal of the oncogene-addicted cancer cell. Currently, three generations of targeted EGFR inhibitors are available and in clinical use for the treatment of *EGFR*-mutant LUAD. First-generation inhibitors are ATP-competitive inhibitors like gefitinib[9,10] and erlotinib[29]. Second-generation inhibitors, like afatinib[30,31] and dacomitinib[32], exhibit an acrylamide moiety, reacting covalently with a cysteine residue in the kinase domain. The introduction of a Michael-acceptor, resulting in a covalent bond formation with the ErbB-kinase, leads to maximized drug-target residence and improved selectivity within the kinome[33]. Despite impressive response rates to these agents, patient outcome is limited by the development of secondary resistance. The predominant mechanism of resistance in patients treated with first- and second-generation inhibitors is the “gatekeeper” mutation (T790M) in exon 20, which led to the development of third-generation EGFR inhibitors like osimertinib[34-36], that covalently bind mutant EGFR and evade the steric clash with T790M and, on top, spare wild type EGFR[37].

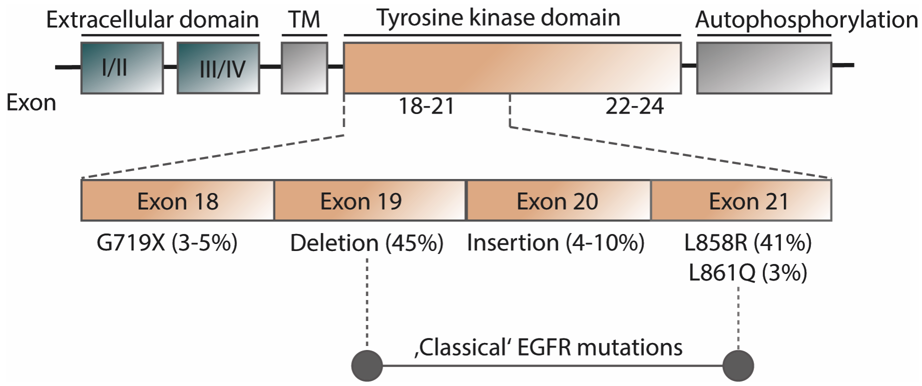

Figure 4: EGFR mutations in non-small cell lung cancer. The classical EGFR mutations are the deletion mutation in Exon 19 (45%) or the activation mutation in exon 21 (L858R 41%). The 'non-classical' mutations are the mutation in the glycine-rich loop (G719X; 3-5%) or insertions in exon 20 (4-10%). Illustration adapted from Sharma et al.[27].

Patients with classical EGFR mutations show remarkable responses to small-molecule EGFR inhibitors, especially to osimertinib. However, a small percentage of patients display mutations in the glycine-rich loop in exon 18 (3-5 %) and insertion mutations in exon 20 (4-10 %), resulting in reduced response to first-, second- or third-generation inhibitors[38,39].

Exon 20 insertion mutations

Insertions or duplications in exon 20 are less common than the classical EGFR mutations and account for 4-10 % within EGFR-mutant LUAD cases[38]. They are enriched in women, never-smokers and patients of Asian background. Till 2021, patients with EGFR exon 20 mutations are treated with chemotherapy, immunotherapy or tyrosine kinase inhibitors (TKIs) approved for other EGFR mutations, but with a response rate below 10 % mainly due to their insensitivity towards standard EGFR TKIs[40-42]. Only a small subset of an atypical EGFR exon 20 insertion mutation (A763_Y764insFQEA) is sensitive towards approved EGFR inhibitors[43]. Besides EGFR, structurally analog exon 20 insertion mutations also occur in HER2. HER2 mutations account for a much lower fraction of cases (~2 % of NSCLC patients), but exon 20 insertions are the predominant type of HER2 aberrations in NSCLC (~90 %). The most prevalent insertion in HER2 is A775_G776insYVMA (77-100 %), and the most common insertion sites in EGFR are D770_N771insX (25.5 %), V769_D770insX (24.6 %) and H773_V774insX (22.6 %)[41,44-46]. At the molecular level, EGFR exon 20 insertions are heterogeneous and can be characterized as in-frame insertions or duplications between 3 and 21 bp, corresponding to 1 to 7 amino acids located in the end of the α-*C*-helix and mainly in the β4-loop following the α-*C*-helix, within a sequence that encodes amino acids 767 to 774 in EGFR (**Figure 5a**). These 1-7 amino acid insertions form a loop structure in direct proximity to the *C*-helix, resulting in a reorientation of the helix and thereby in the constitutive activation of EGFR (**Figure 5b**). The main challenges of designing TKIs that target EGFR exon 20 insertion mutations are the large variety of in-frame insertions and achieving selectivity over wild type (WT) EGFR. Structural modeling of EGFR exon 20 insertions indicates that the insertions at the C-terminal part of the *C*-helix lead to a conformational change, which is similar to the active WT EGFR conformation[47-49].

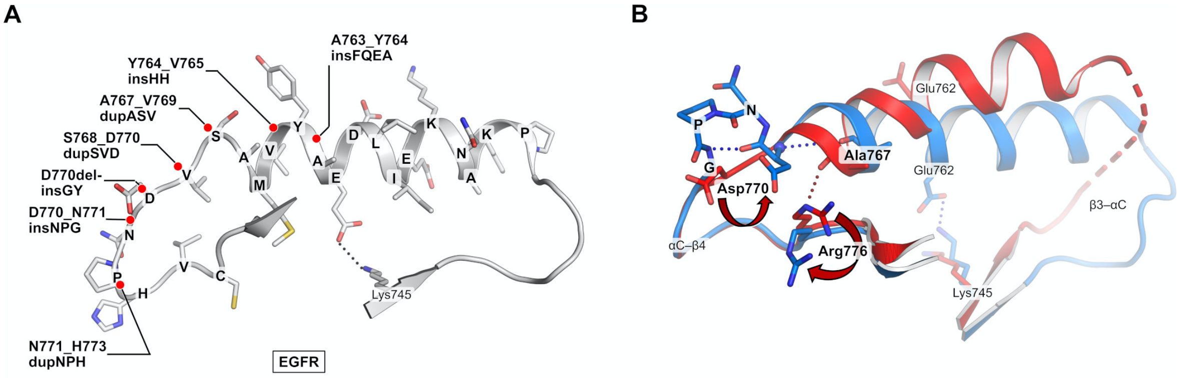

Figure 5: EGFR insertion mutations in exon 20. A) Cartoon structure of EGFR (PDB 1M17). Most prevalent insertion mutations are highlighted. B) Overlay of a crystal structure of EGFR-D770_N771insNPG (blue, PDB 4LMR) and EGFR in an inactive conformation (red, PDB 1XKK)[50].

In the last years, extensive studies have been conducted in order to develop novel therapies to treat EGFR and HER2 exon 20 insertion mutations. Patients treated with first- and second-generation EGFR TKIs show a response rate below 30 % (PFS ~3 months) and patients treated with immune checkpoint inhibitors do not benefit at all (ORR of 0 % and median PFS of 2 months)[48,51-55]. Osimertinib shows clinical efficacy only when used at higher than approved doses (i.e. 160 mg/d; ORR of 25 %, median PFS, 9.7 months)[56-59]. Poziotinib, another covalent EGFR inhibitor, demonstrates promising antitumor activity in vitro, but limited efficacy in patients (ORR of 15 %-19 %, median PFS of 4 to 6 months, median duration of response 7.4 months) combined with high toxicity (rash, diarrhea, stomatitis)[60-62]. In 2021, mobocertinib, a pyrimidine-based, irreversible EGFR inhibitor was approved for the treatment of EGFR exon 20ins-positive NSCLC[63,64]. Another promising new drug is amivantamab, a bispecific antibody that targets EGFR and MET (investigator-assessed response rate, 36%; median PFS, 8.3) has been recently approved by the FDA for the treatment of exon 20 mutated LUAD[47,65,66].

Resistance mechanisms to EGFR TKIs

Despite prolonged disease control and improved overall outcomes, responses to TKIs are often temporary, and acquired drug resistance is one of the major limiting factors preventing cures in cancer patients[67]. On average, TKI resistance inevitably occurs within the first 1-2 years of treatment[68]. The landscape of resistance mutations is quite heterogeneous. It varies from EGFR on-target mutations to target-independent mechanisms like amplifications, fusions/rearrangements, activation of bypass tracks, or histologic and phenotypic transformations[69]. The development of on-target (*EGFR*-dependent) or off-target (*EGFR*-independent) resistance mechanisms differs according to the clinically used TKI.

Despite their different binding features (ability to bind reversible or irreversible), most patients receiving first- and second-generations TKIs predominantly develop *EGFR*-dependent resistance, whereas only 20 % of patients treated with third-generation TKIs exhibit on-target resistance mechanisms[70,71]. This percentage is even lower when osimertinib is used in a first-line setting (on-target resistance: 10-15 %)[72]. **Figure 6** illustrates the spectrum, distribution, and co-occurrence of EGFR on-target resistance mutations occurring after first-line and second- or late-line and osimertinib treatment.

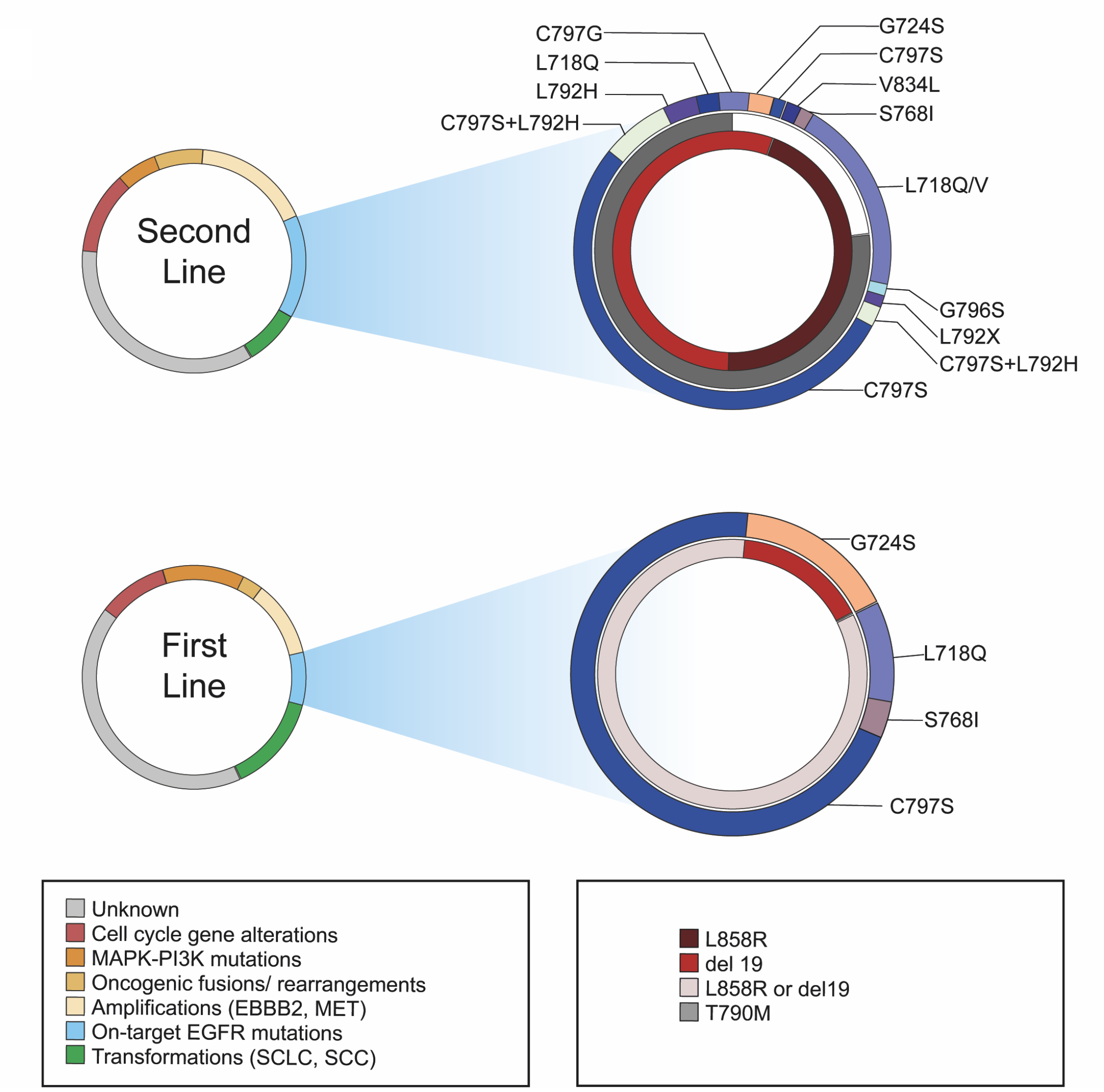

Figure 6: Distribution and co-occurrence of emerging resistance mutations in EGFR after first or second/later line osimertinib treatment. The reading direction is from the inner circle (activation mutation: del19 or L858R) to the outer circles. Possible mutation combinations are in line and the size of the segments is proportional to the percentage of the occurring mutations[73].

Mutations of critical amino acid residues in the kinase domain of EGFR arise quickly after TKI treatment and differ according to the used inhibitor. The most studied on-target resistance mutation is the gatekeeper mutation in exon 20 (T790M), which arises after treatment with first- and second-generation EGFR TKIs and results in a steric clash in the ATP binding pocket[74]. Third-generation inhibitors like osimertinib evade the steric clash with T790M and bind covalently to Cys797. In turn, Cys797 reacts covalently with the acrylamide warhead of osimertinib, forming an irreversible bond between inhibitor and target protein. EGFR-C797X mutations are the most frequent *EGFR* on-target resistance mechanism to osimertinib with serine as the most frequently substituted amino acid (C797S). Surprisingly, the acquired EGFR-C797S mutation was first found in patients treated with third-generation inhibitors, even though second-generation inhibitors bind the same cysteine residue[75-77]. The spectrum of additional, less frequent combinations of on-target resistance mutations is very diverse. EGFR-G724S is a rare mutation in the highly flexible glycine-rich loop in the N-loop of the kinase domain, arising exclusively in patients with EGFR-del19 treated with osimertinib. The mutation results in a rigidification of the glycine-rich loop, hence disrupting the F723-osimertinib contact and resulting in resistance[78-81]. Other rare mutations like EGFR-L718 and EGFR-G719 (exon 18) affect the ATP-binding site and EGFR-G796X on the solvent-front (exon 20), and EGFR-L792X in the hinge pocket inducing steric hindering to osimertinib[72,82-84]. Besides EGFR point mutations, *EGFR* gene amplification may drive resistance mechanism after third-generation EGFR TKI failure[85,86].

EGFR-independent resistance mechanisms involve the activation of alternative cell signaling pathways, most frequently the MET receptor tyrosine kinase signaling pathway (5-22 %). MET mutations, amplifications and increased expression of MET ligands like HGF or MET induce resistance by bypassing EGFR signaling through activation of signal transducer and activator of transcription (STAT), mitogen-activated protein kinase (MAPK) and phosphoinositide 3-kinase (PI3K)[87]. Amplification of *HER2* also mediates EGFR TKI resistance through activation of MAPK and PI3K signaling pathway[88]. In addition, oncogenic fusions and chromosomal rearrangements including, i.a. *RET*, *BRAF*, *NTRK*, *ROS1* and *FGFR* have been identified in 4-7 % as well as mutations in *RAS* (1-7 %), *BRAF* (3 %) and *PIK3CA* (3-12 %) and alterations of cell cycle-related genes (10-12 %) also lead to EGFR TKI resistance. Another off-target resistance mechanism is the histologic and phenotypic transformations into SCLC or squamous cell carcinoma. SCLC transformation is reported in ~14 % of EGFR-mutant cases after first-generation EGFR TKI. In patients treated with third-generation EGFR TKI the rate of SCLC transformation is 4-15 %[69,70]. SCLC transformation occurs in patients with inactivation alterations in tumor suppressor genes *TP53* and *RB1* and recent studies underline that *RB1/TP53*-mutations are necessary but not sufficient for transformation[89]. 3-15 % of EGFR-mutant LUAD patients display squamous cell transformation after first- and second-line osimertinib[69,90-92].

Due to the ever-changing and diverse landscape of resistance mechanisms, the continuous development of next generation TKIs, as well as novel treatment approaches, are required. Therefore, understanding the structural changes inside the kinase domain in case of on-target resistance and the complex molecular biology in case of off-target resistance are key for designing of novel treatment options[73].

1.3 Small-cell lung cancer

Small-cell lung cancer (SCLC) is the deadliest lung cancer subtype with only minor improvements in the overall-survival for decades. Main factors for the poor prognosis are the absence of early detection, the rapidly occurring drug resistance to chemotherapy, and the lack of targetable alterations. In comparison to NSCLC, SCLC lacks alterations in druggable targets like RTKs and consequently targeted therapy with TKIs is not applicable. The standard of care remains conventional, cytotoxic chemotherapy, with the recent addition of immune checkpoint inhibitors against PD-1/PD-L1. Two PD-L1 antibodies – atezolizumab and durvalumab – show, in combination with platinum-based drugs and etoposide, a marginal increase in overall survival[93,94]. While SCLC patients initially show a good response to chemotherapy, most patients relapse rapidly. Therapeutic options for patients with relapsed disease are limited, with a median survival below one year. Several mechanisms that may contribute to chemotherapy resistance have been proposed but seem to be quite heterogenous and context-dependent in their nature[95-97].

SCLC is a fast-growing, early metastatic, high-grade neuroendocrine tumor and predominantly arises in current or former smokers[98]. Accordingly, the mutational profile of SCLC exhibits a clear smoking signature. The biallelic loss of two tumor suppressors *TP53* (98 %) and *RB1* (91 %) is found in the vast majority of SCLC tumors[99]. This concomitant inactivation of tumor suppressors is the defining genetic feature of SCLC compared to other tumors like LUAD, where the activating oncogenic mutations are essential for tumorigenesis[98]. Other inactivating mutations common in SCLC include *NOTCH1* (25 %), *CREBBP* (15 %), *PTEN* (9 %), and *CDKN2A* (5 %), whereas gain of function mutations are found in *KIT* (6 %), *FGFR1* (6 %), *TP73* (13 %) and *PIK3CA* (3 %)[99]. SCLC tumors typically show the expression of one of four predominant transcription factors ASCL1, NEUROD1, POUF2F3, or YAP1 that are partially associated with the neuroendocrine or non-neuroendocrine features of the tumor[100]. Another frequent genetic alteration in SCLC is amplification of the *MYC* family members, or paralogs MYC, MYCN and MYCL, which are found to be activated in up to 20 % of all SCLC patients. A recent study of SCLC patients and patient-derived cell lines found that overexpression of individual MYC paralogs is mutually exclusive[101]. While *MYCL* expression is generally associated with the ASCL1 SCLC subtype, *MYC* is preferentially expressed in the other subtypes[102].

The transcription factor MYC modulates global gene expression and is a master regulator of multiple cellular processes, including proliferation, differentiation, metabolism, apoptosis, and cell cycle[103]. Under physiological conditions, MYC levels are tightly regulated whereas aberrant, increased MYC expression drives tumorigenesis. In cancer cells, MYC regulates cancer cell-intrinsic as well as host-dependent pathways to promote cancer cell growth and survival but can also mediate cancer cell dormancy to overcome nutrient-low environments. Also, MYC activation enables cancer cells to evade and inhibit the host immune system[104,105]. Due to its oncogenic potential and important function for tumor cells, MYC is one of the most valuable targets in cancer[103]. Unfortunately, targeting MYC itself and MYC function is difficult[106]. On the one hand, MYC is rarely mutated but deregulated in ~70 % of all human cancers. On the other hand, MYC is involved in important in several physiological processes. Thus, inhibiting MYC leads to undesirable side effects[107]. Furthermore, MYC is an intrinsically disordered protein with no binding pocket for small molecule inhibitors and its mainly nuclear localization is inapproachable for antibody-based drugs[108]. This is why MYC is currently considered undruggable and therefore, it is vital to understand the complex function of MYC in more detail to uncover new strategies to target MYC-dependent signaling[109,110].

The structure and function of MYC

MYC is a basic helix-loop-helix leucine zipper (bHLHLZ) transcription factor and consists of three, functional domains – a transactivation domain (TAD) at the *N*-terminus, a proline-rich middle segment, glutamic acid, threonine and protein residues (PEST), and a *C*-terminal end containing the basic helix-loop-helix leucine zipper domain (bHLHLZ) (**Figure 7**)[111]. All MYC isoforms share MYC homology boxes (MBs) which are unstructured but acquire partner-induced, specific conformations and contribute to MYC function through interaction with protein-binding partners. The unstructured *N*-terminal region with MYC box I and II is involved in transcriptional activation. Two phosphorylation sites (Thr58 and Ser62) are important for the protein stability and degradation of MYC protein and are located in MB I[112]. The central region consists of the PEST domain, MB III and MB IV and the nuclear localization sequence (NLS). This region is essential for interacting with Smad2 and Smad3, which are important for the MYC-interacting zinc finger protein 1 (MIZ1)-dependent transcriptional activation[113,114]. The *C*-terminal end consists of a basic region (BR), mediating sequence-specific DNA binding and a helix-loop-helix leucine zipper domain (HLH-LZ). Mainly, the MYC-DNA interaction is mediated through a canonical enhancer-box (E-box) DNA element CACGTG. The HLH-LZ domain exhibits an α helical structure and serves as a protein-protein interaction-site for Myc-associated factor X (MAX) and MIZ1[115,116]. MYC DNA binding leads to transcriptional activation or repression, depending on the interaction partner. MYC activates target gene expression as heterodimers with MAX, whereas the MYC/MIZ1 complex mediates both transcriptional activation as well as repression[117].

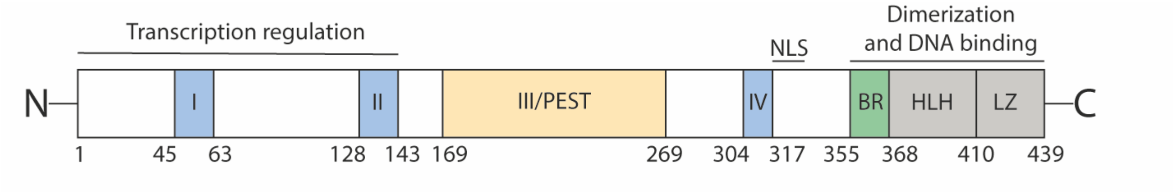

Figure 7: Schematic representation of MYC protein structure. The 439 amino acid protein sequence contains of 4 MYC boxes (I-IV), a PEST segment, a nuclear localization sequence (NLS) and an ~100 amino acid *C*-terminal region consisting of the basic helix-loop-helix leucine zipper (BR–HLH–LZ) domain[117].

MYC-interacting zinc finger protein 1 (MIZ1)

In 1997 MIZ1 (Zbtb17) was first identified by Peukert and colleagues in a yeast two-hybrid screen as a direct protein interacting with the *C*-terminal tail of MYC[116]. The poly-Cys2His2 zinc finger (ZF) transcriptional factor MIZ1 contains an *N*-terminal poxvirus and zinc-finger BTB (Broad complex, Tramtrack, and Bric-a-brac)-POZ (poxvirus and zinc finger) domain followed by 13 zinc fingers at the C terminus (**Figure 8**). In the *C*-terminal end of MIZ1 a short helical domain between zinc finger 12 and 13 interacts with the *C*-terminal domain of MYC. The BTB/POZ domain is a homo- or hetero-oligomerization domain required for chromatin association. Deletion of the POZ domain influences the protein–chromatin interaction and hinders the transcriptional function and was described to impair cell-cycle, apoptosis or early T and B cell development[118-120].

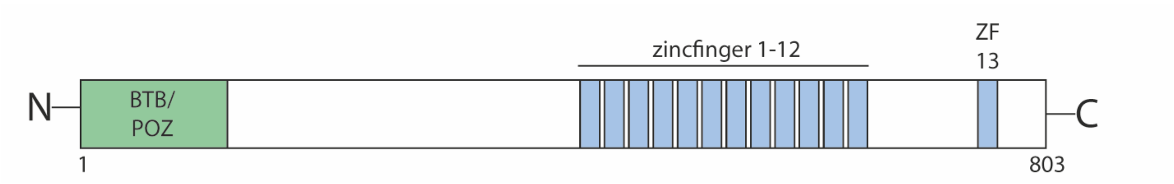

Figure 8: Structure of MIZ1. Miz1 consist in total of 803 amino acids. *N*-terminal located is the BTB/POZ domain, which is necessary for multimerization. In the C-terminus are 13 zincfingers (ZF). They mediate DNA binding and interactions with other proteins (e.g. MIZ1).

MIZ1 is an activator of cell cycle regulatory genes through recruitment of different co-activators, such as histone acetyltransferase p300 and nucleophosmin (Npm1). MIZ1 activates transcription of genes like the cyclin-dependent kinase inhibitors *P15*^{INK4} (*p15*)*, p21*^{CIP1} (*p21*) and *p57*^{KIP2} (*p57*)[121-123]. MIZ1 is also involved in processes like autophagy, endocytosis, vesicular trafficking, inflammation and DNA repair. MYC can directly bind MIZ1, inhibiting the interaction between MIZ1 and its co-activators and thus repressing the expression of *p15*, *p21* and *p57*. For example, in response to DNA damage, MYC inhibits expression of *p21Cip1* through MIZ1 binding. Another group of genes altered by the MYC-MIZ1 complex are cell-adhesion molecules, especially integrins. In breast cancer repression of integrin expression by MYC-MIZ1 complex is associated with the suppression of cell migration and metastasis. This in turn indicates that inhibiting the MYC-MIZ1 complex may promote metastasis. Furthermore, MIZ1 upregulates expression of the antiapoptotic *BCL2* gene family, whereas MIZ1 combined with high levels of MYC represses the expression of *BCL2* genes[101,124,125].

MIZ1 ∆POZ model system

MIZ1 can be both a transcriptional activator or a repressor and the level of interaction with MYC may be a critical determinant that distinguishes the two forms of gene regulation.

Miz1 is essential during mouse early development and mice with a homozygous deletion of *Zbtb17* gene die during early embryogenesis (E7.5). Mice with a Miz1-ΔPOZ deletion die later in embryogenesis[126]. Conditional Miz1 knockout mice demonstrate important roles of Miz1 in B- and T-cell differentiation; keratinocyte adhesion, differentiation and proliferation; hair follicle orientation as well as skin carcinogenesis[118,127-130]. In 2007 Gebhardt et al. generated a mouse model with an inducible, truncated Miz1. Exons encoding the POZ domain are flanked by loxP-sites and deletion is mediated by Cre recombination (**Figure 9**)[127].

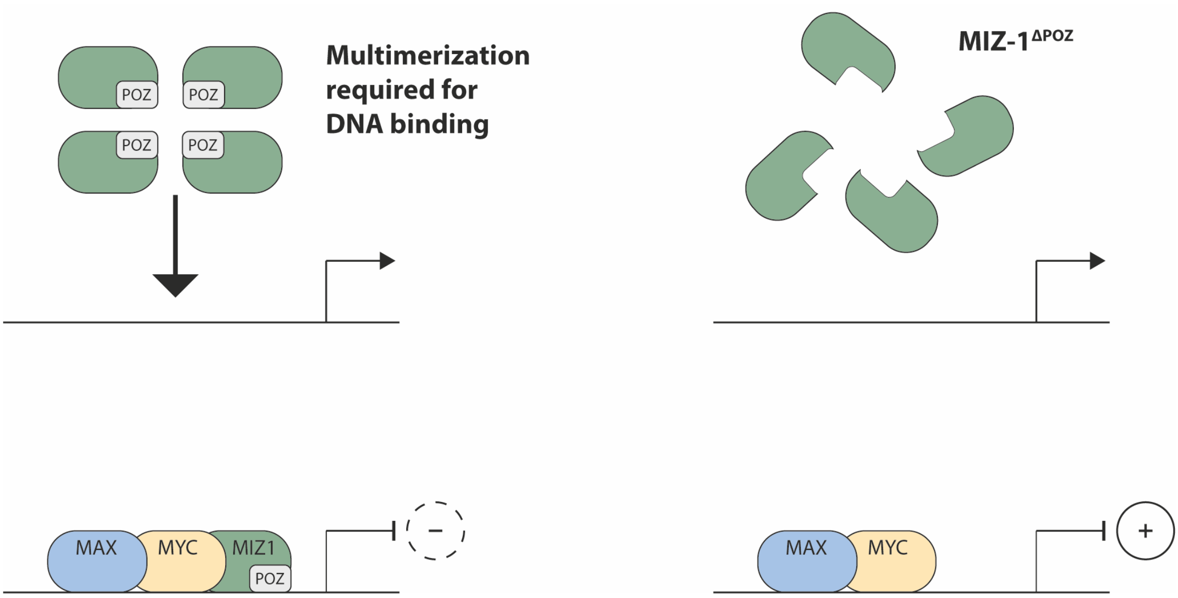

Figure 9: Schematic model of transcriptional regulation by MIZ1. The POZ domain of Miz1 is required for multimerization, which in turn is required for DNA binding. A mutated Miz1 lacking the POZ domain (Miz1$^{\Delta POZ}$) is unable to form multimers and hence inhibited to stably associate with chromatin and regulate transcription. Miz1 can act as activator or repressor of target gene expression. Illustration adapted from Möröy et al.[131].

The POZ domain is required for MIZ1 multimerization which in turn is required for chromatin association. MIZ1, lacking the POZ domain (Miz1$^{\Delta POZ}$) is unable to bind chromatin stably and is nonfunctional as a transcriptional transregulator. Studies in neuroblastoma, medulloblastoma and acute lymphoblastic leukemia (ALL) showed prolonged survival of Miz1$^{\Delta POZ}$-mice compared to wild type Miz1.[119,125,132].

2 Aim of the Thesis

The work aims to gain insight into the complex biology of distinct lung cancer subtypes in order to accelerate the development of novel therapies for genetically defined lung cancer patients.

First, the limited activity of EGFR and HER2 inhibitors developed to tackle classic EGFR/HER2 mutations motivated us to investigate novel targeted TKIs to improve their activity against EGFR exon 20 mutant tumors. Small molecule inhibitors were characterized in vitro and in vivo to obtain insights into their structure-activity relationship (SAR) and aid the iterative optimization of their selectivity profile.

Secondly, co-existing of *BRAF*- and *EGFR*-mutations in *EGFR*-mutant lung cancer patients are investigated. Combination therapies of EGFR and MET inhibitors are evaluated in an effort to overcome co-occurring EGFR/BRAF resistance mutations after EGFR inhibition in lung adenocarcinoma.

Third, the interplay between the transcription factors MYC and MIZ1 in a SCLC background is characterized to decipher the impact of Miz1 in *Myc*-driven SCLC tumorigenesis and to discover transcriptional changes as well as possible vulnerabilities.

3 Publications and Manuscripts

3.1 Insight Into Targeting Exon20 Insertion Mutations of the Epidermal Growth Factor Receptor with Wild Type-Sparing Inhibitors

Jonas Lategahn[1,2,3,‡] Hannah L. Tumbrink,[4,5,‡] Carsten Schultz-Fademrecht,[1,6,‡] Alena Heimsoeth,[4,5] Lisa Werr,[5] Janina Niggenaber,[2,3] Marina Keul,[2,3] Fatma Parmaksiz,[4,5] Matthias Baumann,[6] Sascha Menninger,[6] Eldar Zent,[6] Ina Landel,[2,3] Jörn Weisner,[2,3] Kirujan Jeyakumar,[2,3] Leonie Heyden,[2,3] Nicole Russ,[4,5] Fabienne Müller,[4,5] Carina Lorenz,[4,5] Johannes Brägelmann,[4,5,7,8] Inga Spille,[4,5] Tobias Grabe,[2,3] Matthias P. Müller,[2,3] Johannes M. Heuckmann,[1] Bert Klebl,[6] Peter Nussbaumer,[6] Martin L. Sos[4,5,]* and Daniel Rauh[2,3,]*

[‡]J.L., H.L.T. and C. S-F. contributed equally as co-first authors.

Published in Journal of Medicinal Chemistry, April 29, 2022

DOI: 10.1021/acs.jmedchem.1c02080

3.2 Clonal dynamics of *BRAF*-driven drug resistance in *EGFR*-mutant lung cancer

Diana Schaufler[‡1], David Ast[‡2,3,4], Hannah L. Tumbrink[2,3], Nima Abedpour[3,5], Lukas Maas[3], Ayla Schwäbe[2,3], Inga Spille[2,3], Stefanie Lennartz[2,3], Jana Fassunke[6], Mihaela Aldea[7], Benjamin Besse[7], David Planchard[7], Lucia Nogova[1], Sebastian Michels[1], Carsten Kobe[8], Thorsten Persigehl[9], Theresa Westphal[1], Sophia Koleczko[1], Rieke Fischer[1], Jan-Phillip Weber[1], Janine Altmüller[10], Roman K. Thomas[3,6,11], Sabine Merkelbach-Bruse[6], Oliver Gautschi[12], Laura Mezquita[13], Reinhard Büttner[6], Jürgen Wolf[1], Martin Peifer[3], Johannes Brägelmann*[2,3,4,5], Matthias Scheffler*[1] and Martin L. Sos*[2,3,5]

Published in Nature precision oncology, December 17, 2021

DOI: 10.1038/s41698-021-00241-9

3.3 MIZ1–ΔPOZ shapes treatment response in small cell lung cancer

Hannah L. Tumbrink et al.

Manuscript in preparation

3.1 Insight Into Targeting Exon20 Insertion Mutations of the Epidermal Growth Factor Receptor with Wild Type-Sparing Inhibitors

Jonas Lategahn[1,2,3,‡] *Hannah L. Tumbrink,*[4,5,‡] *Carsten Schultz-Fademrecht,*[1,6,‡] *Alena Heimsoeth,*[4,5] *Lisa Werr,*[5] *Janina Niggenaber,*[2,3] *Marina Keul,*[2,3] *Fatma Parmaksiz,*[4,5] *Matthias Baumann,*[6] *Sascha Menninger,*[6] *Eldar Zent,*[6] *Ina Landel,*[2,3] *Jörn Weisner,*[2,3] *Kirujan Jeyakumar,*[2,3] *Leonie Heyden,*[2,3] *Nicole Russ,*[4,5] *Fabienne Müller,*[4,5] *Carina Lorenz,*[4,5] *Johannes Brägelmann,*[4,5,7,8] *Inga Spille,*[4,5] *Tobias Grabe,*[2,3] *Matthias P. Müller,*[2,3] *Johannes M. Heuckmann,*[1] *Bert Klebl,*[6] *Peter Nussbaumer,*[6] *Martin L. Sos*[4,5,]* *and Daniel Rauh*[2,3,]*

[1]PearlRiver Bio GmbH, Otto-Hahn-Str. 15, 44227 Dortmund, Germany

[2] Faculty of Chemistry and Chemical Biology, TU Dortmund University, Otto-Hahn-Str. 4a, 44227 Dortmund, Germany

[3] Drug Discovery Hub Dortmund (DDHD) am Zentrum für Integrierte Wirkstoffforschung (ZIW), 44227 Dortmund, Germany

[4] Molecular Pathology, Institute of Pathology, University Hospital of Cologne, Kerpener Str. 62, 50937 Cologne, Germany

[5] Department of Translational Genomics, Faculty of Medicine and University Hospital Cologne, University of Cologne, 50931 Cologne, Germany

[6] Lead Discovery Center GmbH, Otto-Hahn-Str. 15, 44227 Dortmund, Germany

[7] Mildred Scheel School of Oncology Cologne, Faculty of Medicine and University Hospital Cologne, University of Cologne, 50931 Cologne, Germany

[8] Center for Molecular Medicine Cologne, Faculty of Medicine and University Hospital Cologne, University of Cologne, 50931 Cologne, Germany

---

[‡]J.L., H.L.T. and C. S-F. contributed equally as co-first authors.

*Correspondence to:

Prof. Dr. Daniel Rauh, TU Dortmund University, Faculty of Chemistry and Chemical Biology, Otto-Hahn-Str. 4a, 44227 Dortmund, Germany, Tel.: +49 231 755 7080, eMail: daniel.rauh@tu-dortmund.de, Twitter: @DDHDortmund, website: DDHDortmund.de;

Prof. Dr. Martin L. Sos, University of Cologne, Faculty of Medicine and University Hospital Cologne, Institute of Pathology, Molecular Pathology & Department of Translational Genomics, Weyertal 115b, 50931 Cologne, Germany. Tel.: +49 221-478 96175; E-Mail: martin.sos@uni-koeln.de

Specific contributions:

- All in vitro cellular characterization of LDC8201 and LDC0496
- In vivo efficiency study of afatinib, poziotinib and LDC8201
- Visualization, Manuscript writing and editing

Journal of
Medicinal
Chemistry

pubs.acs.org/jmc
Article

Insight into Targeting Exon20 Insertion Mutations of the Epidermal Growth Factor Receptor with Wild Type-Sparing Inhibitors

Jonas Lategahn,[◆] Hannah L. Tumbrink,[◆] Carsten Schultz-Fademrecht,[◆] Alena Heimsoeth, Lisa Werr, Janina Niggenaber, Marina Keul, Fatma Parmaksiz, Matthias Baumann, Sascha Menninger, Eldar Zent, Ina Landel, Jörn Weisner, Kirujan Jeyakumar, Leonie Heyden, Nicole Russ, Fabienne Müller, Carina Lorenz, Johannes Brägelmann, Inga Spille, Tobias Grabe, Matthias P. Müller, Johannes M. Heuckmann, Bert M. Klebl, Peter Nussbaumer, Martin L. Sos,[*] and Daniel Rauh[*]

Cite This: *J. Med. Chem.* 2022, 65, 6643−6655

ABSTRACT: Despite the clinical efficacy of epidermal growth factor receptor (EGFR) inhibitors, a subset of patients with non-small cell lung cancer displays insertion mutations in exon20 in EGFR and Her2 with limited treatment options. Here, we present the development and characterization of the novel covalent inhibitors LDC8201 and LDC0496 based on a 1*H*-pyrrolo[2,3-*b*]pyridine scaffold. They exhibited intense inhibitory potency toward EGFR and Her2 exon20 insertion mutations as well as selectivity over wild type EGFR and within the kinome. Complex crystal structures with the inhibitors and biochemical and cellular on-target activity document their favorable binding characteristics. Ultimately, we observed tumor shrinkage in mice engrafted with patient-derived EGFR-H773_V774insNPH mutant cells during treatment with LDC8201. Together, these results highlight the potential of covalent pyrrolopyridines as inhibitors to target exon20 insertion mutations.

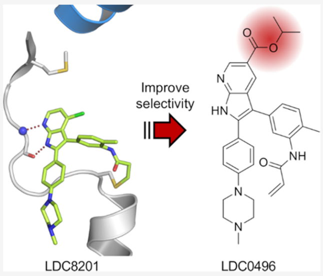

The epidermal growth factor receptor (EGFR) plays a pivotal role in the regulation of cellular proliferation, differentiation, migration, and cell death.[1,2] Mutations perturbing the intracellular kinase domain's function are often linked to the onset and progression of non-small cell lung cancer (NSCLC).[3−6] The most common mutations, exon19 deletions and the L858R point mutation, are sensitive to clinically available tyrosine kinase inhibitors (TKIs).[3,7−10] Among these are erlotinib,[11] afatinib,[12,13] and osimertinib,[14−16] (Figure S1) with osimertinib showing limited EGFR wild type on-target toxicity as well as the ability to overcome acquired drug resistance of the gatekeeper mutation T790M.[16,17] However, approximately 5% of EGFR-mutant NSCLC patients exhibit insertion mutations in exon20.[18−20] These mutations occur predominantly within the C-terminal end of the helix αC and in the following αC-β4 loop, varying from one to seven amino acids and may also be found in the homologous region of Her2 (Figure 1a).[18] Several inhibitors are currently under clinical evaluation to meet the need for a targeted therapy. Among these are the quinazoline-based inhibitor poziotinib[21−23] and the pyrimidine-based inhibitor mobocertinib/TAK-788[24,25] (Figure 1b). To establish a further chemotype as an effective TKI, we developed efficient, EGFR wild type-sparing inhibitors of EGFR and Her2 exon20 insertion mutants based on the 1*H*-pyrrolo[2,3-*b*]pyridine scaffold. Herein, we present the development and characterization of the lead LDC8201 and its derivative LDC0496 (Figure 1b).

■ RESULTS AND DISCUSSION

Earlier structure-based drug design studies established 7*H*-pyrrolo[2,3-*d*]pyrimidines as covalent inhibitors targeting mutant variants of EGFR.[26] The covalent binding of cysteine 797 in EGFR or 805 in Her2 by the introduction of appropriately positioned acrylamide warheads has been a valuable approach, as exemplified by several FDA-approved covalent EGFR/Her2 inhibitors.[9,17] To yield inhibitors effectively targeting exon20 insertion mutations, we modified the core scaffold by means of nitrogen-to-carbon exchange. This modification allowed further modifications of the 5-position as discussed below. The resulting 1*H*-pyrrolo[2,3-*b*]pyridines were designed to act through a covalent mode of action, by the introduction of a phenyl linker in the 3-position to bring an acrylamide warhead in close proximity to the reactive cysteine based on the knowledge gained from previous

Received: December 21, 2021
Published: April 29, 2022

https://doi.org/10.1021/acs.jmedchem.1c02080
J. Med. Chem. 2022, 65, 6643−6655

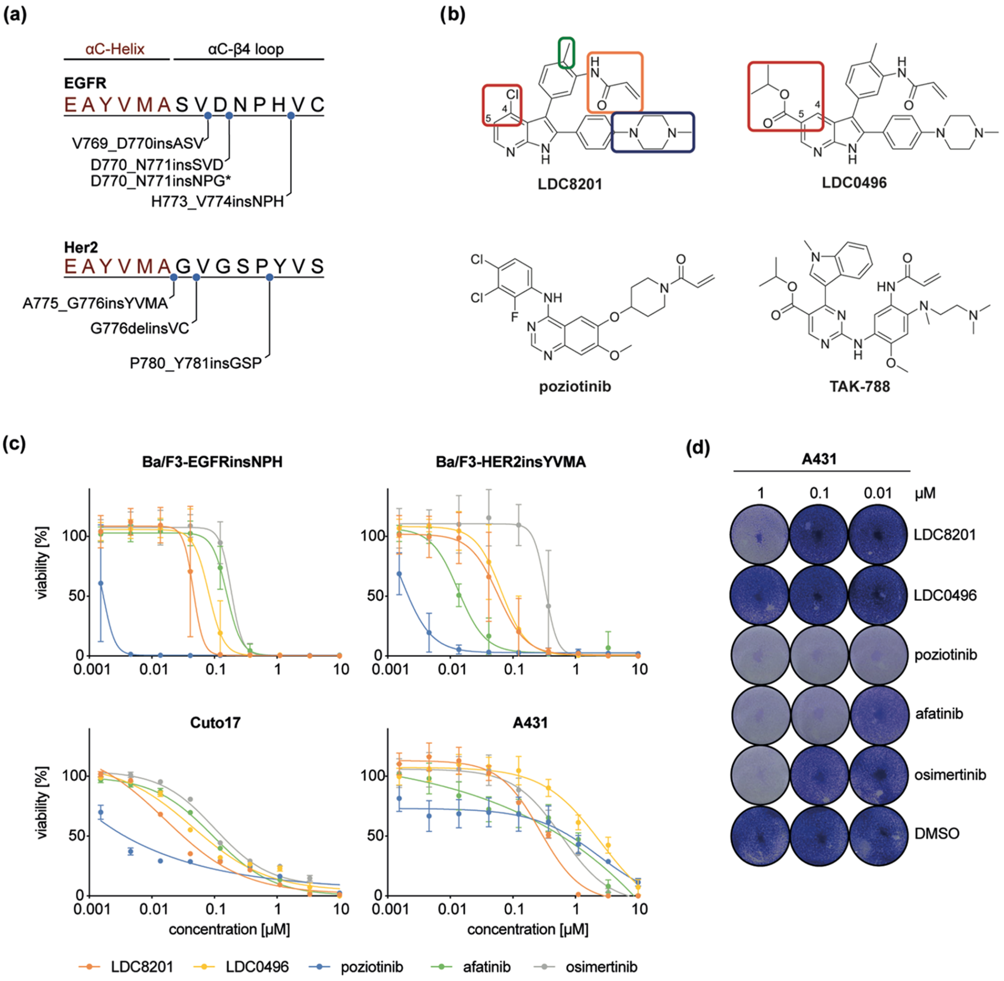

Figure 1. (a) Overview of the most prevalent exon20 insertion mutations in EGFR and Her2 and their point of insertion in the sequence of the loop (shown in black) following helix αC (shown in red). *EGFR-insNPG is less prevalent in patients but used as a model system. (b) Inhibitors targeting EGFR exon20 insertion mutants, such as the lead LDC8201 and its derivative LDC0496 (the SAR is highlighted), as well as poziotinib and mobocertinib/TAK-788. Key structural determinants, according to SAR parameters, are: the methyl group (highlighted in green); the acrylamide warhead (highlighted in orange); the methyl piperazine (highlighted in blue); and positions 4 and 5 (highlighted in red). See also Figure S1. (c) Dose−response curves of cell viability of Ba/F3 cell lines and patient-derived cell lines. Shown is the mean of a minimum of three independent measurements conducted in triplicates; error bars indicate standard deviation (SD). See also Figure S3. (d) Crystal violet staining of EGFR-wt A431 cells.

investigations.[26] Subsequently, intensive medicinal chemistry optimization cycles yielded the lead LDC8201 (Figure 1b). The methyl group (highlighted in green) adjacent to the acrylamide warhead (highlighted in orange) was found to prevent the molecule from degradation in mouse liver microsomes through amide bond hydrolysis (Figure S2a). In addition, we found that the methyl piperazine solubilizing group (highlighted in blue) provided the required features for oral absorption and bioavailability, which might be a consequence of a reduced pK_a value compared to other solubilizing groups investigated (Figure S2b). Reduction of the pK_a results in a decreased fraction of ionized form, which is considered beneficial for absorption across the gut wall. In addition, it facilitated sufficient compound solubility (Table S1). Positions 4 and 5 (highlighted in red) ultimately yielded the tool to adjust selectivity over EGFR wild type.

With these tools in hand, LDC8201 was developed and exhibited moderate *in vitro* clearance of 93 µL/min/mg in

Table 1. Cellular Potency as Determined in a CellTiter-Glo (CTG) Assay of LDC8201, LDC0496, and Compounds 1−6 with Different Substitutions in the 4- and 5-Positions (See Figure 1b)

			CTG EC$_{50}$ [μM][a] (CTG GI$_{50}$ [μM])[b]		
compound	4-R	5-R	Ba/F3 (EGFR-insNPH)	Ba/F3 (Her2-insYVMA)	A431
LDC8201	Cl	H	0.053 ± 0.003 (0.048 ± 0.028)	0.086 ± 0.006 (0.059 ± 0.043)	0.318 ± 0.016 (0.303 ± 0.016)
1	OMe	H	0.052 ± 0.006 (n.d.)	0.082 ± 0.007 (n.d.)	0.289 ± 0.035 (n.d.)
2	H	CN	0.090 ± 0.016 (n.d.)	0.139 ± 0.007 (n.d.)	0.169 ± 0.001 (n.d.)
3	H	CONHBn	0.354 ± 0.049 (n.d.)	0.230 ± 0.013 (n.d.)	0.579 ± 0.025 (n.d.)
4	H	CONH*i*Pr	0.157 ± 0.024 (n.d.)	0.107 ± 0.014 (n.d.)	0.907 ± 0.021 (n.d.)
5	H	COOMe	0.425 ± 0.040 (n.d.)	0.248 ± 0.012 (n.d.)	1.672 ± 0.031 (n.d.)
LDC0496	H	COO*i*Pr	0.152 ± 0.011 (0.083 ± 0.029)	0.162 ± 0.010 (0.070 ± 0.037)	2.660 ± 0.129 (1.965 ± 0.484)
6	H	CHCOO*i*Pr	0.205 ± 0.028 (n.d.)	0.478 ± 0.090 (n.d.)	2.048 ± 0.030 (n.d.)
poziotinib	-	-	0.007 ± 0.001 (0.002 ± 0.001)	0.012 ± 0.001 (0.002 ± 0.001)	1.445 ± 0.168 (0.654 ± 0.547)
afatinib	-	-	0.167 ± 0.010 (0.161 ± 0.038)	0.097 ± 0.034 (0.015 ± 0.002)	0.535 ± 0.040 (0.594 ± 0.277)
osimertinib	-	-	0.199 ± 0.016 (0.192 ± 0.049)	0.545 ± 0.050 (0.347 ± 0.124)	0.956 ± 0.037 (0.596 ± 0.094)

[a] Values are the mean ± standard error of the mean (SEM) of a minimum of two independent measurements in duplicate. [b] Values are the mean ± SD of a minimum of three independent measurements in triplicate; EC$_{50}$ and GI$_{50}$ values were determined in different laboratories with slightly different conditions (see the Experimental Section for details). n.d. = not determined.

mouse liver microsomes and a moderate flux over a Caco-2 monolayer from the apical (A) to the basolateral (B) site with P_{app} = 51 nm/s (Table S1). Accordingly, mouse *in vivo* studies revealed a high bioavailability of F = 59%, an exposure of AUC$_{0\text{-inf,obs}}$ = 2082 h·ng/mL, and a clearance of $t_{1/2}$ = 126 min after oral gavage of 30 mg·kg^{-1} (Table S2 and Figure S2b). The inhibitory potency was assessed using the CellTiter-Glo (CTG) assay with Ba/F3 cells stably transfected with EGFR-H773_V774insNPH and Her2-A775_G776insYVMA (Table 1 and Figures 1c and S3). LDC8201 showed high inhibitory potency in these assays with GI$_{50}$ values of 48 and 59 nM for mutant EGFR and Her2, respectively. The high potency was confirmed in EGFR-mutated patient-derived cell lines Cuto 14 (V769_D770insASV) and Cuto 17 (H773_V774insNPH) with GI$_{50}$ values of 39 and 23 nM, respectively.

Of note, LDC8201 inhibited EGFR wild type-bearing A431 cells with a GI$_{50}$ of 303 nM, resulting in a moderate selectivity of 6-fold for Ba/F3 cells expressing mutant EGFR-H773_V774insNPH. Aiming to increase the selectivity, we introduced different moieties at positions 4 and 5 of the pyrrolopyridine scaffold sites, which have been associated with potency and selectivity (Table 1). We thereby identified LDC0496 (Figure 1b), which harbored an isopropyl ester moiety in the 5-position and exhibited GI$_{50}$ values of 83 and 70 nM toward EGFR-insNPH and Her2-insYVMA-mutated Ba/F3 cells, respectively. Similarly, insASV Cuto 14 and insNPH Cuto 17 cells revealed GI$_{50}$ values of 59 and 55 nM, respectively. Importantly, LDC0496 revealed reduced wild type inhibition in A431 cells with a GI$_{50}$ of 1965 nM, resulting in a remarkable selectivity of 24-fold over EGFR-insNPH and 28-fold over Her2-insYVMA-mutated Ba/F3 cells. To complement this dataset, a crystal violet staining was performed using A431 cells to assess the potency toward wild type (Figure 1d). Across all compounds tested, LDC0496 stood out with clearly visible cell density after treatment with concentrations up to 1 μM, further highlighting the wild type-sparing nature of this inhibitor.

LDC8201 and LDC0496 were further profiled in a panel of patient-derived cell lines comprising EGFR- or Her2-mutated cell lines and cell lines bearing mutations in the KRas, FGFR2, or ALK genes (Figure S3a). These studies revealed the selectivity of LDC8201 and LDC0496 toward EGFR/Her2 mutant cells with GI$_{50}$ values in the ranges of 4−880 and 10−2270 nM, respectively, while the lowest potency was observed with EGFR wild type A431 and EGFR-T790M+C797S mutant PC9 cells. Cancer cell lines with various mutations in other kinases were inhibited to a lower degree by LDC8201 (with GI$_{50}$ values ranging from 300−3040 nM) and were not inhibited by LDC0496 (with GI$_{50}$ values of 1800−6390 nM). In addition, a set of 16 Ba/F3 cell lines transfected with EGFR and Her2 exon20 insertion mutants was analyzed (Figure S3b). These studies revealed the potency of LDC8201 toward several exon20 mutants. The H773_V774insNPH variant was used for routine screening in this project and was found to be among the most resistant mutants, while V774_C775insHV and N771_P772insH revealed the most pronounced potency by LDC8201.

The potency and selectivity of LDC8201 and LDC0496 were further examined at the biochemical level. Incubation of the compound with the purified EGFR kinase domain (EGFR-T790M+V948R used as a model system) resulted in a mass increase corresponding to single labeling with the respective compound, confirming the covalent mode of action (Figure S4). Next, we investigated the potential of LDC8201 and

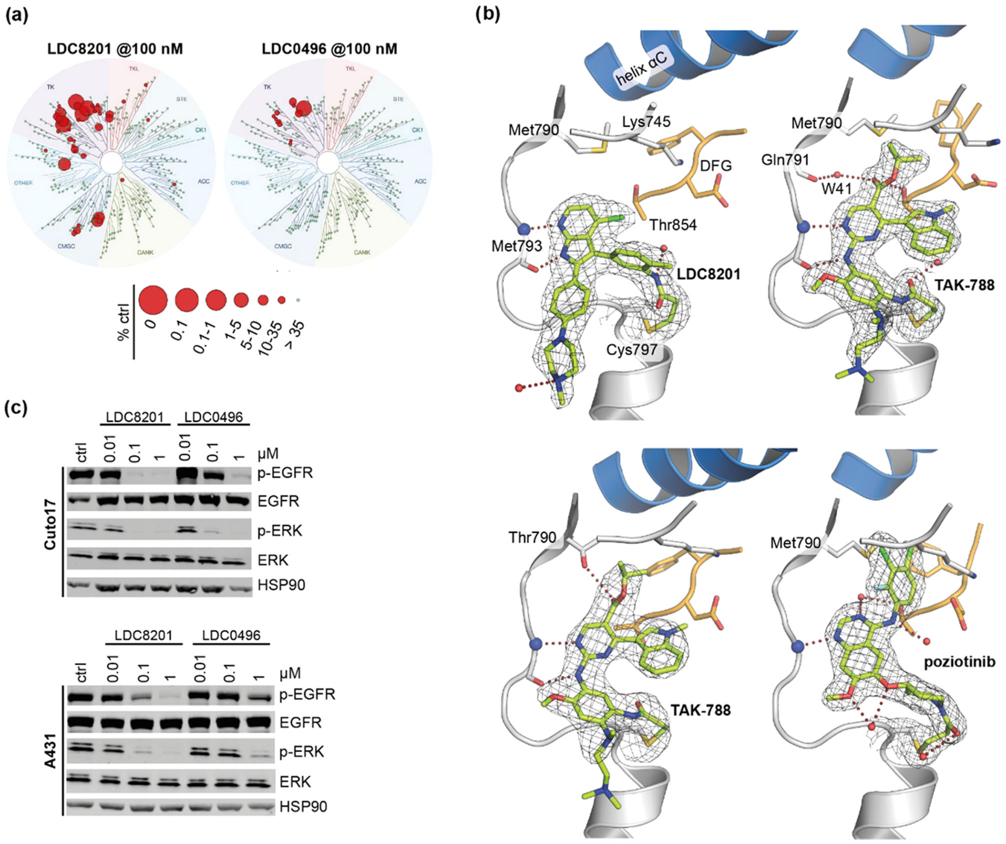

Figure 2. (a) Kinome profiling of LDC8201 and LDC0496 at a concentration of 100 nM against 468 kinases including 403 nonmutant kinases. See also Table S3. (b) Co-crystal structures of inhibitors in complex with EGFR. Diagrams of the experimental electron densities of LDC8201/EGFR-T790M+V948R at 2.4 Å (PDB ID: 7A6I), TAK-788/EGFR-T790M+V948R at 2.0 Å (PDB ID: 7A6K), TAK-788/EGFR-wt at 2.5 Å (PDB ID: 7B85), and poziotinib/EGFR-T790M+V948R at 2.0 Å resolution (PDB ID: 7A6J). 2Fo-Fc map contoured at an r.m.s.d. of 1. See also Table S4 and Figure S5. (c) Western blot analysis of EGFR and downstream cascade phosphorylation inhibition in Cuto 17 and A431 cells. See also Figure S6.

LDC0496 toward the binding of off-target kinases at an inhibitor concentration of 100 nM against a kinome composed of 468 representative kinases, including mutated variants (Figure 2a and Table S3). In this biochemical setup, LDC8201 bound to 44 (11%) nonmutant kinases with $\leq$35% control. The selectivity of LDC0496 was substantially improved, since only 12 (3%) nonmutant kinases were found to meet this threshold, and thereby the approach of exploiting the selectivity pocket adjacent to the 4 and 5 positions of the pyrrolopyridine scaffold was validated. Among the off-targets are kinases exhibiting a cysteine in a similar position to the ErbB family members EGFR, Her2, and Her4 (BLK, BMX, BTK, ITK, JAK3, TEC, TXK). The cysteine residues in EGFR, Her2, Her4, and BLK are reported to be less reactive compared to BMX, BTK, ITK, JAK3, TEC, and TXK.[27,28] We therefore anticipate those being covalent off-targets; however, these are commonly observed with EGFR inhibitors including clinically used inhibitors.[14] We believe that the selectivity over wild type and other kinase targets renders LDC8201 and LDC0496 to be valuable wild type-sparing inhibitors of EGFR and Her2 exon20 insertion mutants.

To gain structural insights into the binding mode, the compounds were subjected to our EGFR crystallization program, which yielded high-resolution crystal structures of LDC8201, TAK-788, and poziotinib in complex with T790M+V948R mutated EGFR as well as of TAK-788 with wild type EGFR (Figures 2b and S5). Of note, LDC8201 revealed a GI$_{50}$ of 18 nM toward EGFR-L858R+T790M mutant H1975 cells supported by immunoblotting studies showing p-EGFR inhibition at concentrations below 10 nM (Figure S6). The structure of LDC8201 (resolution = 2.4 Å; PDB ID: 7A6I) revealed the formation of a covalent bond with Cys797 by clear electron density. Moreover, the core scaffold was engaged in a duplex hydrogen bond with the hinge region's Met793, as well

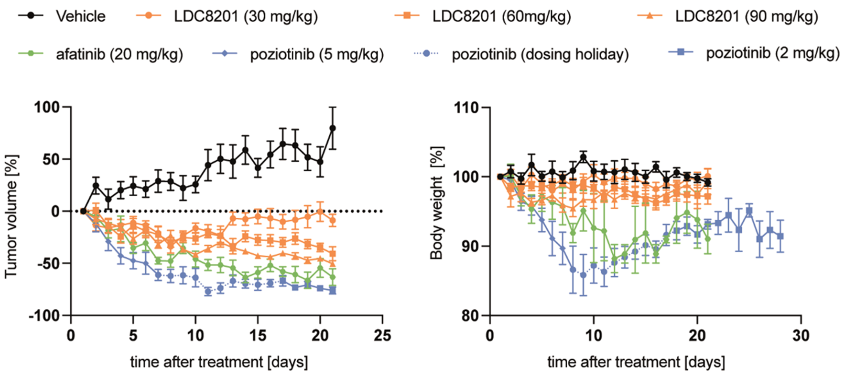

Figure 3. Tumor volume change and body weight change of mice injected with Cuto 17 cells treated with increasing doses of LDC8201 (0, 30, 60, and 90 mg/kg, PO, QD), poziotinib (5 mg/kg → dosing holiday → 2 mg/kg, PO, QD), and afatinib (20 mg/kg, PO, QD); error bars indicate SEM.

as hydrophobic interactions with the critical side chains of Leu718, Val726, Ala743, Met790, and Leu844. The phenyl linker between the scaffold and the warhead occupied the ribose pocket and was locked into position by the glycine-rich loop, specifically the residues Gly719, Ser720, Phe723, and Val726, which were close enough to interact. The aforementioned selectivity pocket was revealed to be formed primarily by the gatekeeper residue Met790, the catalytic lysine Lys745, and the DFG triad preceding Thr854. In line with the observed selectivity discrepancy between LDC8201 and LDC0496, this pocket was only partially occupied by the 4-chlorine substituent of LDC8201, while the crystal structure indicated that the 5-isopropylester of LDC0496 took advantage of these interactions. TAK-788 exhibited an isopropyl ester in the very same position compared to LDC0496. The TAK-788 structure in complex with EGFR-T790M+V948R (resolution = 2.0 Å; PDB ID: 7A6K) revealed that the ester moiety addressed the selectivity pocket. Its carbonyl group is in close proximity to Thr854, which is engaged in a polar interaction in one chain and water-mediated contacts to the Gln791 backbone carbonyl are formed, in addition to the nonpolar interactions with Val726, Ala743, Lys745, and Met790. The EGFR wild type kinase soaked with TAK-788 (resolution = 2.5 Å; PDB ID: 7B85) showed Thr854 to be reoriented and not engaged in polar interactions with the ligand. Instead, the ester moiety was slightly tilted to allow for a polar interaction with the Thr790 gatekeeper sidechain hydroxyl group, which is also present in the exon20 insertion mutants. In contrast, the structure of poziotinib in complex with EGFR-T790M+V948R (resolution = 2.0 Å; PDB ID: 7A6J) showed the halogenated aniline ring to be buried in the selectivity pocket. In the high-resolution structure, water-mediated contacts are evident; however, poziotinib relied predominantly on hydrophobic contacts with Val726, Ala743, Lys745, Met766, Leu788, Met790, Thr854, and Ala859. Of note, although the V948R mutation supports protein crystallization by promoting an inactive kinase conformation to preventing dimerization, LDC8201 exhibited a complex with the active kinase conformation. However, a comparison of the two structures with TAK-788 shows that the binding site of these Type I inhibitors is largely unaffected by the kinase conformation. In addition, we performed docking studies in D770_N771insNPG-mutated EGFR (PDB ID: 4LRM), which revealed similar interactions of these molecules with the selectivity pocket (Figure S5i), supporting the proposal that the crystallization system was a valid model system to assess the binding mode of these inhibitors. We conclude that balanced interactions of polar and nonpolar types with the selectivity pocket are a key driver for the potency and selectivity of LDC0496. These findings provided valuable insights that allow for further optimization of the pyrrolopyridine-based inhibitors in future works.

Ultimately, western blot studies revealed the EGFR on-target engagement of LDC8201 and LDC0496 in H773_V774insNPH patient-derived Cuto 17 cells (Figure 2c) as well as Cuto 14 (Figure S6). Concentrations of 10−100 nM inhibited the EGFR activation mediated by autophosphorylation, as well as the ERK downstream signaling. In these analyses, phospho-EGFR was inhibited in A431 cells with concentrations between 100 nM and 1 μM for LDC8201 and LDC0496, again highlighting the wild type-sparing character of these TKIs. These encouraging results were in line with cellular viability data obtained with the CTG assay. According to *in vitro* ADME data (Table S1) and combined with the favorable exposure determined in mouse plasma after oral gavage (Table S2 and Figure S2), LDC8201 was considered a suitable *in vivo* candidate and was evaluated in efficacy studies in mice.

First, we used mice engrafted with EGFR-L858R+T790M mutant H1975 cells. Oral treatment with LDC8201 (90 mg/kg) resulted in marked tumor shrinkage of 89% after 14 days (Figure S7). After a run-in phase of 6 days BID, we switched to a regimen of daily single-dose gavage. These studies supported the notion that LDC8201 effectively inhibits mutant EGFR signaling *in vivo* and prompted us to perform studies with an exon20 insertion mutated mouse model. We therefore engrafted mice with patient-derived Cuto 17 cells harboring an EGFR-H773_V774insNPH mutation. Here, we monitored mice treated orally with vehicle versus LDC8201 at increasing doses of 30, 60, and 90 mg/kg once daily (Figure 3). We observed a dose-dependent decrease in tumor volume, with the higher doses of 60 and 90 mg/kg provoking a marked regression of tumor (41 and 50% after 21 days, respectively) compared to the 30 mg/kg dose (9% after 21 days). We were delighted to observe no signs of toxicity and no loss in body

https://doi.org/10.1021/acs.jmedchem.1c02080
J. Med. Chem. 2022, 65, 6643−6655

weight in these experiments. Current medicinal chemistry efforts focus on further improved PK properties with longer systemic exposure and coverage of the cellular GI_{50} to result in more pronounced efficacy.

In this study, poziotinib (5 mg/kg) and afatinib (20 mg/kg) were used as controls, which induced an intense response with both compounds exhibiting 63 and 76% tumor shrinkage after 21 days, respectively. Of note, in contrast to LDC8201, mice treated with the anilinoquinazoline-based inhibitors poziotinib or afatinib exhibited weight losses of 13 and 8% after 8 days, which required a drug holiday followed by dose reduction of poziotinib treatment to 2 mg/kg. This finding suggested a toxic character for this class of chemical compounds, with a particularly pronounced outcome with poziotinib.

■ CONCLUSIONS

Exon20 insertion mutations in EGFR and Her2 represent a class of oncogenic drivers that remains therapeutically challenging. Different scaffolds are currently being evaluated as small-molecule inhibitors that can be used for the treatment of cancer patients. We set out to develop and characterize the novel lead LDC8201 and its derivative LDC0496 based on the 1*H*-pyrrolo[2,3-*b*]pyridine scaffold as a distinct chemotype. These TKIs were found to exhibit marked inhibitory potency toward engineered Ba/F3 cells as well as patient-derived cell lines harboring EGFR and Her2 exon20 insertion mutations. Selectivity within the kinome and over wild type EGFR was successfully optimized by SAR analysis and rationalized by insights gained from a set of X-ray crystal structures in complex with selected inhibitors. On-target engagement and efficacy were revealed by biochemical MS experiments and cellular western blot analyses. Moreover, oral absorption and ADME properties were optimized and ultimately resulted in tumor regression in mouse xenograft studies with patient-derived H773_V774insNPH-mutated Cuto 17 cells. In contrast to other inhibitors analyzed, LDC8201 showed no toxicity and no weight loss in mice in these studies. Together, these results highlight the potential of covalent pyrrolopyridine EGFR inhibitors, and they will be developed further in ongoing efforts to yield an efficient cancer therapeutic agent.

■ EXPERIMENTAL SECTION

Synthetic Procedures. All compounds are ≥95% pure by HPLC analysis. Representative HPLC traces are shown in the Supporting Information. Afatinib was purchased from LC Laboratories (A-8644), and Poziotinib was purchased from MedChemExpress (HY-15730).

General Information. All reactions involving air- or moisture-sensitive reagents or intermediates were carried out in flame-dried glassware under an argon atmosphere. Dry solvents (THF, toluene, MeOH, DMF, DCM) were used as commercially available. ^{1}H NMR and ^{13}C NMR were recorded on a Bruker DRX400 (400 MHz). Multiplicities are indicated as: br s (broadened singlet), s (singlet), d (doublet), t (triplet), q (quartet), quin (quintet), and m (multiplet), and coupling constants (J) are given in hertz (Hz). HPLC-electrospray mass spectra (HPLC ES-MS) were obtained using a Waters Acquity Performance Liquid Chromatography (UPLC) equipped SQ 3100 mass detector spectrometer. Column: Acquity UPLC BEH C18 1.7 μm, 2.1 mm × 50 mm. Flow: 0.5 mL/min. Eluents: A: H_2O with 0.05% formic acid and B: MeCN with 0.05% TFA. All chemicals and solvents were purchased from commercial sources like Sigma-Aldrich, Fluka, TCI, Acros Organics, ABCR, Alfa Aesar, Enamine, VWR, Combi-Blocks, Apollo Scientific, Aquilla Pharmatech, Ark Pharm, D-L Chiral Chemicals, ChemBridge, Renno Tech, Accela, KeyOrganics, Pharmablock, and Chem lmpex. Unless otherwise noted, all commercially available compounds were used as received without further purifications.

Isopropyl 2-((5-Acrylamido-4-((2-(dimethylamino)ethyl)-(methyl)amino)-2-methoxyphenyl)amino)-4-(1-methyl-1H-indol-3-yl)pyrimidine-5-carboxylate (TAK-788). ^{1}H NMR (500 MHz, DMSO-d_6) δ ppm 1.12 (d, J = 6.26 Hz, 6H) 2.21 (s, 6H) 2.33 (br. s., 2H) 2.72 (s, 3H) 2.89 (t, J = 5.65 Hz, 2H) 3.81 (s, 3H) 3.87 (s, 3H) 4.99 (spt, J = 6.26 Hz, 1 H) 5.77 (dd, J = 10.22, 1.98 Hz, 1H) 6.27 (dd, J = 16.94, 1.98 Hz, 1H) 6.43 (dd, J = 16.94, 10.22 Hz, 1H) 6.99−7.09 (m, 2H) 7.18 (t, J = 7.32 Hz, 1H) 7.48 (d, J = 8.24 Hz, 1H) 7.72 (br. s., 1H) 8.17 (br. s., 1H) 8.65 (s, 1H) 8.67 (s, 1H) 8.82 (br. s., 1H) 10.16 (br. s., 1H). HRMS (ESI$^+$) (m/z) calculated for $[C_{32}H_{39}N_7O_4 + H]^+$ 586.3136, found 586.3134.

*4-Chloro-3-(4-methyl-3-nitrophenyl)-2-(trimethylsilyl)-1H-pyrrolo[2,3-b]pyridine (**9**).* 4-Chloro-3-iodopyridine-2-amine (**7a**) (5.0 g, 19.0 mmol, 1.0 equiv), trimethyl((4-methyl-3-nitrophenyl)-ethynyl)silane (**8**) (5.7 g, 25.0 mmol, 1.25 equiv), 1,4-diazabicyclo[2.2.2]octane (3.6 g, 32.3 mmol, 1.7 equiv), and dichlorobis(triphenylphosphine)palladium(II) (1.4 g, 2.0 mmol, 0.1 equiv) in dry DMF (40 mL) under N_2 atmosphere was split in three microwave vials. Each vial was heated in the microwave at 145 °C for 2 h. EtOAc (250 mL) was added, and the organic phase was washed three times with aq. sat. $NaHCO_3$-solution. The organic phase was dried over $MgSO_4$, and the solvents were removed *in vacuo*. The crude product was purified by flash chromatography on silica gel (cHex/EtOAc = 100:0 to 1:1) to yield the desired product **9** (3.9 g, 10.8 mmol, 57%) as a beige solid.^{1}H NMR (400 MHz, DMSO-d_6, 300 K) δ 0.11 (s, 9H), 2.58 (s, 3H), 7.12 (d, J = 5.0 Hz, 1H), 7.52 (d, J = 7.9 Hz, 1H), 7.63 (d, J = 7.9 Hz, 1H), 7.91 (s, 1H), 8.21 (d, J = 5.0 Hz, 1H), 12.04 (s, 1H). MS (ES) $C_{17}H_{18}ClN_3O_2Si$ requires: 359, found: 360 $(M + H)^+$.

*5-(4-Chloro-2-(trimethylsilyl)-1H-pyrrolo[2,3-b]pyridin-3-yl)-2-methylaniline (**10**).* A solution of 4-chloro-3-(4-methyl-3-nitrophenyl)-2-(trimethylsilyl)-1*H*-pyrrolo[2,3-*b*]pyridine (**9**) (5.6 g, 15.56 mmol, 1.0 equiv) and iron (4.3 g, 77.8 mmol, 5 equiv) in EtOH (100 mL) and aq. sat. NH_4Cl-solution (10 mL) was stirred for 5 h at 80 °C. The solution was filtered through a pad of Celite. Solvents were removed *in vacuo*. The crude was dissolved in EtOAc and washed twice with aq. sat. $NaHCO_3$-solution. The organic phase was dried over $MgSO_4$, and the solvent was removed *in vacuo*. The crude product was purified by flash chromatography on silica gel (cHex/EtOAc = 100:0 to 0:100) to yield the desired product **10** (5.0 g, 15.2 mmol, 97%) as a beige solid.^{1}H NMR (400 MHz, DMSO-d_6, 300 K) δ 0.10 (s, 9H), 2.10 (s, 3H), 4.76 (br s, 2H), 6.44 (d, J = 7.4 Hz, 1H), 6.60 (s, 1H), 6.89 (d, J = 7.4 Hz, 1H), 7.04 (d, J = 5.1 Hz, 1H), 8.15 (d, J = 5.1 Hz, 1H), 11.71 (s, 1H). MS (ES) $C_{17}H_{20}ClN_3Si$ requires: 329, found: 330 $(M + H)^+$.

*N-(5-(4-Chloro-2-(trimethylsilyl)-1H-pyrrolo[2,3-b]pyridin-3-yl)-2-methylphenyl)acrylamide (**11**).* To a solution of 5-(4-Chloro-2-(trimethylsilyl)-1*H*-pyrrolo[2,3-*b*]pyridin-3-yl)-2-methylaniline (**10**) (2760 mg, 8.4 mmol, 1.0 equiv) and DIPEA (14.6 mL, 84.0 mmol, 10.0 equiv) in dry DCM (100 mL) at 0 °C was added slowly acryloyl chloride (757 mg, 8.4 mmol, 1.0 equiv) in dry DCM (5 mL). The mixture was stirred for 5 min. The solution was diluted with EtOAc and washed twice with aq. sat. $NaHCO_3$-solution. The organic phase was dried over $MgSO_4$, and the solvent was removed *in vacuo*. The crude product was purified by flash chromatography on silica gel (cHex/EtOAc = 100:0 to 1:1) to yield the desired product **11** (3070 mg, 8.0 mmol, 95%) as a white solid.^{1}H NMR (400 MHz, DMSO-d_6, 300 K) δ 0.11 (s, 9H), 2.28 (s, 3H), 5.72 (dd, J = 2.1 Hz, J = 10.2 Hz, 1H), 6.22 (dd, J = 2.1 Hz, J = 16.9 Hz, 1H), 6.55 (dd, J = 10.2 Hz, J = 16.9 Hz, 1H), 7.07 (m, 2H), 7.22 (d, J = 7.7 Hz, 1H), 7.56 (s, 1H), 8.17 (d, J = 5.0 Hz, 1H), 9.42 (s, 1H), 11.83 (s, 1H). MS (ES) $C_{20}H_{22}ClN_3OSi$ requires: 383, found: 384 $(M + H)^+$.

*N-(5-(4-Chloro-2-iodo-1H-pyrrolo[2,3-b]pyridin-3-yl)-2-methylphenyl)acrylamide (**12**).* *N*-(5-(4-Chloro-2-(trimethylsilyl)-1*H*-pyrrolo[2,3-*b*]pyridin-3-yl)-2-methylphenyl)acrylamide (**11**) (890 mg, 2.32 mmol, 1.0 equiv) and *N*-iodosuccinimide (937 mg, 4.18 mmol, 1.8 equiv) were dissolved in dry DCM (300 mL) and stirred for 15 h at RT. The organic phase was washed once with aq.

https://doi.org/10.1021/acs.jmedchem.1c02080
J. Med. Chem. 2022, 65, 6643−6655

sat. $Na_2S_2O_3$-sol. and three times with aq. sat. $NaHCO_3$-solution. The organic phase was dried over Na_2SO_4, and the solvents were removed *in vacuo* yielding the desired product **12** (970 mg, 2.21 mmol, 95%) as a yellow solid. The crude was used without purification in the next step. MS (ES) $C_{17}H_{13}ClIN_3O$ requires: 437, found: 438 $(M + H)^+$.

N-(5-(4-Chloro-2-(4-(4-methylpiperazin-1-yl)phenyl)-1H-pyrrolo-[2,3-b]pyridin-3-yl)-2-methylphenyl)acrylamide 2,2,2-Trifluoroacetate (LDC8201). A mixture of *N*-(5-(4-chloro-2-iodo-1*H*-pyrrolo[2,3-*b*]pyridin-3-yl)-2-methylphenyl)acrylamide (**12**) (40 mg, 0.09 mmol, 1.0 equiv), 4-(4-methyl-1-piperazinyl)phenylboronic acid (31 mg, 0.14 mmol, 1.5 equiv), and K_3PO_4 (38 mg, 0.18 mmol, 2.0 equiv) in dioxane/H_2O (3/0.6 mL) was degassed with a stream of N_2 for 5 min. [1,1′-Bis(diphenylphosphino)ferrocene]palladium dichloride dichloromethane adduct (8 mg, 0.01 mmol, 0.1 equiv) was added, and the reaction mixture was heated to 130 °C for 2 h in the microwave oven. The reaction mixture was diluted with EtOAc and washed three times with aq. sat. $NaHCO_3$-solution. The organic phase was dried over $MgSO_4$, and the solvents were removed *in vacuo*. The crude was purified by reversed-phase RP-HPLC (column: C18), using H_2O (0.1% TFA) and MeCN (0.1% TFA) as eluents. The desired fractions were lyophilized to yield the title compound (5 mg, 0.01 mmol, 8%) as a yellow powder.^{1}H NMR (400 MHz, DMSO-d_6, 300 K) δ 2.28 (s, 3H), 2.81/2.82 (s, 3H), 3.07 (m, 4H), 3.45 (m, 2H), 3.90 (d, *J* = 11.5 Hz, 2H), 5.72 (dd, *J* = 10.0 Hz, *J* = 2.0 Hz, 1H), 6.20 (dd, *J* = 2.0 Hz, *J* = 16.6 Hz, 1H), 6.55 (dd, *J* = 10.0 Hz, *J* = 16.6 Hz, 1H), 6.94 (d, *J*= 8.9 Hz, 2H), 7.04 (d, *J* = 7.8 Hz, 1H), 7.09 (d, *J* = 5.1 Hz, 1H), 7.22 (d, *J* = 7.8 Hz, 1H), 7.38 (d, *J* = 8.9 Hz, 2H), 7.55 (s, 1H), 8.13 (d, *J* = 5.1 Hz, 1H), 9.48 (s, 1H), 10.25 (s, 1H), 12.33 (s, 1H). HRMS (ESI$^+$) (*m/z*) calculated for $[C_{28}H_{28}ClN_5O + H]^+$ 486.20551, found 486.20488.

*3-(4-Methyl-3-nitrophenyl)-2-(trimethylsilyl)-1H-pyrrolo[2,3-b]-pyridine-5-carbonitrile (**13**).* **13** (2.6 g, 7.43 mmol, 40%, yellow solid) was prepared from 6-amino-5-bromonicotinonitrile (**7b**) (3.6 g, 18.2 mmol, 1.00 equiv) and trimethyl((4-methyl-3-nitrophenyl)ethynyl)-silane (**8**) (4.5 g, 19.0 mmol, 1.05 equiv) according to the synthesis of compound **9** reported above. MS (ES) $C_{18}H_{18}N_4O_2Si$ requires: 350, found: 351 $(M + H)^+$.

*2-Iodo-3-(4-methyl-3-nitrophenyl)-1H-pyrrolo[2,3-b]pyridine-5-carbonitrile (**14**).* 3-(4-Methyl-3-nitrophenyl)-2-(trimethylsilyl)-1*H*-pyrrolo[2,3-*b*]pyridine-5-carbonitrile (**13**) (270 mg, 0.8 mmol, 1.0 equiv) and *N*-iodosuccinimide (208 mg, 0.96 mmol, 1.2 equiv) were dissolved in dry DCM (40 mL) and stirred for 15 h at RT. The organic phase was washed once with aq. sat. $Na_2S_2O_3$-solution and three times with aq. sat. $NaHCO_3$-solution. The organic phase was dried over Na_2SO_4, and the solvents were removed *in vacuo* yielding the desired product **14** (123 mg, 0.30 mmol, 38%) as a brown solid. The crude was used without purification in the next step. MS (ES) $C_{15}H_9IN_4O_2$ requires: 403, found: 404 $(M + H)^+$.

*3-(4-Methyl-3-nitrophenyl)-2-(4-(4-methylpiperazin-1-yl)-phenyl)-1H-pyrrolo[2,3-b]pyridine-5-carbonitrile (**15**).* A mixture of 2-Iodo-3-(4-methyl-3-nitrophenyl)-1*H*-pyrrolo[2,3-*b*]pyridine-5-carbonitrile (**14**) (1.41 g, 3.5 mmol, 1.0 equiv), 4-(4-methylpiperazin-1-yl)phenylboronic acid (1.14 mg, 5.2 mmol, 1.5 equiv), and K_3PO_4 (1.47 g, 7.0 mmol, 2.0 equiv) in dioxane/H_2O (40/4 mL) was degassed with a stream of N_2 for 5 min. [1,1′Bis(diphenylphosphino)-ferrocene]palladium dichloride dichloromethane adduct (284 mg, 0.35 mmol, 0.1 equiv) was added, and the reaction mixture was heated to 130 °C for 2 h in a microwave oven. The reaction mixture was diluted with EtOAc and washed three times with aq. sat. $NaHCO_3$ solution. The organic phase was dried over $MgSO_4$, and the solvents were removed *in vacuo*. The crude product was purified by flash chromatography on silica gel (DCM/MeOH with 0.1% NEt_3 = 100:0 to 1:1) to yield the desired product **15** (500 mg, 1.10 mmol, 32%) as a yellow solid. MS (ES) $C_{26}H_{24}N_6O_2$ requires: 452, found: 453 $(M + H)^+$.

*Isopropyl 3-(4-Methyl-3-nitrophenyl)-2-(4-(4-methylpiperazin-1-yl)phenyl)-1H-pyrrolo[2,3-b]pyridine-5-carboxylate (**16**).* A mixture of 3-(4-methyl-3-nitrophenyl)-2-(4-(4-methylpiperazin-1-yl)phenyl)-1*H*-pyrrolo[2,3-*b*]pyridine-5-carbonitrile (**15**) (100 mg, 0.2 mmol), and conc. H_2SO_4 (1 mL) in isopropyl alcohol (2 mL) was heated for 48 h at 80 °C. After cooling to RT, EtOAc and sat. aq. $NaHCO_3$ solution were added. The aq. phase was extracted with EtOAc (3×), and the combined organic phase was dried over $MgSO_4$. Evaporation of solvents yielded the crude product **16** (28 mg, 0.05 mmol, 27%) as a yellow solid. The crude was used in the next step without further purification. MS (ES) $C_{29}H_{31}N_5O_4$ requires: 513, found: 514 $(M + H)^+$.

*Isopropyl 3-(3-Amino-4-methylphenyl)-2-(4-(4-methylpiperazin-1-yl)phenyl)-1H-pyrrolo[2,3-b]pyridine-5-carboxylate (**17**).* Isopropyl 3-(4-methyl-3-nitrophenyl)-2-(4-(4-methylpiperazin-1-yl)phenyl)-1*H*-pyrrolo[2,3-*b*]pyridine-5-carboxylate (**16**) (28 mg, 0.05 mmol, 1.0 equiv) and iron (15 mg, 0.3 mmol, 5 equiv) in EtOH (5 mL) and sat. aq. NH_4Cl-solution (1 mL) were heated for 3 h at 80 °C, sat. aq. $NaHCO_3$ solution was added, and the aq. phase was extracted with DCM (3×). The organic phase was dried over $MgSO_4$, and the solvents were removed *in vacuo*. The crude product was purified by flash chromatography on silica gel (DCM/MeOH with 0.1% NEt_3 = 100:0 to 1:1) to yield the desired product **17** (25 mg, 0.05 mmol, 94%) as a brown solid. MS (ES) $C_{29}H_{33}N_5O_2$ requires: 483, found: 484 $(M + H)^+$.

Isopropyl 3-(3-Acrylamido-4-methylphenyl)-2-(4-(4-methylpiperazin-1-yl)phenyl)-1H-pyrrolo[2,3-b]pyridine-5-carboxylate 2,2,2-Trifluoroacetate (LDC0496). LDC0496 (2 mg, 0.003 mmol, 4%, yellow solid) was prepared from **17** according to the synthesis of compound **11** reported above. The crude product was purified reversed-phase RP-HPLC (column: C18), using H_2O (0.1% TFA) and MeCN (0.1% TFA) as eluents. The desired fractions were lyophilized to yield the title compound LDC0496 as a yellow solid.^{1}H NMR (400 MHz, DMSO-d_6, 300 K) δ 1.31 (d, *J* = 6.2 Hz, 6H), 2.26 (s, 3H), 2.85 (s, 3H), 2.98 (t, *J* = 13.0 Hz, 2H), 3.10 (m, 2H), 3.50 (d, *J* = 12.0 Hz, 2H), 3.92 (d, *J* = 13.0 Hz, 2H), 5.14 (quint., *J* = 6.2 Hz, 1H), 5.72 (dd, *J* = 10.2 Hz, *J* = 2.0 Hz, 1H), 6.21 (dd, *J* = 17.1 Hz, *J* = 2.0 Hz, 1H), 6.55 (dd, *J* = 10.2 Hz, *J* = 17.1 Hz, 1H), 6.99 (d, *J* = 8.6 Hz, 2H), 7.25 (d, *J* = 7.9 Hz, 1H), 7.45 (d, *J* = 8.6 Hz, 2H), 7.64 (s, 1 H), 8.31 (d, *J* = 2.0 Hz, 1H), 8.79 (d, *J* = 2.0 Hz, 1H), 9.50 (s, 1H), 9.58 (br. s, 1H), 12.43 (s, 1H). HRMS (ESI$^+$) (*m/z*) calculated for $[C_{32}H_{35}N_5O_3 + H]^+$ 538.28127, found 538.28048.

The following compounds were synthesized similarly to the procedures given above (further details are described in WO2020/039060A1):

N-(3-Methoxy-5-(2-(4-(4-methylpiperazin-1-yl)phenyl)-1H-pyrrolo[2,3-b]pyridin-3-yl)phenyl)acrylamide (LDC9305). ^{1}H NMR (400 MHz, $CDCl_3$, 300 K) δ 2.37 (s, 3H), 2.60 (m, 4H), 3.28 (m, 4H), 3.78 (s, 3H), 5.76 (d, *J* = 10.1 Hz, 1H), 6.22 (dd, *J* = 10.1 Hz, *J* = 16.8 Hz, 1H), 6.43 (d, *J* = 16.8 Hz, 1H), 6.78 (s, 1H), 6.90 (m, 3H), 7.08 (dd, *J* = 5.0 Hz, *J* = 7.6 Hz, 1H), 7.26 – 7.28 (m, 1H), 7.43 (d, *J* = 8.5 Hz, 2H), 7.59 (s, 1H), 7.97 (d, *J* = 7.8 Hz, 1H), 8.19 (d, *J* = 3.3 Hz, 1H), 10.52 (s, 1H). MS (ES) $C_{28}H_{29}N_5O_2$ requires: 467 found: 468 $(M + H)^+$.

N-(3-(2-(4-(1-Methylpiperidin-4-yl)phenyl)-1H-pyrrolo[2,3-b]-pyridin-3-yl)phenyl)acrylamide (LDC9413). ^{1}H NMR (400 MHz, $CDCl_3$, 300 K) δ 1.87 (m, 4H), 2.13 (m, 2H), 2.38 (s, 3H), 2.52 (m, 1H), 3.05 (m, 2H), 5.76 (d, *J* = 10.3 Hz, 1H), 6.24 (dd, *J* = 10.3 Hz, *J* = 16.8 Hz, 1H), 6.44 (d, *J* = 16.8 Hz, 1H), 7.10 (dd, *J* = 4.8 Hz, *J* = 7.9 Hz, 1H), 7.16 (d, *J* = 7.6 Hz, 1H), 7.23 (d, *J* = 7.9 Hz, 2H), 7.30 (m, 1H), 7.36 (t, *J* = 7.9 Hz, 1H), 7.47 (d, *J* = 8.0 Hz, 2H), 7.54 (m, 1H), 7.69 (m, 1H), 8.00 (d, *J* = 7.8 Hz, 1H), 8.26 (d, *J* = 4.7 Hz, 1H), 10.37 (s, 1H). MS (ES) $C_{28}H_{28}N_4O$ requires: 436 found: 437 $(M + H)^+$.

3-(2-(4-(1-Methylpiperidin-4-yl)phenyl)-1H-pyrrolo[2,3-b]-pyridin-3-yl)aniline 2,2,2-Trifluoroacetate (LDC3790). MS (ES) $C_{25}H_{26}N_4$ requires: 382 found: 383 $(M + H)^+$.

N-(5-(4-Chloro-2-(4-(1-methylpiperidin-4-yl)phenyl)-1H-pyrrolo-[2,3-b]pyridin-3-yl)-2-methylphenyl)acrylamide 2,2,2-Trifluoroacetate (LDC8320). MS (ES) $C_{29}H_{29}ClN_4O$ requires: 484 found: 485 $(M + H)^+$.

*N-(5-(4-Methoxy-2-(4-(4-methylpiperazin-1-yl)phenyl)-1H-pyrrolo[2,3-b]pyridin-3-yl)-2-methylphenyl)acrylamide 2,2,2-Trifluoroacetate (**1**).* ^{1}H NMR (400 MHz, MeOD-d_4, 300 K) δ 2.30 (s, 3H), 2.96 (s, 3H), 3.08 (m, 2H), 3.26 (m, 2H), 3.57 (m, 2H), 3.91 (m, 2H), 3.98 (s, 3H), 5.78 (dd, *J* = 10.2 Hz, *J* = 1.5 Hz, 1H), 6.34

(dd, J = 17.0 Hz, J = 1.5 Hz, 1H), 6.51 (dd, J = 10.2 Hz, J = 17.0 Hz, 1H), 6.99 (d, J = 8.8 Hz, 2H), 7.03 (d, J = 6.7 Hz, 1H), 7.08 (d, J = 8.1 Hz, 1H), 7.19 (d, J = 7.8 Hz, 1H), 7.38 (d, J = 8.8 Hz, 2H), 7.46 (s, 1 H), 8.22 (d, J = 7.6 Hz, 1H). MS (ES) $C_{29}H_{31}N_5O_2$ requires: 481, found: 482 $(M + H)^+$.

*N-(5-(5-Cyano-2-(4-(4-methylpiperazin-1-yl)phenyl)-1H-pyrrolo[2,3-b]pyridin-3-yl)-2-methylphenyl)acrylamide 2,2,2-Trifluoroacetate (**2**).* ^{1}H NMR (400 MHz, MeOH-d_4, 300 K) δ 2.31 (s, 3H), 2.95 (s, 3H), 3.30 - 3.48 (m, 8H), 5.79 (dd, J = 1.6 Hz, J = 10.2 Hz, 1H), 6.36 (dd, J = 1.6 Hz, J = 17.0 Hz, 1H), 6.52 (dd, J = 10.2 Hz, J = 17.0 Hz, 1H), 7.02 (d, J = 9.0 Hz, 2H), 7.09 (d, J = 8.1 Hz, 1H), 7.27 (d, J = 7.8 Hz, 1H), 7.50 (m, 3H), 8.23 (d, J = 1.9 Hz, 1H), 8.51 (d, J = 1.9 Hz, 1H). HRMS (ESI$^+$) (m/z) calculated for $[C_{29}H_{28}N_6O + H]^+$ 477.23974, found 477.23879.

*3-(3-Acrylamido-4-methylphenyl)-N-benzyl-2-(4-(4-methylpiperazin-1-yl)phenyl)-1H-pyrrolo[2,3-b]pyridine-5-carboxamide 2,2,2-Trifluoroacetate (**3**).* ^{1}H NMR (400 MHz, MeOH-d_4, 300 K) δ 2.30 (s, 3H), 2.97 (s,3H), 3.07 (t, J = 12.4 Hz, 2H), 3.26 (m, 2H), 3.61 (d, J = 12.4 Hz, 2H), 3.93 (d, J = 13.7 Hz, 2H), 4.59 (s, 2H), 5.77 (dd, J = 10.2 Hz, J = 1.7 Hz, 1H), 6.32 (dd, J = 17.0 Hz, J = 1.7 Hz, 1H), 6.50 (dd, J = 10.2 Hz, J = 17.0 Hz, 1H), 7.01 (d, J = 8.9 Hz, 2H), 7.12 (d, J = 8.1 Hz, 1H), 7.20−7.37 (m, 6H), 7.50 (d, J = 8.9 Hz, 2H), 7.54 (s, 1H), 8.48 (d, J = 2.1 Hz, 1H), 8.75 (d, J = 2.1 Hz, 1H). HRMS (ESI$^+$) (m/z) calculated for $[C_{36}H_{36}N_6O_2 + H]^+$ 585.29725, found 585.29641.

*3-(3-Acrylamido-4-methylphenyl)-N-isopropyl-2-(4-(4-methylpiperazin-1-yl)phenyl)-1H-pyrrolo[2,3-b]pyridine-5-carboxamide 2,2,2-Trifluoroacetate (**4**).* ^{1}H NMR (400 MHz, MeOH-d_4, 300 K) δ 1.26 (d, J = 6.6 Hz, 6H), 2.31 (s, 3H), 2.97 (s, 3H), 3.07 (m, 2H), 3.27 (m, 2H), 3.60 (m, 2H), 3.92 (m, 2H), 4.24 (septett, J = 6.6 Hz, 1H), 5.79 (dd, J = 1.8 Hz, J = 10.3 Hz, 1H), 6.36 (dd, J = 17.0 Hz, J = 1.8 Hz, 1H), 6.52 (dd, J = 10.3 Hz, J = 17.0 Hz, 1H), 7.02 (d, J = 8.9 Hz, 2H), 7.13 (d, J = 8.0 Hz, 1H), 7.27 (d, J = 7.9 Hz, 1H), 7.51 (d, J = 7.9 Hz, 2H), 7.54 (m, 1H), 8.40 (d, J = 2.0 Hz, 1H), 8.71 (d, J = 2.0 Hz, 1H). MS (ES) $C_{32}H_{36}N_6O_2$ requires: 536 found: 537 $(M + H)^+$.

*Methyl 3-(3-Acrylamido-4-methylphenyl)-2-(4-(4-methylpiperazin-1-yl)phenyl)-1H-pyrrolo[2,3-b]pyridine-5-carboxylate 2,2,2-Trifluoroacetate (**5**).* ^{1}H NMR (400 MHz, DMSO-d_6, 300 K) δ 2.26 (s, 3H), 2.84 (s, 3H), 2.98 (t, J = 12.0 Hz, 2H), 3.11 (m, 2H), 3.50 (t, J = 12.0 Hz, 2H), 3.84 (s, 3H), 3.92 (d, J = 13.3 Hz, 2H), 5.72 (dd, J = 10.2 Hz, J = 2.0 Hz, 1H), 6.21 (dd, J = 17.0 Hz, J = 2.0 Hz, 1H), 6.54 (dd, J = 17.0 Hz, J = 10.2 Hz, 1H), 6.99 (d, J = 9.0 Hz, 2H), 7.02 (m, 1H), 7.26 (d, J = 7.9 Hz, 1H), 7.44 (d, J = 9.0 Hz, 2H), 7.58 (s, 1H), 8.26 (d, J = 2.1 Hz, 1H), 8.80 (d, J = 2.1 Hz, 1H), 9.52 (s, 1H), 9.72 (s, 1H), 12.45 (s, 1H). HRMS (ESI$^+$) (m/z) calculated for $[C_{30}H_{31}N_5O_3 + H]^+$ 510.24997, found 510.24917.

*Isopropyl 2-(3-(3-Acrylamido-4-methylphenyl)-2-(4-(4-methylpiperazin-1-yl)phenyl)-1H-pyrrolo[2,3-b]pyridin-5-yl)acetate 2,2,2-Trifluoroacetate (**6**).* ^{1}H NMR (400 MHz, MeOD-d_4, 300 K) δ 1.22 (d, J = 6.3 Hz, 6H), 2.30 (s, 3H), 2.98 (s, 3H), 3.07 (m, 2H), 3.27 (m, 2H), 3.60 (m, 2H), 3.73 (s, 2H), 3.93 (m, 2H), 4.98 (septet, J = 6.3 Hz, 1H), 5.79 (dd, J = 1.7 Hz, 10.0 Hz, 1H), 6.35 (dd, J = 1.7 Hz, J = 17.0 Hz, 1H), 6.51 (dd, J = 10.0 Hz, J = 17.0 Hz, 1H), 7.01 (d, J = 9.0 Hz, 2H), 7.09 (d, J = 7.9 Hz, 1H), 7.23 (d, J = 7.9 Hz, 1H), 7.50 (m, 3H), 7.91 (d, J = 1.9 Hz, 1H), 8.13 (d, J = 1.9 Hz, 1H). HRMS (ESI$^+$) (m/z) calculated for $[C_{33}H_{37}N_5O_3 + H]^+$ 552.29692, found 552.29644.

Cell Culture. Human cell lines were obtained from ATCC or the Deutsche Sammlung von Mikroorganismen und Zellkulturen (DSMZ) and verified by STR profiling. H520, H358, HCC827, Cuto17, Cuto14, PC9, H1581, A549, H23, H1781, H2228, H1975, and Ba/F3 cell lines were cultured in RPMI media, and A431 cells were cultured in DMEM. All media were supplemented with 10% fetal bovine serum, 1% penicillin/streptomycin, and L-glutamine. All cells were grown at 37 °C in a humidified atmosphere with 5% CO_2. Cell lines expressing recombinant EGFR or HER2 variants were generated by retroviral transduction. In brief, cDNA sequences were cloned into a pBabe-puro vector and co-transfected with pCL-Eco helper plasmid into HEK 293T cells using TransIT-LT1 reagent (Mirus). After 48 h of transfection, retroviral particles were collected for infection of Ba/F3 cells. After 24 h of infection, the medium was replenished with a growth medium containing puromycin (3 μg/mL) to select for transduced cell clones.

Viability Assay. To assess cell viability, CellTiter-Glo (CTG) assays (Promega) were performed, based on the quantification of ATP, indicating the presence of metabolically active cells.

Half-maximal effective concentration (EC_{50}) values were determined as follows: Cells were seeded on day 1 in 384-well plates at cell numbers that ensure linearity and optimal signal intensity. After culturing for 24 h in serum-containing media in humidified chambers at 37 °C/5% CO_2, the cells were incubated for 72 h with inhibitors in serial dilutions (14 nM to 30 μM) and DMSO as control. Viability studies were carried out on day 5 using the CellTiter-Glo assay (Promega). For these studies, CellTiter-Glo reagent was prepared according to the instructions of the kit. Thereon, reagent and assay plates were equilibrated at room temperature for 20 min. Equal volumes of the reagent were added to the volume of culture medium present in each well. The plates were mixed for 2 min on an orbital shaker. The microplates were then incubated at room temperature for 10 min for stabilization of the luminescent signal. Following incubation, the luminescence was recorded on a Victor microplate reader (PerkinElmer) using 200 ms integration time. The data were then analyzed with Excel using the XLfit-Plugin (dose−response fit 205) for GI_{50} determination. For quality control, the Z′-factor was calculated from 16 positive and negative control values. Only assay results showing a Z′-factor $\geq$ 0.5 were used for further analysis. All experimental points were measured in duplicate for each plate and were replicated in at least two plates.

Half-maximal growth inhibitory (GI_{50}) values were determined as follows: Cells were plated in 96-well plates in triplicate, and compounds were added at 8 decreasing compound concentrations 24 h after seeding. After 72 h, the cell viability was measured *via* CellTiter-Glo (CTG) assay (Promega) and was normalized to DMSO-treated controls. Half-maximal growth inhibitory (GI_{50}) concentrations of cell viability were inferred by fitting sigmoidal dose−response curves using the Prism 8 software (GraphPad).

Crystal Violet Assay. 1.5×10^5 cells were plated into one well of a 12-well plate, and 24 h later, treated with TKIs. And 74 h after treatment, the cells were fixed with 4%-paraformaldehyde in PBS (37 °C, 20 min), stained with 0.5% crystal violet solution (RT, 20 min, tilting shaker), and rinsed in PBS before image acquisition. Methanol was added to the stained cells to resolve the crystal violet. The optical density was determined with Tecan (570 nm).

Western Blotting. Cell lysates were prepared using RIPA buffer supplemented with protease inhibitors (cOmplete Mini Protease Inhibitor Cocktail, Roche). Protein concentration was determined by BCA assay (Pierce), and equal amounts of protein were separated on 4−20% Tris-glycine sodium dodecyl sulfate-polyacrylamide gel electrophoresis (SDS-PAGE) gels (Thermo Fisher Scientific) and transferred to PVDF-FL membrane (Millipore). Membranes were blocked in 5% milk/TBS, incubated with primary antibodies in 5% milk/TBS-T, washed, and incubated with fluorescently labeled secondary antibodies prior to detection with Odyssey CLx imaging system (LI-COR Biosciences). Images were processed using the Image Studio Software (LI-COR Biosciences). Primary antibodies are: HSP90 (#4877, Cell Signaling Technology, 1:2000), EGFR (#2232, Cell Signaling Technology, 1:1000), p-EGFR (3777#, Cell Signaling Technology, 1:1000), ERK (#4696, Cell Signaling Technology, 1:1000), p-ERK (#4370, Cell Signaling Technology, 1:1000). Secondary antibodies are: goat anti-rabbit 800CW (#926-32211, LI-COR Biosciences, 1:10 000), goat anti-mouse 800CW (#926-3220, LI-COR Biosciences, 1:10 000).

Mass Spectrometry Experiments. The concentrated protein EGFR-T790M+V948R (1.0 mg/mL) was incubated with a 3-fold excess of inhibitors LDC8201, LDC0496, poziotinib, and TAK-788 (10 mM DMSO stock) for 1−2 h on ice in buffer (100 mM NaCl, 25 mM Tris−HCl, 10% glycerol and 1 mM TCEP, pH 8.0).

We analyzed the aliquots by ESI-MS using a Thermo Fisher Scientific Dionex UltiMate 3000 HPLC system connected to a Thermo Fisher Scientific Velos Pro (2d ion trap). Therefore, 2 μL of the sample was injected and separated using a Vydac 214TP C4 5 μm column (150 mm × 2.1 mm) starting at 20% of solvent B for 5 min followed by a gradient up to 90% of solvent B over 14 min with a flow rate of 210 μL/min with 0.1% TFA in water as solvent A and 0.1% TFA in MeCN as solvent B. A mass range of 700−2000 m/z was scanned, and raw data were deconvoluted and analyzed with MagTran software (Z.Q. Zhang, A.G. Marshall, *J. Am. Soc. Mass. Spectr.* 1998, 9, 225-233).

Construct Design of EGFR-WT and EGFR-T790M+V948R. For crystallographic studies, codon-optimized DNA encoding residues 696−1022 of the human EGFR with an N-terminal His$_6$-tag and thrombin cleavage site was cloned into a pIEX/Bac-3 vector. For EGFR-T790M+V948R the point mutations T790M and V948R were introduced by site-directed mutagenesis (QuikChange, Stratagene/Agilent Technologies). Transfection, virus generation, amplification, and expression were carried out in *Spodoptera frugiperda* cell line *Sf9* following the *flash*BAC protocol.

Protein Expression and Purification of EGFR-WT and EGFR-T790M+V948R. After 3 days of expression (27 °C, 110 rpm), the *Sf9*-cells were harvested (3000*g*, 20 min), resuspended in lysis buffer (600 mM NaCl, 50 mM Tris−HCl pH 7.5, 15% glycerol, 1 mM TCEP), supplemented with a protease inhibitor cocktail (Complete EDTA-free), homogenized, lysed, and incubated with CHAPS (1 h, 4 °C) followed by centrifugation (20 500 rpm, 1 h, 4 °C). The filtered supernatant was loaded onto a nickel-affinity column. The protein was eluted with 500 mM NaCl, 25 mM Tris−HCl pH 8, 250 mM imidazole, 10% glycerol, and 1 mM TCEP followed by cleavage with thrombin to remove the His$_6$-tag and a second nickel-affinity chromatography capturing the flow through. Finally, the protein was purified by size exclusion chromatography (100 mM NaCl, 25 mM Tris−HCl pH 8, 10% glycerol, and 1 mM TCEP) and concentrated to 6.8−7.5 mg/mL. Protein identity was confirmed by ESI-MS analysis.

Co-Crystallization of EGFR-T790M+V948R with LDC8201, Poziotinib, and TAK-788. The concentrated protein EGFR-T790M+V948R (6.8−7.5 mg/mL) was incubated with a 3-fold excess of inhibitors LDC8201, poziotinib, and TAK-788 (10 mM DMSO stock) for 2 h on ice. Crystals were grown at 20 °C by the hanging drop vapor diffusion method. The protein−compound complex was mixed in a 1:1 ratio (1 μL of protein and 1 μL of reservoir solution containing 15−37.5% PEG3350, 100−200 mM MgSO$_4$, 0−4% ethylene glycol). Crystals grew within 1−2 weeks and were harvested and flash-cooled in liquid nitrogen. Diffraction data were collected at the PXII X10SA beamline at the Swiss Light Source (PSI, Villigen, Switzerland). The data were processed using XDS and scaled using XSCALE (W. Kabsch, XDS. Acta Cryst. 2010, D66, 125-132).

Soaking of EGFR-WT with TAK-788. Crystals of the EGFR-WT apo-protein were grown at 20 °C by the hanging drop vapor diffusion method. The protein was mixed in a 1:1 ratio (1 μL protein and 1 μL reservoir solution containing 1.6 M K-Na-tartrate and 100 mM Na-MES pH 7.0). Crystals grew within 4 days. Before soaking of EGFR-WT crystals, the DMSO of the 10 mM stock of TAK-788 was evaporated by vacuum centrifugation. The solid material was resuspended in the same volume of the final purification buffer; 0.2 μL of this solution was added to the crystallization drop with the grown crystals. After 2 days, the crystals were harvested and flash-cooled in liquid nitrogen. Diffraction data were collected at the PXII X10SA beamline at the Swiss Light Source (PSI, Villigen, Switzerland). The data were processed using XDS and scaled using XSCALE (W. Kabsch, XDS. Acta Cryst. 2010, D66, 125-132).

Structure Determination and Refinement. The complex crystal structures of EGFR-T790M+V948R in complex with LDC8201, poziotinib, and TAK-788 and of EGFR-WT in complex with TAK-788 were solved by molecular replacement with PHASER (R. J. Read, *Acta Crystallogr., Sect. D: Biol. Crystallogr.* 2001, 57, 1373−1382) using structure PDB ID: 6S8A as template. The molecules in the asymmetric unit were manually adjusted using the program COOT (P. Emsley, K. Cowtan, *Acta Crystallogr., Sect. D: Biol. Crystallogr.* 2004, 60, 2126−2132). The refinement was performed with Phenix.refine 1.17.1 (P. D. Adams, P. V. Afonine, G. Bunkoczi, V. B. Chen, I. W. Davis, N. Echols, J. J. Headd, L. W. Hung, G. J. Kapral, R. W. Grosse-Kunstleve, A. J. McCoy, N. W. Moriarty, R. Oeffner, R. J. Read, D. C. Richardson, J. S. Richardson, T. C. Terwilliger, P. H. Zwart, *Acta Cryst.* 2010, *D66*, 213−221). Inhibitor topology files were generated using eLBOW of the Phenix 1.17.1 program package. Refined structures were validated with the PDB validation server. Data collection, structure refinement statistics, PDB ID codes, and further details for data collection are provided in Table S4. PyMOL (W.L. DeLano, *The PyMOL Molecular Graphics System*) was used for generating the figures.

Molecular Modeling. Molecular modeling experiments were carried out with the Schrödinger Maestro Suite. Protein Preparation Wizard was used to prepare the structure 4LRM (EGFR-D770_N771insNPG in complex with PD168393) for the calculations. Afterward, the covalent bond to the Cys800 of the inhibitor PD168393 was cleaved yielding the corresponding reversible inhibitor with an ethyl amide moiety. Then, a local minimization of the ethyl amide and Cys800 was performed. Receptor Grid Preparation (Glide) was used to generate the protein grid that was subsequently utilized in docking experiments. The van der Waals radius scaling factor was set to 1.0 with a partial charge cutoff of 0.25. Met796 was used as constraints (H-bond acceptor and donator). The receptor groups Ser720, Thr725, Tyr727, Cys778, Thr793, and Cys800 were allowed to rotate. Ligand preparation for docking was carried out with LigPrep in Maestro and the OPLS3 force field. Epika was used to generate possible states at target pH 7.0 ± 2.0. Ligand docking options in Glide were used for reversible docking experiments of the ligands. Under Setting, SP (standard precision), Dock flexibly, Sample nitrogen inversions, Sample ring conformation, and Epik state penalties to docking score were selected, and amide bonds were penalized for nonplanar conformation. Under the Ligands section, the van der Walls radius scaling factor was set to 0.8 and the docking was set to match at least one out of two constraints. Several high-score binding poses were generated and subsequently submitted for Covalent Docking. Hereby, Cys800 was chosen as the reactive residue and the reaction type was defined as Michael Addition. Finally, several high score poses of ligands covalently bound to EGFR-D770_N771insNPG were obtained. PyMOL (W.L. DeLano, *The PyMOL Molecular Graphics System*) was used for generating the figures.

Determination of *In Vitro* ADMET Parameters. Aqueous solubility (SolRank) was determined by spectrophotometrical measurement of the kinetic solubility of a 500 μM compound solution in aqueous buffer pH 7.4 compared to a solution in the organic solvent acetonitrile after 90 min of vigorous shaking at room temperature.

Microsomal metabolic stability (CL$_{\text{int}}$) of test compounds under oxidative conditions was determined at a final concentration of 1 μM by incubation with liver microsomes (XenoTech, tebu-bio, Germany) derived from different species supplemented with NADP, glucose-6-phosphate (G6P), and G6P-dihydrogenase. Compound depletion was measured over time by LC-MS/MS to calculate compound half-life $t_{1/2}$. Conversion to the *in vitro* intrinsic clearance CL$_{\text{int}}$ expressed in [μL/min/mg] was performed using the following equation: CL$_{\text{int}}$ [μL/min/mg] = (0.693/$t_{1/2}$ [min]) × (reaction volume [μL]/microsomal protein [mg]).

Microsomal metabolic stability of test items under conjugative conditions (Phase II) was measured in the glucuronidation assay by LC/MS-based determination of %remaining of test compounds at a concentration of 5 μM following incubation with liver microsomes supplemented with UDPGA for 1 h at 37 °C.

Plasma stability was determined by LC-MS/MS-based quantification of compound concentrations after 1 h of incubation of 5 μM test compound at 37 °C with plasma obtained from different species. Plasma stability was expressed as [%remaining] after normalization to the starting concentration.

To determine hepatocyte stability, 1 × 10^6 cryopreserved hepatocyte suspension cells/mL from different species (BioIVT, West Sussex, United Kingdom) were incubated with the test item at 37 °C over a 60 min time period. To stop the reaction, samples were removed into acetonitrile at 5, 10, 20, 40, and 60 min of incubation and centrifuged through a filter plate prior to LC/MS measurement. Based on the calculated compound half-life $t_{1/2}$, *in vitro* intrinsic clearance CL_{int} was calculated using the following equation: Cl_{int} [μL/min/10^6 cells] = (0.693/$t_{1/2}$ [min]) × (reaction volume [μL]/million cells [10^6 cells])

Plasma protein binding was measured by equilibrium dialysis of 5 μM test compound in 50% plasma from different species against PBS. After 6 h of incubation at 37 °C, compound concentrations on both sides of the membrane were measured by LC/MS. Plasma protein binding expressed as [%bound] was calculated using the following equation: % bound = $(C_{plasma} - C_{PBS})/C_{plasma} \times 100\%$

Permeability through artificial membranes (PAMPA) was performed at a concentration of 500 μM of test compound in the donor compartment of 96-well transwell plates. Filters were covered with a membrane-forming solution consisting of 10% 1,2-dioleyl-sn-glycero-3-phosphocholine (Sigma-Aldrich) and 0.5% (w/v) cholesterol (Sigma-Aldrich) in dodecane. After an incubation period of 20 h, absorption of the receiver wells was measured by spectrophotometry and permeation was calculated by normalization of the compound flux across a blank filter.

To measure cellular permeability, test compounds were applied at a concentration of 10 μM in HBSS to either the apical (A) or basolateral (B) side of a Caco-2 cell (ATCC) monolayer grown on 96-well transwell plates and incubated for 2 h at 37 °C. The test compound concentrations on each side of the monolayer were determined by LC/MS and the apparent permeability (P_{app}) was calculated for the apical to basolateral (A → B) and basolateral to apical (B → A) directions according to the following equation: $P_{app} = 1/(A \times C_0) \times (dQ/dt)$, where A is the membrane surface area, C_0 is the donor drug concentration at $t = 0$, and dQ/dt is the amount of drug transported within the given time period.

Chemical stability was determined by incubating test compounds at a final concentration of 2 μM in PBS at pH 7.4 for 24 h. The percentage of remaining compound (%remain) in relation to the zero time point was calculated following LC/MS-based measurement of sample aliquots of each time point.

GSH reactivity was determined by pre-incubating 971 μL of IMDM, 60 μL of GSH stock solution (100 mM), and 163 μL of PBS for a minimum of 10 min at 37 °C and orbital shaking at 1200 rpm. Then, 6 μL of test article solutions (2 mM in DMSO) were added for a final concentration of 10 μM and a DMSO percentage of 0.5%. Samples were incubated at 37 °C and 1200 rpm. At predefined time points, 200 μL aliquots have been extracted and added over microcentrifuge tubes containing 600 μL of quenching solution (glyburide 25 μM and ethacrynic acid 2 mM in ACN), vortexed for 15−20 seconds, and stored in ice. Time zero samples were extracted just after initial homogenization. Samples were centrifuged at 5000*g* for 15 min at 4 °C. The remaining percentage of test article and internal standard were quantified in the supernatant by mass spectrometry.

The cytotoxic potential of test compounds was investigated using peripheral blood mononuclear cells (PBMCs) isolated from buffy coats; 50 000 cells/well were seeded into 384-well plates 24 h prior to the transfer of titrated test compound concentrations. After 72 h, IC_{50} values of test compounds were determined with the CellTiter-Glo (Promega) Luminescent Cell Viability Assay (CTG assay). Luminescence values were measured with a Victor X5 2030 Multilabel reader (PerkinElmer). IC_{50} values were determined using a sigmoidal curve fitting model.

To determine the hepatotoxic potential of test compounds, HepG2 cells (450 cells/well) were seeded into collagen-coated 384-well plates. After 24 h, titrated compound concentrations were transferred followed by the determination of cell viability after 72 h using the CellTiter-Glo (Promega) Luminescent Cell Viability Assay. Luminescence values were measured with a Victor X5 2030 Multilabel reader (PerkinElmer). IC_{50} values were determined using a sigmoidal curve fitting model.

To detect potential mitochondrial impairment, we compared the toxic effects of compounds in glucose-containing and galactose-containing media using HepG2 cells. HepG2 cells (450 cells/well) were seeded into collagen-coated 384-well plates. After 24 h, the compounds were transferred as a titrated concentration series. After 72 h, the IC_{50} values of tested compounds were determined with the CellTiter-Glo (Promega) Luminescent Cell Viability Assay. Luminescence values were measured with a Victor X5 2030 Multilabel reader (PerkinElmer). IC_{50} values were determined using a sigmoidal curve fitting model.

The potential interaction of the test compounds with the human ether-a-go-go-related gene (hERG) potassium channel was determined by the Predictor hERG Fluorescence Polarization Assay (Thermo Fisher Scientific) following the transfer of titrated compound concentrations according to the instructions by the manufacturer. Fluorescence polarization was measured with a Wallac EnVision 2103 Multilabel Reader (PerkinElmer) prior to the calculation of IC_{50} values using a sigmoidal curve fitting model.

To measure CYP450 inhibition, decreased formation of CYP450 isozyme-specific metabolites in the presence of titrated test item concentrations was used to calculate IC_{50} values for the individual CYP450 isozymes CYP3A4 (Midazolam-hydroxylation), CYP2D6 (dextromethorphan-demethylation), CYP2C9 (tolbutamide-hydroxylation), CYP2C19 (mephenytoin-hydroxylation), and CYP1A2 (phenacetin-*O*-deethylation). Metabolite formation was analyzed by LC/MS using human liver microsomes.

***In Vivo* Pharmacokinetics.** Female FVB mice, age 8−10 weeks, were purchased from Janvier, Saint-Berthevin Cedex, France. All experimental mice were housed in a temperature-controlled room (20−24 °C) and a 12 h day/night cycle for at least 7 days prior to the pharmacokinetic study. The animals were fed ad libitum with Allein-Futter für Ratten-/Mäusehaltung from Sniff Special Diets GmbH, Germany, and had free access to water. To determine the pharmacokinetic parameters, the mice received single administrations of test items either by intravenous (IV) bolus injection, by intraperitoneal (IP) injection or by oral (PO) gavage at dosing volumes of 2, 5, or 10 mL/kg, respectively. All animal experiments were approved by and were conducted in accordance with the regulations of the local Animal Welfare authorities (Landesamt für Verbraucherschutz, Amtstierärztlicher Dienst und Lebensmittelüberwachung, Konrad-Zuse-Strasse 11, 66115 Saarbrücken, Germany).

Blood samples (80 μL) were collected from the retrobulbar venous plexus under short isoflurane anesthesia at 5, 15, 30, 60, 120, 240, and 480 min after the administration of the test item. These series of blood samples were transferred into 1.5 mL heparinized tubes and immediately centrifuged for 10 min at 5000 rpm at 4 °C. Separated plasma was stored at -80 °C until LC/MS analysis.

Prior to LC/MS analysis, plasma proteins were precipitated with acetonitrile containing an internal standard, and samples were filtered. A calibration curve was obtained from spiked blank plasma samples. Plasma samples containing test items were measured using a Shimadzu UPLC system connected to a QTrap 5500 hybrid triple quadrupole/linear ion trap mass spectrometer (AB Sciex). The regression equation of the calibration curve was used to calculate total plasma concentrations. Pharmacokinetic parameters were determined by noncompartmental analysis using the PKSolver software2.

***In Vivo* Efficacy.** The local authorities and the animal protection committee approved all animal procedures of this study.

NCI-H1975 cells (5×10^6) were inoculated into the right flank region of 7- to 8-week-old Balb/c nude mice (Beijing AniKeeper Biotech Co., Ltd.), and treatment was initiated when tumors reached a mean volume of approximately 136 mm^3. The mice were treated daily for 14 days orally with vehicle solution (20% PEG400 + 80% PBS) BID, which was changed on day 7 to QD, osimertinib (10 mg/kg in 1% DMSO + 30% PEG300 + ddH_2O) QD, or LDC8201 (90 mg/kg in 20% PEG400 + 80% PBS) BID, which was changed on day 7 to QD. Each group comprised five mice. Tumor volumes were measured twice weekly in two dimensions using a caliper, and the volume was expressed in mm^3 using the formula: $V = 0.5 \times (\text{length} \times \text{width}^2)$, where V is the tumor volume, length is the longest tumor dimension, and width is the longest tumor dimension perpendicular to the length.

For each tumor, 5×10^6 Cuto17 cells were resuspended in 100 μL of Matrigel Matrix (#354234, Corning) and injected subcutaneously in both flanks into 8- to 12-week-old female nude mice (RJ:NMRI-Foxn1nu/nu, Janvier Labs). Upon formation of palpable subcutaneous tumors (150−300 mm^3 tumor volume), the mice were treated with vehicle solution (20% PEG400 + 80% PBS, G1), LDC8201 (30 mg/kg, G2; 60 mg/kg, G3; 90 mg/kg, G4 in 20% PEG400 + 80% PBS), afatinib (20 mg/kg, G5 in 2% DMSO + 30% PEG300, 5% Tween80 + 62% ddH_2O) or poziotinib (5 mg/kg, G6 in 20% PEG400 + 3% Tween80 + 77% H_2O). The groups G1−G6 comprised 8, 8, 8, 7, 5, and 8 mice harboring 8, 9, 9, 9, 9, and 8 tumors, respectively. The mice were treated with vehicle, afatinib, poziotinib, or LDC8201 daily for up to 21 days by oral gavage. Tumor volume (V) was monitored every day using perpendicular diameters by an external caliper and calculated using the modified ellipsoid formula: $V = 0.5 \times (\text{length} \times \text{width}^2)$.

■ ASSOCIATED CONTENT

Supporting Information

The Supporting Information is available free of charge at https://pubs.acs.org/doi/10.1021/acs.jmedchem.1c02080.

In vitro pharmacokinetic parameters; kinome profiling; refinement statistics of complex crystal structures; chemical structures of selected EGFR-targeted TKIs; MS-based analysis of covalent bond formation; Western blot analysis of EGFR in relevant cell lines (PDF)

Molecular formula strings (CSV)

Validation report, LDC8201/EGFR-T790M+V948R (PDB ID: 7A6I) (PDF)

Validation report, poziotinib/EGFR-T790M+V948R (PDB ID: 7A6J) (PDF)

Validation report, TAK-788/EGFR-T790M+V948R (PDB ID: 7A6K) (PDF)

Validation report, TAK-788/EGFR-wt (PDB ID: 7B85) (PDF)

Accession Codes

PDB IDs are 7A6I, LDC8201/EGFR-T790M+V948R; 7A6K, TAK-788/EGFR-T790M+V948R; 7B85, TAK-788/EGFR-wt; 7A6J, poziotinib/EGFR-T790M+V948R.

■ AUTHOR INFORMATION

Corresponding Authors

Martin L. Sos − *Molecular Pathology, Institute of Pathology, University Hospital of Cologne, 50937 Cologne, Germany; Department of Translational Genomics, Faculty of Medicine and University Hospital Cologne, University of Cologne, 50931 Cologne, Germany; Center for Molecular Medicine Cologne, Faculty of Medicine and University Hospital Cologne, University of Cologne, 50931 Cologne, Germany;* Phone: +49 221 478 96175; Email: martin.sos@uni-koeln.de

Daniel Rauh − *Faculty of Chemistry and Chemical Biology, TU Dortmund University, 44227 Dortmund, Germany; Drug Discovery Hub Dortmund (DDHD) am Zentrum für Integrierte Wirkstoffforschung (ZIW), 44227 Dortmund, Germany;* orcid.org/0000-0002-1970-7642; Phone: +49 231 755 7080; Email: daniel.rauh@tu-dortmund.de, @DDHDortmund, DDHDortmund.de

Authors

Jonas Lategahn − *PearlRiver Bio GmbH, 44227 Dortmund, Germany; Faculty of Chemistry and Chemical Biology, TU Dortmund University, 44227 Dortmund, Germany; Drug Discovery Hub Dortmund (DDHD) am Zentrum für Integrierte Wirkstoffforschung (ZIW), 44227 Dortmund, Germany;* orcid.org/0000-0001-5993-7082

Hannah L. Tumbrink − *Molecular Pathology, Institute of Pathology, University Hospital of Cologne, 50937 Cologne, Germany; Department of Translational Genomics, Faculty of Medicine and University Hospital Cologne, University of Cologne, 50931 Cologne, Germany*

Carsten Schultz-Fademrecht − *PearlRiver Bio GmbH, 44227 Dortmund, Germany; Lead Discovery Center GmbH, 44227 Dortmund, Germany*

Alena Heimsoeth − *Molecular Pathology, Institute of Pathology, University Hospital of Cologne, 50937 Cologne, Germany; Department of Translational Genomics, Faculty of Medicine and University Hospital Cologne, University of Cologne, 50931 Cologne, Germany*

Lisa Werr − *Department of Translational Genomics, Faculty of Medicine and University Hospital Cologne, University of Cologne, 50931 Cologne, Germany*

Janina Niggenaber − *Faculty of Chemistry and Chemical Biology, TU Dortmund University, 44227 Dortmund, Germany; Drug Discovery Hub Dortmund (DDHD) am Zentrum für Integrierte Wirkstoffforschung (ZIW), 44227 Dortmund, Germany;* orcid.org/0000-0003-2942-263X

Marina Keul − *Faculty of Chemistry and Chemical Biology, TU Dortmund University, 44227 Dortmund, Germany; Drug Discovery Hub Dortmund (DDHD) am Zentrum für Integrierte Wirkstoffforschung (ZIW), 44227 Dortmund, Germany*

Fatma Parmaksiz − *Molecular Pathology, Institute of Pathology, University Hospital of Cologne, 50937 Cologne, Germany; Department of Translational Genomics, Faculty of Medicine and University Hospital Cologne, University of Cologne, 50931 Cologne, Germany*

Matthias Baumann − *Lead Discovery Center GmbH, 44227 Dortmund, Germany*

Sascha Menninger − *Lead Discovery Center GmbH, 44227 Dortmund, Germany*

Eldar Zent − *Lead Discovery Center GmbH, 44227 Dortmund, Germany*

Ina Landel − *Faculty of Chemistry and Chemical Biology, TU Dortmund University, 44227 Dortmund, Germany; Drug Discovery Hub Dortmund (DDHD) am Zentrum für Integrierte Wirkstoffforschung (ZIW), 44227 Dortmund, Germany*

Jörn Weisner − *Faculty of Chemistry and Chemical Biology, TU Dortmund University, 44227 Dortmund, Germany; Drug Discovery Hub Dortmund (DDHD) am Zentrum für Integrierte Wirkstoffforschung (ZIW), 44227 Dortmund, Germany*

Kirujan Jeyakumar − *Faculty of Chemistry and Chemical Biology, TU Dortmund University, 44227 Dortmund, Germany; Drug Discovery Hub Dortmund (DDHD) am Zentrum für Integrierte Wirkstoffforschung (ZIW), 44227 Dortmund, Germany;* orcid.org/0000-0002-0184-6775

Leonie Heyden − *Faculty of Chemistry and Chemical Biology, TU Dortmund University, 44227 Dortmund, Germany; Drug Discovery Hub Dortmund (DDHD) am Zentrum für Integrierte Wirkstoffforschung (ZIW), 44227 Dortmund, Germany*

Nicole Russ − *Molecular Pathology, Institute of Pathology, University Hospital of Cologne, 50937 Cologne, Germany; Department of Translational Genomics, Faculty of Medicine* *and University Hospital Cologne, University of Cologne, 50931 Cologne, Germany*

Fabienne Müller – *Molecular Pathology, Institute of Pathology, University Hospital of Cologne, 50937 Cologne, Germany; Department of Translational Genomics, Faculty of Medicine and University Hospital Cologne, University of Cologne, 50931 Cologne, Germany*

Carina Lorenz – *Molecular Pathology, Institute of Pathology, University Hospital of Cologne, 50937 Cologne, Germany; Department of Translational Genomics, Faculty of Medicine and University Hospital Cologne, University of Cologne, 50931 Cologne, Germany*

Johannes Brägelmann – *Molecular Pathology, Institute of Pathology, University Hospital of Cologne, 50937 Cologne, Germany; Department of Translational Genomics, Faculty of Medicine and University Hospital Cologne, University of Cologne, 50931 Cologne, Germany; Mildred Scheel School of Oncology Cologne, Faculty of Medicine and University Hospital Cologne, University of Cologne, 50931 Cologne, Germany; Center for Molecular Medicine Cologne, Faculty of Medicine and University Hospital Cologne, University of Cologne, 50931 Cologne, Germany*

Inga Spille – *Molecular Pathology, Institute of Pathology, University Hospital of Cologne, 50937 Cologne, Germany; Department of Translational Genomics, Faculty of Medicine and University Hospital Cologne, University of Cologne, 50931 Cologne, Germany*

Tobias Grabe – *Faculty of Chemistry and Chemical Biology, TU Dortmund University, 44227 Dortmund, Germany; Drug Discovery Hub Dortmund (DDHD) am Zentrum für Integrierte Wirkstoffforschung (ZIW), 44227 Dortmund, Germany*

Matthias P. Müller – *Faculty of Chemistry and Chemical Biology, TU Dortmund University, 44227 Dortmund, Germany; Drug Discovery Hub Dortmund (DDHD) am Zentrum für Integrierte Wirkstoffforschung (ZIW), 44227 Dortmund, Germany;* orcid.org/0000-0002-1529-8933

Johannes M. Heuckmann – *PearlRiver Bio GmbH, 44227 Dortmund, Germany*

Bert M. Klebl – *Lead Discovery Center GmbH, 44227 Dortmund, Germany; The Norwegian College of Fishery Science, UiT The Arctic University of Norway, N-9037 Tromsø, Norway*

Peter Nussbaumer – *Lead Discovery Center GmbH, 44227 Dortmund, Germany;* orcid.org/0000-0002-2761-629X

Complete contact information is available at:
https://pubs.acs.org/10.1021/acs.jmedchem.1c02080

Author Contributions

◆J.L., H.L.T., and C.S.-F. contributed equally. The manuscript was written through contributions of all authors. All authors have given approval to the final version of the manuscript.

Notes

The authors declare the following competing financial interest(s): J.L., C.S.-F., and J.M.H. are founder and full-time employees of PearlRiver Bio GmbH and shareholder of Centessa Pharmaceuticals plc. M.L.S. and D.R. are founder and consultants of PearlRiver Bio GmbH and shareholder of Centessa Pharmaceuticals plc. H.L.T. is a consultant of PearlRiver Bio GmbH. The Lead Discovery Center GmbH is founder of PearlRiver Bio GmbH and shareholder of Centessa Pharmaceuticals plc. PearlRiver Bio GmbH is part of Centessa Pharmaceuticals plc. M.B., S.M., E.Z., B.M.K., and P.N. are full-time employees of the Lead Discovery Center GmbH.

■ ACKNOWLEDGMENTS

The authors are thankful to Roman K. Thomas for fruitful discussions. They also thank Anke Unger and Mia Zischinsky for their support regarding pharmacological evaluations. This work was co-funded by the Deutsche Forschungsgemeinschaft (DFG), the German federal state North Rhine-Westphalia (NRW), and the European Union (European Regional Development Fund: Investing In Your Future) (EFRE-800400), NEGECA (PerMed NRW), EMODI (to M.L.S., D.R., Lead Discovery Center GmbH), and Drug Discovery Hub Dortmund (DDHD). This work was supported by the Bundesministerium für Bildung und Forschung (e:Med initative; 01ZX1901A to M.L.S.) and the Deutsche Krebshilfe (70112888 to M.L.S.). This work was supported by the Lead Discovery Center GmbH.

■ ABBREVIATIONS USED

ADME, absorption, distribution, metabolism, and excretion; ALK, anaplastic lymphoma kinase; AUC, area under the curve; BID, bis in die/twice daily; CTG, CellTiter-Glo; EGFR, epidermal growth factor receptor; ERK, extracellular-signal regulated kinases; FDA, Food and Drug Administration; FGFR2, fibroblast growth factor receptor 2; KRas, Kirsten rat sarcoma; MS, mass spectrometry; NSCLC, non-small cell lung cancer; PDB, protein data bank; PO, per os/orally; QD, quaque die/once daily; SAR, structure–activity relationship; SD, standard deviation; SEM, standard error of the mean; TKIs, tyrosine kinase inhibitors

■ REFERENCES

(1) Alroy, I.; Yarden, Y. The ErbB signaling network in embryogenesis and oncogenesis: signal diversification through combinatorial ligand-receptor interactions. *FEBS Lett.* **1997**, *410*, 83–86.

(2) Mendelsohn, J.; Baselga, J. The EGF receptor family as targets for cancer therapy. *Oncogene* **2000**, *19*, 6550–6565.

(3) Sordella, R.; Bell, D. W.; Haber, D. A.; Settleman, J. Gefitinib-sensitizing EGFR mutations in lung cancer activate anti-apoptotic pathways. *Science* **2004**, *305*, 1163–1167.

(4) Greulich, H.; Chen, T. H.; Feng, W.; Jänne, P. A.; Alvarez, J. V.; Zappaterra, M.; Bulmer, S. E.; Frank, D. A.; Hahn, W. C.; Sellers, W. R.; Meyerson, M. Oncogenic transformation by inhibitor-sensitive and -resistant EGFR mutants. *PLoS Med.* **2005**, *2*, No. e313.

(5) Jiang, J.; Greulich, H.; Jänne, P. A.; Sellers, W. R.; Meyerson, M.; Griffin, J. D. Epidermal growth factor-independent transformation of Ba/F3 cells with cancer-derived epidermal growth factor receptor mutants induces gefitinib-sensitive cell cycle progression. *Cancer Res.* **2005**, *65*, 8968–8974.

(6) Schlessinger, J. Cell signaling by receptor tyrosine kinases. *Cell* **2000**, *103*, 211–225.

(7) Mok, T. S.; Wu, Y. L.; Thongprasert, S.; Yang, C. H.; Chu, D. T.; Saijo, N.; Sunpaweravong, P.; Han, B.; Margono, B.; Ichinose, Y.; Nishiwaki, Y.; Ohe, Y.; Yang, J. J.; Chewaskulyong, B.; Jiang, H.; Duffield, E. L.; Watkins, C. L.; Armour, A. A.; Fukuoka, M. Gefitinib or carboplatin-paclitaxel in pulmonary adenocarcinoma. *N. Engl. J. Med.* **2009**, *361*, 947–957.

(8) Yang, J.C.-H.; Shih, J. Y.; Su, W. C.; Hsia, T. C.; Tsai, C. M.; Ou, S. H.; Yu, C. J.; Chang, G. C.; Ho, C. L.; Sequist, L. V.; Dudek, A. Z.; Shahidi, M.; Cong, X. J.; Lorence, R. M.; Yang, P. C.; Miller, V. A. Afatinib for patients with lung adenocarcinoma and epidermal growth factor receptor mutations (LUX-Lung 2): a phase 2 trial. *Lancet Oncol.* **2012**, *13*, 539–548.

(9) Soria, J.-C.; Ohe, Y.; Vansteenkiste, J.; Reungwetwattana, T.; Chewaskulyong, B.; Lee, K. H.; Dechaphunkul, A.; Imamura, F.; Nogami, N.; Kurata, T.; Okamoto, I.; Zhou, C.; Cho, B. C.; Cheng, Y.; Cho, E. K.; Voon, P. J.; Planchard, D.; Su, W.-C.; Gray, J. E.; Lee, S.-M.; Hodge, R.; Marotti, M.; Rukazenkov, Y.; Ramalingam, S. S. Osimertinib in untreated EGFR-mutated advanced non−small-cell lung cancer. *N. Engl. J. Med.* **2018**, *378*, 113−125.

(10) Tumbrink, H. L.; Heimsoeth, A.; Sos, M. L. The next tier of EGFR resistance mutations in lung cancer. *Oncogene* **2021**, *40*, 1−11.

(11) Wakeling, A. E.; Guy, S. P.; Woodburn, J. R.; Ashton, S. E.; Curry, B. J.; Barker, A. J.; Gibson, K. H. ZD1839 (iressa): An orally active inhibitor of epidermal growth factor signaling with potential for cancer therapy. *Cancer Res.* **2002**, *62*, 5749−5754.

(12) Li, D.; Ambrogio, L.; Shimamura, T.; Kubo, S.; Takahashi, M.; Chirieac, L. R.; Padera, R. F.; Shapiro, G. I.; Baum, A.; Himmelsbach, F.; Rettig, W. J.; Meyerson, M.; Solca, F.; Greulich, H.; Wong, K. K. BIBW2992, an irreversible EGFR/HER2 inhibitor highly effective in preclinical lung cancer models. *Oncogene* **2008**, *27*, 4702−4711.

(13) Dungo, R. T.; Keating, G. M. Afatinib: first global approval. *Drugs* **2013**, *73*, 1503−1515.

(14) Finlay, M. R. V.; Anderton, M.; Ashton, S.; Ballard, P.; Bethel, P. A.; Box, M. R.; Bradbury, R. H.; Brown, S. J.; Butterworth, S.; Campbell, A.; Chorley, C.; Colclough, N.; Cross, D. A.; Currie, G. S.; Grist, M.; Hassall, L.; Hill, G. B.; James, D.; James, M.; Kemmitt, P.; Klinowska, T.; Lamont, G.; Lamont, S. G.; Martin, N.; McFarland, H. L.; Mellor, M. J.; Orme, J. P.; Perkins, D.; Perkins, P.; Richmond, G.; Smith, P.; Ward, R. A.; Waring, M. J.; Whittaker, D.; Wells, S.; Wrigley, G. L. Discovery of a potent and selective EGFR inhibitor (AZD9291) of both sensitizing and T790M resistance mutations that spares the wild type form of the receptor. *J. Med. Chem.* **2014**, *57*, 8249−8267.

(15) Ward, R. A.; Anderton, M. J.; Ashton, S.; Bethel, P. A.; Box, M.; Butterworth, S.; Colclough, N.; Chorley, C. G.; Chuaqui, C.; Cross, D. A.; Dakin, L. A.; Debreczeni, J. E.; Eberlein, C.; Finlay, M. R.; Hill, G. B.; Grist, M.; Klinowska, T. C.; Lane, C.; Martin, S.; Orme, J. P.; Smith, P.; Wang, F.; Waring, M. J. Structure- and reactivity-based development of covalent inhibitors of the activating and gatekeeper mutant forms of the epidermal growth factor receptor (EGFR). *J. Med. Chem.* **2013**, *56*, 7025−7048.

(16) Cross, D. A.; Ashton, S. E.; Ghiorghiu, S.; Eberlein, C.; Nebhan, C. A.; Spitzler, P. J.; Orme, J. P.; Finlay, M. R.; Ward, R. A.; Mellor, M. J.; Hughes, G.; Rahi, A.; Jacobs, V. N.; Red Brewer, M.; Ichihara, E.; Sun, J.; Jin, H.; Ballard, P.; Al-Kadhimi, K.; Rowlinson, R.; Klinowska, T.; Richmond, G. H.; Cantarini, M.; Kim, D. W.; Ranson, M. R.; Pao, W. AZD9291, an irreversible EGFR TKI, overcomes T790M-mediated resistance to EGFR inhibitors in lung cancer. *Cancer Discovery* **2014**, *4*, 1046−1061.

(17) Jänne, P. A.; Yang, J. C.; Kim, D. W.; Planchard, D.; Ohe, Y.; Ramalingam, S. S.; Ahn, M. J.; Kim, S. W.; Su, W. C.; Horn, L.; Haggstrom, D.; Felip, E.; Kim, J. H.; Frewer, P.; Cantarini, M.; Brown, K. H.; Dickinson, P. A.; Ghiorghiu, S.; Ranson, M. AZD9291 in EGFR inhibitor-resistant non-small-cell lung cancer. *N. Engl. J. Med.* **2015**, *372*, 1689−1699.

(18) Arcila, M. E.; Nafa, K.; Chaft, J. E.; Rekhtman, N.; Lau, C.; Reva, B. A.; Zakowski, M. F.; Kris, M. G.; Ladanyi, M. EGFR exon 20 insertion mutations in lung adenocarcinomas: Prevalence, molecular heterogeneity, and clinicopathologic characteristics. *Mol. Cancer Ther.* **2013**, *12*, 220−229.

(19) Leduc, C.; Merlio, J. P.; Besse, B.; Blons, H.; Debieuvre, D.; Bringuier, P. P.; Monnet, I.; Rouquette, I.; Fraboulet-Moreau, S.; Lemoine, A.; Pouessel, D.; Mosser, J.; Vaylet, F.; Langlais, A.; Missy, P.; Morin, F.; Moro-Sibilot, D.; Cadranel, J.; Barlesi, F.; Beau-Faller, M.; French Cooperative Thoracic Intergroup. Clinical and molecular characteristics of non-small-cell lung cancer (NSCLC) harboring EGFR mutation: Results of the Nationwide French Cooperative Thoracic Intergroup (IFCT) program. *Ann. Oncol.* **2017**, *28*, 2715−2724.

(20) Arcila, M. E.; Chaft, J. E.; Nafa, K.; Roy-Chowdhuri, S.; Lau, C.; Zaidinski, M.; Paik, P. K.; Zakowski, M. F.; Kris, M. G.; Ladanyi, M. Prevalence, clinicopathologic associations, and molecular spectrum of ErbB2 (HER2) tyrosine kinase mutations in lung adenocarcinomas. *Clin. Cancer Res.* **2012**, *18*, 4910−4908.

(21) Cha, M. Y.; Lee, K. O.; Kim, M.; Song, J. Y.; Lee, K. H.; Park, J.; Chae, Y. J.; Kim, Y. H.; Suh, K. H.; Lee, G. S.; Park, S. B.; Kim, M. S. Antitumor activity of HM781-36B, a highly effective pan-HER inhibitor in erlotinib-resistant NSCLC and other EGFR-dependent cancer models. *Int. J. Cancer* **2012**, *130*, 2445−2454.

(22) Robichaux, J. P.; Elamin, Y. Y.; Tan, Z.; Carter, B. W.; Zhang, S.; Liu, S.; Li, S.; Chen, T.; Poteete, A.; Estrada-Bernal, A.; Le, A. T.; Truini, A.; Nilsson, M. B.; Sun, H.; Roarty, E.; Goldberg, S. B.; Brahmer, J. R.; Altan, M.; Lu, C.; Papadimitrakopoulou, V.; Politi, K.; Doebele, R. C.; Wong, K. K.; Heymach, J. V. Mechanisms and clinical activity of an EGFR and HER2 exon 20-selective kinase inhibitor in non-small cell lung cancer. *Nat. Med.* **2018**, *24*, 638−646.

(23) Robichaux, J. P.; Elamin, Y. Y.; Vijayan, R. S. K.; Nilsson, M. B.; Hu, L.; He, J.; Zhang, F.; Pisegna, M.; Poteete, A.; Sun, H.; Li, S.; Chen, T.; Han, H.; Negrao, M. V.; Ahnert, J. R.; Diao, L.; Wang, J.; Le, X.; Meric-Bernstam, F.; Routbort, M.; Roeck, B.; Yang, Z.; Raymond, V. M.; Lanman, R. B.; Frampton, G. M.; Miller, V. A.; Schrock, A. B.; Albacker, L. A.; Wong, K. K.; Cross, J. B.; Heymach, J. V. Pan-cancer landscape and analysis of ERBB2 mutations identifies poziotinib as a clinically active inhibitor and enhancer of T-DM1 activity. *Cancer Cell* **2019**, *36*, 444−457 e447.

(24) Gonzalvez, F.; Vincent, S.; Baker, T. E.; Gould, A. E.; Li, S.; Wardwell, S. D.; Nadworny, S.; Ning, Y.; Zhang, S.; Huang, W. S.; Hu, Y.; Li, F.; Greenfield, M. T.; Zech, S. G.; Das, B.; Narasimhan, N. I.; Clackson, T.; Dalgarno, D.; Shakespeare, W. C.; Fitzgerald, M.; Chouitar, J.; Griffin, R. J.; Liu, S.; Wong, K. K.; Zhu, X.; Rivera, V. M. Mobocertinib (TAK-788): A targeted inhibitor of EGFR exon 20 insertion mutants in non-small cell lung cancer. *Cancer Discovery* **2021**, *11*, 1672−1687.

(25) Vasconcelos, P. E.; Kobayashi, I. S.; Kobayashi, S. S.; Costa, D. B. Preclinical characterization of mobocertinib highlights the putative therapeutic window of this novel EGFR inhibitor to EGFR exon 20 insertion mutations. *JTO Clin. Res. Rep.* **2021**, *2*, 1−7.

(26) Lategahn, J.; Keul, M.; Klövekorn, P.; Tumbrink, H. L.; Niggenaber, J.; Müller, M. P.; Hodson, L.; Flasshoff, M.; Hardick, J.; Grabe, T.; Engel, J.; Schultz-Fademrecht, C.; Baumann, M.; Ketzer, J.; Mühlenberg, T.; Hiller, W.; Günther, G.; Unger, A.; Müller, H.; Heimsoeth, A.; Golz, C.; Blank-Landeshammer, B.; Kollipara, L.; Zahedi, R. P.; Strohmann, C.; Hengstler, J. G.; van Otterlo, W. A. L.; Bauer, S.; Rauh, D. Inhibition of osimertinib-resistant epidermal growth factor receptor EGFR-T790M/C797S. *Chem. Sci.* **2019**, *10*, 10789−10801.

(27) Liu, R.; Zhan, S.; Che, Y.; Shen, J. Reactivities of the front pocket N-terminal cap cysteines in human kinases. *J. Med. Chem.* **2022**, *65*, 1525−1535.

(28) Barf, T.; Covey, T.; Izumi, R.; van de Kar, B.; Gulrajani, M.; van Lith, B.; van Hoek, M.; de Zwart, E.; Mittag, D.; Demont, D.; Verkaik, S.; Krantz, F.; Pearson, P. G.; Ulrich, R.; Kaptein, A. Acalabrutinib (ACP-196): A covalent bruton tyrosine kinase inhibitor with a differentiated selectivity and in vivo potency profile. *J. Pharmacol. Exp. Ther.* **2017**, *363*, 240−252.

3.2 Clonal dynamics of *BRAF*-driven drug resistance in *EGFR*-mutant lung cancer

Diana Schaufler‡[1], David Ast‡[2,3,4], Hannah L. Tumbrink[2,3], Nima Abedpour[3,5], Lukas Maas[3], Ayla Schwäbe[2,3], Inga Spille[2,3], Stefanie Lennartz[2,3], Jana Fassunke[6], Mihaela Aldea[7], Benjamin Besse[7], David Planchard[7], Lucia Nogova[1], Sebastian Michels[1], Carsten Kobe[8], Thorsten Persigehl[9], Theresa Westphal[1], Sophia Koleczko[1], Rieke Fischer[1], Jan-Phillip Weber[1], Janine Altmüller[10], Roman K. Thomas[3,6,11], Sabine Merkelbach-Bruse[6], Oliver Gautschi[12], Laura Mezquita[13], Reinhard Büttner[6], Jürgen Wolf[1], Martin Peifer[3], Johannes Brägelmann*[2,3,4,5], Matthias Scheffler*[1] and Martin L. Sos*[2,3,5]

[1]University of Cologne, Faculty of Medicine and University Hospital Cologne, Department I of Internal Medicine, Center for Integrated Oncology Aachen Bonn Cologne Duesseldorf, Network Genomic Medicine, Lung Cancer Group Cologne, Cologne, Germany

[2]University of Cologne, Faculty of Medicine and University Hospital Cologne, Institute of Pathology, Molecular Pathology, Cologne, Germany

[3]University of Cologne, Faculty of Medicine and University Hospital Cologne, Department of Translational Genomics, Cologne, Germany

[4]Mildred Scheel School of Oncology, Faculty of Medicine and University Hospital Cologne, University of Cologne, Cologne, Germany

[5]University of Cologne, Faculty of Medicine and University Hospital Cologne, Center for Molecular Medicine Cologne, Cologne, Germany

[6]University of Cologne, Faculty of Medicine and University Hospital Cologne, Institute of Pathology, Network Genomic Medicine, Cologne, Germany

[7]Department of medical oncology, Thoracic Group, Gustave Roussy, Villejuif, Paris Sud University Orsay, Paris, France

[8]University of Cologne, Faculty of Medicine and University Hospital Cologne, Department of Nuclear Medicine, Cologne, Germany

[9]University of Cologne, Faculty of Medicine and University Hospital Cologne, Institute of Diagnostic and Interventional Radiology, Cologne, Germany

[10]Cologne Center for Genomics, University of Cologne, Cologne, Germany

[11]DKFZ, German Cancer Research Center, German Cancer Consortium (DKTK), Heidelberg, Germany

[12]University of Bern and Cantonal Hospital of Lucerne, Switzerland

[13]Medical Oncology Department, Hospital Clinic, Laboratory of Translational Genomics and Targeted therapies in Solid Tumors, IDIBAPS; Barcelona, Spain

‡D.S. and D.A. contributed equally as co-first authors.

*Correspondence to:

Dr. Johannes Brägelmann, University of Cologne, Faculty of Medicine and University Hospital Cologne, Molecular Pathology, Institute of Pathology, Molecular Pathology & Department of Translational Genomics, Weyertal 115b, 50931 Cologne, Germany. Tel.: +49 221 478 98777; E-Mail: johannes.braegelmann@uni-koeln.de

Priv.-Doz. Dr. Matthias Scheffler, University of Cologne, Faculty of Medicine and University Hospital Cologne, Department I of Internal Medicine, Center for Integrated Oncology Aachen Bonn Cologne Duesseldorf, Network Genomic Medicine, Lung Cancer Group Cologne, Kerpener Str. 62, 50937 Cologne, Germany. Tel.: +49 221 478 85495; E-Mail: matthias.scheffler@uk-koeln.de

Prof. Dr. Martin L. Sos, University of Cologne, Faculty of Medicine and University Hospital Cologne, Institute of Pathology, Molecular Pathology & Department of Translational Genomics, Weyertal 115b, 50931 Cologne, Germany. Tel.: +49 221-478 96175; E-Mail: martin.sos@uni-koeln.de

Specific contributions:

- In vitro FACS analysis
- In vivo combination efficiency study of osimertinib and trametinib
- Data analysis of xenograft experiments
- Manuscript editing

npj | Precision Oncology

www.nature.com/npjprecisiononcology

ARTICLE **OPEN**

Clonal dynamics of *BRAF*-driven drug resistance in *EGFR*-mutant lung cancer

Diana Schaufler[1,14], David F. Ast[2,3,4,14], Hannah L. Tumbrink[2,3], Nima Abedpour[3,5], Lukas Maas[3], Ayla E. Schwäbe[2,3], Inga Spille[2,3], Stefanie Lennartz[2,3], Jana Fassunke[6], Mihaela Aldea[7], Benjamin Besse[7], David Planchard[7], Lucia Nogova[1], Sebastian Michels[1], Carsten Kobe[8], Thorsten Persigehl[9], Theresa Westphal[1], Sophia Koleczko[1], Rieke Fischer[1], Jan-Phillip Weber[1], Janine Altmüller[10], Roman K. Thomas[3,6,11], Sabine Merkelbach-Bruse[6], Oliver Gautschi[12], Laura Mezquita[13], Reinhard Büttner[6], Jürgen Wolf[1], Martin Peifer[3], Johannes Brägelmann[2,3,4,5]✉, Matthias Scheffler[1]✉ and Martin L. Sos[2,3,5]✉

Activation of MAPK signaling via *BRAF* mutations may limit the activity of EGFR inhibitors in *EGFR*-mutant lung cancer patients. However, the impact of *BRAF* mutations on the selection and fitness of emerging resistant clones during anti-EGFR therapy remains elusive. We tracked the evolution of subclonal mutations by whole-exome sequencing and performed clonal analyses of individual metastases during therapy. Complementary functional analyses of polyclonal *EGFR*-mutant cell pools showed a dose-dependent enrichment of *BRAF*^{V600E} and a loss of EGFR inhibitor susceptibility. The clones remain stable and become vulnerable to combined EGFR, RAF, and MEK inhibition. Moreover, only osimertinib/trametinib combination treatment, but not monotherapy with either of these drugs, leads to robust tumor shrinkage in *EGFR*-driven xenograft models harboring *BRAF*^{V600E} mutations. These data provide insights into the dynamics of clonal evolution of *EGFR*-mutant tumors and the therapeutic implications of *BRAF* co-mutations that may facilitate the development of treatment strategies to improve the prognosis of these patients.

npj Precision Oncology (2021)5:102 ; https://doi.org/10.1038/s41698-021-00241-9

INTRODUCTION

Targeted treatment of epidermal growth factor receptor (*EGFR*)-mutant non-small cell lung cancer (NSCLC) is a landmark for rational therapy addressing molecular vulnerabilities[1]. Treatment with first- and second-generation EGFR tyrosine kinase inhibitors (TKIs) markedly improved the clinical outcome of patients with advanced *EGFR*-mutant NSCLC[2–5]. Currently, osimertinib is the only third-generation EGFR inhibitor approved for the sequential treatment of patients with acquired *EGFR*^{T790M} resistance mutation occurring after first- and second-generation TKIs[6,7]. In addition, osimertinib became the new standard-of-care in the first-line treatment of patients with *EGFR*-mutant NSCLC[8,9].

Despite the clinical efficacy of osimertinib in the first- and second-line treatment of *EGFR*-mutant NSCLC, drug resistance with disease progression is inevitable[10–18]. Various *EGFR*-dependent and *EGFR*-independent resistance mechanisms have been identified including *EGFR*^{C797S} and *EGFR*^{G724S} mutations, *MET*/*HER2* amplification, activation of the RAS–mitogen-activated protein kinase (MAPK) or RAS–phosphatidylinositol 3-kinase (PI3K) pathways, new fusions, and histological transformation. RAS–MAPK pathway aberrations that are known to confer resistance to osimertinib include *BRAF*, *NRAS*, and *KRAS* mutations[10,19,20]. *BRAF* mutations occur in 2–4% of NSCLC patients and the vast majority are localized in the kinase domain, including the most common mutation *BRAF*^{V600E}. *BRAF* mutations can be categorized into three classes based on their ability to act as monomers or dimers and based on their kinase activity. *BRAF*^{V600E} mutations represent class I mutations that, similarly to class II *BRAF* mutations (*RAS*-independent), result in activation of the BRAF kinase and the MAPK pathway (gain of function). Class III *BRAF* mutations (*RAS*-dependent) result in an impaired BRAF kinase activity and amplify ERK signaling depending on upstream activating signals (e. g. *RAS* activating mutations, *NF1* tumor suppressor deletion)[21]. All classes of *BRAF* mutations are recognized as oncogenic driver mutations, yet only *BRAF*^{V600E} mutations represent clinically actionable drug targets in cancer patients[22,23].

BRAF^{V600E} mutations have been identified as a resistance mechanism to osimertinib in roughly 3% of cases with *EGFR*-mutant lung cancer, with or without concurrent *EGFR*^{T790M} mutation[10,19,20]. Several combination therapies have been proposed for *BRAF* resistance in *EGFR*-mutant lung cancer, but an integrated genomic analysis of these tumors is lacking and precludes an optimization of therapeutic regimen[24–27]. Furthermore, the current understanding of the clonal evolution of *EGFR*-mutant cells that concomitantly acquire *BRAF* mutations during anti-EGFR therapy remains limited.

---

[1]University of Cologne, Faculty of Medicine and University Hospital Cologne, Department I of Internal Medicine, Center for Integrated Oncology Aachen Bonn Cologne Duesseldorf, Network Genomic Medicine, Lung Cancer Group Cologne, Cologne, Germany. [2]University of Cologne, Faculty of Medicine and University Hospital Cologne, Institute of Pathology, Molecular Pathology, Cologne, Germany. [3]University of Cologne, Faculty of Medicine and University Hospital Cologne, Department of Translational Genomics, Cologne, Germany. [4]Mildred Scheel School of Oncology, Faculty of Medicine and University Hospital Cologne, University of Cologne, Cologne, Germany. [5]University of Cologne, Faculty of Medicine and University Hospital Cologne, Center for Molecular Medicine Cologne, Cologne, Germany. [6]University of Cologne, Faculty of Medicine and University Hospital Cologne, Institute of Pathology, Network Genomic Medicine, Cologne, Germany. [7]Department of medical oncology, Thoracic Group, Gustave Roussy, Villejuif, Paris Sud University Orsay, Paris, France. [8]University of Cologne, Faculty of Medicine and University Hospital Cologne, Department of Nuclear Medicine, Cologne, Germany. [9]University of Cologne, Faculty of Medicine and University Hospital Cologne, Institute of Diagnostic and Interventional Radiology, Cologne, Germany. [10]Cologne Center for Genomics, University of Cologne, Cologne, Germany. [11]DKFZ, German Cancer Research Center, German Cancer Consortium (DKTK), Heidelberg, Germany. [12]University of Bern and Cantonal Hospital of Lucerne, Lucerne, Switzerland. [13]Medical Oncology Department, Hospital Clinic, Laboratory of Translational Genomics and Targeted therapies in Solid Tumors, IDIBAPS, Barcelona, Spain. [14]These authors contributed equally: Diana Schaufler, David F. Ast. ✉email: johannes.braegelmann@uni-koeln.de; matthias.scheffler@uk-koeln.de; martin.sos@uni-koeln.de

Published in partnership with The Hormel Institute, University of Minnesota

Within the present study, we aimed for a comprehensive and translational approach to systematically characterize the role of co-occurring *EGFR*/*BRAF* mutations in patients with advanced lung adenocarcinoma.

RESULTS

Targeting *BRAF*-driven resistance in *EGFR*-mutant lung cancer

To characterize the role of *BRAF* mutations in the context of druggable *EGFR* mutations, data of eligible patients from several centers were analyzed (see "Methods"). This led to the identification of 15 patients with lung adenocarcinoma harboring activating *EGFR* mutations and co-occurring *BRAF* mutations (Fig. 1a, Table 1). In five cases, *EGFR* and *BRAF* mutations were detected at the time of initial diagnosis, whereas in ten patients, *BRAF* mutations were acquired after anti-EGFR therapy (Table 1). In eight patients, *BRAF* mutations occurred after osimertinib treatment, in one patient after gefitinib treatment, and in one patient after afatinib treatment. The treatment history of these ten patients before the detection of acquired *BRAF* mutations is outlined in Supplementary Fig. 1. The median duration of time elapsed from diagnosis of *EGFR*-mutant lung cancer to the detection of acquired *BRAF* mutation was 33.8 months (95% CI: 9.0–99.1 months) (Fig. 1b). Six patients were evaluable for analysis of subsequent treatment and outcome after detection of acquired *BRAF* mutation (Fig. 1c, Table 2). Median overall survival (OS) for these six patients after detection of *BRAF*-driven acquired resistance was 7.8 months (95% CI: 5.1–10.5 months; Fig. 1c). Of which, four patients (P12–P15) presenting with acquired activating *BRAF*^{V600E} and *BRAF*^{K601E} (gain of function) mutations received either osimertinib and bevacizumab ($n = 2$), osimertinib and chemotherapy ($n = 1$), or chemotherapy plus bevacizumab ($n = 1$) as the next line of treatment after detection of the *BRAF* mutation (Table 2). In the Cologne cohort, we detected 26/1951 co-occurrences of *EGFR* and *BRAF* mutations (1.3%) but narrowed it down to clearly activating *EGFR* mutations. In the Paris cohort, we detected 4/184 co-occurrences of *EGFR* and *BRAF* mutations (2.2%). Overall, our data show that *BRAF* mutations represent a resistance mechanism in a relevant proportion of *EGFR*-mutant patients, warranting further investigation of the underlying clinical and evolutionary dynamics.

Next, we selected two patients (P01, P04) who acquired *BRAF*^{V600E} mutation under osimertinib treatment to evaluate the safety and efficacy of various drug combinations including EGFR, RAF, MEK, or MET inhibitors, chemotherapy, or bevacizumab (Table 2, Fig. 1d, Supplementary Fig. 2a). We chose functional imaging by FDG-PET for (early) metabolic response evaluation during our investigational conduct (Supplementary Table 1) and monitored treatment-related adverse events that were predominantly of low grade and manageable (Supplementary Table 2). Osimertinib treatment was initiated and carried out for 16 months in P01 and 7 months in P04 before the detection of progressive disease. While in P01 *EGFR*^{T790M} mutation was sustained, in P04, we observed a loss of *EGFR*^{T790M} mutation. Both patients started with dabrafenib and trametinib, which in both cases did not lead to a confirmed metabolic response. Both patients underwent a rebiopsy of progressive lesions and started immediately with osimertinib and dabrafenib. In P01, the rebiopsy revealed an *EGFR*^{del19} mutation, loss of *EGFR*^{T790M}, no *BRAF*^{V600E} mutation and an intermediate-level *MET* amplification (GCN 5.58, FISH). Subsequent doublet combinations of osimertinib plus dabrafenib and afatinib plus crizotinib showed either primary refractory disease or metabolic responses that could not be confirmed in the next scans. In contrast, the triple combination of osimertinib, dabrafenib, and trametinib led to a prolonged metabolic response and clinical benefit (Supplementary Table 1, Table 2). In P04, doublet combinations of osimertinib and dabrafenib led only to a short metabolic response not confirmed in the next scan, and with the addition of trametinib, we then observed a marked metabolic response in the primary lung tumor but not in the hepatic metastases. Rebiopsy of the hepatic lesions revealed an *EGFR*^{del19} mutation with T790M and C797S resistance mutations in *cis* and no *BRAF* mutation. Treatment was thus changed to osimertinib plus chemotherapy/transarterial chemoembolization due to progressive liver metastases. The patient, unfortunately, died a year after detection of *BRAF*^{V600E} resistance. Thus, biopsy-guided mutational profiling in conjunction with FDG-PET imaging can guide effective combination therapies to overcome resistance in these patients.

To investigate the clonal dynamics during the development of resistance, we performed whole-exome sequencing (WES) of biopsies from multiple time points and different metastatic sites obtained from P01 to P04 (Fig. 1d–i (P04), Supplementary Fig. 2 (P01)). For patient P01 WES could be performed on the primary tumor and two metastatic samples (Supplementary Fig. 2), while insufficient tissue, unfortunately, precluded analysis of the *BRAF*-mutant metastasis. Pairwise clustering based on the cancer cell fractions of the mutations (CCFs, i.e. frequency of occurrence in cancer cells after adjustment for purity, ploidy, and copy number (CN)[28] revealed a high proportion of private mutations, while only a few mutations (e.g., *EGFR*^{del19}) were clonal in all samples (Supplementary Fig. 2b–d). Due to the sequencing quality, an intra-biopsy heterogeneity analysis was not undertaken, but phylogenetic tree analysis between biopsies indicated a branched evolution during resistance development (Supplementary Fig. 2e). Interestingly, a common ancestor gave rise to the pleural upper lung lobe metastasis and clones subsequently developing into the pleural metastasis and the primary tumor. In accordance with this branching model, the CN profiles show shared alterations between all three available samples, but also CN segments exclusive to just one or a pair of samples (Supplementary Fig. 2f). Our data indicate early branching during tumor development and is in accordance with a scenario where resistant cells develop in parallel to the primary tumor even before treatment pressure is applied.

For patient P04 WES was performed on a peritoneal metastasis that occurred during initial inhibitor treatment (*EGFR*^{del19} and *EGFR*^{T790M}), a liver metastasis 6 months after treatment had been switched to osimertinib (*EGFR*^{del19} and *BRAF*^{V600E}) and a rebiopsy of the same liver lesion at progressive disease under dabrafenib and trametinib treatment (*EGFR*^{del19} and *BRAF*^{V600E}) (Fig. 1d). Comparative pairwise CCF-based clustering showed only a few mutations to be shared between the peritoneal biopsy and the first liver biopsy (e.g., *EGFR*^{del19}), while the majority was private for each one of metastases (e.g., *EGFR*^{T790M} and *BRAF*^{V600E}, respectively) (Fig. 1e). In contrast, almost all mutations were found to be shared between both biopsies of the liver lesion (Fig. 1f). Subclonal composition analysis of the peritoneal metastasis revealed two subclones (C1 60%, C3 40%), while the liver metastases presented with one dominant clone each (Fig. 1g).

For subsequent phylogenetic analyses, a founder clone C0 was derived based on the mutations shared by all biopsies since the material of the primary tumor was unavailable for WES. Tracking the genomic development from C0 indicated a branched evolution diverging towards the peritoneal metastasis carrying *EGFR*^{T790M} with its first subclone C1, which further spawned a new subclone C3 present in the same biopsy (Fig. 1h). The liver metastasis appeared to have developed from C0 independently of the peritoneal metastasis by acquiring the *BRAF*^{V600E} mutation (C2). The rebiopsy of that lesion showed a distinguishable clone C4 which only carried one additional non-synonymous mutation of unknown biological relevance indicating a high degree of genetic similarity (Fig. 1h). In addition, genetic similarities between lesions were quantified to gain further insight into the clonal evolution toward therapy resistance (see Supplementary Material for further details). This analysis supports a branched evolution

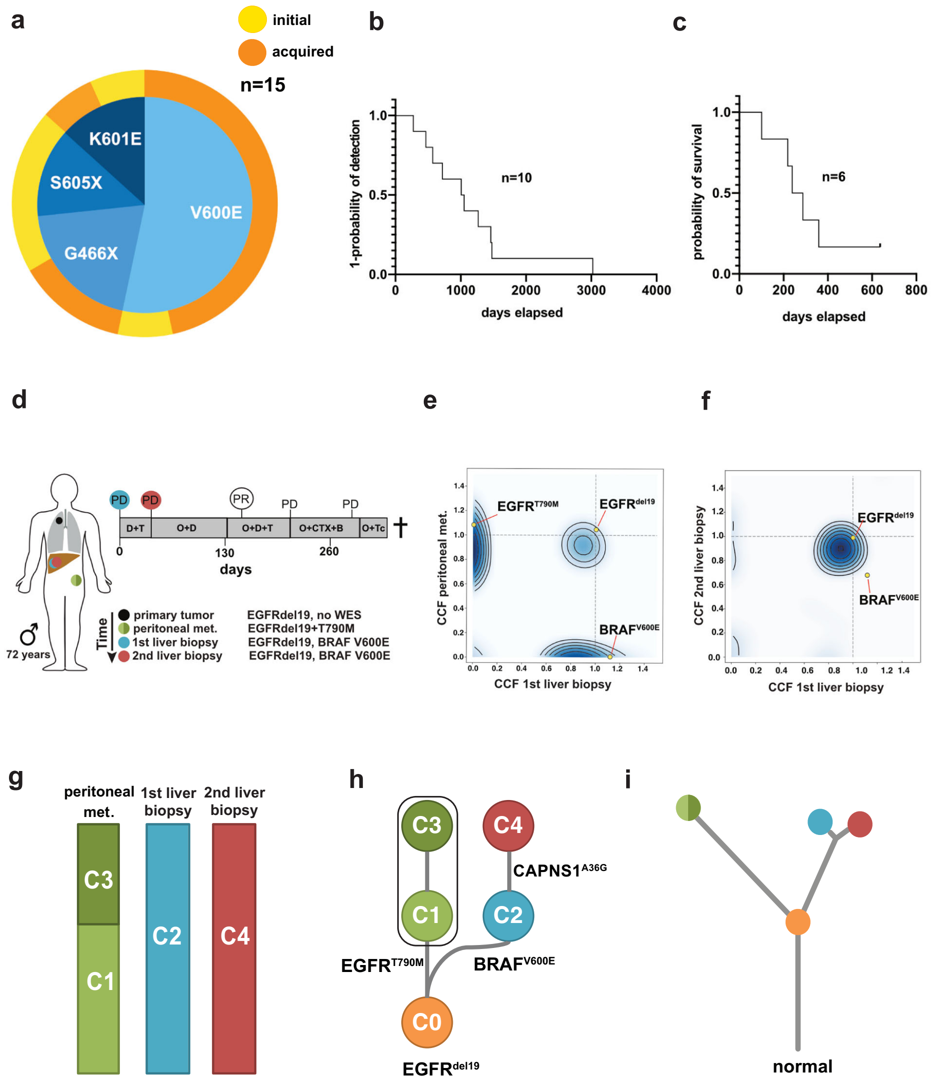

Fig. 1 **Clinicopathological characteristics for the study cohort and clonal evolution.** **a** Spectrum and distribution of *BRAF* co-mutations in patients with *EGFR*-mutant lung adenocarcinoma. **b** Kaplan–Meier curve of the time elapsed from the detection of the *EGFR* mutation until the detection of the acquired *BRAF* mutation (as events) in days. **c** Kaplan–Meier curve of overall survival for patients P01, P04, P12–P15 that were available for survival analysis. **d** Overview of the biopsies and key molecular findings by NGS for patient P04. Flow chart (top right) summarizes lines of therapy approaches overtime after the acquisition of *BRAF*^{V600E} mutation. **e, f** Clustering of WES-derived mutations based on their CCFs between pairs of tumor biopsies to detect clusters of shared clonal and private mutations. Candidate mutations in *EGFR* and *BRAF* are highlighted. **g** Subclonal composition in individual biopsies indicating two subclones (C1, C3) in the peritoneal metastasis and single clones in the liver metastases. **h** Clonal evolution of reconstructed cell populations presented as a phylogenetic tree. The computationally inferred most common ancestor C0 is common to all subsequent clones and highlighted mutations are present in descendent clones. (**i**) Visualization of evolutionary genetic distances between normal tissue and longitudinal biopsies. WES whole-exome sequencing, NGS next-generation sequencing, PD progressive disease, PR partial response, D + T dabrafenib+trametinib, O + D(+ T) osimertinib+dabrafenib(+trametinib), O + CTX + B osimertinib+chemotherapy+bevacizumab, O + Tc TACE osimertinib+transarterial chemoembolization, C clone, CCF cancer cell fraction.

Table 1. Clinicopathological characteristics for the study cohort.

Patient ID	Sex	Age	Biopsy	*EGFR* mutation	*BRAF* mutation		Co-mutations	
01	F	70	TB	E746_A750del, T790M	V600E	Class I	Acquired (osimertinib)	Persistent T790M
02	F	71	TB	E746_A750del, T790M	S605C	Not classified	Initial	TP53 R273H
03	M	61	TB	L858R	K601E	Class II	Initial	DDR2 R279M
04	M	72	TB	E746_A750del, T790M	V600E	Class I	Acquired (osimertinib)	loss of T790M
05	M	77	TB	L861Q	G466A	Class III	Acquired (afatinib)	ERBB2 G815A, TP53 S166*
06	M	66	TB	L858R, V834L	V600E	Class I	Acquired (osimertinib)	loss of *EGFR* mutations
07	F	84	TB	L858R	V600E	Class I	Initial	–
08	F	74	TB	L858R	G466E	Class III	Acquired (gefitinib)	–
09	M	50	TB	E746_A750del	V600E	Class I	Acquired (osimertinib)	CCDC6-RET
10	F	67	TB	L747_P753delinsS	G466E	Class III	Initial	*KRAS* A59E
11	F	75	TB	E746_A750del	S605N	Not classified	Initial	–
12	F	61	LB	E746_A750del, 790M, C797S, C797G	V600E	Class I	Acquired (osimertinib)	TP53 splice
13	M	50	LB	L747_S752del	K601E	Class II	Acquired (osimertinib)	TP53 R248G
14	F	70	TB	L858R, T790M, C797S	V600E	Class I	Acquired (osimertinib)	TP53 K120E, BRCA S237Y (VUS)
15	M	52	TB	L747_A750delinsP T790M, C797G	V600E	Class I	Acquired (osimertinib)	CTNNB1 S37C, ATM R1437K (VUS)

Patients with lung adenocarcinoma harboring activating *EGFR* mutations and co-occurring *BRAF* mutations were collected from three different cancer centers. Class I and class II (RAS-independent) *BRAF* mutations result in activation of the BRAF kinase and the MAPK pathway. Class III (RAS-dependent) *BRAF* mutations result in impaired BRAF kinase activity and amplify ERK signaling based upon upstream activating signals. *BRAF*$^{S605C/N}$ mutations (variants) lie within the kinase domain of the BRAF protein, they are not yet functionally classified. TB tissue biopsy, LB liquid biopsy.

Table 2. Systemic treatment lines and outcome evaluable for six patients after detection of the acquired *BRAF* mutation.

Patient ID	*BRAF* mutation	Time to detection of *BRAF* mutation after diagnosis (months)	Treatment after detection of *BRAF* mutation	TTD (days)	OS (days)	Outcome
01	V600E (Class I)	96	Dabrafenib+trametinib (1 L)	74	636	Alive
			Osimertinib+dabrafenib (2 L)	27		
			Afatinib+crizotinib (3 L)	65		
			Osimertinib+dabrafenib + (4 L) trametinib	288		
			Osimertinib+bevacizumab (5 L)	53		
			Afatinib+crizotinib (6 L)	105		
			Osimertinib+dabrafenib + (7 L) trametinib	na		
04	V600E (Class I)	47	Dabrafenib+trametinib (1 L)	38	287	Deceased
			Osimertinib+dabrafenib (2 L)	93		
			Osimertinib+dabrafenib + (3 L) trametinib	77		
			Osimertinib+carboplatin + (4 L)	75		
			Pemetrexed+bevacizumab osimertinib+TACE (5 L)	na		
12	V600E (Class I)	38	Carboplatin+paclitaxel + (1 L) bevacizumab	68	101	Deceased
13	K601E (Class II)	26	Osimertinib+paclitaxel (1 L)	50	239	Deceased
14	V600E (Class I)	34	Osimertinib+bevacizumab (1 L), carboplatin +gemcitabine (2 L)	92, 40	359	Deceased
15	V600E (Class I)	51	Osimertinib+bevacizumab (1 L) carboplatin +paclitaxel + (2 L) bevacizumab	57, 163	219	Deceased

BRAF^{V600E} and *BRAF*^{K601E} mutations result in an increased BRAF kinase activity. See also Fig. 1c for the Kaplan–Meier curve of OS. TTD time-to-treatment discontinuation, OS overall survival: time from acquired resistance (date of biopsy) until death/last day of follow-up, TACE transarterial chemoembolization.

trajectory model with a common ancestor giving rise to the peritoneal metastasis and liver metastases (Fig. 1i). While the peritoneal metastasis and liver metastases are not closely related, only minor changes occurred between the first and second biopsy of the liver lesion (Fig. 1i). Accordingly, the CN landscape is very similar between the peritoneal metastasis and liver metastases, but almost identical between both liver biopsies (Supplementary Fig. 3). This highlights that the different metastases and resistance mechanisms (*EGFR*^{T790M} and *BRAF*^{V600E}, respectively) developed independently from a common ancestral clone rather than in a linear relationship. Also, the remarkably high similarity between both liver biopsies indicates that selection pressure did not give rise to a highly distinct new subclone, potentially due to the lack of an EGFR inhibitor in the combination treatment. However, it may also be due to resistance to anti-BRAF therapy already being present in the clone C2 that propagates to C4 or may have a non-genomic basis not detectable by WES.

For a third patient (P14) we obtained a biopsy at the time of progression under osimertinib treatment (Supplementary Fig. 4a). WES of this biopsy showed the presence of several oncogenic *EGFR* mutations, namely L858R, T790M, and C797S (Supplementary Fig. 4b). All of those mutations were clonal, the T790M and C797S mutations are in agreement with previously described resistance mechanisms to EGFR inhibitors. Interestingly, we also detected a *BRAF*^{V600E} mutation (Supplementary Fig. 4b, Table 1). In contrast to the *EGFR* mutations, the *BRAF* mutation was subclonal and may thus indicate the branching of a newly developing subclone. This further highlights the complexity of disease resistance, which may incorporate several mechanisms of resistance development in parallel. Overall, the clonal analyses highlight that a process of branched evolution underlies resistance to targeted treatments in patients with *EGFR*-mutant tumors and may give rise to various independent resistance mechanisms.

Resistance through the selection of *BRAF*^{V600E}-positive clones

To functionally validate our clinical observations, we overexpressed *BRAF*^{V600E} in *EGFR*^{del19}-mutant PC9 cells. To compare *BRAF*^{V600E}-mediated effects to upstream activation of MAPK signaling, we generated cells expressing *NRAS*^{Q61K}, a mutation reported in preclinical models of acquired EGFR-inhibitor resistance[16,19]. In a polyclonal pool of PC9 cells stably expressing *BRAF*^{V600E} or *NRAS*^{Q61K}, only modest activation of the MAPK signaling was detected as determined by immunoblotting of phospho-ERK (Fig. 2a). However, residual phospho-ERK-levels after osimertinib treatment were detected only in cells with *BRAF*^{V600E} or *NRAS*^{Q61K} overexpression but not in control PC9 empty vector (EV) cells. During 7-14 day treatment the insufficient inhibition of MAPK signaling translated into the outgrowth of osimertinib-resistant clones in cells expressing *BRAF*^{V600E} or *NRAS*^{Q61K} (Fig. 2b, c). In line with this observation, only ≤0.3% of PC9 (EV) cells were found to be able to give rise to colonies during increasing doses of osimertinib treatment (Fig. 2d). However, overexpression of *BRAF*^{V600E} or *NRAS*^{Q61K} significantly enhanced the pool of cells with the capacity to outgrow during therapy to 5.2% (*BRAF*) and 4.5% (*NRAS*) or less in a dose-dependent manner (Fig. 2d).

The next question was whether the enrichment of cells with high *BRAF*^{V600E} or *NRAS*^{Q61K} expression would have an impact on EGFR inhibitor sensitivity. Therefore, polyclonal PC9$^{\text{BRAF-V600E}}$ and PC9$^{\text{NRAS-Q61K}}$ cells were preselected either with 10 nM (PC9$^{\text{BRAF/NRAS}}$ OS 10 nM) or 100 nM (PC9$^{\text{BRAF/NRAS}}$ OS 100 nM) of osimertinib over the course of >30 days. Using RT-PCR a dose-dependent elevation of RNA levels of the respective resistance alleles was found in PC9$^{\text{BRAF}}$ OS and PC9$^{\text{NRAS}}$ OS cells after osimertinib selection (Fig. 2e, f). Osimertinib-preselected cells exhibited a higher induction of *BRAF*^{V600E} expression (9.39-fold) than *NRAS*^{Q61K} expression (4.25-fold, $p = 0.036$). Accordingly, untreated osimertinib-preselected cells with high *BRAF*^{V600E} expression displayed stronger phospho-ERK staining when compared to *NRAS*^{Q61K} (Fig. 2g). Both osimertinib-preselected PC9$^{\text{BRAF-V600E}}$ and PC9$^{\text{NRAS-Q61K}}$ cells showed higher levels of sustained phospho-ERK during osimertinib treatment (Fig. 2g) and a higher degree of resistance in viability assays compared to non-selected cells (Fig. 2h). A similar degree of resistance was observed against the EGFR inhibitors erlotinib or afatinib (Supplementary Fig. 5a, b) but not against the non-specific, chemotherapeutic cisplatin (Supplementary Fig. 5c).

To further substantiate our data in an independent model, *BRAF*^{V600E} was overexpressed in the *EGFR*^{del19}-mutant HCC827 cell line. Again, a dose-dependent induction of resistance through osimertinib-preselection was observed in polyclonal HCC827$^{\text{BRAF-V600E}}$ cell pools (Supplementary Fig. 5d). These findings are in line with our clinical observations and previous cases that identified *BRAF*-mediated resistance in *EGFR*-mutant tumors during anti-EGFR therapy. Our results suggest that *BRAF*-mutant clones are enriched through EGFR-directed therapy in *EGFR*-mutant adenocarcinoma.

Overcoming *BRAF*^{V600E}-mediated resistance in *EGFR*-mutant cells

Previous studies have found that concomitant *KRAS* and *EGFR* mutations may increase the cell death rate of adenocarcinoma cells through hyperactivation of ERK signaling[29,30]. We tested whether the activation of MAPK signaling via *BRAF*^{V600E} may have a similar effect in *EGFR*-mutant PC9 cells. To this end, the cell proliferation of PC9$^{\text{BRAF-V600E}}$ and PC9$^{\text{NRAS-Q61K}}$ was measured over 5 days, but no major differences were observed compared to EV cells (Fig. 3a). We also did not detect any differences in the basal cell death rate between cell lines (Supplementary Fig. 6a). Consequently, cells with high expression of mutant *BRAF*/*NRAS* did not get counter-selected after the withdrawal of osimertinib (Fig. 3b, c).

Next, we tested combination therapies by targeting EGFR and MAPK signaling individually in PC9$^{\text{BRAF-V600E}}$ and PC9$^{\text{NRAS-Q61K}}$ cells (Fig. 3d). Both MEK inhibition and BRAF inhibition, as monotherapy, had a limited effect on the viability of PC9$^{\text{BRAF-V600E}}$ mutant cells (Supplementary Fig. 6b, c). In contrast, the combination of osimertinib and MEK or BRAF inhibition effectively prevented the outgrowth of colonies (Fig. 3d). To further validate our previous findings on a transcriptional level, we performed RNA sequencing of PC9 (EV), PC9$^{\text{BRAF-V600E}}$, and PC9$^{\text{BRAF-V600E}}$ OS 100 nM cells treated with osimertinib, trametinib, a combination of both or control for 48 h (see Supplementary Material). As expected, a principal component analysis showed that osimertinib monotherapy had strong effects only on PC9$^{\text{BRAF-V600E}}$ cells, while trametinib plus osimertinib comparably impacted both PC9$^{\text{BRAF-V600E}}$ and PC9$^{\text{BRAF-V600E}}$ OS 100 nM cells (Supplementary Fig. 6d). We next clustered samples based on the expression of E2F target genes to assess the impact on cell cycle-related gene expression as a surrogate marker for the cytotoxic effects of the given perturbation (Fig. 3e). In this analysis, the strongest downregulation of E2F genes was present in the group of cell line/treatment combinations that led to reduced cell numbers in crystal violet assays (Fig. 3d). Repression of E2F target genes was lower in unselected PC9$^{\text{BRAF-V600E}}$ cells with osimertinib compared to PC9 EV cells or compared to combination treatment (Fig. 3d). This indicates the limited efficacy of osimertinib monotherapy treatment if a *BRAF* mutation is present even without prior selection and supports the use of combination treatment. Furthermore, in PC9$^{\text{BRAF-V600E}}$ OS 100 nM cells the expression of MAPK pathway responsive genes was only perturbed during osimertinib and trametinib treatment (Supplementary Fig. 7a)[31]. Next, we assessed the synergy between osimertinib and trametinib, using ZIP-based synergy analysis, and found a strong

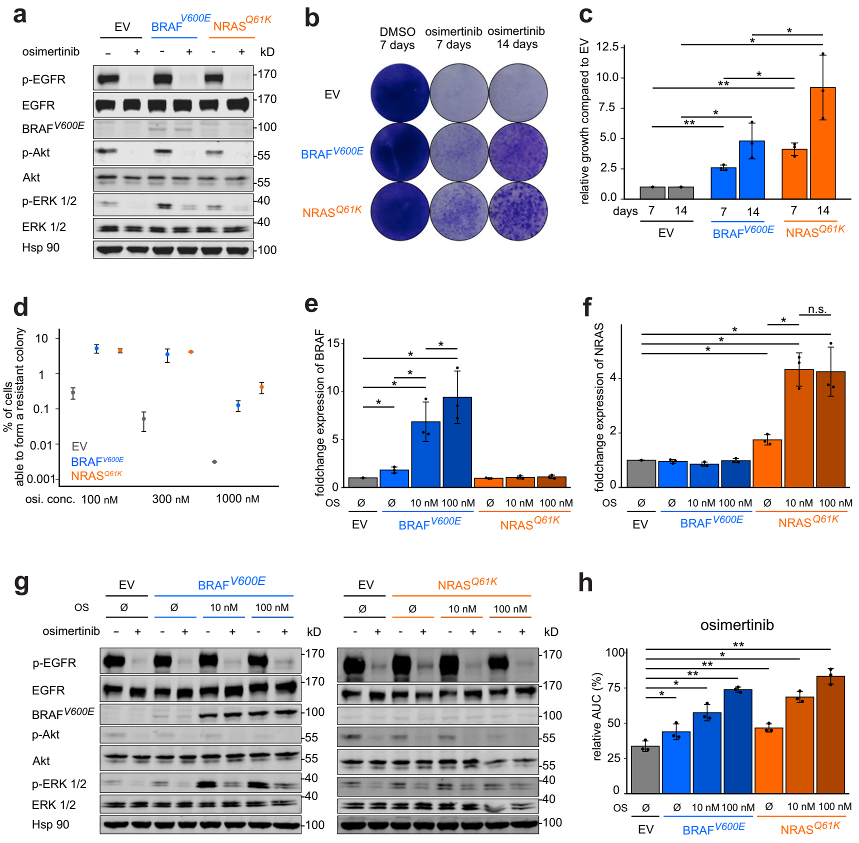

Fig. 2 Selection of *BRAF*^{V600E}-positive clones in *EGFR*-mutant cells. **a** Immunoblotting of PC9 cells expressing the annotated constructs, treated with (+) or without (−) osimertinib (48 h). Hsp90 is used as a loading control. **b** Clonogenicity assays of PC9 derived cell lines treated with osimertinib for 7 and 14 days or DMSO control for 7 days are displayed. **c** Quantitative analysis of (**b**) normalized to PC9 (EV). **d** Limited dilution assay of PC9-derived cell lines treated for 21 days before analysis. **e**, **f** qRT-PCR analysis of mRNA expression in **e** *BRAF* and **f** *NRAS* in PC9 derived cell lines normalized to EV. **g** Immunoblotting of PC9 cells expressing the annotated constructs that were treated as in (**a**). **h** Viability curves of PC9 cells expressing the annotated constructs treated with osimertinib (72 h) are shown. The relative area under the curve (AUC) in % compared to a theoretical non-responding AUC. Error bars indicate mean ± SD. Two-tailed paired *t* tests, ***$p < 0.001$, **$p < 0.01$, *$p \leq 0.05$, $^{n.s.}p > 0.05$. *EGFR* epidermal growth factor receptor, *BRAF* B-rapidly accelerated fibrosarcoma, *NRAS* neuroblastoma rat sarcoma, EV empty vector.

synergy that correlated with the expression of BRAF-V600E in PC9 cells (Fig. 3f, see Methods). The calculated synergy score for osimertinib and vemurafenib was limited and we found an antagonism for the combination of trametinib and vemurafenib inhibition in PC9$^{BRAF\text{-}V600E}$ mutant cells (Supplementary Fig. 7b, c). Finally, using a three-fold titration matrix, we observed a considerably low synergy for osimertinib and vemurafenib treatment compared to osimertinib and trametinib treatment, which was not further increased in a triple combination by adding vemurafenib (Supplementary Fig. 7d). In accordance with the synergy results, osimertinib with trametinib in contrast to osimertinib alone resulted in full inhibition of phospho-ERK signaling. Vemurafenib did not fully abrogate the sustained phospho-ERK signaling, as it also hyperactivated phospho-ERK as monotherapy, most likely due to the paradoxical effect on the endogenous wild type BRAF kinase (Fig. 3g)[32]. To further validate our in vitro results, we performed an in vivo study with xenografts implanted with PC9$^{BRAF\text{-}V600E}$ cells that were preselected for high *BRAF*^{V600E} expression. Once the mice developed tumors, we started with the treatment regimen consisting of vehicle, osimertinib, trametinib or the combination of osimertinib and trametinib for 21 days (Fig. 3h). Compared to vehicle treatment, trametinib did not significantly decrease tumor volume, and osimertinib monotherapy led to a measurable tumor growth reduction. However, only, combination therapy led to robust tumor shrinkage in these xenografts (Fig. 3h). Thus, our in vivo data largely reflects our in vitro findings and suggests that combination therapy is necessary to induce substantial tumor shrinkage in tumors harboring activating *EGFR* and *BRAF* mutations. Of importance, none of the mice in the individual treatment arms experienced weight loss (Supplementary Fig. 7e) or any other severe treatment-associated side effects.

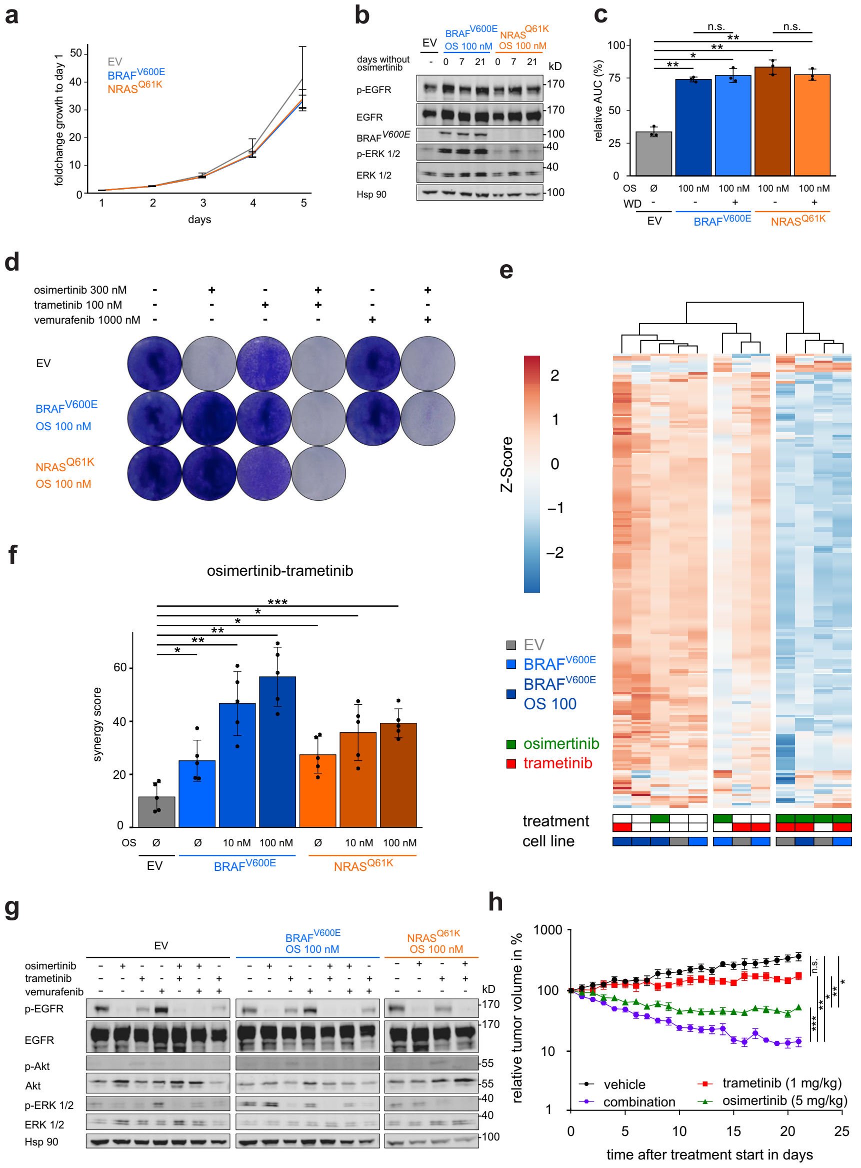

DISCUSSION

Osimertinib replaced other EGFR inhibitors in the early lines of therapy. This development had a major impact on the resistance profiles and development of effective salvage therapies[10–15,18,33]. The activation of MAPK signaling seems to play a more prominent role in patients' progressive on third-generation EGFR inhibitors when compared to first- and second-generation EGFR inhibitors[11,16,19,20,34]. Our comprehensive genomics study of *EGFR*-mutant patients with co-occurring *BRAF* mutations provides insights into the evolution of MAPK-driven resistance and its impact on *EGFR*-directed treatment.

Our combination of longitudinal clinical and genomic analyses provides insight into the subclonal heterogeneity of the individual tumors and corresponding metastases during resistance evolution. Our clonality analyses revealed that resistance to osimertinib (initiated at detection of *EGFR^{T790M}* mutation) and subsequent

Fig. 3 Overcoming *BRAF*^{V600E}-mediated resistance in *EGFR*-mutant cells. a Growth series of PC9 derived cell lines counted for 5 days every 24 h (see Methods). **b** Immunoblotting of PC9$^{\text{BRAF-V600E}}$ OS 100 nM, PC9$^{\text{NRAS-Q61K}}$ OS 100 nM, and PC9 (EV). Osimertinib-preselected cells were cultured for 0, 7, and 21 days without osimertinib treatment and plated 48 h before lysis. **c** Cell viability assay of PC9 cells expressing the annotated constructs treated for 72 h with osimertinib is shown. The relative AUC (see Methods) of BRAF$^{\text{V600E}}$ OS 100 nM and NRAS$^{\text{Q61K}}$ OS 100 nM after osimertinib withdrawal for >40 days are shown. **d** Clonogenicity assay of PC9 cells expressing the annotated constructs treated for 14 days with indicated compounds before staining. **e** RNA-seq based expression of E2F gene set genes (rows) in PC9 derived cell lines (columns) after 48 h treatment with indicated inhibitors. Expression was normalized as *z*-score per gene. **f** Synergy screen of osimertinib and trametinib combination treatment in PC9 derived cell lines for 72 h are displayed. **g** Immunoblotting of PC9 cells expressing the annotated constructs is shown. Treatment with indicated compounds 48 h before lysis. **h** Relative tumor volume of xenograft mice injected with PC9$^{\text{BRAF-V600E}}$ OS 100 nM cells in % compared to day 0 of the treatment regimen (see Methods). Error bars indicate mean ± SD. Two-tailed paired *t* tests (all except (**h**); two-tailed Welch's *t* tests with Bonferonni-correction), $^{***}p < 0.001$, $^{**}p < 0.01$, $^{*}p < 0.05$, $^{\text{n.s.}}p > 0.05$. *EGFR* epidermal growth factor receptor, *BRAF* B-rapidly accelerated fibrosarcoma, *NRAS* neuroblastoma rat sarcoma, EV empty vector.

combination of dabrafenib plus trametinib (initiated at detection of *BRAF*^{V600E} mutation) was driven by an evolutionary branching process rather than a linear trajectory of one clone that continues to acquire additional resistance mutations. Moreover, in both patients, the different metastases are genetically distinct from each other but arise from common ancestors that do not carry a resistance mutation. Even within our limited cohort, we observe different patterns of clonal evolution: while for P04 a common ancestor most likely from the primary tumor gave rise to the different metastases, for patient P01 phylogenetic analyses are in accordance with a model supporting much earlier branching. Of note, resistance mutations such as *EGFR*^{T790M} and *BRAF*^{V600E} were not detected by either panel sequencing or WES in samples still sensitive to the respective inhibitors. This may indicate that they developed either de novo during treatment or were pre-existent, but at a frequency to low to be detected without selection pressure.

Overall, our results demonstrate the presence and further development of tumor heterogeneity that can give rise to multiple resistance mechanisms due to treatment selection pressure. Moreover, our genomic analysis emphasizes that we are faced with a complex mutational landscape based on intra-tumoral, inter-tumoral, and inter-patient heterogeneity. It thus constitutes a major clinical challenge for the development of an efficient treatment strategy to counteract tumor progression. Based on the present findings a diagnostic strategy aiming to address the multilayered heterogeneity e.g. using liquid biopsies or multiple re-biopsies appears warranted to optimize treatment schedules. Our data suggest that one promising treatment strategy for patients with concurrent *EGFR* and MAPK pathway activation may require alternating treatment regimens with intermittent changes between drug combinations based upon observed heterogenic tumor response and emerging resistance patterns. To facilitate this strategy FDG-PET can be quite useful for rapid treatment evaluation and hence, dynamic clinical management as demonstrated by our investigational approach. However, we are aware that more patients need to be profiled in the future to compliment our results.

We and others have previously found that acquired resistance through activation of MAPK signaling via *KRAS* mutations can be detected in patients receiving third-generation EGFR inhibitors[11,12]. *BRAF* mutations and *BRAF* rearrangements have also been shown to play a similar role like *KRAS* in the resistance setting of *EGFR*-mutant adenocarcinoma[16,19,34]. This is surprising as previous functional analyses indicated that mutant *KRAS* mutations may augment the cell death rate of *EGFR*-mutant cells and thereby limit the outgrowth of resistant clones[29]. Our cell line models indicate that concomitant MAPK pathway signaling is tolerated when *BRAF* or *NRAS* are activated. This corresponds with our clinical observation that *BRAF* mutations can co-occur with *EGFR* mutations even before anti-EGFR therapy. Interestingly, the levels of phospho-ERK activation differ strongly between *BRAF*- and *NRAS*-mutant cells but we did not observe major differences in the ability of these alleles to promote resistance or cell death in *EGFR*-mutant cells. These functional observations are also in line with our finding that *BRAF*/*EGFR*-mutant lung tumors are recurrently found across different cancer centers, indicating a basis for the co-existence of *BRAF*/*EGFR* mutations without selection pressure. Future studies are required to fully decipher the potential differences between MAPK signaling activation at different levels of the pathway in the context of *EGFR*-mutant lung adenocarcinoma. Nevertheless, our in vitro and in vivo findings fully support the notion that EGFR/MEK combination might be a viable option to overcome *BRAF*-driven resistance in patients with *EGFR*-mutant lung adenocarcinoma.

In summary, our data uncover basic principles of drug-induced evolutionary paths underlying *BRAF*-driven resistance in patients with lung adenocarcinoma. The integrated analyses support a model in which concomitant activation of EGFR and BRAF is selected through anti-EGFR therapy that combines well with EGFR, BRAF, and MEK inhibitors to overcome resistance. Our systematic exploration of clinically relevant drug combinations may offer additional avenues for follow-up investigations into novel targeted treatment strategies for patients with co-occurring *EGFR* and *BRAF* mutations.

METHODS

Patients

We compiled a cohort of 15 patients with lung adenocarcinoma and activating *EGFR* mutations that harbored co-occurring *BRAF* mutations with and without prior anti-EGFR treatment. Patients were identified within the Network Genomic Medicine (NGM) Lung Cancer in Cologne, Germany, Institute Gustave Roussy in Paris, France, and Cantonal Hospital of Lucerne, Switzerland. Treatment, genetic findings, and survival of these patients were evaluated. All patients consented to be analyzed. The study was conducted in concordance with local ethical guidelines and was reviewed by the institutional ethics committee. Selected patients were treated with different lines of therapy including combinations of osimertinib, dabrafenib, and trametinib. These patients provided written informed consent for a prospective investigational molecular- and imaging-guided personalized treatment approach. Rebiopsies were acquired at disease progression. Tissue biopsy was performed through core needle biopsy according to local standard procedures. Survival of all patients was calculated using the Kaplan Meier method.

Molecular analyses

The vast majority of the specimens analyzed in our study consisted of tumor tissue ($n = 13$). For two patients, liquid biopsies were evaluated. (Table 1). Next-generation sequencing (NGS)-based molecular profiling was performed for each patient either on tumor tissue or on circulating tumor DNA (ctDNA). For patients, P01 and P04 whole-exome sequencing was additionally performed on the tumor tissue. For patients P01 and P04, we obtained longitudinally serial repeated tissue biopsies of the leading tumor lesions at each time of progression during treatment with different combinations of osimertinib, dabrafenib and trametinib, and other therapies. NGS of tumor tissue was performed as previously described[35–38]. Plasma analysis of ctDNA was performed as previously reported[39].

PET-CT assessments

The efficacy of treatment was evaluated by positron emission tomography (PET)/computed tomography (CT) scans using radiolabeled ^{18}F-2-fluoro-2-deoxy-D-glucose (FDG). Scans were acquired at baseline, and as early as 2 weeks (early assessment) and again at regular intervals roughly every 6 or more weeks (late assessments) after initiation or change of therapy to capture early metabolic response (measured by standard uptake value (SUV)max) and morphologic response over time. Scans were conducted as previously described and performed on a Biograph mCT Flow-Edge 128 PET/CT-system (Siemens Medical Solutions) with a 128-slice spiral CT component from the base of the skull to the mid-thigh[40]. We followed Positron Emission Response Criteria in Solid Tumors version 1.0 guidelines, assuming that response is characterized by an SUV reduction of at least 30% in the hottest lesion[41].

Whole-exome sequencing (WES)

WES was performed on FFPE-derived DNA from serial tumor tissue rebiopsies obtained at the time of tumor progression during treatment of patients P01 and P04. In addition, for one patient DNA was extracted from the primary tumor using the truXTRAC FFPE DNA extraction kit (Covaris, USA, Cat. No. 520307). Exomes were individually prepared using 200 ng of DNA using standard protocol SureSelectXT Automated Target Enrichment for Illumina Paired-End Multiplexed Sequencing and Agilent Bravo automated liquid handling platform. As for patient P14, there was only a post-osimertinib tumor biopsy available for WES, which was enriched using the Agilent SureSelect CR kit (Agilent, USA). After validation (2200 TapeStation, Agilent Technologies) and quantification (Qubit System, Invitrogen, Waltham, USA) pools of libraries were generated. The pools were quantified using the KAPA Library Quantification kit (Peqlab, Germany, KAPBKK4854) and 7900HT Sequence Detection System (Applied Biosystems, Waltham, USA) and subsequently sequenced at 140× mean coverage on an Illumina NovaSeq6000 sequencing instrument using a paired-end 2 × 100 bp protocol.

WES and clonality analysis

Analysis of raw sequencing data and clonality analyses were performed using an established pipeline[42]: After alignment of the raw sequencing data to the hg19 reference genome in total 137–325 million reads could successfully be mapped per sample corresponding to a mean coverage of 93×–200× per sample and covering all intended exonic target region with ≥20× coverage for 90–98% of those. In summary, of the 42.3 megabases of exonic regions as defined by the GRCh 37/hg19 RefSeq genome annotation, 39–40 megabases of exons were sufficiently covered for mutation calling and subsequent analyses. Thus, allelic fractions of somatic mutations were corrected for purity and CN changes to determine cancer cell fractions (CCF). The distribution of CCFs was then searched for distinct subpopulations by using a nonparametric method to deconvolute the noise in the CCFs. This allows for the identification of genetically distinct tumor subclones and the reconstruction of tumor evolutionary histories.

Cell culture and functional analyses

Human NSCLC cell lines were verified by STR profiling at the Institute for Forensic Medicine of the University Hospital of Cologne. PC9, HCC827, and HEK293T cell lines were obtained from ATCC. PC9 and HCC827 cells and their osimertinib-preselected derivatives were cultured in RPMI (Fisher Scientific, USA, Cat. No. 12004997) HEK293T cells were cultured in DMEM (Fisher Scientific, USA, Cat. No. 61965-026). All media were supplemented with 10% fetal bovine serum (Fisher Scientific, USA, Cat. No. 10270-106) and 1% penicillin/streptomycin (Fisher Scientific, USA, Cat. No. 15070-063). All cells were grown at 37 °C in a humidified atmosphere with 5% CO_2.

Reagents

For cell culture studies, osimertinib (LC Laboratories, USA, Cat. No. 1421373-65-0), trametinib (LC Laboratories, USA, Cat. No. 871700-17-3), and vemurafenib (LC Laboratories, USA, Cat. No. 918504-65-1) were dissolved in dimethyl sulfoxide (DMSO) (Carl Roth, Germany, Cat. No. 4720.4) to a final stock concentration of 10 mM. Cisplatin (pharmacy of University Hospital of Cologne) was diluted to 3.33 mM in 0.9% NaCl.

Crystal violet assay

Totally, 10^5 cells were plated into one well of a 6-well plate and treated with DMSO (control), 300 nM osimertinib, 100 nM trametinib, 1 µM vemurafenib, and combinations osimertinib plus trametinib and osimertinib plus vemurafenib. Seven or 14 days after treatment, cells were fixed in 4% paraformaldehyde (Carl Roth, Germany, Cat. No. CP10.1) in phosphate-buffered saline (PBS) (Fisher Scientific, USA, Cat. No. 14190144), stained with 0.1% crystal violet (Sigma Aldrich, USA, Cat. No. C3886-25G) in PBS, and rinsed in PBS before image acquisition. For quantification, the Crystal Violet dye was dissolved in 2 ml methanol (Carl Roth, Germany, Cat. No. CP43.4) in the 6-well plate. Twenty microlitres of this solution were diluted 1:10 with methanol and injected into 96-well plates. The read-out was the absorption at 560 nm wavelength. The results per cell line were normalized against their DMSO-controls and then against the empty vector (EV) control cell line.

Protein overexpression experiments

Vectors pBABE puro, pBABE-puro-BRAF^{V600E}, and pBABE-NRAS^{Q61K} were cotransfected with a helper plasmid into HEK 293T cells using TransIT-LT1 reagent (Mirus, USA, Cat. No. MIR2300). Forty-eight hour post transfection, replication-incompetent retroviruses were collected from the supernatant for infection of PC9 and HCC827 in the presence of 8 µg/ml polybrene (Merck Millipore, USA, Cat. No. TR1003-G). Twenty-four hour after infection, the growth medium was changed and 3 µg/ml (PC9) or 2 µg/ml (HCC827) puromycin (Sigma Aldrich, USA, Cat. No. p8833) was added for selection for 7 days. After selection, cells were analyzed for protein expression.

pBABE-puro was a gift from Hartmut Land & Jay Morgenstern & Bob Weinberg (Addgene plasmid # 1764; RRID:Addgene_1764).

pBabe-Puro-BRAF^{V600E} was a gift from William Hahn (Addgene plasmid # 15269; RRID:Addgene_15269).

pBabe-NRAS^{Q61K} was a gift from Channing Der (Addgene plasmid # 12543; RRID:Addgene_12543).

Cell viability screening

To assess cell viability, cells were plated in 96-well plates in triplicates, and compounds were added at 9 decreasing compound concentrations 24 h after seeding. Seventy-two hours later, cell viability was measured via Cell Titer-Glo (CTG) assay (Promega, USA, Cat. No. g7573) and was normalized to DMSO-treated controls. Resistance in % was calculated as the area under the curve (AUC), calculated via Gauss's trapezoid area formula and then divided by a theoretical non-responding AUC, all calculated in R. Data are represented as mean ± standard error of the mean and significance was calculated by paired Student's *t* tests.

RNA isolation and qRT-PCR

Totally, 5×10^5 cells were plated into one well of a 6-well plate and harvested after 24 h. Total RNA was isolated using the RNeasy-kit (Qiagen, Germany, Cat. No. 74106) according to the manufacturer's instructions, including DNAse I digestion (Qiagen, Germany, Cat. No. 79256). In all, 1.5 µg of total RNA was reverse transcribed using Super-script II (Thermo Fisher Scientific, USA, Cat. No. 18064022) with random hexamer primers. Quantitative real-time PCR (qPCR) was performed using the QuantStudio 3 Real-Time PCR System (Thermo Fisher Scientific) and Power SYBR Green PCR Master Mix (Thermo Fisher Scientific, USA, Cat. No. 4309155). Data were normalized to GAPDH RNA levels and are presented as mean ± SD and significance was calculated by paired Student's *t* tests.

Flow cytometry

Cell lines were seeded into 6-well plates (1×10^5 cells/well). Twenty-four-hour later Staurosporine (Sigma Aldrich, USA, S4400) or DMSO control was added to the medium. Twenty-four-hour later supernatant was collected, cells were trypsinized (Fisher Scientific, USA, Cat. No. 11560626), washed with ice-cold PBS, and resuspended in antibody-binding buffer (10 mM HEPES pH 7.4 (Fisher Scientific, USA, Cat. No. 15630080), 140 mM NaCl; 2.5 mM $CaCl_2$). Cells were stained for Annexin-V (BD Biosciences, USA, Cat. No. 556420) and 50 µg/mL propidium iodide (Carl Roth, Germany, Cat. No. CN74). After 20 min of incubation in the dark, samples were analyzed on a FACS Gallios Flow Cytometer (Beckman Coulter). We used FACS Kaluza software (Beckman Coulter) to quantify populations. At least 5×10^4 events were assessed per measurement. All measurements were performed as duplicates. Gates used can be found in Supplementary Fig. 8. Data are presented as mean ± SD.

Immunoblot

Cell lysates were prepared using RIPA buffer supplemented with protease inhibitors (Complete Mini Protease Inhibitor Cocktail, Roche, Switzerland, Cat. No. 11836170001). Protein concentration was determined by BCA assay (Thermo Fisher Scientific, USA, Cat. No. 23225) and equal amounts of protein (20 µg) were separated on 4–12% Tris-glycine sodium dodecyl sulfate-polyacrylamide gel electrophoresis gels (Thermo Fisher Scientific, USA, Cat. No. XP04125BOX) and transferred to PVDF-FL membrane (Sigma Aldrich, USA, Cat. No. IPFL00010). Membranes were blocked in 5% milk (Carl Roth, Germany, Cat. No. T145.1) blocking buffer in Tris-buffered saline (TBS), incubated with primary antibodies, washed, and incubated with fluorescently labeled secondary antibodies before detection with Odyssey CLx imaging system (LI-COR Biosciences). Images were processed using the Image Studio Software (LI-COR Biosciences). Primary antibodies are EGFR (Cell Signaling, USA, Cat. No. CS-4267), p-EGFR (Cell Signaling, USA, Cat. No. CS-3777), BRAF-V600E (Spring Bioscience, USA, Cat. No. E-19290), BRAF (Santa Cruz Biotechnology, USA, Cat. No. SC-5284), ERK (Cell Signaling, USA, Cat. No. CS-9102), p-ERK (Cell Signaling, USA, Cat. No. CS-4370), Akt (Cell Signaling, USA, Cat. No. CS-2920), p-Akt (Cell Signaling, USA, Cat. No. CS-9271) and Hsp90 (Cell Signaling, USA, Cat. No. CS-4877). All primary antibodies were diluted 1:1000 in 5% milk blocking buffer in TBS with 0.2% Tween®20 (Sigma Aldrich, USA, Cat. No. P7949-500ML). Secondary antibodies are goat anti-rabbit 800CW (LI-COR Biosciences, USA, Cat. No. 926-32211), goat anti-mouse 800CW (LI-COR Biosciences, USA, Cat. No. 926-3220), goat anti-rabbit 680LT (LI-COR Biosciences, USA, Cat. No. #926-68021), and goat anti-mouse 680LT (LI-COR Biosciences, USA, Cat. No. 926-68020). All secondary antibodies were diluted 1:20,000 in 2.5% milk blocking buffer in TBS with 0.2% Tween®20 and 0.01% sodium dodecyl sulfate (SDS) (Carl Roth, Germany, Cat. No. 8029.4).

All blots derive from the same experiment and were processed in parallel. Uncropped blots can be found in Supplementary Figs. 9–13.

Synergy screen

Cells were plated in a 6 × 6 wells matrix in 96-well plates. After 24 h cells were treated with five decreasing concentrations of compound A plus DMSO control starting from right to left. Cells were also treated at the same time with five decreasing concentrations of compound B plus DMSO control starting from the bottom to the top. The topmost left well is only treated with DMSO, while the bottommost right well is treated with the highest concentration of both compounds. The following starting concentrations were used: 300 nM of osimertinib, 100 nM of trametinib, and 1 µM of vemurafenib. Seventy-two hours after treatment, cell viability was measured via CTG assay and was normalized to DMSO-treated controls. Synergy scores were then calculated in R using the SynergyFinder Package and the Zero Interaction Potency (ZIP) reference model as implemented in the package. The mean of the nine highest synergy scores from each matrix is presented ±SD and significance were calculated by paired Student's *t* tests.

3D Synergy screen

Cells were plated as described in "Synergy screen", just on six plates, each with a set concentration of vemurafenib to add a third dimension. Cells were treated for the same time and with the same concentration as in "Synergy screen". Cell viability was measured the same way as in "Synergy screen". The expected drug combination responses were calculated based on ZIP reference model using SynergyFinder[43]. Deviations between observed and expected responses with positive and negative values denote synergy and antagonism, respectively.

Growth series

Totally, 1×10^5 cells per well were plated 5 times in triplicates per cell line in 6-well plates. For 5 days, always after 24 h, one triplicate of each cell line was trypsinized and counted via Z Series Coulter Counter (Beckmann Coulter). Results were normalized to day 1 and were anticipated from the slope of a best-fitting line through each data set Data are presented as mean ± SD.

Generating osimertinib selected cell lines

$PC9^{BRAF\text{-}V600E}$, $PC9^{NRAS\text{-}Q61K}$, and $HCC827^{BRAF\text{-}V600E}$ cell lines were each treated with 10 nM or 100 nM osimertinib respectively for >30 days. After that cells were labeled osimertinib selected (OS) 10 nM or 100 nM, respectively, and experiments were performed. Even after >30 days osimertinib treatment in cell culture, cells were continuously kept under osimertinib treatment.

3′UTR-RNA sequencing

For each cell line (PC9 pBABE EV, PC9 pBABE $BRAF^{V600E}$, and PC9 pBABE $BRAF^{V600E}$ OS 100) 5×10^5 cells were plated and left to adhere overnight. The next day they were treated with 300 nM osimertinib, 100 nM trametinib, a combination of both, or DMSO control for 48 h. RNA extraction and sequencing were performed using the Qiagen RNeasy Mini kit following the manufacturer's instruction. Totally, 500 ng total RNA were used to prepare 3′ UTR mRNA libraries using the Lexogen QuantSeq kit (Lexogen, Austria, Cat. No. 015.96) according to the standard protocol[44]. Quality controlled cDNA pools were quantified with the KAPA Library Quantification kit and sequenced on a NovaSeq sequencer (Illumina, USA) with a 1 × 100 bp protocol. Raw data were aligned to the human genome reference GRCh38 using STAR aligner[45] and gene expression was quantified with RSEM[46] prior to downstream analysis with the R package DESeq2[47]. E2F target genes were obtained from the MSigDB Hallmark collection and MAPK feedback genes from a recently published MAPK activity score[31].

In vivo xenograft model

The local authorities and the animal protection committee approved all animal procedures of this study.

$PC9^{BRAF\text{-}V600E}$ OS100 nM cells (5×10^6) were resuspended in 100 µL PBS and then inoculated subcutaneously in both flanks of 8- to 12-week-old female nude mice (RJ:NMRI-FOXN1 NU, Janvier Labs) and treatment was initiated when tumors reached a mean volume of approximately 50 mm³. Mice were treated daily for 21 days orally with vehicle solution (1% DMSO, 30% PEG300, 0.5% hydroxypropyl methylcellulose, 0.2% Tween-80, ddH_2O) QD, osimertinib (5 mg/kg in 1% DMSO + 30% PEG300 + ddH_2O) QD, trametinib (1 mg/kg in 0.5% hydroxypropyl methylcellulose, 0.2% Tween-80, ddH_2O) QD or combination (osimertinib as described before and trametinib as described before) Tumor volumes were measured daily in two dimensions using a caliper, and the volume was expressed in mm³ using the formula: $V = 0.5 \times (\text{length} \times \text{width}^2)$, where V is tumor volume, length is the longest tumor dimension and width is the longest tumor dimension perpendicular to the length.

Reporting summary

Further information on research design is available in the Nature Research Reporting Summary linked to this article.

DATA AVAILABILITY

The data generated and analyzed during this study are described in the manuscript and Supplementary Material. WES data were uploaded to The European Genome-phenome Archive (EGA) with the accession code EGAS00001005614. RNA sequencing data were uploaded to ArrayExpress with the accession code E-MTAB-11004. All relevant data and materials that support the findings of this work are available from the corresponding authors upon reasonable request.

CODE AVAILABILITY

No custom code or algorithms were created.

Received: 25 February 2021; Accepted: 16 November 2021;
Published online: 17 December 2021

REFERENCES

1. Skoulidis, F. & Heymach, J. V. Co-occurring genomic alterations in non-small-cell lung cancer biology and therapy. *Nat. Rev. Cancer* **19**, 495–509 (2019).
2. Mok, T. S. et al. Gefitinib or carboplatin–paclitaxel in pulmonary adenocarcinoma. *N. Engl. J. Med.* **361**, 947–957 (2009).
3. Rosell, R. et al. Erlotinib versus standard chemotherapy as first-line treatment for European patients with advanced EGFR mutation-positive non-small-cell lung cancer (EURTAC): a multicentre, open-label, randomised phase 3 trial. *Lancet Oncol.* **13**, 239–246 (2012).
4. Sequist, L. V. et al. Phase III study of afatinib or cisplatin plus pemetrexed in patients with metastatic lung adenocarcinoma with EGFR mutations. *J. Clin. Oncol.* **31**, 3327–3334 (2013).
5. Wu, Y.-L. et al. Dacomitinib versus gefitinib as first-line treatment for patients with EGFR-mutation-positive non-small-cell lung cancer (ARCHER 1050): a randomised, open-label, phase 3 trial. *Lancet Oncol.* **18**, 1454–1466 (2017).

6. Cross, D. A. E. et al. AZD9291, an irreversible EGFR TKI, overcomes T790M-mediated resistance to EGFR inhibitors in lung cancer. *Cancer Discov.* **4**, 1046–1061 (2014).
7. Jänne, P. A. et al. AZD9291 in EGFR inhibitor-resistant non-small-cell lung cancer. *N. Engl. J. Med.* **372**, 1689–1699 (2015).
8. Soria, J.-C. et al. Osimertinib in untreated EGFR-mutated advanced non-small-cell lung cancer. *N. Engl. J. Med.* **378**, 113–125 (2018).
9. Ramalingam, S. S. et al. Overall survival with osimertinib in untreated, EGFR-mutated advanced NSCLC. *N. Engl. J. Med* https://doi.org/10.1056/nejmoa1913662 (2019).
10. Leonetti, A. et al. Resistance mechanisms to osimertinib in EGFR-mutated non-small cell lung cancer. *Br. J. Cancer* **121**, 725–737 (2019).
11. Ortiz-Cuaran, S. et al. Heterogeneous mechanisms of primary and acquired resistance to third-generation EGFR inhibitors. *Clin. Cancer Res.* https://doi.org/10.1158/1078-0432.ccr-15-1915 (2016).
12. Michels, S. et al. Genomic profiling identifies outcome-relevant mechanisms of innate and acquired resistance to third-generation epidermal growth factor receptor tyrosine kinase inhibitor therapy in lung cancer. *JCO Precis. Oncol.* https://doi.org/10.1200/po.18.00210 (2019).
13. Tumbrink, H. L., Heimsoeth, A. & Sos, M. L. The next tier of EGFR resistance mutations in lung cancer. *Oncogene* https://doi.org/10.1038/s41388-020-01510-w (2020).
14. Thress, K. S. et al. Acquired EGFR C797S mutation mediates resistance to AZD9291 in non-small cell lung cancer harboring EGFR T790M. *Nat. Med.* https://doi.org/10.1038/nm.3854 (2015).
15. Chabon, J. J. et al. Circulating tumour DNA profiling reveals heterogeneity of EGFR inhibitor resistance mechanisms in lung cancer patients. *Nat. Commun.* **7**, 11815 (2016).
16. Eberlein, C. A. et al. Acquired resistance to mutant-selective EGFR inhibitor AZD9291 is associated with increased dependence on RAS signaling in preclinical models. *Cancer Res.* https://doi.org/10.1158/0008-5472.can-14-3167 (2015).
17. Ricordel, C., Friboulet, L., Facchinetti, F. & Soria, J.-C. Molecular mechanisms of acquired resistance to third-generation EGFR-TKIs in EGFR T790M-mutant lung cancer. *Ann. Oncol.* **29**, i28–i37 (2018).
18. Fassunke, J. et al. Overcoming EGFRG724S-mediated osimertinib resistance through unique binding characteristics of second-generation EGFR inhibitors. *Nat. Commun.* **9**, 4655 (2018).
19. Ohashi, K. et al. Lung cancers with acquired resistance to EGFR inhibitors occasionally harbor BRAF gene mutations but lack mutations in KRAS, NRAS, or MEK1. *Proc. Natl Acad. Sci. USA* **109**, E2127–E2133 (2012).
20. Ho, C.-C. et al. Acquired BRAF V600E mutation as resistant mechanism after treatment with osimertinib. *J. Thorac. Oncol.* **12**, 567–572 (2017).
21. Bracht, J. W. P. et al. BRAF mutations classes I, II, and III in NSCLC patients included in the SLLIP trial: the need for a new pre-clinical treatment rationale. *Cancers* **11**, 1381 (2019).
22. Planchard, D. et al. Dabrafenib plus trametinib in patients with previously treated BRAF(V600E)-mutant metastatic non-small cell lung cancer: an open-label, multicentre phase 2 trial. *Lancet Oncol.* **17**, 984–993 (2016).
23. Planchard, D. et al. Dabrafenib plus trametinib in patients with previously untreated BRAFV600E-mutant metastatic non-small-cell lung cancer: an open-label, phase 2 trial. *Lancet Oncol.* **18**, 1307–1316 (2017).
24. Ding, H. et al. Durable clinical response of advanced lung adenocarcinoma harboring EGFR-19del/T790M/BRAF^{V600E} mutations after treating with osimertinib and dabrafenib plus trametinib: a case report. *Oncotargets Ther.* **ume 13**, 7933–7939 (2020).
25. Huang, Y., Gan, J., Guo, K., Deng, Y. & Fang, W. Acquired BRAF V600E mutation mediated resistance to osimertinib and responded to osimertinib, dabrafenib, and trametinib combination therapy. *J. Thorac. Oncol.* **14**, e236–e237 (2019).
26. Meng, P. et al. Combined osimertinib, dabrafenib and trametinib treatment for advanced non-small-cell lung cancer patients with an osimertinib-induced BRAF V600E mutation. *Lung Cancer* **146**, 358–361 (2020).
27. Xie, Z. et al. Lung adenocarcinoma harboring concomitant EGFR mutations and BRAF V600E responds to a combination of osimertinib and vemurafenib to overcome osimertinib resistance. *Clin. Lung Cancer* https://doi.org/10.1016/j.cllc.2020.06.008 (2020).
28. Cun, Y., Yang, T.-P., Achter, V., Lang, U. & Peifer, M. Copy-number analysis and inference of subclonal populations in cancer genomes using Sclust. *Nat. Protoc.* **13**, 1488–1501 (2018).
29. Unni, A. M. et al. Hyperactivation of ERK by multiple mechanisms is toxic to RTK-RAS mutation-driven lung adenocarcinoma cells. *Elife* **7**, e33718 (2018).
30. McFadden, D. G. et al. Mutational landscape of EGFR-, MYC-, and Kras-driven genetically engineered mouse models of lung adenocarcinoma. *Proc. Natl Acad. Sci. USA* **113**, E6409–E6417 (2016).
31. Wagle, M.-C. et al. A transcriptional MAPK Pathway Activity Score (MPAS) is a clinically relevant biomarker in multiple cancer types. *Npj Precis. Oncol.* **2**, 7 (2018).
32. Poulikakos, P. I., Zhang, C., Bollag, G., Shokat, K. M. & Rosen, N. RAF inhibitors transactivate RAF dimers and ERK signalling in cells with wild-type BRAF. *Nature* **464**, 427–430 (2010).
33. Oxnard, G. R. et al. Assessment of resistance mechanisms and clinical implications in patients with EGFR T790M-positive lung cancer and acquired resistance to osimertinib. *JAMA Oncol.* **4**, 1527–1534 (2018).
34. Vojnic, M. et al. Acquired BRAF rearrangements induce secondary resistance to EGFR therapy in EGFR-mutated lung cancers. *J. Thorac. Oncol.* **14**, 802–815 (2019).
35. König, K. et al. Implementation of amplicon parallel sequencing leads to improvement of diagnosis and therapy of lung cancer patients. *J. Thorac. Oncol.* **10**, 1049–1057 (2015).
36. Peifer, M. et al. Integrative genome analyses identify key somatic driver mutations of small-cell lung cancer. *Nat. Genet* **44**, 1104–1110 (2012).
37. George, J. et al. Comprehensive genomic profiles of small cell lung cancer. *Nature* **524**, 47–53 (2015).
38. Recondo, G. et al. Feasibility and first reports of the MATCH-R repeated biopsy trial at Gustave Roussy. *Npj Precis. Oncol.* **4**, 27 (2020).
39. Remon, J. et al. Real-world utility of an amplicon-based next-generation sequencing liquid biopsy for broad molecular profiling in patients with advanced non–small-cell lung cancer. *JCO Precis. Oncol.* **3**, 1–14 (2019).
40. Kuhnert, G. et al. Impact of PET/CT image reconstruction methods and liver uptake normalization strategies on quantitative image analysis. *Eur. J. Nucl. Med. Mol. Imaging* **43**, 249–258 (2016).
41. Wahl, R. L., Jacene, H., Kasamon, Y. & Lodge, M. A. From RECIST to PERCIST: evolving considerations for PET response criteria in solid tumors. *J. Nucl. Med.* **50**, 122S–150S (2009).
42. Herling, C. D. et al. Clonal dynamics towards the development of venetoclax resistance in chronic lymphocytic leukemia. *Nat. Commun.* **9**, 727 (2018).
43. Ianevski, A., Giri, K. A. & Aittokallio, T. SynergyFinder 2.0: visual analytics of multi-drug combination synergies. *Nucleic Acids Res.* **48**, W488–W493 (2020).
44. Brägelmann, J. et al. Systematic kinase inhibitor profiling identifies CDK9 as a synthetic lethal target in NUT midline carcinoma. *Cell Rep.* **20**, 2833–2845 (2017).
45. Dobin, A. et al. STAR: ultrafast universal RNA-seq aligner. *Bioinformatics* **29**, 15–21 (2013).
46. Li, B. & Dewey, C. N. RSEM: accurate transcript quantification from RNA-Seq data with or without a reference genome. *BMC Bioinforma.* **12**, 323 (2011).
47. Love, M. I., Huber, W. & Anders, S. Moderated estimation of fold change and dispersion for RNA-seq data with DESeq2. *Genome Biol.* **15**, 550 (2014).

ACKNOWLEDGEMENTS

We thank all members of the Sos lab and Peifer lab for their fruitful comments, especially Katia Garbert. We furthermore thank the Regional Computing Center of the University of Cologne (RRZK) for providing computing time on the DFG-funded HPC cluster CHEOPS as well as support and Graziella Bosco for data archiving at EGA. This work was supported by the Bundesministerium für Bildung und Forschung [e:Med initiative; 01ZX1901A to M.L.S., M.P. and R.K.T.]; a research grant by the Thyssen Foundation [10.19.2.025MN to M.L.S.] and the Deutsche Krebshilfe [70112888 to M.L.S., Mildred Scheel Nachwuchszentrum Grant 70113307 to J.B. and D.F.A.]; and the Else Kröner Fresenius Stiftung [Memorial Grant 2018_EKMS.35 to J.B.]. The funding sources had no involvement in the conceptual or executive process of this study.

AUTHOR CONTRIBUTIONS

Each author confirms that he or she has made substantial contributions to the conception or design of the work or the acquisition, analysis, interpretation, and assembly of the data; contributed to paper writing; all authors approved the final paper; all authors are accountable for all aspects of the work. D.S. and D.F.A. contributed equally to this work as co-first authors. J.B., M.S., and M.L.S. contributed equally to this work as co-senior authors.

FUNDING

Open Access funding enabled and organized by Projekt DEAL.

COMPETING INTERESTS

D.S. has received honoraria for advisory roles or lectures from BMS, Boehringer-Ingelheim, MSD, Novartis, Roche, Healthcare Consulting Cologne, Abbvie; and has received travel and accommodation support from AstraZeneca, BMS, Boehringer-Ingelheim, MSD, Novartis, Roche, Abbvie. J.F. has received honoraria from AstraZeneca. B.B. has received sponsored research at Gustave Roussy Cancer Center from Abbvie, Amgen, AstraZeneca, BioGen, Blueprint Medicines, BMS, Boehringer Ingelheim, Celgene, Cristal Therapeutics, Daiichi-Sankyo, Eli Lilly, GSK, Ignyta, IPSEN, Inivata, Janssen, Merck KGaA, MSD, Nektar, Onxeo, OSE immunotherapeutics, Pfizer, Pharma Mar, Roche-Genentech, Sanofi, Servier, Spectrum Pharmaceuticals, Takeda, Tiziana Pharma, Tolero Pharmaceuticals. D.P. has had consulting or advisory roles for AstraZeneca, BMS, Boehringer Ingelheim, Celgene, Daiichi Sankyo, Eli Lilly, Merck, Novartis, Pfizer, prIME Oncology, Peer CME, Roche, Samsung Bioepis; and has received honoraria from AstraZeneca, BMS, Boehringer Ingelheim, Celgene, Eli Lilly, Merck, Novartis, Pfizer, prIME Oncology, Peer CME, Roche, Samsung Bioepis; and has done clinical trials research as principal or co-investigator (institutional financial interests) with support from AstraZeneca, BMS, Boehringer Ingelheim, Eli Lilly, Merck, Novartis, Pfizer, Roche, Medimmun, Sanofi-Aventis, Taiho Pharma, Novocure, Inivata, Takeda, Pharma Mar, Janssen, Daiichi Sankyo; and has received travel and accommodation support from AstraZeneca, Roche, Novartis, Pfizer. L.N. has received honoraria from Pfizer, Celgene, Novartis, Roche, Boehringer Ingelheim, Janssen, BMS, Takeda, Bayer; and has had consulting or advisory roles for Novartis, Boehringer Ingelheim, BMS, Roche, Janssen, Pfizer, Takeda, Bayer; and has received research funding from Pfizer, Novartis, MSD, Janssen, Amgen; and has received travel and accommodation support from Novartis, Pfizer, Celgene, Boehringer Ingelheim, Janssen. S.M. has received honoraria from Pfizer, Novartis, AstraZeneca; and has received research support from Novartis, Pfizer, BMS, Janssen. R.K.T. is the founder/shareholder and has had a consultancy/advisory role of/for PearlRiver Bio GmbH; is the founder/shareholder and has had a consultancy/advisory role of/for Epiphanes Inc; and is the founder/shareholder and has had a consultancy/advisory role of/for CDL Therapeutics GmbH; and has a stock or other ownership and has had a consultancy/advisory role of/for Merck, J&J, AstraZeneca, Bayer; and has a stock or other ownership and has had a consultancy/advisory role of/for Roche; and has a commercial research grant from Roche; and has a stock or other ownership of Novartis, GSK; and has had a consultancy/advisory role for New Oncology AG, Clovis, Daiichi-Sankyo, Boehringer Ingelheim, MSD, Lilly, Sanofi-Aventis, Puma. S.M.-B. has received honoraria for advisory boards or lectures from BMS, Novartis, Roche, Pfizer, Bayer, Molecular Health, Targos, Astra Zeneca; and has received non-financial support from BMS, Janssen. O.G. has received honoraria for advisory boards from AMGEN, LILLY, BAYER. L.M. has had consulting or advisory roles for Roche Diagnostics, Takeda, Roche; and has had a lecture or educational activities for BMS, Tecnofarma, Roche; and has received travel and accommodation support from BMS, Roche; and has received Mentorship program with key opinion leaders from AstraZeneca; and has received sponsored research from Amgen, BMS, Boehringer Ingelheim. T.W. has had an advisory role for Lilly; and has received speakers honoraria from Novartis; and has received travel support from Roche, Pfizer. R.B. is co-founder and chief scientific officer of Targos Mol Inc., Kassel Germany; and has received personal fees and others for advisory boards or lectures from BMS, MSD, Novartis, Roche, Lilly, AstraZeneca, Illumina, AbbVie, Amgen, Boehringer-Ingelheim, Merk-Serono, Qiagen, Pfizer. J.W. has received honoraria for advisory roles or lectures from Amgen, AstraZeneca, Blueprint, BMS, Boehringer Ingelheim, Chugai, Daiichi Sankyo, Ignyta, Janssen, Lilly, Loxo, MSD, Novartis, Pfizer, Roche, Seattle Genetics, Takeda; and has received research support from BMS, Janssen Pharmaceutica, Novartis, Pfizer. M.S. has received honoraria for advisory roles from Pfizer, Roche, AMGEN, Novartis, Takeda, Boehringer Ingelheim; and has received institutional research support from AMGEN, Dracen Pharmaceuticals. M.L.S. is a founder, shareholder and advisor of PearlRiver Bio – a Centessa Pharmaceuticals company - and MLS has a commercial research grant from PearlRiver Bio - a Centessa company. The remaining authors declare no competing interests.

ADDITIONAL INFORMATION

Supplementary information The online version contains supplementary material available at https://doi.org/10.1038/s41698-021-00241-9.

Correspondence and requests for materials should be addressed to Johannes Brägelmann, Matthias Scheffler or Martin L. Sos.

Reprints and permission information is available at http://www.nature.com/reprints

Publisher's note Springer Nature remains neutral with regard to jurisdictional claims in published maps and institutional affiliations.

3.3 MIZ1-ΔPOZ shapes treatment response in small cell lung cancer

Hannah L. Tumbrink et al.

Specific contributions:

- Generation of all in vitro and in vivo data in this study
- Analysis of all data besides the RNAseq (Jenny Ostendorp) and single cell RNAseq data (Johannes Brägelmann)
- IHC staining was performed by Alexandra Florin
- Manuscript writing

ABSTRACT

Small cell lung cancer (SCLC) is an aggressive, neuroendocrine cancer and accounts for 15 % of all lung cancer cases worldwide with a 5-year survival rate below 5 %. Initial high sensitivity to chemotherapy is followed by the rapid development of resistance to chemo/radiation therapies, and the limited efficacy of immunotherapies and targeted therapies results in a high mortality rate. Virtually all SCLC patients display universal *TP53* and *RB1* gene inactivation, and 20 % display genomic amplifications of MYC paralogs (MYC, MYCN and MYCL). By now, no specific drug is available to target MYC and it remains unclear whether MYC activity impacts the response or resistance to chemotherapy. A dimeric MYC/MAX complex activates gene transcription, whereas MYC in complex with MIZ1 can also act as a transcriptional repressor. In SCLC, the role of the complex interplay of MYC–MIZ1 remains unclear. To further investigate Myc–Miz1 in SCLC, we developed a novel SCLC mouse model by crossing the RPM ($Rb1^{fl/fl}Trp53^{fl/fl}Myc^{LSL/LSL}$) mice with a Miz1-ΔPOZ allele (RPMM= $Rb1^{fl/fl}Trp53^{fl/fl}Myc^{LSL/LSL}MIZ1^{\Delta POZfl/fl}$). A truncated Miz1 protein lacking the POZ domain is unable to multimerize and thereby fails to stably associate with chromatin. Surprisingly, we found that tumor-onset and tumor localization is only minimally affected by the truncated Miz1 allele in the background of Myc-driven SCLC. On the transcriptional level, these tumors show upregulated Myc target genes, genes associated with the DNA damage machinery and downregulations of genes associated with the inflammatory response. Interestingly, RPMM-derived cell lines are more sensitive toward etoposide when compared to RPM-derived cells expressing wild type Miz1. In vivo, RPMM and RPM treated mice showed similar overall survival, however, only in RPMM mice tumor growth was largely repressed at the endpoint of the treatment. These data suggest that the interplay between Myc/Miz1 may potentially be critical to drive tumor relapse in chemotherapy treated SCLC.

Keywords: Small cell lung cancer, Miz1, Myc, chemo-resistance

INTRODUCTION

Lung cancer is the leading cause of cancer-related death worldwide and can be subdivided into non-small cell lung cancer (NSCLC) and small cell lung cancer (SCLC)[133]. SCLC makes up about 15 % of all lung cancer cases and is described as a high-grade neuroendocrine, extremely lethal tumor with a 5-year survival rate below 5 %[98]. The standard therapy is still platinum-based chemotherapy with etoposide with the recent addition of immune checkpoint inhibitors[13]. SCLC development is mainly driven by the concomitant inactivation of two tumor suppressors, p53 and RB (encoded by *TP53* and *RB1*). Moreover, 20 % of all SCLC patients exhibit amplifications of MYC family genes (*MYC, MYCN* and *MYCL*)[99]. Several studies have demonstrated the importance of MYC family members in SCLC and highlighted potential vulnerabilities dependent on which MYC family member is predominantly expressed in SCLC[101,102,134,135]. The recently developed RPM genetically engineered mouse model (GEMM), is a *Myc*-driven mouse model with aggressive and metastatic tumors[102]. Attempts to target MYC, directly or indirectly, failed in the clinic[106,136]. However, the in-depth characterization of MYC, its interaction partners and the subsequent tumorigenic programs may open up novel avenues to tackle this target in SCLC and potentially other cancers.

The transcription factor MIZ1 (Myc-interaction zinc-finger protein-1; Zbtb17) contains a N-terminal BTB (Broad complex, Tramtrack, and Bric-a-brac)-POZ (poxvirus and zinc finger) domain followed by 13 classical zinc fingers[137]. The MIZ1–MYC interaction occurs within a short helical domain of MIZ1 between zinc finger 12 and 13 and the amino acid valine 394 is essential for their interaction. MYC in complex with MAX activates gene transcription, whereas MYC in complex with MIZ1 mainly represses target gene transcription but can also act as activator[124,132]. The POZ domains are homo-and hetero-oligomerization domains and play a critical role in chromatin association. Deletions of the POZ domain abrogate chromatin association by losing the potential to multimerize and the introduction of a Cre-inducible ΔPOZ-Miz1 allele into mouse models of neuroblastoma, medulloblastoma and ALL demonstrated the lineage-dependent effects of Miz1[119,124,125,127,131]. Here we describe a new GEMM to investigate and determine the impact of Miz1 in *Myc*-driven SCLC tumor development and the sensitivity towards chemotherapy.

RESULTS

Functional MIZ1 is dispensable for the development of SCLC but alters SCLC tumorigenesis

To study the role of the MIZ1 in SCLC tumor biology, we introduced a truncated variant of Miz1 (Miz1-$\Delta POZ^{fl/fl}$) to a published mouse model for *Myc*-driven SCLC (RPM) resulting in the $Rb1^{fl/fl}Trp53^{fl/fl}Myc^{LSL/LSL}MIZ1^{\Delta POZfl/fl}$ (RPMM) mouse model (**Figure 1a, b**). In particular, we crossed the RPM mice, which carry a *Cre* recombinase inducible knockout of *Rb1* and *Trp53* and a *Cre*-inducible Myc^{T58A} (Lox-Stop-Lox (LSL)-Myc^{T58A}) allele in the H11 locus, with *Cre* recombinase inducible Miz1-$\Delta POZ^{fl/fl}$ mice. The point mutation Myc-T58A leads to a non-degradable Myc version and after *Cre* induction, Myc accumulates over time and thereby mimics increased Myc levels[102]. Upon Cre induction, the Miz1 POZ domain is deleted in the RPMM model, thereby the ability of Miz1 to multimerize and stably bind chromatin is lost[131].

To probe tumor-forming propensity of the RPMM ($Rb1^{fl/fl}Trp53^{fl/fl}Myc^{LSL/LSL}MIZ1^{\Delta POZfl/fl}$) mouse model in comparison to the RPM ($Rb1^{fl/fl}Trp53^{fl/fl}Myc^{LSL/LSL}$), RPMM and RPM mice were intratracheally infected with adenovirus carrying *Cre* driven by Cytomegalovirus (CMV) promotor. Both mouse models infected with the CMV virus showed no differences in tumor onset, development and survival (median survival of 43 days (RPMM) vs. 44 days (RPM)) (**Supplement Figure S1a**). Previous studies utilizing SCLC mouse models described Calcitonin gene-related peptide (CGRP)-expressing cells as the predominant cell of origin of SCLC, therefore we infected RPM and RPMM mice with adenovirus carrying *Cre* driven by a neuroendocrine Cgrp promoter[138]. Comparing survival data, we observed a modest but significantly longer survival of RPMM mice compared to RPM (median survival of 66 days vs. 57 days, $p=0.0004$) (**Figure 1c**).

To monitor tumor development, we imaged RPM and RPMM mice weekly starting three weeks after *Cre* infection using MRI imaging. As expected, RPM and RPMM tumors were centrally located (**Figure 1d**) and we detected no differences in tumor onset (**Figure 1c**). Both RPM and RPMM tumors showed typical morphological patterns of SCLC in H&E and immunohistochemical (IHC) staining for the Neural cell adhesion molecule (NCAM; CD56) (**Figure 1e, f**). Quantification of RPM and RPMM tumor area (NCAM area) showed no significant differences in tumor size between the groups. As expected, RPM and RPMM tumors displayed high levels of Myc in IHC staining's (**Figure 1e, h**). Previous studies have shown Myc-driven tumors to be highly metastatic and compared to other, classical SCLC GEMMs, such as the RP mouse model[139]. To assess the influence of truncated Miz1 on the metastatic pattern, we collected livers from tumor-bearing RPMM mice and RPM mice as a control. Seven out of eight livers from RPMM mice (87,5 %) exhibited liver metastases and eight out of eight from RPM mice (100 %) presenting as multiple micro-metastases (**Figure 1j**). Taken together the expression of the Miz1-ΔPOZ allele does not have a major impact on the metastatic spread in the MYC-driven SCLC background.

Because human SCLC is described to be highly proliferative and apoptotic and known to express cell death markers and Miz1 expression may regulate cell death pathway components, we examined cleaved caspase-3 (CC3), a marker of apoptosis, in RPM and RPMM tumors, using IHC[101,102]. Here, we observed a non-significant trend of an increased percentage of CC3-positive cells in RPMM tumors, indicating slightly higher levels of apoptosis in RPMM tumors compared to RPM tumors (**Figure 1e, i**).

Overall, these data demonstrate that the loss of wild type Miz1 in the Cgrp-*Cre*-induced RPM background slows down SCLC tumor formation with minimal effects on the metastatic spread and apoptotic markers.

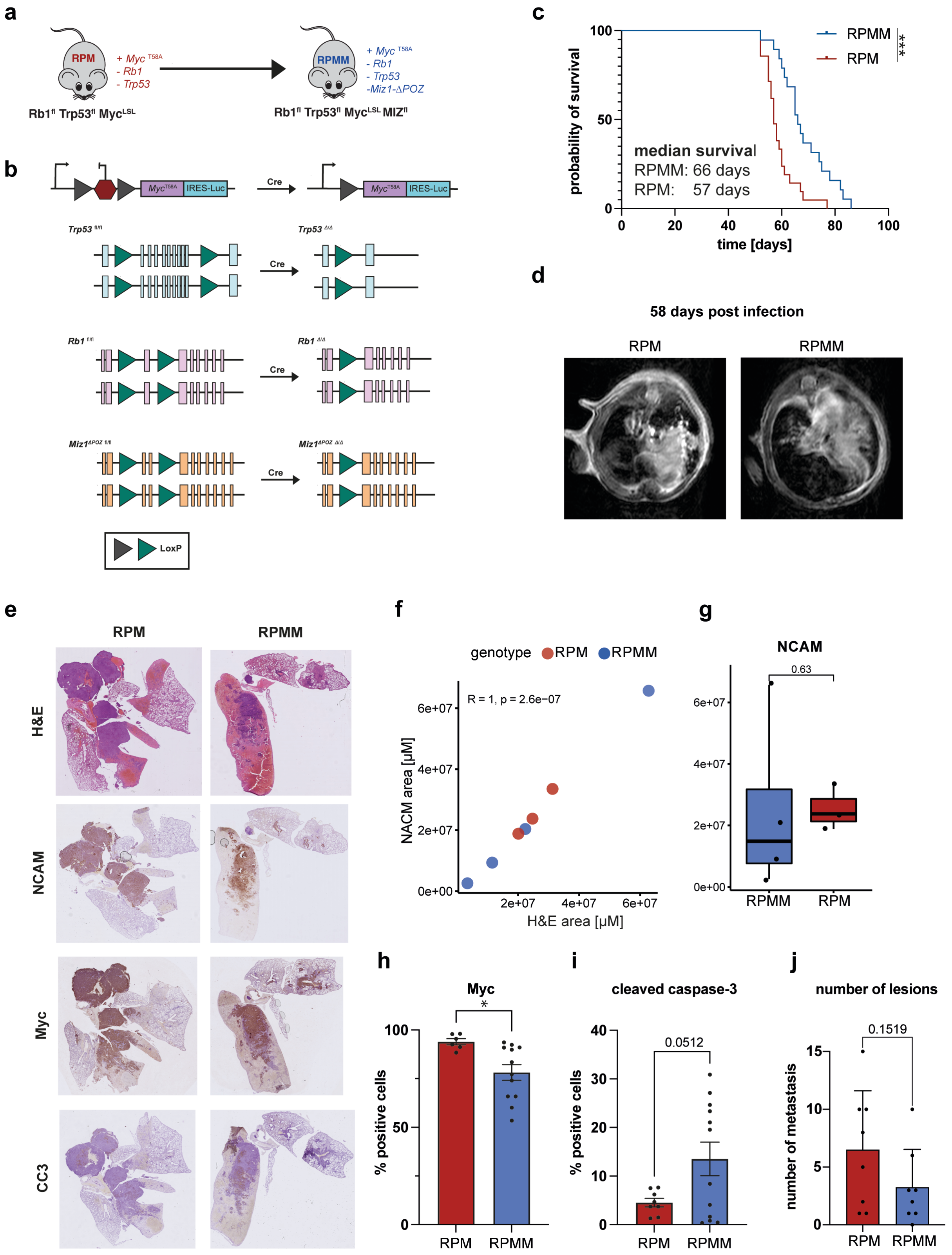
a
RPM
+ Myc T58A
- Rb1
- Trp53
Rb1fl Trp53fl MycLSL
RPMM
+ Myc T58A
- Rb1
- Trp53
-Miz1-ΔPOZ
Rb1fl Trp53fl MycLSL MIZfl
b
MycT58A
IRES-Luc
Cre
Trp53 fl/fl
Trp53 Δ/Δ
Rb1 fl/fl
Rb1 Δ/Δ
Miz1ΔPOZ fl/fl
Miz1ΔPOZ Δ/Δ
LoxP
c
probability of survival
time [days]
RPMM
RPM
***
median survival
RPMM: 66 days
RPM: 57 days
d
58 days post infection
RPM
RPMM
e
RPM
RPMM
H&E
NCAM
Myc
CC3
f
genotype ● RPM ● RPMM
R = 1, p = 2.6e−07
NACM area [μM]
H&E area [μM]
g
NCAM
0.63
RPMM
RPM
h
Myc
*
% positive cells
RPM
RPMM
i
cleaved caspase-3
0.0512
% positive cells
RPM
RPMM
j
number of lesions
0.1519
number of metastasis
RPM
RPMM

Figure 1: Truncated Miz1 alter SCLC tumor-biology. (a) Schematic overview of the novel RPMM mouse model. (b) Cartoon diagram of the LsL-*Myc*^{T58A} allele in the *H11* locus, combined with *Trp53*, *Rb1* and *Miz*$^{\Delta POZ}$ conditional alleles before and after Cre induction. Cartoon triangles represents LoxP sites. (c) Kaplan-Meier survival of RPM and RPMM mice infected with Cgrp-Cre. Gehan-Breslow-Wilcoxon test, **p*= 0.033, ***p*=0.002, ****p*<0.001. (d) Representative MRI images taken 58 days post infection. (e) Representative RPM and RPMM H&E images, IHC of NCAM, Myc and cleaved caspase-3 (CC3). (f) Correlation of H&E and NCAM area. (g) Quantification of NCAM in lung tumor tissue from RPM and RPMM mice. (h, i) Quantification of IHC stained positive cells for Myc (h) and cleaved caspase-3 (CC3) (i) from mice in (c), error bars indicate mean ± SME with unpaired t-test. One dot represents one lung. (j) Number of metastatic lesions in liver tissue from RPM and RPMM mice in (c), error bars indicate mean ± SME with unpaired t-test. One dot represents one lung. **p*= 0.033, ***p*=0.002, ****p*<0.001.

Ablation of Miz1$^{\Delta POZ}$ domain does not change basic SCLC markers nor immune cell infiltration

We performed single cell RNA sequencing (scRNA-Seq) to characterize further the cellular composition and functional states of those cells within the tumors of the RPMM mouse model at single cell resolution. To this end, we isolated tumor cells from Cgrp-*Cre* infected RPM and RPMM mice (4000-6500 cells/sample). Unsupervised t-stochastic neighbor embedding (tSNE) clustering revealed six clusters (**Figure 2a**). Besides cluster one and five, both RPM and RPMM cells are detected in all clusters (**Figure 2b**). Cluster one and five are composed of cells derived from RPM tumors. RPMM cells are predominantly enriched in cluster zero. Expression of NCAM, a marker for SCLC, is present in all clusters but NCAM-positive cells are enriched in cluster zero and one. Cells in cluster zero, one and four are positive for Myc and Miz1 (Zbtb17). SCLC was classified in four subtypes expressing four different transcription factors: NE *ASCL1*, neurogenic differentiation factor 1 (*NEUROD1*), non-NE POU class 2 homebox 3 (*POU2F3*) and yes-associated protein 1 (*YAP1*)[100]. In RPMM tumors, most cells express high levels of Ascl1, a neuroendocrine marker expressed in a SCLC subtype usually characterized by low Myc levels, whereas only a few cells express Neurod1[102,140]. In comparison, in RPM tumors, Ascl1 and Neurod1 positive cells are equally abundant. While we observe some YAP1 expressing cells in RPM tumors, only a minimal number of Yap- expressing cells was captured from RPMM tumors, indicating a more neuroendocrine phenotype of RPMM tumors (**Figure 2c**). To analyze whether disrupted chromatin binding of Miz1 influences the tumor immune cell infiltration, we determined the fraction of leucocytes (*Ptprc*$^{+}$), T-cells (*Cd3d*$^{+}$) and cytotoxic T cells (*Cd8a*$^{+}$) from single cell expression profiles. In line with previous studies reporting SCLC tumors to be immunologically cold[141], we captured only a few Ptprc (CD45) expressing cells and nearly zero CD3d or CD8a expressing cells in both mouse models.

In order to validate the rare immune cell infiltration on protein level we conducted flow cytometric analysis of whole tumor bearing lungs. We detected no significant differences between RPM and RPMM in CD45$^+$ cells, T cells or natural killer (NK) cells. The proportion of CD4$^+$ cells (T helper cells) is higher as the CD8$^+$ cells (cytotoxic T cells) (**Supplement Figure S1b**). In conclusion, on single cell level, RPM and RPMM tumors exhibit heterogenous patterns of neuroendocrine markers and a similar composition of immune cells in the tumor microenvironment.

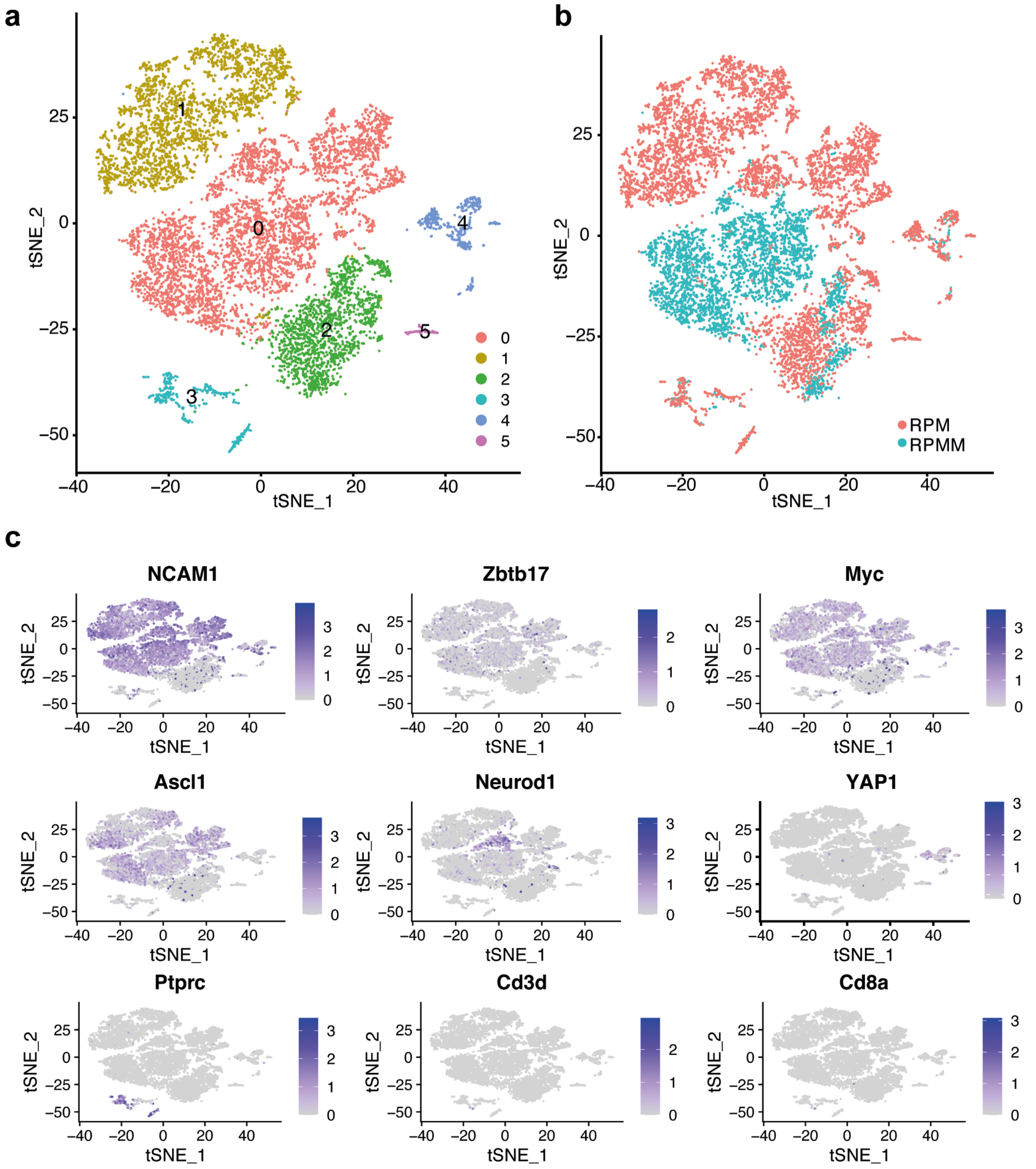

Figure 2: Miz1-ΔPOZ mice exhibit SCLC phenotype and are immunologically cold. (a, b) tSNE projections of single cell RNA profiles from RPM and RPMM tumors. Colors indicating detected clusters (a) and genotype (b). (c) tSNE projections of single cell RNA profiles from RPM and RPMM tumors. Colors indicate expression levels of indicated genes.

Miz1$^{\Delta POZ}$ expression influences Myc transcriptional activity and renders the sensitivity towards chemotherapy

Because MIZ1 is important for the transcriptional activity of MYC we compared bulk RNA sequencing profiles from Miz1-ΔPOZ tumors (RPMM) and Miz1 wild type tumors (RPM). Differential gene expression revealed several Myc target gene sets[142] to be upregulated in RPMM compared to RPM tumors, in line with previous reports of a repressive effect of MIZ1 on the transcriptional activity of MYC (**Figure 3a, b**).

In addition to upregulated Myc target genes, genes associated with G2M- and G1/S DNA damage checkpoint and DNA repair, were found to be upregulated. Downregulated genes are associated with TNFα signaling, inflammatory response, interferon-α (IFNα) and interferon-γ (IFNγ) (**Figure 3a, c**).

To further analyze changes in the DNA damage response (DDR) machinery, we measured protein levels of phosphorylated-histone H2A.X (γH2AX) in cell lines generated from CMV-*Cre* and Cgrp-*Cre* infected *Trp53*/*Rb1*-deficient (RP), RPM and RPMM tumors. While both the RPM and RPMM cell lines express high levels of Myc, but only RPM cell lines exhibit increased steady-state DNA damage (**Figure 3d**).

Given the growing evidence that DDR signaling and the cell cycle machinery may present therapeutic opportunities in SCLC, we compared the efficacy of agents that induce genotoxic stress and perturb cell cycle checkpoints in cell lines derived from RP, RPM or RPMM tumors (**Figure 3e**)[101,102,143-146]. Cisplatin as wells as the PARP inhibitor olaparib showed no effect on either RP, RPM or RPMM cells ($GI_{50} \geq 10$ µM). In comparison, talazoparib, a PARP inhibitor with improved PARP trapping compared to olaparib, showed high inhibitory potency in the viability assays with GI_{50} values of 454.2 nM (RPM) and 380.8 nM (RPMM) but reduced activity in RP cells (4718 nM). In general, cells with higher Myc levels (RPM and RPMM) are more sensitive toward DDR pathway inhibitors than RP cells which is in line with previous studies[101]. In contrast, no significantly different GI_{50} values of adavosertib (WEE1), ceralasertib (ATR), alisertib (AurKA) as well as the chemotherapeutical topotecan (topoisomerase I), cytarabine (nucleoside analog) and doxorubicin (topoisomerase I+II) were observed between RPM and RPMM cell lines. Interestingly, we observed a higher sensitivity to prexasertib (Chk1) and etoposide (topoisomerase II) in RPMM cell lines, compared to RPM cell lines (**Supplement Figure S1c**).

To validate these results, we performed flow cytometry to measure the percentage of living cells after etoposide treatment (**Figure 3f**). Therefore, RP, RPM and RPMM cells were treated with 1 µM etoposide for 72 h. We detected a significant increase of dead cells after chemotreatment in cell lines derived from RPMM tumors compared to RP and RPM cell lines (% living cells: RP=83.33 %, RPM=49.03 %, RPMM=30.77 %).

Taken together, Miz1-ΔPOZ affects gene expression and the sensitivity towards a subset of agents targeting the DDR pathway.

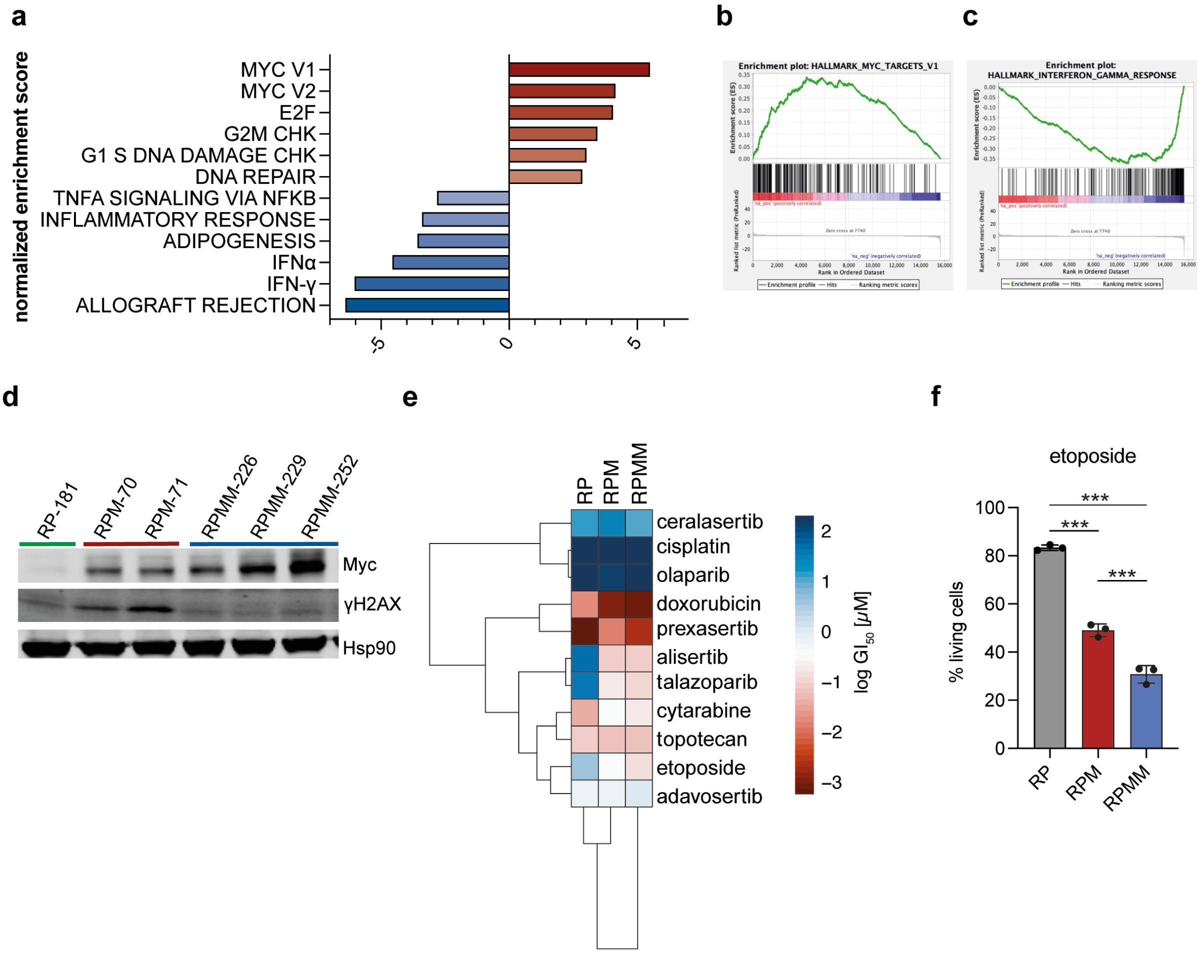

Figure 3: Ablation of the Miz1 POZ domain in Myc-driven SCLC alters DNA damage repair pathways and renders sensitivity to DDR pathway inhibitors. (a) Top 6 normalized enrichment scores (NES) from RPMM vs RPM tumors (n=2). (b+c) GSEA analysis from RPMM vs RPM tumors with NES. (d) Western blot of Myc and γH2AX in RP, RPM and RPMM cell lines. HSP90 was used as loading control. (e) Heatmap of log GI_{50} values for the mean of 2-4 murine RP, PRM and RPMM cell lines treated with indicated drugs for 72 h. (f) FACS analysis of 2-4 murine RP, RPM and RPMM cell lines treated with 1 µM etoposide for 72 h. Error bars indicate mean ± SME with ordinary one-way ANOVA. **p*= 0.033, ***p*=0.002, ****p*<0.001.

Miz1-ΔPOZ SCLC is responsive to Chemotherapy

In the clinical setting, SCLC is highly responsive to first-line cisplatin and etoposide, but almost every patient inevitably develops chemoresistance within months, resulting in death within one year[96]. This rapid shift between initial chemosensitive and a chemoresistant state remains elusive. The RPM mouse model has been reported to recapitulate this human phenotype in initial response to combination chemotherapy (5 mg/kg cisplatin and 10 mg/kg etoposide) and consecutive development of acquired chemotherapy resistance[102].

To examine the role of MIiz1-ΔPOZ in presence of high Myc levels in the response to chemotherapy in SCLC, we treated Cgrp-*Cre* infected RPM and RPMM mice with a combination of cisplatin and etoposide in a regimen consisting of cisplatin on day 1 and etoposide on day 1, 2 and 3. Tumor formation was monitored using MRI imaging (**Figure 4a**). Miz1-ΔPOZ and Miz1-WT vehicle-treated RPM mice exhibit rapid tumor growth, while mice treated with combination chemotherapy exhibit prolonged survival in RPM and RPMM. Chemotherapy treated RPMM mice showed a similar survival benefit compared to RPM mice, especially when considering the slower tumor formation of RPMM tumors (RPM vehicle=8 days, RPMM vehicle=17 days, RPM chemo=26 days and RPMM chemo=37 days) (**Figure 4b**). In total, we administered four cycles of chemotherapy. Weekly MRI imaging revealed an initial chemotherapy response, but a tumor regrowth after 10 days of treatment in RPM mice. In contrast, RPMM mice responded to chemotherapy and we detected reduced tumor regrowth (**Figure 4c**). In both RPM and RPMM mice, we noticed weight loss due to dose-limiting toxicity (**Supplement figure 1d**). To capture the amount of remaining tumor cells, we measured NCAM in end point lungs (**Figure 4d**). In whole lungs, we detected ~55 % positive NCAM cells in the vehicle groups (RPM=57.3 % and RPMM=51.4 %) and 37.5 % positive cells in RPM chemotherapy treated lungs. A significantly reduced number of tumor cells were detected in RPMM chemotherapy treated mice (3.39 %) (**Figure 4e**). Next, we measured the amount of apoptosis using IHC staining for CC3. An increase of apoptotic cells was detected in RPMM chemotherapy treated tumors, indicating most cell death events occurring in Miz1-ΔPOZ chemotherapy treated mice.

Thus, Miz1-ΔPOZ tumors may have a significantly lower capacity to regrow during chemotherapy compared to Miz1 wild type tumors, indicating a potential role of Miz1 during cellular adaptation during genotoxic stress.

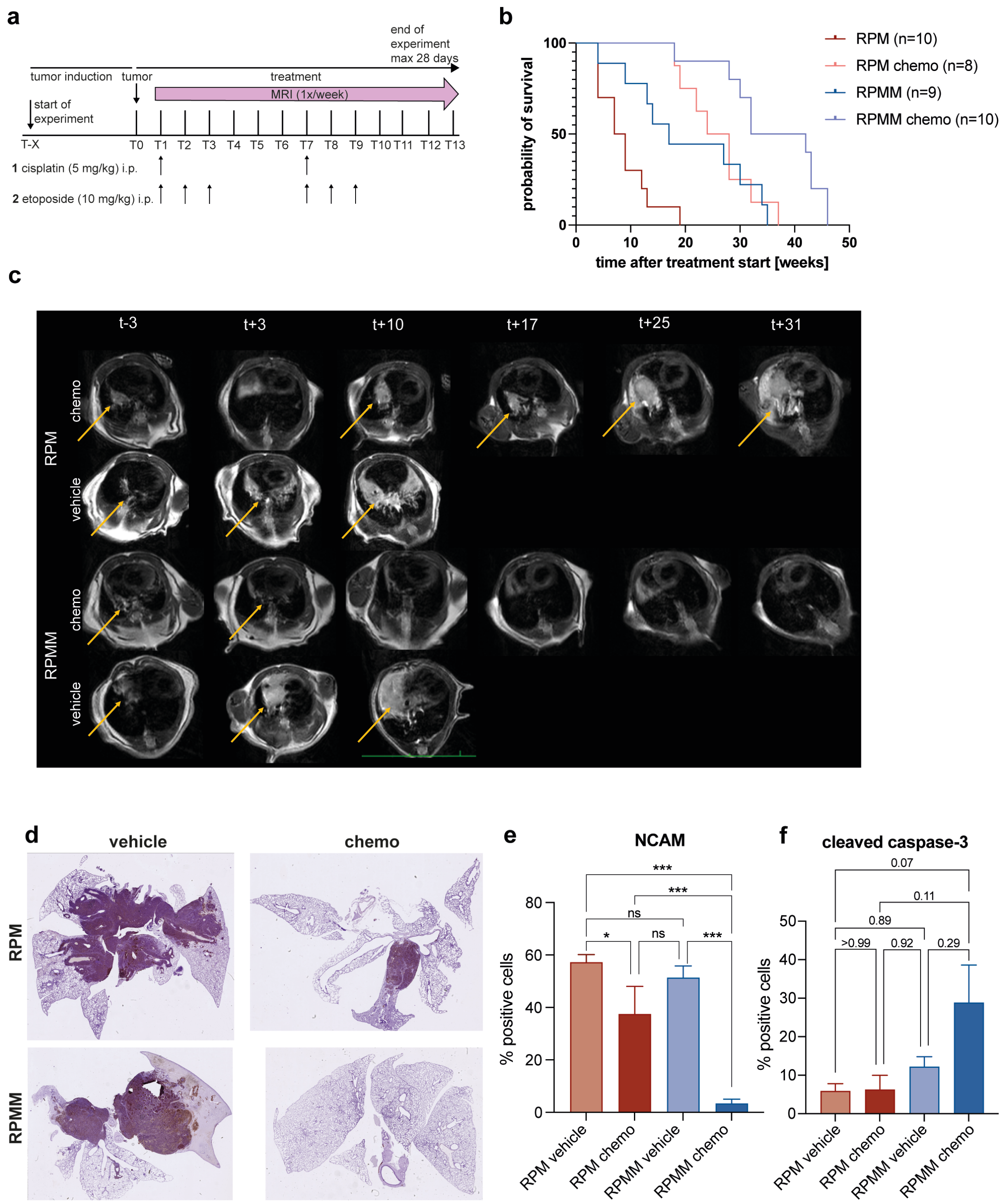

Figure 4: Miz1-ΔPOZ sensitizes SCLC tumor cells to chemotherapy. (a) Schematic treatment regime. After tumor detection mice were treated with four weekly cycles of 5 mg/kg cisplatin on day 1 and 10 mg/kg etoposide on day 1,2 and 3. (b) Kaplan-Meier survival analysis of RPM and RPMM mice treated with 5 mg/kg (1x week) and 10 mg/kg etoposide (3x week). (c) Representative weekly MRI images. Yellow arrows highlight tumors. (d) Representative IHC staining for NCAM. (e, f) Automated quantification of IHC for NCAM (e) and CC3 (f) from mice in (b), error bars indicate mean ± SME with ordinary one-way ANOVA. **p*= 0.033, ***p*=0.002, ****p*<0.001.

DISCUSSION

In this study, we investigated the role of Miz1-ΔPOZ in Myc-driven SCLC using a novel mouse model: $Rb1^{fl/fl}Trp53^{fl/fl}Myc^{LSL/LSL}Miz1^{\Delta POZ fl/fl}$ (RPMM). Compared to the Myc-driven Miz1 wild type SCLC model RPM, RPMM mice display a similar SCLC phenotype and scarce immune cell infiltration. However, RPMM tumor-bearing mice live significantly longer, show a trend towards increased expression of the apoptotic marker CC3, and reduced metastatic spread. Chan et al. reported cooperation of Myc/Miz1 with Skp2 to activate RohA gene transcription and thereby promote metastasis[147]. Based on this finding, we hypothesize the perturbated Myc/Miz1 interaction plays an important role in the reduction of metastatic spread in the RPMM mouse model compared to the RPM mouse model. However, further investigation of the specific mechanism behind the regulation of metastatic spread in this context is needed.

Notably, RPMM mice live longer only if they have been infected with the Cgrp-*Cre* virus targeting neuroendocrine cells and not if they have been infected with CMV-*Cre* virus targeting all cells. RPM and RPMM mice infected with CMV-*Cre* rapidly develop tumors after 3-4 weeks and have a median survival of 44 days (RPM) and 43 days (RPMM). One explanation could be that the tumor development is too fast and aggressive to distinguish differences between the groups. Compared to cancer mouse models of ALL and medulloblastoma, the detected Miz1-ΔPOZ survival benefit is minor, and a functional Miz1 is not required for SCLC development[119,125]. In medulloblastoma (MB) Myc–Miz1 interaction is critical for Group 3 MB development[125] and in T-ALL and B-ALL/lymphoma a functional Miz1 is essential for tumor development, regardless of the oncogenic driver. But the inhibitory function of Miz1-ΔPOZ on lymphomagenesis is only present with intact *Trp53*[119]. This observation is in line with the minor impact on survival of Miz1-ΔPOZ in *Trp53* deficient SCLC tumorigenesis and indicates that the prolonged survival benefit of Miz1-ΔPOZ depletion is potentially *Trp53*-dependent. In other studies, MIZ1 is described to upregulate expression of the antiapoptotic *BCL2* gene[129]. One potential hypothesis is that the deletion of the Miz1-POZ domain in RPMM could lead to reduced BCL2 levels and, thereby, to the increased apoptotic CC3 marker. We present evidence that a truncated Miz1 significantly alters SCLC tumorigenesis with a less aggressive phenotype and a higher apoptotic potential than Miz1 wild type SCLC.

On RNA level, the gene expression signature changes in Miz1-ΔPOZ tumors, and we observed an upregulation of Myc target genes. This upregulation of Myc target genes could be due to the release of Myc-Miz1 repressor activity. The detected tumor latency in our novel RPMM mouse model could be mediated by altered Myc function either by perturbated Myc/Miz1 interaction, changes in the expression of Myc target genes or by Myc independent alteration mediated by Miz1-ΔPOZ.

Besides upregulated Myc target genes, our bulk sequencing data shows upregulation of gene sets associated with DNA damage repair/checkpoint pathway. RPMM tumor cells may activate DNA repair or DNA damage checkpoint pathways to enable DNA repair or cell death to prevent the cell from the accumulation of DNA damage. In line with this, steady-state γH2AX signal measured by western blot analysis is reduced in RPMM cell lines. We identified an increased vulnerability to chemotherapy (etoposide) in cells derived from RPMM tumors than in cells derived from RP and RPM tumors.

Cell survival or cell death following DNA damage underlies a complex signaling network. The decision between survival or death depends on factors involved in DNA damage recognition, repair and tolerance as well as on the complex protein–protein network of regulated cell death[148]. Mice with truncated Miz1 show an increased level of apoptosis after chemotherapy compared to Miz wild type, indicating that a functional Miz1 is important for cell survival and important for resistance to chemotherapy.

Upregulation of *p21Cip1* expression in response to DNA damage requires MIZ1 function[149] and in breast cancer, p21 is important to protect cancer cells from apoptosis after CDK4/6 inhibitor treatment[150]. Furthermore, Rodriguez et al. described cells with Chk1 and p21 depletion undergo apoptosis after replication fork stress, indicating an important role of p21 in cell death[151]. This is in line with our observation that RPMM cells are more sensitive to the Chk1 inhibitor prexasertib than RPM cells. In which way depletion of Miz1-POZ alters components in cell death pathways or DDR machinery and thereby drives cell death has to be further investigated. We further observed an extended response of RPMM mice to chemotherapy compared to RPM mice, and further IHC staining confirmed a reduced tumor regrowth and increased CC3-positive cells in chemo-treated RPMM mice. In summary, ablation of Miz1-ΔPOZ prolongs survival, and a combination of Miz1-ΔPOZ and chemotherapy reduces the amount of tumor cells compared to the combination of Miz-1 wild type and chemotherapy. SCLC with a truncated Miz1 remains chemosensitive, indicating a crucial role of Miz1 in the process of chemoresistance.

The present study suggests further investigation of Miz1 as a potential target in a Myc-driven SCLC. It remains to be investigated whether the increased sensitivity towards chemotherapy due to Miz1-ΔPOZ is dependent or independent from Myc. Recent studies described the druggability of POZ domains in general by small molecules or peptides, exemplified by targeting the BCL6 POZ domain by peptides and small molecules, which leads to growth inhibition of diffuse large B-cell lymphoma (DLBCL) cell lines[152]. The fact that POZ domains have highly conserved structures and targeting POZ domains in other contexts, as mentioned above could indicate the druggability of the MIZ1-POZ domain and thereby provide a new approach to disturb the MYC/MIZ1 interaction in SCLC[153,154]. More recently, Orth et al. identified an atypical binding site in the MIZ1-BTB domain. Compared to other BTB domains, this atypical binding site exhibit an unusual accessibility which can serve as a possible target site for small molecules or peptidomimetics[155].

Furthermore, our data suggest that a combination of potential novel drugs targeting the MIZ1 POZ domain with chemotherapy may have the potential for an effective SCLC treatment and may overcome chemoresistance.

METHODS

Cell culture

RP, RPM and RPMM cells were cultured in RPMI 1640 medium supplemented with 10 % fetal bovine serum (Gibco) and 1 % penicillin/streptomycin (Gibco) and kept at 37 °C in a humidified atmosphere with 5 % CO_2.

Murine cell line generation

Murine SCLC cell lines (RP181 and RP1380) were derived from lung tumors of a genetically engineered mouse model (GEMM) for SCLC driven by the loss of *Trp53* and *Rb1* provided by the lab of H.C. Reinhardt. RPM (RPM70, RPM71, RPM150 and RPM237) and RPMM (RPMM226, RPMM229, RPMM252, RPMM388, RPMM390, RPMM399) were derived from lung of SCLC GEMMs driven either by the loss of *Trp53* and *Rb1 plus* Myc^{T58A} *(RPM) or Trp53, Rb1,* $Miz1^{\Delta POZ}$ loss plus Myc^{T58A} (RPMM). RPM and RPMM lung tumors were minced and enzymatically dissociated with the murine dissociation kit (Tumor Dissociation Kit, mouse #130-096-730, Miltenyi Biotec) according to the protocol.

Cell viability assay

To assess cell viability, CellTiter-Glo (CTG) assays (Promega, USA) were performed, which is based on quantification of ATP, indicating the presence of metabolically active cells.

Half-maximal growth inhibitory (GI_{50}) values were determined as follows: Cells were plated in 96-well plates in triplicates and compounds were added at 8 decreasing compound concentrations 24 h after seeding. Seventy-two hours later, cell viability was measured via Cell Titer-Glo (CTG) assay (Promega) and was normalized to DMSO-treated controls. Half-maximal growth inhibitory (GI_{50}) concentrations of cell viability were inferred by fitting sigmoidal dose–response curves using the Prism 8 software (GraphPad).

Western blotting

Cell lysates were prepared using RIPA buffer supplemented with protease inhibitors (cOmplete Mini Protease Inhibitor Cocktail, Roche). Protein concentration was determined by BCA assay (Pierce) and equal amounts of protein were separated on 4–20 % Tris-glycine sodium dodecyl sulfate-polyacrylamide gel electrophoresis (SDS-PAGE) gels (Thermo Fisher Scientific) and transferred to PVDF-FL membrane (Millipore). Membranes were blocked in 5 % milk/TBS or 2 % Fish/TBS, incubated with primary antibodies in 5 % milk/TBS-T or 2 % fish/TBS-T, washed, and incubated with fluorescently labeled secondary antibodies prior to detection with Odyssey CLx imaging system (LI-COR Biosciences). Images were processed using the Image

Studio Software (LI-COR Biosciences). Primary antibodies are: HSP90 (#4877, Cell Signaling Technology, 1:2000), MYC (#9402, Cell Signaling Technology, 1:1000), pyH2AX (#05-636, Merck, 1:500). Secondary antibodies are: goat anti-rabbit 800CW (#926-32211, LI-COR Biosciences, 1:10,000), goat anti-mouse 800CW (#926-3220, LI-COR Biosciences, 1:10,000).

Flow cyctometry

Cell lines were seeded into 6-well plates (1 x 10^5 cells/well). 24 hours later etoposide or DMSO control was added to the medium. 72 hours later supernatant was collected, cells were trypsinized washed with ice-cold PBS, and resuspended in antibody-binding buffer (10 mM HEPES pH 7.4 (Fisher Scientific, USA, Cat. No. 15630080), 140 mM NaCl; 2.5 mM $CaCl_2$). Cells were stained for Annexin-V (15 min, RT, dark) (BD Biosciences, USA, Cat. No. 556420) and 50 µg/mL DAPI. Samples were analyzed on a FACS MACSQuant16 (Miltenyi) and analyzed using FlowJo.

Mice

The local authorities and the animal protection committee approved all animal procedures of this study.

RPM mice are available at the Jackson Laboratory as stock no. 029971. For induction of lung tumors mice at 8-12 weeks of age were anesthetized with Ketavet (100 mg/kg) and Rompun (20 mg/kg) and were infected with 10^6 – 10^8 plaque-forming units of Ad5-CMV-Cre or Ad5-CGRP-Cre viruses (University of Iowa) by intratracheal instillation. Both male and female mice were equally divided between all experiments. RPM (Rb1$^{fl/fl}$ Trp53$^{fl/fl}$ Myc$^{LSL/LSL}$) mice were crossed to Miz1-*ΔPOZ*$^{fl/fl}$ (exon 3 and exon 4 of *Miz1*, encoding the POZ/BTB domain, were flanked by loxP sites) mice to generated RPMM mice. The Miz1-*ΔPOZ*$^{fl/fl}$ mice were provided by M. Eilers (Würzburg).

MRI scans and treatment

Three weeks after tumor induction, tumor formations were monitored weekly by magnetic resonance imaging (MRI). A 3.0 T Philips Achieva clinical MRI (Philips Best, the Netherlands) in combination with a solenoid coil designed for small animal were used for imaging. T2-weighted MR images were acquired in the axial plane using turbo-spin echo (TSE) sequence [repetition time (TR) = 3819 ms, echo time (TE) = 60 ms, field of view (FOV) = 40 × 40 × 20 mm^3, reconstructed voxel size = 0.13 × 0.13 × 1.0 mm^3, number of averages = 1) Mice were scanned under isoflurane (2.5 %) anesthesia. MR images (DICOM filed) were analyzed using Horos software. Once tumors were detected, mice were randomized into two groups and treated with either vehicle or chemotherapy (5 mg/kg cisplatin, 1x per week, i.p. and 10 mg/kg etoposide, 3x per week, i.p.) for 28 days.

Immunohistochemisty

For Immunohistochemisty tissue were fixed in 4 % formaldehyde solution (24 h, RT) (Walter) and afterwards embedded in paraffin. Paraffin-embedded (FFPE) tissue were sectioned at 3-4 µM, deparaffinized and treated according to standard protocols of the routine diagnostics pipeline (Institute of Pathology, University Hospital Cologne, Germany). Staining was performed using hematoxylin & eosin (H&E) and primary antibodies against CD3 (Epredia #RM-9107, 1:50), CD8 (Abcam #ab237723, 1:200), CD45 (Bdbiosciences #550539, 1:25), CD56 (Zytomed Systems #RBK050-05, 1:50) Cleaved Caspase-3 (CC3) (Cell signaling #9661, 1:100), CD4 (abcam #ab183685, 1:1000), Phospho-Histone H2A.X (Cell signaling #9718, 1:100). Histofine simple Stain antibody detection kit (Medac, Wedel, Germany) were used as secondary antibodies. The slides were scanned by the S360 Hamamatsu Slidescanner and analyzed with QuPath.

RNA sequencing

Fresh frozen tumor tissue was sectioned in 20 µM slices and homogenized using ceramic grinding balls. RNA was extracted using the Qiagen RNeasy Mini Kit. Total RNA's were used to prepare 3′ UTR mRNA libraries using the Lexogen QuantSeq kit according to the standard protocol. 500 ng total RNA were used to prepare 3′ UTR mRNA libraries using the Lexogen QuantSeq kit (Lexogen, Austria, Cat. No. 015.96) according to the standard protocol[156]. Quality controlled cDNA pools were quantified with the KAPA Library Quantification kit and sequenced on a NovaSeq sequencer (Illumina, USA) with a 1x100bp protocol. Raw data was aligned to the murine genome reference GRCm38.95 using STAR aligner[157] and gene expression was quantified with RSEM[158] prior to downstream analysis with the R package DESeq2[159]. E2F and Myc target genes were obtained from the MSigDB Hallmark collection.

Single cell (sc)RNA-seq analysis

Murine lung tumors were isolated from mouse lungs and minced in small pieces. To obtain single cells the tumor pieces were enzymatically dissociated with the human tumor dissociation kit according to the protocol (Tumor Dissociation Kit, human #130-095-929, Miltenyi Biotec). Red blood cells were removed (ACK lysing buffer, Lonza, 2 min, RT), the single cells were filtered and washed with PBS. To remove dead cells and gain a viability >75 % the single cells were added to Ficoll (10 mL Ficoll + 5 mL cell suspension) and centrifuged (300 g, 20 min, no break, decal). The cell layer (middle layer) was washed two times with PBS and resuspended in 1X PBS containing 0.004 % BSA. For scRNA library construction we used the Chromium Next GEM Single Cell 3’ Reagent Kits v3.1 and the Chromium controller (10x Genomic, USA). Cells are delivered at a limiting dilution, such that the majority (~90- 99%) of generated gel in emulsion beads (GEMs) contains no cell, while the remainder largely contain a single cell. 10.000 cells per sample were targeted. Upon dissolution of the Single Cell 3’ Gel Bead in a GEM, primers containing (i) an Illumina R1 sequence (read 1 sequencing primer), (ii) a 16 bp 10x Barcode, (iii) a 12 bp Unique Molecular Identifier (UMI) and (iv) a poly-dT primer sequence are released and mixed with cell lysate and Master Mix. Incubation of the GEMs then produces barcoded, full-length cDNA from poly-adenylated mRNA. Subsequently GEMs are broken, the pooled fractions are recovered and silane magnetic beads are used to remove leftover biochemical reagents and primers from the mixture. Full-length, barcoded cDNA is then amplified by PCR to generate sufficient mass for library construction. Enzymatic Fragmentation and Size Selection are used to optimize the cDNA amplicon size prior to library construction. R1 (read 1 primer sequence) are added to the molecules during GEM incubation. P5, P7, a sample index and R2 (read 2 primer sequence) are added during library construction via End Repair, A-tailing, Adaptor Ligation and PCR. The final libraries contain the P5 and P7 primers used in Illumina bridge amplification. A Single Cell 3’ Library comprises standard Illumina paired-end constructs which begin and end with P5 and P7. Libraries were pooled and sequenced on an Ilumina NovaSeq 6000 (Illumina, USA) aiming at >50k reads/cell. Resulting FASTQ-files were processed using the Cellranger Pipeline 6.0.0 (10x Genomics, USA) including alignment to GRCm38. Filtered gene barcode matrices were further analyzed using the R package Seurat v4.1.1.[160] Cells with at least 200 detected genes and genes detected in at least 3 cells were retained. Expression levels were normalized including adjustment for fraction of mitochondrial reads and cell cycle by regression. Subsequently PCA was performed on the merged and normalized samples, clustered by shared nearest neighbor graph construction and visualized using t-Stochastic Neighbor Embedding (tSNE) dimension reduction technique. Expression of selected genes was visualized per cell based on the tSNE embedding and clustering.

4 Discussion

4.1 Insight Into Targeting Exon20 Insertion Mutations of the Epidermal Growth Factor Receptor with Wild Type-Sparing Inhibitors

Targeting non-classical *EGFR* exon 20 insertion mutations and sparing wild type EGFR remains challenging. Exon 20 mutations are located in the α-*C*-helix–β4-loop and push the α*C*-helix in its inward position, which corresponds to the active conformation. Consequently, exon 20 insertion mutations cause a conformational change that closely mimics the active form of wild type EGFR, without rendering the ATP binding pocket. In contrast, the structure of classical EGFR mutations like the activation mutation L858R and the deletion mutation in exon 19 affects the ATP binding pocket and creates an altered structure compared to wild type EGFR. Consequently, this unique structure of the mutant EGFR ATP binding pocket can be used as a binding site for TKIs. Thereby wild type sparing activity against mutant EGFR can be archived. However, since the ATP binding pocket is unaffected in the case of exon 20 insertion mutations, the development of wild type sparing EGFR inhibitors has been complex.

In the present study, we present two novel small molecule inhibitors targeting EGFR and HER2 exon 20 mutations in LUAD. We combined biochemical selectivity assays and in vivo efficacy studies to archive on-target activity while avoiding off-target side effects and on-target toxicity. LDC8201 and LDC0496 share a 1*H*-pyrrolo[2,3-*b*]pyridine scaffold as well as the acrylamide warhead targeting Cys797 covalently. Computational models highlighted the similarity of exon 20 insertion mutations and the wild type form, but also unraveled a distinct cleft that is not addressed by previous TKIs. The introduction of the 5-isopropylester (LDC0496) occupies the selectivity pocket (orange circle) that is slightly targeted by the 4-chlorine substituent of LDC8201 and not addressed by the third-generation TKI osimertinib (**Figure 10**). Besides cellular viability assays, both compounds were tested in specific biochemical assays, to pinpoint the target identity. The performed kinome scan, where the potential of off-target binding of LDC8201 and LDC0496 was investigated, validated the approach of exploiting the selectivity pocket adjacent to the 4 and 5 positions of the pyrolopyridine scaffold.

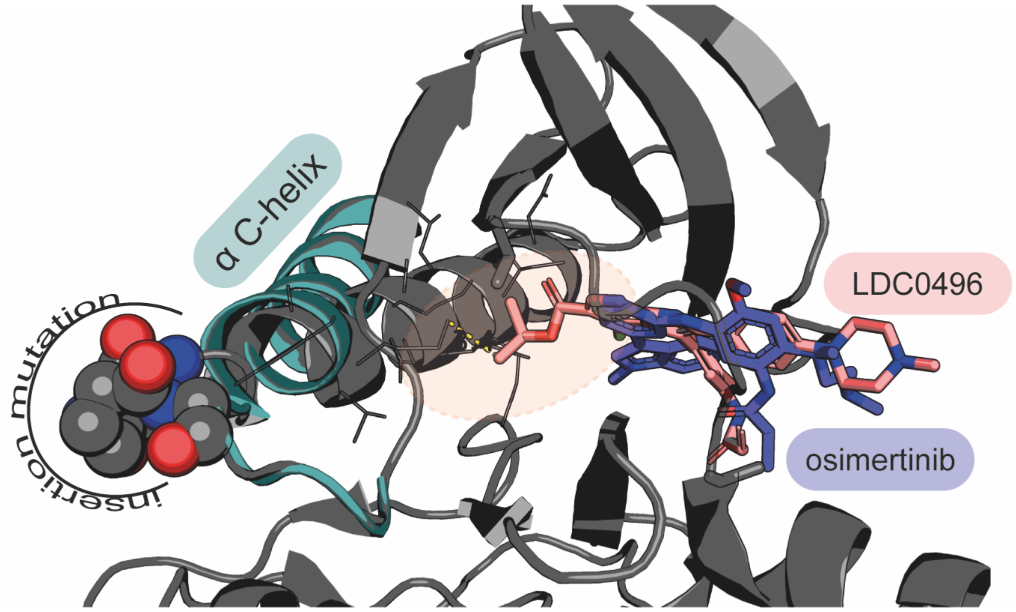

Figure 10: Structure properties of exon 20 insertion mutations and distinct binding features of osimertinib and LDC0496. Overlay of EGFR ex20ins (gray, PDB:4lrm) and the EGFR α*C*-helix in an inactive conformation (cyan, PDB:1xkk). The overlay of the inactive EGFR conformation (cyan) and the crystal structure of EGFR-D770_N771insNPG (gray) indicate the structural changes induced by the insertion mutation. Osimertinib (blue, PDB:7LGS).

Previous studies used poziotinib, a pan ERBB small molecule with an anilino-quinazoline scaffold, to effectively inhibit tumor growth in exon 20 mutated cell lines as well as in vivo xenograft models. To measure specificity for exon 20 mutant EGFR, this study compared inhibitory activity against T790M mutant EGFR and showed significantly higher activity in exon 20 mutant EGFR. However, this selectivity over T790M can be explained by a sterical clash introduced by the gatekeeper mutation and is clinically irrelevant since the occurrence of exon 20 mutations in the context of T790M mutant EGFR have not been described yet. The investigators should have assessed wild type toxicity in terms of drug safety instead of highlighting their profile towards T790M selectivity[60]. Nevertheless, unlike T790M mutant EGFR, wild type EGFR is inhibited by poziotinib leading to on-target toxicity and consequently severe side effects in patients. This leads to the discontinuation of the drug in nearly all patients receiving poziotinib. In conclusion, the wild type sparing inhibitor LDC0496 in our study outperforms poziotinib, in terms of wild type selectivity and thereby presents a promising alternative.

In 2021 the FDA approved mobocertinib for the treatment of patients with exon 20 mutant LUAD. Mobocertinib is an indole-pyrimidine-base irreversible EGFR inhibitor that share nearly all structure similarities with osimertinib. Additionally, mobocertinib exhibit on the same position like LDC0496 the C5-carboxylate isopropyl ester, occupying the identical selectivity pocket like LDC0496[49]. The introduction of a moiety on position C5 on LDC8201 and osimertinib, resulting in LDC0496 and mobocertinib, revolutionized the selectivity profile of TKIs targeting exon 20 insertions mutations. The development of mobocertinib and LDC0496 highlighted the power of computer-assisted- and structure-guided drug design, including precise untangled structure-activity relationships (SARs) of every single compound moiety. Structural similarities between mobocertinib and LDC0496 suggest similar activity profiles, however, comprehensive comparisons have not been conducted yet. Of note, the first instances of resistance-conferring mutations against mobocertinib were reported[66,161].

Despite these few promising approaches to develop TKIs targeting exon 20 mutant EGFR, general limitations of TKIs need to be considered: the selectivity profile, on- and off-target side effects, or emerging secondary resistance mutations. Especially in the context of secondary resistance mutations, complementary non-TKI approaches can provide a substantial benefit. Amivantamab (JNJ-61186372), an EGFR–MET bispecific antibody which was FDA approved for exon 20 mutant LUAD in May 2021, represents such a complementary approach. Amivantamab, inhibits ligand-mediated receptor activation and leads to EGFR and MET internalization and downregulation. Enhanced blocking of downstream signaling is potentially mediated through dual targeting of EGFR and MET expressed on the same tumor cell. Additionally, amivantamab activates immune cell–directing activity such as antibody-dependent cytotoxicity (ADCC) or trogocytosis[162]. It is assumed that the major treatment effect is due to the oncogenic addiction of the cancer cell, whereby cancer cells die after EGFR downregulation caused by the antibody[163]. In initial clinical studies, amivantamab showed and superior ORR of 40 % (PFS: 8.3 month) compared to mobocertinib, with an ORR 28 % (PFS: 7.3 month), but both treatment strategies show limitations (amivantamab: most common adverse event are rash and infusion-related reaction; mobocertinib: most common adverse event are diarrhea, rash, paronychia). Direct comparisons of activity and toxicity profiles between LDC0496 or LDC8201 and amivantamab have not been conducted yet.

To sum up, although the targeting of exon 20 mutant EGFR has proven to be challenging in the past, few promising approaches have been developed in the last years. Among those approaches are the two novel compounds LDC0496 or LDC8201, which stand out in their favorable selectivity profile and potentially provide an additional treatment option for patients with exon 20 mutant LUAD.

4.2 Clonal dynamics of *BRAF*-driven drug resistance in *EGFR*-mutant lung cancer

EGFR-mutant NSCLC patients benefit from the development of tailored drugs, targeting the mutant kinase domain and thereby sparing non-mutant cells. Unfortunately, drug resistance occurs in nearly all cases. Previously, osimertinib was approved only for patients with acquired *EGFR*-T790M after first and second-generation TKI. More recently, osimertinib was also approved as first-line treatment of patients with *EGFR*-mutant NSCLC. Consequently, the introduction of osimertinib as first-line treatment has changed the landscape of arising resistance mutations. The set of described resistance mechanisms to EGFR inhibition comprises on-target resistance and target-independent resistance mechanisms such as MET/HER2 amplification, fusions, histological transformations, or activation of bypass. Especially, the activation of the bypass RAS–MAPK signaling pathway, due to *BRAF*, *NRAS,* and *KRAS* mutations are more often found in patients who received third-generation inhibitors than first- or second-generation inhibitors. *BRAF*^{V600E} resistance mutations are found in ~3 % of *EGFR*-mutant lung cancer treated with osimertinib.

In the present study, the role of both co-occurring and acquired *BRAF* mutations in patients with activating *EGFR* mutations was investigated. The analyzed cohort consisted of 15 patients, of which five exhibited co-occurring *BRAF* and *EGFR* mutations at the time of diagnosis, whereas 10 had acquired *BRAF* mutations as a mechanism of resistance to anti-EGFR therapy. This finding demonstrates that besides *BRAF* mutations as a resistance mechanism occurring after TKI treatment NSCLC patients harbor co-occurring *EGFR/BRAF* mutations even before anti-EGFR therapy. On the contrary, previous reports indicated synthetic lethality preventing activation of both EGFR and the MAPK signaling pathway via mutation in *KRAS*[164]. To validate our clinical finding that the co-occurrence does not provide a fitness disadvantage we introduced an additional *BRAF* mutation into an *EGFR*-mutant NSCLC cell line model. These experiments revealed that additional BRAF does not induce synthetic lethality in EGFR-driven NSCLC or provide a fitness disadvantage. In support of our findings, other studies described that concomitant *EGFR* and *BRAF* mutations are not only tolerated but also collude with a feed-forward circuit that connects BRAF signaling and subsequent EGFR ligand expression and EGFR activation[165].

To find therapeutic approaches to tackle the problem of resistance to EGFR inhibition induced by co-occurrence of *BRAF* mutations, we performed a synergy screen in *EGFR*- and *BRAF*-mutant cells to find a combination therapy to overcome resistance and target co-existing *EGFR*-

and *BRAF*-mutant cells. Our in vitro data indicate that the combination of the MEK inhibitor trametinib and the EGFR inhibitor osimertinib inhibit PC9$^{BRAF\text{-}V600E}$ cells, whereas the monotherapy had a limited effect. The in vivo data support EGFR/MEK combination as a treatment option for patients with *EGFR* and *BRAF* mutations.

Due to longitudinal and multi-site sampling of patients, we were able to deciphered subclonal structure of these tumors. Our study indicated that the evolutionary branching process rather than a linear trajectory of one clone gives rise to resistance to EGFR inhibition. In addition, we detected substantially heterogeneous mutational profiles from different tumor sites within a given patient. These findings highlight the importance of multiple sampling in order to capture the full spectrum of alterations.

The major clinical challenge is to design personalized treatment regimens incorporating all potentially targetable lesions. This study highlights the need to individually characterize the tumor at base-line as well as serially throughout the course of therapy in order to adjust the treatment regime and combat drug resistance.

4.3 MIZ1-ΔPOZ shapes treatment response in small cell lung cancer

SCLC is a highly aggressive, early metastatic cancer with an initial good response to chemotherapy but inevitably develops chemoresistance with no further treatment options. Frequent amplifications of *MYC* family members in SCLC and their functional importance for SCLC tumors highlight the potential to find strategies to target MYC, but this remains challenging. To understand the molecular function of Myc in SCLC in more detail, we investigated the interplay of Myc and Miz1 by creating a novel SCLC mouse model RPMM combining Myc^{T58A} and Miz1-ΔPOZ, which ablates Miz1 binding to chromatin. SCLC-bearing RPMM mice live longer than their RPM counterparts and exhibit reduced metastasis and an increase in apoptotic cells. However, tumor onset, size, and localization, as well as Myc levels and immune cell infiltration are not altered in Miz1-ΔPOZ tumors. DDR pathway inhibitors are more potent in RPMM cells, especially the chemotherapeutic agent etoposide, which is in line with several other studies that showed efficacy of chemotherapy and targeting of the DDR pathways in SCLC[101,143,144]. The molecular basis of sensitivity towards DDR agents in SCLC is not fully understood but SCLC is highly dependent on functional DNA damage repair and the DDR machinery to deal with constant DNA damage. The further increase in sensitivity against DDR inhibitors of Miz1-ΔPOZ seems paradoxical since we observed increased expression of members of the DDR machinery and lower γH2AX, i.e. DNA damage levels in

RPMM cells compared to RPM cells. Consistently, we observed a trend towards higher chemosensitivity and delayed chemoresistance in RPMM compared to RPM mice. Further studies are needed to elucidate the biological function of Miz1-ΔPOZ in this context and evaluate whether targeting the Miz1-POZ domain could be an effective new approach in the treatment of Myc-driven SCLC. Targeting POZ domains in other cancer entities showed promising results[152-154]. The three-dimensional structure of POZ domains suggests the presence of charged pockets as potential target sites for novel small molecule inhibitors to perturb MIZ1-mediated transcription regulation. The majority of SCLC exhibits low or no *MYC* expression, so it is vital to investigate the effect of MIZ1-ΔPOZ in SCLC in the absence of high MYC levels to judge how our findings are influenced by MYC overexpression and separate MIZ1 effects from MYC/MIZ1 effects. These studies will determine whether overcoming chemoresistance in SCLC by targeting MIZ1 POZ in combination with chemotherapy is a potential therapeutic strategy in SCLC per se or whether it is limited to MYC-driven SCLC.

5 Concluding remarks

Precision medicine dramatically changed the therapeutic landscape in cancer therapy. Targeted drugs shifted the treatment from cytotoxic, unspecific chemotherapy towards tailored drugs, which not only increases survival but also improves the quality of life under treatment. In the early 2000s, the TKI gefitinib fundamentally changed the treatment of *EGFR*-mutant LUAD. For the development of targeted drugs, the understanding of the genetic background, as well as the underlying biology of distinct patients, is crucial.

Consistently, an in-depth molecular characterization of the mode-of-action of novel TKIs is necessary for pre-clinical research to drive and enhance faithful clinical translation of these novel therapeutics. Despite the increasing number and specificity TKIs, resistance mutations inevitably occur. The multitude of target-dependent and target-independent resistance mechanisms poses a substantial challenge for the future development of TKIs, which, in part, might be addressed by combining TKIs with other drugs like chemotherapy. Furthermore, sequential tumor monitoring during disease is essential to detect resistance mechanisms as early as possible. In addition, a recent study highlighted that multi-sampling is required to detect inter- and intra-tumoral heterogeneity and that the mutational landscape changes from the time of diagnosis and during treatment, depending on the used drug[166]. Besides drug-induced, elevated heterogeneity, late-stage disease also increases the probability of a heterogenic tumor. Treatment of a heterogenic tumor is challenging, and agents are needed to target the predominate clone and the subclones.

Compared to NSCLC, SCLC lacks drug targets, and the standard of care is still chemotherapy with the recent addition of immunotherapy. Not only drug targets are missing, also the rapid development of chemoresistance results contributes to the poor prognosis. Further studies of SCLC tumor biology are needed to understand chemoresistance and to find alternative approaches to target SCLC.

The development of better detection methods to discover early-stage diseases with a lower heterogeneity is urgently needed. Better early detection methods, and the understanding of molecular tumor biology to identify tumor- and patient-specific vulnerabilities combined with rational drug design and well-considered clinical trials will all be essential prerequisites for the advancement of precision medicine.

References

1 Schabath, M. B. & Cote, M. L. Cancer Progress and Priorities: Lung Cancer. *Cancer Epidemiol Biomarkers Prev* **28**, 1563-1579, doi:10.1158/1055-9965.EPI-19-0221 (2019).

2 Sung, H. *et al.* Global Cancer Statistics 2020: GLOBOCAN Estimates of Incidence and Mortality Worldwide for 36 Cancers in 185 Countries. *CA Cancer J Clin* **71**, 209-249, doi:10.3322/caac.21660 (2021).

3 Thai, A. A., Solomon, B. J., Sequist, L. V., Gainor, J. F. & Heist, R. S. Lung cancer. *The Lancet* **398**, 535-554, doi:10.1016/s0140-6736(21)00312-3 (2021).

4 Siegel, R. L., Miller, K. D. & Jemal, A. Cancer statistics, 2019. *CA Cancer J Clin* **69**, 7-34, doi:10.3322/caac.21551 (2019).

5 Society., A. C. Cancer facts & figures. *Atlanta, GA: American Cancer Society* (2019).

6 Siegel, R. L., Miller, K. D., Fuchs, H. E. & Jemal, A. Cancer statistics, 2022. *CA Cancer J Clin* **72**, 7-33, doi:10.3322/caac.21708 (2022).

7 Corrales, L. *et al.* Lung cancer in never smokers: The role of different risk factors other than tobacco smoking. *Crit Rev Oncol Hematol* **148**, 102895, doi:10.1016/j.critrevonc.2020.102895 (2020).

8 Gridelli, C. *et al.* Non-small-cell lung cancer. *Nat Rev Dis Primers* **1**, 15009, doi:10.1038/nrdp.2015.9 (2015).

9 Barker, A. J. *et al.* Studies leading to the identification of ZD1839 (iressa™): an orally active, selective epidermal growth factor receptor tyrosine kinase inhibitor targeted to the treatment of cancer. *Bioorganic & Medicinal Chemistry Letters* **11**, 1911-1914, doi:10.1016/s0960-894x(01)00344-4 (2001).

10 Wakeling, A. E. *et al.* ZD1839 (Iressa): an orally active inhibitor of epidermal growth factor signaling with potential for cancer therapy. *Cancer Res* **62**, 5749-5754 (2002).

11 Paez, J. G. *et al.* EGFR mutations in lung cancer: correlation with clinical response to gefitinib therapy. *Science* **304**, 1497-1500, doi:10.1126/science.1099314 (2004).

12 Wang, Z. *et al.* Current therapy and development of therapeutic agents for lung cancer. *Cell Insight* **1**, doi:10.1016/j.cellin.2022.100015 (2022).

13 Iams, W. T., Porter, J. & Horn, L. Immunotherapeutic approaches for small-cell lung cancer. *Nat Rev Clin Oncol* **17**, 300-312, doi:10.1038/s41571-019-0316-z (2020).

14 Sanchez-Vega, F. *et al.* Oncogenic Signaling Pathways in The Cancer Genome Atlas. *Cell* **173**, 321-337 e310, doi:10.1016/j.cell.2018.03.035 (2018).

15 Ellrott, K. *et al.* Scalable Open Science Approach for Mutation Calling of Tumor Exomes Using Multiple Genomic Pipelines. *Cell Syst* **6**, 271-281 e277, doi:10.1016/j.cels.2018.03.002 (2018).

16 Hoadley, K. A. *et al.* Cell-of-Origin Patterns Dominate the Molecular Classification of 10,000 Tumors from 33 Types of Cancer. *Cell* **173**, 291-304 e296, doi:10.1016/j.cell.2018.03.022 (2018).

17 Imielinski, M. *et al.* Mapping the hallmarks of lung adenocarcinoma with massively parallel sequencing. *Cell* **150**, 1107-1120, doi:10.1016/j.cell.2012.08.029 (2012).

18 Kadara, H. *et al.* Whole-exome sequencing and immune profiling of early-stage lung adenocarcinoma with fully annotated clinical follow-up. *Ann Oncol* **28**, 75-82, doi:10.1093/annonc/mdw436 (2017).

19 Jordan, E. J. *et al.* Prospective Comprehensive Molecular Characterization of Lung Adenocarcinomas for Efficient Patient Matching to Approved and Emerging Therapies. *Cancer Discov* **7**, 596-609, doi:10.1158/2159-8290.CD-16-1337 (2017).

20 Frampton, G. M. *et al.* Activation of MET via diverse exon 14 splicing alterations occurs in multiple tumor types and confers clinical sensitivity to MET inhibitors. *Cancer Discov* **5**, 850-859, doi:10.1158/2159-8290.CD-15-0285 (2015).

21 Skoulidis, F. & Heymach, J. V. Co-occurring genomic alterations in non-small-cell lung cancer biology and therapy. *Nat Rev Cancer* **19**, 495-509, doi:10.1038/s41568-019-0179-8 (2019).

22 Andre, P. *et al.* Anti-NKG2A mAb Is a Checkpoint Inhibitor that Promotes Anti-tumor Immunity by Unleashing Both T and NK Cells. *Cell* **175**, 1731-1743 e1713, doi:10.1016/j.cell.2018.10.014 (2018).

23 Jura, N. *et al.* Mechanism for activation of the EGF receptor catalytic domain by the juxtamembrane segment. *Cell* **137**, 1293-1307, doi:10.1016/j.cell.2009.04.025 (2009).

24 Hynes, N. E. & Lane, H. A. ERBB receptors and cancer: the complexity of targeted inhibitors. *Nat Rev Cancer* **5**, 341-354, doi:10.1038/nrc1609 (2005).

25 Shi, K. *et al.* Emerging strategies to overcome resistance to third-generation EGFR inhibitors. *J Hematol Oncol* **15**, 94, doi:10.1186/s13045-022-01311-6 (2022).

26 Yarden, Y. & Sliwkowski, M. X. Untangling the ErbB signalling network. *Nat Rev Mol Cell Biol* **2**, 127-137, doi:10.1038/35052073 (2001).

27 Sharma, S. V., Bell, D. W., Settleman, J. & Haber, D. A. Epidermal growth factor receptor mutations in lung cancer. *Nature Reviews Cancer* **7**, 169-181, doi:10.1038/nrc2088 (2007).

28 Weinstein, I. B. Cancer. Addiction to oncogenes--the Achilles heal of cancer. *Science* **297**, 63-64, doi:10.1126/science.1073096 (2002).

29 Moyer, J. D. *et al.* Induction of apoptosis and cell cycle arrest by CP-358,774, an inhibitor of epidermal growth factor receptor tyrosine kinase. *Cancer Res* **57**, 4838-4848 (1997).

30 Li, D. *et al.* BIBW2992, an irreversible EGFR/HER2 inhibitor highly effective in preclinical lung cancer models. *Oncogene* **27**, 4702-4711, doi:10.1038/onc.2008.109 (2008).

31 Dungo, R. T. & Keating, G. M. Afatinib: first global approval. *Drugs* **73**, 1503-1515, doi:10.1007/s40265-013-0111-6 (2013).

32 Gonzales, A. J. *et al.* Antitumor activity and pharmacokinetic properties of PF-00299804, a second-generation irreversible pan-erbB receptor tyrosine kinase inhibitor. *Mol Cancer Ther* **7**, 1880-1889, doi:10.1158/1535-7163.MCT-07-2232 (2008).

33 Barf, T. & Kaptein, A. Irreversible protein kinase inhibitors: balancing the benefits and risks. *J Med Chem* **55**, 6243-6262, doi:10.1021/jm3003203 (2012).

34 Cross, D. A. *et al.* AZD9291, an irreversible EGFR TKI, overcomes T790M-mediated resistance to EGFR inhibitors in lung cancer. *Cancer Discov* **4**, 1046-1061, doi:10.1158/2159-8290.CD-14-0337 (2014).

35 Finlay, M. R. V. *et al.* Discovery of a Potent and Selective EGFR Inhibitor (AZD9291) of Both Sensitizing and T790M Resistance Mutations That Spares the Wild Type Form of the Receptor. *Journal of Medicinal Chemistry* **57**, 8249-8267, doi:10.1021/jm500973a (2014).

36 Ward, R. A. *et al.* Structure- and reactivity-based development of covalent inhibitors of the activating and gatekeeper mutant forms of the epidermal growth factor receptor (EGFR). *J Med Chem* **56**, 7025-7048, doi:10.1021/jm400822z (2013).

37 Engel, J., Lategahn, J. & Rauh, D. Hope and Disappointment: Covalent Inhibitors to Overcome Drug Resistance in Non-Small Cell Lung Cancer. *ACS Med Chem Lett* **7**, 2-5, doi:10.1021/acsmedchemlett.5b00475 (2016).

38 Leduc, C. *et al.* Clinical and molecular characteristics of non-small-cell lung cancer (NSCLC) harboring EGFR mutation: results of the nationwide French Cooperative Thoracic Intergroup (IFCT) program. *Ann Oncol* **28**, 2715-2724, doi:10.1093/annonc/mdx404 (2017).

39 Robichaux, J. P. *et al.* Structure-based classification predicts drug response in EGFR-mutant NSCLC. *Nature* **597**, 732-737, doi:10.1038/s41586-021-03898-1 (2021).

40 Kian, W. *et al.* Real-world efficacy and safety of mobocertinib in EGFR exon 20 insertion-mutated lung cancer. *Front Oncol* **12**, 1010311, doi:10.3389/fonc.2022.1010311 (2022).

41 Vyse, S. & Huang, P. H. Targeting EGFR exon 20 insertion mutations in non-small cell lung cancer. *Signal Transduct Target Ther* **4**, 5, doi:10.1038/s41392-019-0038-9 (2019).

42 Oxnard, G. R. *et al.* Natural history and molecular characteristics of lung cancers harboring EGFR exon 20 insertions. *J Thorac Oncol* **8**, 179-184, doi:10.1097/JTO.0b013e3182779d18 (2013).

43 Vasconcelos, P. *et al.* EGFR-A763_Y764insFQEA Is a Unique Exon 20 Insertion Mutation That Displays Sensitivity to Approved and In-Development Lung Cancer EGFR Tyrosine Kinase Inhibitors. *JTO Clin Res Rep* **1**, doi:10.1016/j.jtocrr.2020.100051 (2020).

44 Arcila, M. E. *et al.* Prevalence, clinicopathologic associations, and molecular spectrum of ERBB2 (HER2) tyrosine kinase mutations in lung adenocarcinomas. *Clin Cancer Res* **18**, 4910-4918, doi:10.1158/1078-0432.CCR-12-0912 (2012).

45 Tomizawa, K. *et al.* Prognostic and predictive implications of HER2/ERBB2/neu gene mutations in lung cancers. *Lung Cancer* **74**, 139-144, doi:10.1016/j.lungcan.2011.01.014 (2011).

46 Mazieres, J. *et al.* Lung cancer that harbors an HER2 mutation: epidemiologic characteristics and therapeutic perspectives. *J Clin Oncol* **31**, 1997-2003, doi:10.1200/JCO.2012.45.6095 (2013).

47 Gonzalvez, F. *et al.* Mobocertinib (TAK-788): A Targeted Inhibitor of EGFR Exon 20 Insertion Mutants in Non-Small Cell Lung Cancer. *Cancer Discov* **11**, 1672-1687, doi:10.1158/2159-8290.CD-20-1683 (2021).

48 Riely, G. J. *et al.* Activity and Safety of Mobocertinib (TAK-788) in Previously Treated Non-Small Cell Lung Cancer with EGFR Exon 20 Insertion Mutations from a Phase I/II Trial. *Cancer Discov* **11**, 1688-1699, doi:10.1158/2159-8290.CD-20-1598 (2021).

49 Wang, J., Lam, D., Yang, J. & Hu, L. Discovery of mobocertinib, a new irreversible tyrosine kinase inhibitor indicated for the treatment of non-small-cell lung cancer harboring EGFR exon 20 insertion mutations. *Med Chem Res* **31**, 1647-1662, doi:10.1007/s00044-022-02952-5 (2022).

50 Niggenaber, J., Hardick, J., Lategahn, J. & Rauh, D. Structure Defines Function: Clinically Relevant Mutations in ErbB Kinases. *J Med Chem* **63**, 40-51, doi:10.1021/acs.jmedchem.9b00964 (2020).

51 Udagawa, H. *et al.* OA07.03 Clinical Outcome of Non-Small Cell Lung Cancer with EGFR/HER2 Exon 20 Insertions Identified in the LC-SCRUM-Japan. *Journal of Thoracic Oncology* **14**, doi:10.1016/j.jtho.2019.08.443 (2019).

52 Arcila, M. E. *et al.* EGFR exon 20 insertion mutations in lung adenocarcinomas: prevalence, molecular heterogeneity, and clinicopathologic characteristics. *Mol Cancer Ther* **12**, 220-229, doi:10.1158/1535-7163.MCT-12-0620 (2013).

53 Yang, J. C. H. *et al.* Clinical activity of afatinib in patients with advanced non-small-cell lung cancer harbouring uncommon EGFR mutations: a combined post-hoc analysis of LUX-Lung 2, LUX-Lung 3, and LUX-Lung 6. *The Lancet Oncology* **16**, 830-838, doi:10.1016/s1470-2045(15)00026-1 (2015).

54 Naidoo, J. *et al.* Epidermal growth factor receptor exon 20 insertions in advanced lung adenocarcinomas: Clinical outcomes and response to erlotinib. *Cancer* **121**, 3212-3220, doi:10.1002/cncr.29493 (2015).

55 Kobayashi, Y. & Mitsudomi, T. Not all epidermal growth factor receptor mutations in lung cancer are created equal: Perspectives for individualized treatment strategy. *Cancer Sci* **107**, 1179-1186, doi:10.1111/cas.12996 (2016).

56 Piotrowska, Z., Fintelmann, F. J., Sequist, L. V. & Jahagirdar, B. Response to Osimertinib in an EGFR Exon 20 Insertion-Positive Lung Adenocarcinoma. *J Thorac Oncol* **13**, e204-e206, doi:10.1016/j.jtho.2018.05.017 (2018).

57 Piotrowska, Z., Wang, Y., Sequist, L. V. & Ramalingam, S. S. ECOG-ACRIN 5162: A phase II study of osimertinib 160 mg in NSCLC with EGFR exon 20 insertions. *Journal of Clinical Oncology* **38**, 9513-9513, doi:10.1200/JCO.2020.38.15_suppl.9513 (2020).

58 Riess, J. *et al.* Antitumor activity of osimertinib in NSCLC harboring EGFR exon 20 insertions. *Journal of Clinical Oncology* **35**, 9030-9030, doi:10.1200/JCO.2017.35.15_suppl.9030 (2017).

59 van Veggel, B. *et al.* Osimertinib treatment for patients with EGFR exon 20 mutation positive non-small cell lung cancer. *Lung Cancer* **141**, 9-13, doi:10.1016/j.lungcan.2019.12.013 (2020).

60 Robichaux, J. P. *et al.* Mechanisms and clinical activity of an EGFR and HER2 exon 20-selective kinase inhibitor in non-small cell lung cancer. *Nat Med* **24**, 638-646, doi:10.1038/s41591-018-0007-9 (2018).

61 Le, X. *et al.* Poziotinib shows activity and durability of responses in subgroups of previously treated EGFR exon 20 NSCLC patients. *Journal of Clinical Oncology* **38**, 9514-9514, doi:10.1200/JCO.2020.38.15_suppl.9514 (2020).

62 Prelaj, A. *et al.* 1388P Poziotinib in advanced NSCLC with EGFR or HER2 exon 20 insertion mutation: Initial results from a single site expanded access program. *Annals of Oncology* **31**, doi:10.1016/j.annonc.2020.08.1702 (2020).

63 Imran, M. *et al.* Discovery, Development, Inventions, and Patent Trends on Mobocertinib Succinate: The First-in-Class Oral Treatment for NSCLC with EGFR Exon 20 Insertions. *Biomedicines* **9**, doi:10.3390/biomedicines9121938 (2021).

64 Hou, J. *et al.* EGFR exon 20 insertion mutations in advanced non-small-cell lung cancer: current status and perspectives. *Biomark Res* **10**, 21, doi:10.1186/s40364-022-00372-6 (2022).

65 Park, K. *et al.* Amivantamab (JNJ-61186372), an anti-EGFR-MET bispecific antibody, in patients with EGFR exon 20 insertion (exon20ins)-mutated non-small cell lung cancer (NSCLC). *Journal of Clinical Oncology* **38**, 9512-9512, doi:10.1200/JCO.2020.38.15_suppl.9512 (2020).

66 Yun, J. *et al.* Antitumor Activity of Amivantamab (JNJ-61186372), an EGFR-MET Bispecific Antibody, in Diverse Models of EGFR Exon 20 Insertion-Driven NSCLC. *Cancer Discov* **10**, 1194-1209, doi:10.1158/2159-8290.CD-20-0116 (2020).

67 Vasan, N., Baselga, J. & Hyman, D. M. A view on drug resistance in cancer. *Nature* **575**, 299-309, doi:10.1038/s41586-019-1730-1 (2019).

68 Cross, D. A. *et al.* AZD9291, an irreversible EGFR TKI, overcomes T790M-mediated resistance to EGFR inhibitors in lung cancer. *Cancer Discov* **4**, 1046-1061, doi:10.1158/2159-8290.CD-14-0337 (2014).

69 Passaro, A., Janne, P. A., Mok, T. & Peters, S. Overcoming therapy resistance in EGFR-mutant lung cancer. *Nat Cancer* **2**, 377-391, doi:10.1038/s43018-021-00195-8 (2021).

70 Sequist, L. V. *et al.* Genotypic and histological evolution of lung cancers acquiring resistance to EGFR inhibitors. *Sci Transl Med* **3**, 75ra26, doi:10.1126/scitranslmed.3002003 (2011).

71 Papadimitrakopoulou, V. A. *et al.* Analysis of resistance mechanisms to osimertinib in patients with EGFR T790M advanced NSCLC from the AURA3 study. *Annals of Oncology* **29**, doi:10.1093/annonc/mdy424.064 (2018).

72 Ramalingam, S. S. *et al.* Mechanisms of acquired resistance to first-line osimertinib: Preliminary data from the phase III FLAURA study. *Annals of Oncology* **29**, doi:10.1093/annonc/mdy424.063 (2018).

73 Tumbrink, H. L., Heimsoeth, A. & Sos, M. L. The next tier of EGFR resistance mutations in lung cancer. *Oncogene* **40**, 1-11, doi:10.1038/s41388-020-01510-w (2021).

74 Pao, W. *et al.* Acquired resistance of lung adenocarcinomas to gefitinib or erlotinib is associated with a second mutation in the EGFR kinase domain. *PLoS Med* **2**, e73, doi:10.1371/journal.pmed.0020073 (2005).

75 Ortiz-Cuaran, S. *et al.* Heterogeneous Mechanisms of Primary and Acquired Resistance to Third-Generation EGFR Inhibitors. *Clin Cancer Res* **22**, 4837-4847, doi:10.1158/1078-0432.CCR-15-1915 (2016).

76 Niederst, M. J. *et al.* The Allelic Context of the C797S Mutation Acquired upon Treatment with Third-Generation EGFR Inhibitors Impacts Sensitivity to Subsequent Treatment Strategies. *Clin Cancer Res* **21**, 3924-3933, doi:10.1158/1078-0432.CCR-15-0560 (2015).

77 Thress, K. S. *et al.* Acquired EGFR C797S mutation mediates resistance to AZD9291 in non-small cell lung cancer harboring EGFR T790M. *Nat Med* **21**, 560-562, doi:10.1038/nm.3854 (2015).

78 Brown, B. P. *et al.* On-target Resistance to the Mutant-Selective EGFR Inhibitor Osimertinib Can Develop in an Allele-Specific Manner Dependent on the Original EGFR-Activating Mutation. *Clin Cancer Res* **25**, 3341-3351, doi:10.1158/1078-0432.CCR-18-3829 (2019).

79 Fassunke, J. *et al.* Overcoming EGFR(G724S)-mediated osimertinib resistance through unique binding characteristics of second-generation EGFR inhibitors. *Nat Commun* **9**, 4655, doi:10.1038/s41467-018-07078-0 (2018).

80 Oztan, A. *et al.* Emergence of EGFR G724S mutation in EGFR-mutant lung adenocarcinoma post progression on osimertinib. *Lung Cancer* **111**, 84-87, doi:10.1016/j.lungcan.2017.07.002 (2017).

81 Zhang, Y., He, B., Zhou, D., Li, M. & Hu, C. Newly emergent acquired EGFR exon 18 G724S mutation after resistance of a T790M specific EGFR inhibitor osimertinib in non-small-cell lung cancer: a case report. *Onco Targets Ther* **12**, 51-56, doi:10.2147/OTT.S188612 (2019).

82 Yang, Z. *et al.* Investigating Novel Resistance Mechanisms to Third-Generation EGFR Tyrosine Kinase Inhibitor Osimertinib in Non-Small Cell Lung Cancer Patients. *Clin Cancer Res* **24**, 3097-3107, doi:10.1158/1078-0432.CCR-17-2310 (2018).

83 Ou, S. I. *et al.* Emergence of novel and dominant acquired EGFR solvent-front mutations at Gly796 (G796S/R) together with C797S/R and L792F/H mutations in one EGFR (L858R/T790M) NSCLC patient who progressed on osimertinib. *Lung Cancer* **108**, 228-231, doi:10.1016/j.lungcan.2017.04.003 (2017).

84 Zheng, D. *et al.* EGFR G796D mutation mediates resistance to osimertinib. *Oncotarget* **8**, 49671-49679, doi:10.18632/oncotarget.17913 (2017).

85 Chabon, J. J. *et al.* Circulating tumour DNA profiling reveals heterogeneity of EGFR inhibitor resistance mechanisms in lung cancer patients. *Nat Commun* **7**, 11815, doi:10.1038/ncomms11815 (2016).

86 Nukaga, S. *et al.* Amplification of EGFR Wild-Type Alleles in Non-Small Cell Lung Cancer Cells Confers Acquired Resistance to Mutation-Selective EGFR Tyrosine Kinase Inhibitors. *Cancer Res* **77**, 2078-2089, doi:10.1158/0008-5472.CAN-16-2359 (2017).

87 Engelman, J. A. *et al.* MET amplification leads to gefitinib resistance in lung cancer by activating ERBB3 signaling. *Science* **316**, 1039-1043, doi:10.1126/science.1141478 (2007).

88 Takezawa, K. *et al.* HER2 amplification: a potential mechanism of acquired resistance to EGFR inhibition in EGFR-mutant lung cancers that lack the second-site EGFRT790M mutation. *Cancer Discov* **2**, 922-933, doi:10.1158/2159-8290.CD-12-0108 (2012).

89 Offin, M. *et al.* Concurrent RB1 and TP53 Alterations Define a Subset of EGFR-Mutant Lung Cancers at risk for Histologic Transformation and Inferior Clinical Outcomes. *J Thorac Oncol* **14**, 1784-1793, doi:10.1016/j.jtho.2019.06.002 (2019).

90 Izumi, H. *et al.* Squamous Cell Carcinoma Transformation from EGFR-mutated Lung Adenocarcinoma: A Case Report and Literature Review. *Clin Lung Cancer* **19**, e63-e66, doi:10.1016/j.cllc.2017.10.005 (2018).

91 Hakozaki, T., Kitazono, M., Takamori, M. & Kiriu, T. Combined Small and Squamous Transformation in EGFR-mutated Lung Adenocarcinoma. *Intern Med* **59**, 1291-1294, doi:10.2169/internalmedicine.3542-19 (2020).

92 Schoenfeld, A. J. *et al.* Tumor Analyses Reveal Squamous Transformation and Off-Target Alterations As Early Resistance Mechanisms to First-line Osimertinib in EGFR-Mutant Lung Cancer. *Clin Cancer Res* **26**, 2654-2663, doi:10.1158/1078-0432.CCR-19-3563 (2020).

93 Horn, L. *et al.* First-Line Atezolizumab plus Chemotherapy in Extensive-Stage Small-Cell Lung Cancer. *N Engl J Med* **379**, 2220-2229, doi:10.1056/NEJMoa1809064 (2018).

94 Paz-Ares, L. *et al.* Durvalumab plus platinum–etoposide versus platinum–etoposide in first-line treatment of extensive-stage small-cell lung cancer (CASPIAN): a randomised, controlled, open-label, phase 3 trial. *The Lancet* **394**, 1929-1939, doi:10.1016/s0140-6736(19)32222-6 (2019).

95 Abughanimeh, O., Ernani, V., Marr, A. & Ganti, A. K. Current updates in management of relapsed/refractory small cell lung cancer. *Journal of Cancer Metastasis and Treatment* **2020**, doi:10.20517/2394-4722.2020.110 (2020).

96 Gardner, E. E. *et al.* Chemosensitive Relapse in Small Cell Lung Cancer Proceeds through an EZH2-SLFN11 Axis. *Cancer Cell* **31**, 286-299, doi:10.1016/j.ccell.2017.01.006 (2017).

97 Grunblatt, E. *et al.* MYCN drives chemoresistance in small cell lung cancer while USP7 inhibition can restore chemosensitivity. *Genes Dev* **34**, 1210-1226, doi:10.1101/gad.340133.120 (2020).

98 Rudin, C. M., Brambilla, E., Faivre-Finn, C. & Sage, J. Small-cell lung cancer. *Nat Rev Dis Primers* **7**, 3, doi:10.1038/s41572-020-00235-0 (2021).

99 George, J. *et al.* Comprehensive genomic profiles of small cell lung cancer. *Nature* **524**, 47-53, doi:10.1038/nature14664 (2015).

100 Rudin, C. M. *et al.* Molecular subtypes of small cell lung cancer: a synthesis of human and mouse model data. *Nature Reviews Cancer* **19**, 289-297, doi:10.1038/s41568-019-0133-9 (2019).

101 Dammert, M. A. *et al.* MYC paralog-dependent apoptotic priming orchestrates a spectrum of vulnerabilities in small cell lung cancer. *Nat Commun* **10**, 3485, doi:10.1038/s41467-019-11371-x (2019).

102 Mollaoglu, G. *et al.* MYC Drives Progression of Small Cell Lung Cancer to a Variant Neuroendocrine Subtype with Vulnerability to Aurora Kinase Inhibition. *Cancer Cell* **31**, 270-285, doi:10.1016/j.ccell.2016.12.005 (2017).

103 Dhanasekaran, R. *et al.* The MYC oncogene - the grand orchestrator of cancer growth and immune evasion. *Nat Rev Clin Oncol* **19**, 23-36, doi:10.1038/s41571-021-00549-2 (2022).

104 Casey, S. C., Baylot, V. & Felsher, D. W. The MYC oncogene is a global regulator of the immune response. *Blood* **131**, 2007-2015, doi:10.1182/blood-2017-11-742577 (2018).

105 Zimmerli, D. *et al.* MYC promotes immune-suppression in triple-negative breast cancer via inhibition of interferon signaling. *Nat Commun* **13**, 6579, doi:10.1038/s41467-022-34000-6 (2022).

106 Wolf, E. & Eilers, M. Targeting MYC Proteins for Tumor Therapy. *Annual Review of Cancer Biology* **4**, 61-75, doi:10.1146/annurev-cancerbio-030518-055826 (2020).

107 Kalkat, M. *et al.* MYC Deregulation in Primary Human Cancers. *Genes (Basel)* **8**, doi:10.3390/genes8060151 (2017).

108 Wang, C. *et al.* Alternative approaches to target Myc for cancer treatment. *Signal Transduct Target Ther* **6**, 117, doi:10.1038/s41392-021-00500-y (2021).

109 Carabet, L. A., Rennie, P. S. & Cherkasov, A. Therapeutic Inhibition of Myc in Cancer. Structural Bases and Computer-Aided Drug Discovery Approaches. *Int J Mol Sci* **20**, doi:10.3390/ijms20010120 (2018).

110 Masso-Valles, D. & Soucek, L. Blocking Myc to Treat Cancer: Reflecting on Two Decades of Omomyc. *Cells* **9**, doi:10.3390/cells9040883 (2020).

111 Beaulieu, M. E., Castillo, F. & Soucek, L. Structural and Biophysical Insights into the Function of the Intrinsically Disordered Myc Oncoprotein. *Cells* **9**, doi:10.3390/cells9041038 (2020).

112 Sears, R. *et al.* Multiple Ras-dependent phosphorylation pathways regulate Myc protein stability. *Genes Dev* **14**, 2501-2514, doi:10.1101/gad.836800 (2000).

113 Feng, X.-H., Liang, Y.-Y., Liang, M., Zhai, W. & Lin, X. Direct Interaction of c-Myc with Smad2 and Smad3 to Inhibit TGF-β-Mediated Induction of the CDK Inhibitor p15Ink4B. *Molecular Cell* **9**, 133-143, doi:10.1016/s1097-2765(01)00430-0 (2002).

114 Staller, P. *et al.* Repression of p15INK4b expression by Myc through association with Miz-1. *Nat Cell Biol* **3**, 392-399, doi:10.1038/35070076 (2001).

115 Blackwood, E. M. & Eisenman, R. N. Max: a helix-loop-helix zipper protein that forms a sequence-specific DNA-binding complex with Myc. *Science* **251**, 1211-1217, doi:10.1126/science.2006410 (1991).

116 Peukert, K. *et al.* An alternative pathway for gene regulation by Myc. *EMBO J* **16**, 5672-5686, doi:10.1093/emboj/16.18.5672 (1997).

117 Conacci-Sorrell, M., McFerrin, L. & Eisenman, R. N. An overview of MYC and its interactome. *Cold Spring Harb Perspect Med* **4**, a014357, doi:10.1101/cshperspect.a014357 (2014).

118 Kosan, C. *et al.* Transcription factor miz-1 is required to regulate interleukin-7 receptor signaling at early commitment stages of B cell differentiation. *Immunity* **33**, 917-928, doi:10.1016/j.immuni.2010.11.028 (2010).

119 Ross, J. *et al.* Deletion of the Miz-1 POZ Domain Increases Efficacy of Cytarabine Treatment in T- and B-ALL/Lymphoma Mouse Models. *Cancer Res* **79**, 4184-4195, doi:10.1158/0008-5472.CAN-18-3038 (2019).

120 Wolf, E. *et al.* Miz1 is required to maintain autophagic flux. *Nat Commun* **4**, 2535, doi:10.1038/ncomms3535 (2013).

121 Capelluto, D. G. *et al.* The DIX domain targets dishevelled to actin stress fibres and vesicular membranes. *Nature* **419**, 726-729, doi:10.1038/nature01056 (2002).

122 Wanzel, M. *et al.* A ribosomal protein L23-nucleophosmin circuit coordinates Mizl function with cell growth. *Nat Cell Biol* **10**, 1051-1061, doi:10.1038/ncb1764 (2008).

123 van Riggelen, J. *et al.* The interaction between Myc and Miz1 is required to antagonize TGFbeta-dependent autocrine signaling during lymphoma formation and maintenance. *Genes Dev* **24**, 1281-1294, doi:10.1101/gad.585710 (2010).

124 Wiese, K. E. *et al.* The role of MIZ-1 in MYC-dependent tumorigenesis. *Cold Spring Harb Perspect Med* **3**, a014290, doi:10.1101/cshperspect.a014290 (2013).

125 Vo, B. T. *et al.* The Interaction of Myc with Miz1 Defines Medulloblastoma Subgroup Identity. *Cancer Cell* **29**, 5-16, doi:10.1016/j.ccell.2015.12.003 (2016).

126 Adhikary, S. *et al.* Miz1 is required for early embryonic development during gastrulation. *Mol Cell Biol* **23**, 7648-7657, doi:10.1128/MCB.23.21.7648-7657.2003 (2003).

127 Gebhardt, A. *et al.* Miz1 is required for hair follicle structure and hair morphogenesis. *J Cell Sci* **120**, 2586-2593, doi:10.1242/jcs.007104 (2007).

128 Gebhardt, A. *et al.* Myc regulates keratinocyte adhesion and differentiation via complex formation with Miz1. *J Cell Biol* **172**, 139-149, doi:10.1083/jcb.200506057 (2006).

129 Saba, I., Kosan, C., Vassen, L. & Moroy, T. IL-7R-dependent survival and differentiation of early T-lineage progenitors is regulated by the BTB/POZ domain transcription factor Miz-1. *Blood* **117**, 3370-3381, doi:10.1182/blood-2010-09-310680 (2011).

130 Honnemann, J., Sanz-Moreno, A., Wolf, E., Eilers, M. & Elsasser, H. P. Miz1 is a critical repressor of cdkn1a during skin tumorigenesis. *PLoS One* **7**, e34885, doi:10.1371/journal.pone.0034885 (2012).

131 Moroy, T., Saba, I. & Kosan, C. The role of the transcription factor Miz-1 in lymphocyte development and lymphomagenesis-Binding Myc makes the difference. *Semin Immunol* **23**, 379-387, doi:10.1016/j.smim.2011.09.001 (2011).

132 Walz, S. *et al.* Activation and repression by oncogenic MYC shape tumour-specific gene expression profiles. *Nature* **511**, 483-487, doi:10.1038/nature13473 (2014).

133 Bray, F. *et al.* Global cancer statistics 2018: GLOBOCAN estimates of incidence and mortality worldwide for 36 cancers in 185 countries. *CA Cancer J Clin* **68**, 394-424, doi:10.3322/caac.21492 (2018).

134 Sos, M. L. *et al.* A framework for identification of actionable cancer genome dependencies in small cell lung cancer. *Proc Natl Acad Sci U S A* **109**, 17034-17039, doi:10.1073/pnas.1207310109 (2012).

135 Bragelmann, J. *et al.* Family matters: How MYC family oncogenes impact small cell lung cancer. *Cell Cycle* **16**, 1489-1498, doi:10.1080/15384101.2017.1339849 (2017).

136 Llombart, V. & Mansour, M. R. Therapeutic targeting of "undruggable" MYC. *EBioMedicine* **75**, 103756, doi:10.1016/j.ebiom.2021.103756 (2022).

137 Bedard, M., Roy, V., Montagne, M. & Lavigne, P. Structural Insights into c-Myc-interacting Zinc Finger Protein-1 (Miz-1) Delineate Domains Required for DNA Scanning and Sequence-specific Binding. *J Biol Chem* **292**, 3323-3340, doi:10.1074/jbc.M116.748699 (2017).

138 Sutherland, K. D. *et al.* Cell of origin of small cell lung cancer: inactivation of Trp53 and Rb1 in distinct cell types of adult mouse lung. *Cancer Cell* **19**, 754-764, doi:10.1016/j.ccr.2011.04.019 (2011).

139 Meuwissen, R. *et al.* Induction of small cell lung cancer by somatic inactivation of both Trp53 and Rb1 in a conditional mouse model. *Cancer Cell* **4**, 181-189, doi:Doi 10.1016/S1535-6108(03)00220-4 (2003).

140 Cardnell, R. J. *et al.* Protein expression of TTF1 and cMYC define distinct molecular subgroups of small cell lung cancer with unique vulnerabilities to aurora kinase inhibition, DLL3 targeting, and other targeted therapies. *Oncotarget* **8**, 73419-73432, doi:10.18632/oncotarget.20621 (2017).

141 Calles, A., Aguado, G., Sandoval, C. & Alvarez, R. The role of immunotherapy in small cell lung cancer. *Clin Transl Oncol* **21**, 961-976, doi:10.1007/s12094-018-02011-9 (2019).

142 Liberzon, A. *et al.* The Molecular Signatures Database (MSigDB) hallmark gene set collection. *Cell Syst* **1**, 417-425, doi:10.1016/j.cels.2015.12.004 (2015).

143 Sen, T. *et al.* Targeting DNA Damage Response Promotes Antitumor Immunity through STING-Mediated T-cell Activation in Small Cell Lung Cancer. *Cancer Discov* **9**, 646-661, doi:10.1158/2159-8290.CD-18-1020 (2019).

144 Sen, T. *et al.* CHK1 Inhibition in Small-Cell Lung Cancer Produces Single-Agent Activity in Biomarker-Defined Disease Subsets and Combination Activity with Cisplatin or Olaparib. *Cancer Res* **77**, 3870-3884, doi:10.1158/0008-5472.CAN-16-3409 (2017).

145 Christensen, C. L. *et al.* Targeting transcriptional addictions in small cell lung cancer with a covalent CDK7 inhibitor. *Cancer Cell* **26**, 909-922, doi:10.1016/j.ccell.2014.10.019 (2014).

146 Farago, A. F. *et al.* Combination Olaparib and Temozolomide in Relapsed Small-Cell Lung Cancer. *Cancer Discov* **9**, 1372-1387, doi:10.1158/2159-8290.CD-19-0582 (2019).

147 Chan, C. H. *et al.* Deciphering the transcriptional complex critical for RhoA gene expression and cancer metastasis. *Nat Cell Biol* **12**, 457-467, doi:10.1038/ncb2047 (2010).

148 Roos, W. P., Thomas, A. D. & Kaina, B. DNA damage and the balance between survival and death in cancer biology. *Nat Rev Cancer* **16**, 20-33, doi:10.1038/nrc.2015.2 (2016).

149 Herold, S. *et al.* Negative regulation of the mammalian UV response by Myc through association with Miz-1. *Mol Cell* **10**, 509-521, doi:10.1016/s1097-2765(02)00633-0 (2002).

150 Kartika, I. D. *et al.* Protective role of cytoplasmic p21Cip1/Waf1 in apoptosis of CDK4/6 inhibitor-induced senescence in breast cancer cells. *Cancer Med* **10**, 8988-8999, doi:10.1002/cam4.4410 (2021).

151 Rodriguez, R. & Meuth, M. Chk1 and p21 cooperate to prevent apoptosis during DNA replication fork stress. *Mol Biol Cell* **17**, 402-412, doi:10.1091/mbc.e05-07-0594 (2006).

152 Cerchietti, L. C. *et al.* A small-molecule inhibitor of BCL6 kills DLBCL cells in vitro and in vivo. *Cancer Cell* **17**, 400-411, doi:10.1016/j.ccr.2009.12.050 (2010).

153 Puccetti, E. *et al.* The integrity of the charged pocket in the BTB/POZ domain is essential for the phenotype induced by the leukemia-associated t(11;17) fusion protein PLZF/RARalpha. *Cancer Res* **65**, 6080-6088, doi:10.1158/0008-5472.CAN-04-3631 (2005).

154 Stogios, P. J., Downs, G. S., Jauhal, J. J., Nandra, S. K. & Prive, G. G. Sequence and structural analysis of BTB domain proteins. *Genome Biol* **6**, R82, doi:10.1186/gb-2005-6-10-r82 (2005).

155 Orth, B. *et al.* Identification of an atypical interaction site in the BTB domain of the MYC-interacting zinc-finger protein 1. *Structure* **29**, 1230-1240 e1235, doi:10.1016/j.str.2021.06.005 (2021).

156 Bragelmann, J. *et al.* Systematic Kinase Inhibitor Profiling Identifies CDK9 as a Synthetic Lethal Target in NUT Midline Carcinoma. *Cell Rep* **20**, 2833-2845, doi:10.1016/j.celrep.2017.08.082 (2017).

157 Dobin, A. *et al.* STAR: ultrafast universal RNA-seq aligner. *Bioinformatics* **29**, 15-21, doi:10.1093/bioinformatics/bts635 (2013).

158 Li, B. & Dewey, C. N. RSEM: accurate transcript quantification from RNA-Seq data with or without a reference genome. *BMC Bioinformatics* **12**, 323, doi:10.1186/1471-2105-12-323 (2011).

159 Love, M. I., Huber, W. & Anders, S. Moderated estimation of fold change and dispersion for RNA-seq data with DESeq2. *Genome Biol* **15**, 550, doi:10.1186/s13059-014-0550-8 (2014).

160 Stuart, T. *et al.* Comprehensive Integration of Single-Cell Data. *Cell* **177**, 1888-1902 e1821, doi:10.1016/j.cell.2019.05.031 (2019).

161 Zhang, W. & Dong, X. Positive progress for non-small cell lung cancer with epidermal growth factor receptor exon 20 insertion mutations: A novel targeted therapy option. *J Oncol Pharm Pract* **27**, 2007-2009, doi:10.1177/10781552211044980 (2021).

162 Cho, B. C. *et al.* Amivantamab, an epidermal growth factor receptor (EGFR) and mesenchymal-epithelial transition factor (MET) bispecific antibody, designed to enable

multiple mechanisms of action and broad clinical applications. *Clinical Lung Cancer*, doi:10.1016/j.cllc.2022.11.004 (2022).

163 Brazel, D., Kroening, G. & Nagasaka, M. Non-small Cell Lung Cancer with EGFR or HER2 Exon 20 Insertion Mutations: Diagnosis and Treatment Options. *BioDrugs*, doi:10.1007/s40259-022-00556-4 (2022).

164 Unni, A. M., Lockwood, W. W., Zejnullahu, K., Lee-Lin, S. Q. & Varmus, H. Evidence that synthetic lethality underlies the mutual exclusivity of oncogenic KRAS and EGFR mutations in lung adenocarcinoma. *Elife* **4**, e06907, doi:10.7554/eLife.06907 (2015).

165 Lin, L. *et al.* Mapping the molecular determinants of BRAF oncogene dependence in human lung cancer. *Proc Natl Acad Sci U S A* **111**, E748-757, doi:10.1073/pnas.1320956111 (2014).

166 Schaufler, D. *et al.* Clonal dynamics of BRAF-driven drug resistance in EGFR-mutant lung cancer. *NPJ Precis Oncol* **5**, 102, doi:10.1038/s41698-021-00241-9 (2021).

Appendix

Supplement: Insight Into Targeting Exon20 Insertion Mutations of Epidermal Growth Factor Receptor with Wild Type-Sparing Inhibitors

Table S1. *In vitro* pharmacokinetic parameters.

	LDC8201	**LDC0496**	**osimertinib**
SolRank [µM]	49	2	281
Cl$_{int}$ [µL·min^{-1}·mg^{-1}]	13 / 62 / 93[a]	1 / 38 / 21[a]	4 / n.d. / 81[a]
Microsomal Stability Phase II [% Remain]	75 / 95 / 84[a]	100 / 100 / 85[a]	100 / n.d. / 99[a]
Plasma Stability [% Remain]	75 / 95 / 84[a]	91 / 86 / 100[a]	78 / n.d. / 75[a]
Hepatocyte Cl$_{int}$ [µL·min^{-1}·10^{6} cells]	17 / 22 / 85[a]	13 / 1 / 12[a]	n.d. / n.d. / n.d.[a]
PPB [%]	98.0 / 97.6 / 99.5[a]	98.1 / 99.8 / 99.5[a]	97.1 / n.d. / 97.6[a]
PAMPA [%]	34	n.d.	88
Caco-2 P$_{app}$ [10^{-6} cm·s^{-1}] A–B / B–A	5.1 / 15.0	0.2 / 0.7	5.0 / 6.8
Chemical Stability [% Remain 24 h] pH=9 / pH=7.4 / pH=1	90 / 95 / 100	96 / 100 / 100	n.d.
GSH Reactivity [% Remain 120 h]	44	n.d.	n.d.
hPBMCs CTG IC$_{50}$ [nM]	2895	5365	7250
HepTox HepG2 IC$_{50}$ [nM]	1925	2420	2120
MitoTox Glu IC$_{50}$ [nM]	1925	2420	2120
MitoTox Gal IC$_{50}$ [nM]	2570	1670	3390

hERG IC$_{50}$ [nM] Predictor Assay / Patch Clamp	755 / 4950	1810 / n.d.	2260 / n.d.
CYP inhibition IC$_{50}$ [nM]			
3A4	25700	n.d.	n.d.
2D6	>50000		
2C9	19180		
2C19	32500		
1A2	>50000		

[a]human / rat / mouse; n.d. = not determined; PPB = plasma protein binding; PAMPA = parallel artificial membrane permeability assay.

Table S2. *In vivo* pharmacokinetic parameters following intraperitoneal (IP), and oral (PO) administration in mice.

Cpd	**Route (dose)**	**$t_{1/2}$** [min]	**C_{max}** [µM]	**$AUC_{0\text{-}inf,obs}$** [$h \cdot ng \cdot mL^{-1}$]	**F** [%]
LDC9305	IP (3 mg/kg)	54	0.27	80	52
	PO (10 mg/kg)	64	0.09	66	13
LDC8320	IP (10 mg/kg)	49	1.41	778	110
	PO (10 mg/kg)	492	0.02	97	14
LDC8201	IP (10 mg/kg)	40	2.62	1319	112
	PO (30 mg/kg)	126	1.91	2081	59
	PO (60 mg/kg)	677	1.23	3817	54
	PO (90 mg/kg)	138	4.13	7147	67

Table S3. Kinome profiling of LDC8201 and LDC0496 at a concentration of 100 nM against 468 kinases including 403 non-mutant kinases.[a]

Target kinase	**%Ctrl @ 100 nM**	
	LDC8201	**LDC0496**
Selectivity Score S(35), Hits:	44 (11%)	12 (3%)
Selectivity Score S(10), Hits:	23 (6%)	5 (1%)
Selectivity Score S(1), Hits:	10 (3%)	1 (0.2%)
BTK	0	5.9
EGFR(L747-E749del,A750P)	0	2.1
ERBB2	0	3.7
ERBB4	0	3.7
FLT3(N841I)	0	45
JAK3(JH1domain-catalytic)	0	0
STK16	0.1	67
EGFR(L861Q)	0.15	2.3
VPS34	0.25	100
BLK	0.3	6.6
EGFR(T790M)	0.35	3.9
ITK	0.4	30
EGFR(L747-T751del,Sins)	0.45	0.15
CLK1	0.95	99
CLK4	0.95	100
EGFR(L858R)	1.1	4.1
IRAK1	1.1	82
IRAK3	1.3	91
EPHB6	1.5	100
JNK1	1.6	99
TEC	2	31
TXK	2.8	15
EGFR(L858R,T790M)	2.9	6.1
ABL1(H396P)-nonphosphorylated	3.2	100
PIKFYVE	3.4	52
EGFR	3.7	12
ALK	4.6	100
DDR1	4.6	89
EGFR(S752-I759del)	5.3	6.5
CSF1R-autoinhibited	6.7	96

Target kinase	**%Ctrl @ 100 nM**	
	LDC8201	**LDC0496**
ABL1(Q252H)-nonphosphorylated	7.1	94
EGFR(E746-A750del)	7.7	3.5
JNK3	7.9	93
ABL1(T315I)-phosphorylated	8.9	96
EGFR(L747-S752del,P753S)	9.2	3.5
SYK	9.7	100
ABL1(M351T)-phosphorylated	10	92
DLK	10	84
ABL1(Y253F)-phosphorylated	11	100
STK33	11	97
TRKA	11	71
ABL1(H396P)-phosphorylated	12	81
ABL1-phosphorylated	12	56
EGFR(G719S)	12	39
FLT3	12	27
JAK2(JH1domain-catalytic)	12	94
SRC	12	88
FLT3(ITD,D835V)	13	100
ABL1(F317L)-phosphorylated	14	100
ABL1(Q252H)-phosphorylated	14	100
ABL1-nonphosphorylated	14	89
ABL1(E255K)-phosphorylated	15	87
FLT3(ITD)	17	63
PYK2	17	100
ALK(L1196M)	19	97
EGFR(G719C)	20	63
FLT3(D835Y)	20	89
JNK2	20	89
LTK	20	100
ABL1(T315I)-nonphosphorylated	21	100
AURKA	21	100
BMX	22	14
HPK1	22	73
ROS1	22	93
FLT3(D835H)	23	69

Target kinase	**%Ctrl @ 100 nM**	
	LDC8201	**LDC0496**
JAK1(JH2domain-pseudokinase)	23	100
MUSK	24	100
BMPR1B	25	100
EPHA1	26	100
FLT3(D835V)	27	28
S6K1	27	94
CSF1R	28	98
FLT3(K663Q)	28	34
ALK(C1156Y)	30	100
CLK2	30	100
FLT3(ITD,F691L)	33	64
FLT1	34	99
AXL	38	100
FAK	39	94
HIPK1	39	83
DDR2	40	100
INSR	40	96
RIOK2	40	99
IGF1R	41	98
FRK	43	98
RIPK1	43	91
TRKB	43	100
YSK4	43	65
PRKG1	44	67
RET(M918T)	46	86
SNARK	47	98
TTK	49	97
CAMKK2	50	100
LCK	50	97
MELK	50	95
ABL2	51	100
CAMKK1	52	100
TYK2(JH1domain-catalytic)	52	86
CDKL2	53	40
FGR	53	90

Target kinase	**%Ctrl @ 100 nM**	
	LDC8201	**LDC0496**
FLT3(R834Q)	53	84
RET	53	100
TGFBR2	54	100
VEGFR2	54	100
HASPIN	55	100
INSRR	55	100
MAP4K2	55	100
TAOK2	55	100
HIPK2	56	100
RET(V804L)	56	93
SIK	56	93
MERTK	57	88
SLK	57	97
ACVR1	58	95
PLK4	59	100
PFCDPK1(P,falciparum)	60	84
TBK1	60	96
ABL1(F317L)-nonphosphorylated	61	100
MARK4	61	99
p38-gamma	61	99
FLT3-autoinhibited	62	73
LZK	62	100
MEK4	62	100
PAK2	62	100
TAK1	63	94
CDK7	64	100
GRK2	64	95
PIM1	64	100
ABL1(F317I)-phosphorylated	65	100
PHKG1	65	77
SRMS	65	100
CASK	66	95
ERK4	66	100
MEK3	66	100
PIP5K2C	66	71

Target kinase	%Ctrl @ 100 nM	
	LDC8201	LDC0496
FER	67	86
NEK6	67	77
TRKC	67	100
AAK1	68	100
KIT-autoinhibited	68	100
PIK3CA(H1047Y)	68	100
RSK3(Kin,Dom,1-N-terminal)	68	100
ACVR1B	69	100
AURKB	69	91
CSNK2A2	69	99
GRK1	69	84
PFPK5(P,falciparum)	69	100
PIK3CA	69	100
PIK3CG	69	100
TGFBR1	69	100
ZAP70	69	93
MAP3K3	70	100
NIK	70	100
PAK4	70	99
CAMK1G	71	100
ERBB3	71	99
MLCK	71	88
PIK3C2G	71	100
SRPK1	71	100
IKK-alpha	72	99
ULK2	72	96
CSNK2A1	73	100
KIT(D816H)	73	95
KIT(L576P)	73	99
BMPR2	74	94
BUB1	74	100
LRRK2(G2019S)	74	100
PIP5K1C	74	82
TAOK1	74	100
QSK	75	64

Target kinase	**%Ctrl @ 100 nM**	
	LDC8201	**LDC0496**
RIPK4	75	100
ULK3	75	83
MYLK	76	100
PKNB(M,tuberculosis)	76	100
STK39	76	100
TAOK3	76	99
CDKL3	77	100
MEK5	77	100
MEK6	77	100
NEK1	77	95
PIK3CA(C420R)	77	100
PIK3CA(E545A)	77	100
PRKX	77	98
RET(V804M)	77	100
SGK2	77	100
AURKC	78	93
BMPR1A	78	100
MAP4K3	78	100
MET	78	87
NDR2	78	100
PHKG2	78	100
PIK3CA(E545K)	78	100
RSK2(Kin,Dom,1-N-terminal)	78	100
SGK	78	100
SgK110	78	59
BRAF(V600E)	79	97
FYN	79	98
GSK3A	79	95
HIPK3	79	100
PCTK1	79	94
PRKCI	79	98
STK35	79	100
YANK3	79	93
CSNK1A1	80	100
MAP4K5	80	100

Target kinase	**%Ctrl @ 100 nM**	
	LDC8201	**LDC0496**
MEK2	80	100
MET(M1250T)	80	100
MET(Y1235D)	80	100
p38-delta	80	92
PAK6	80	100
PIP5K1A	80	100
TNK1	80	65
WNK2	80	100
YES	80	91
ASK2	81	78
HCK	81	91
MAP3K1	81	90
NEK10	81	100
PAK7	81	100
PIK3C2B	81	100
PIK3CD	81	100
BRAF	82	100
CDKL1	82	89
DCAMKL1	82	100
DRAK1	82	92
FGFR1	82	100
GCN2(Kin,Dom,2,S808G)	82	99
KIT(V559D,T670I)	82	100
MARK1	82	100
NDR1	82	100
PDGFRA	82	76
PDGFRB	82	31
WNK3	82	100
BRK	83	100
CDK11	83	100
DYRK1A	83	83
MYLK2	83	98
RSK1(Kin,Dom,1-N-terminal)	83	100
TIE1	83	94
TYK2(JH2domain-pseudokinase)	83	79

Target kinase	%Ctrl @ 100 nM	
	LDC8201	LDC0496
BIKE	84	97
CSK	84	100
DAPK2	84	100
NEK4	84	93
PIM3	84	96
ROCK2	84	100
RSK2(Kin,Dom,2-C-terminal)	84	100
ULK1	84	100
GRK7	85	100
IKK-epsilon	85	100
MARK2	85	100
MINK	85	100
NEK3	85	92
PIK3CA(H1047L)	85	100
TIE2	85	100
BRSK2	86	100
CIT	86	92
DAPK3	86	100
DYRK2	86	66
MKK7	86	100
RSK1(Kin,Dom,2-C-terminal)	86	100
CAMK2B	87	100
EPHB4	87	93
KIT(D816V)	87	95
MKNK1	87	100
p38-alpha	87	92
PIK3CA(M1043I)	87	100
RAF1	87	100
RSK3(Kin,Dom,2-C-terminal)	87	100
TLK2	87	99
TNIK	87	100
TNK2	87	97
ERK3	88	91
LYN	88	100
p38-beta	88	99

Target kinase	**%Ctrl @ 100 nM**	
	LDC8201	**LDC0496**
PRKG2	88	100
TRPM6	88	100
CDK4	89	100
CDK4-cyclinD1	89	96
DRAK2	89	98
ERK8	89	100
IKK-beta	89	100
MYLK4	89	100
SGK3	89	100
AKT1	90	95
CHEK2	90	100
CSNK1G3	90	100
GSK3B	90	94
ICK	90	100
LIMK1	90	100
LKB1	90	75
CSNK1G2	91	99
EPHB2	91	100
KIT(V559D,V654A)	91	87
MAPKAPK5	91	100
MYO3A	91	99
NEK7	91	100
PLK3	91	100
RIPK5	91	100
RPS6KA4(Kin,Dom,2-C-terminal)	91	100
YSK1	91	96
ACVRL1	92	99
BRSK1	92	85
CSNK1D	92	100
ERK1	92	97
ERN1	92	100
KIT	92	98
LATS2	92	100
MAK	92	93
MEK1	92	100

Target kinase	**%Ctrl @ 100 nM**	
	LDC8201	**LDC0496**
PIK3CA(I800L)	92	100
PLK2	92	96
PRKCD	92	97
SNRK	92	100
STK36	92	100
VRK2	92	100
CAMK1	93	99
CAMK2A	93	100
CDC2L5	93	99
CDK2	93	100
FES	93	100
GRK4	93	86
MAP3K15	93	100
MLK2	93	100
MST1R	93	92
MST2	93	100
MTOR	93	55
NIM1	93	88
PIK4CB	93	100
SBK1	93	89
AMPK-alpha1	94	97
ARK5	94	100
CDC2L2	94	96
CSNK1A1L	94	100
DAPK1	94	100
DMPK2	94	90
EPHA3	94	100
EPHA4	94	98
EPHA6	94	96
EPHB1	94	96
EPHB3	94	92
ERK2	94	90
GAK	94	100
LIMK2	94	81
MST4	94	100

Target kinase	**%Ctrl @ 100 nM**	
	LDC8201	**LDC0496**
NEK11	94	100
PDPK1	94	100
YANK1	94	100
FLT4	95	97
IRAK4	95	100
MAP3K2	95	100
MKNK2	95	100
OSR1	95	100
PAK1	95	94
PFTK1	95	98
PRKD1	95	100
WNK1	95	100
CAMK1B	96	69
CAMK2G	96	100
CDK8	96	67
CLK3	96	99
CSNK1E	96	99
EPHA2	96	89
FGFR3	96	97
KIT(V559D)	96	94
PAK3	96	100
RPS6KA4(Kin,Dom,1-N-terminal)	96	76
RPS6KA5(Kin,Dom,2-C-terminal)	96	75
SRPK2	96	100
WEE1	96	79
WEE2	96	100
ANKK1	97	100
CHEK1	97	100
EPHA5	97	98
FGFR4	97	100
HIPK4	97	91
KIT(A829P)	97	100
LOK	97	92
MAP4K4	97	100
MAPKAPK2	97	100

Target kinase	**%Ctrl @ 100 nM**	
	LDC8201	**LDC0496**
MLK1	97	91
MST3	97	100
PKAC-alpha	97	100
PKMYT1	97	99
ROCK1	97	100
RPS6KA5(Kin,Dom,1-N-terminal)	97	99
RSK4(Kin,Dom,1-N-terminal)	97	100
ACVR2A	98	100
ADCK3	98	92
AKT2	98	93
CAMK4	98	99
MLK3	98	100
PIM2	98	100
PKN1	98	82
PRKR	98	98
SIK2	98	97
ABL1(F317I)-nonphosphorylated	99	100
AMPK-alpha2	99	99
CDK3	99	88
PCTK2	99	100
PKN2	99	68
PLK1	99	100
RSK4(Kin,Dom,2-C-terminal)	99	100
SRPK3	99	86
ACVR2B	100	91
ADCK4	100	91
AKT3	100	63
ASK1	100	92
CAMK1D	100	100
CAMK2D	100	100
CDC2L1	100	100
CDK4-cyclinD3	100	100
CDK5	100	98
CDK9	100	100
CDKL5	100	94

Target kinase	**%Ctrl @ 100 nM**	
	LDC8201	**LDC0496**
CSNK1G1	100	100
CTK	100	98
DCAMKL2	100	92
DCAMKL3	100	100
DMPK	100	75
DYRK1B	100	81
EIF2AK1	100	100
EPHA7	100	98
EPHA8	100	100
ERK5	100	100
FGFR2	100	93
FGFR3(G697C)	100	99
GRK3	100	77
HUNK	100	92
JAK1(JH1domain-catalytic)	100	100
LATS1	100	100
LRRK2	100	100
MAP3K4	100	100
MARK3	100	93
MAST1	100	94
MRCKA	100	71
MRCKB	100	100
MST1	100	96
MYO3B	100	92
NEK2	100	99
NEK5	100	89
NEK9	100	100
NLK	100	100
PCTK3	100	98
PFTAIRE2	100	100
PIK3CA(E542K)	100	100
PIK3CA(Q546K)	100	100
PIK3CB	100	97
PIP5K2B	100	100
PKAC-beta	100	65

Target kinase	**%Ctrl @ 100 nM**	
	LDC8201	**LDC0496**
PRKCE	100	54
PRKCH	100	100
PRKCQ	100	97
PRKD2	100	100
PRKD3	100	97
PRP4	100	100
RIOK1	100	91
RIOK3	100	94
RIPK2	100	88
TESK1	100	100
TLK1	100	100
TNNI3K	100	100
TSSK1B	100	90
TSSK3	100	98
TYRO3	100	96
WNK4	100	100
YANK2	100	100
ZAK	100	100

[a]Generated with the KINOMEscan™ Profiling Service from DiscoverX.

Table S4. Data collection and refinement statistics of complex crystal structures.[a]

	EGFR-T790M+V948R with LDC8201 PDB ID: 7A6I	**EGFR-T790M+V948R with TAK-788** PDB ID: 7A6K	**EGFR-wt with TAK-788** PDB ID: 7B85	**EGFR-T790M+V948R with poziotinib** PDB ID: 7A6J
Data collection				
Space group	I 2(1) 2(1) 2(1) (#24)	P 1 2(1) 1 (#4)	I 2 3 (#197)	P 2(1) 2(1) 2(1) (#19)
Cell dimensions				
a, b, c [Å]	68.76, 90.14, 107.71	74.95, 82.01, 89.68	144.28, 144.28, 144.28	76.33, 81.76, 89.85
α, β, γ [°]	90.0, 90.0, 90.0	90.0, 91.0, 90.0	90.0, 90.0, 90.0	90.0, 90.0, 90.0
Resolution [Å]	45.08—2.40 (2.50—2.40)	47.49—2.00 (2.10—2.00)	46.63—2.50 (2.60—2.50)	44.92—2.00 (2.10—2.00)
R_{meas} [%]	10.2 (116.1)	7.8 (96.1)	9.6 (163.6)	8.9 (144.1)
$I / \sigma I$	19.07 (2.29)	13.50 (2.20)	14.93 (2.01)	18.78 (1.80)
Completeness [%]	99.7 (99.8)	99.9 (100.0)	100.0 (99.9)	99.8 (99.9)
$CC_{1/2}$	99.9 (77.4)	99.9 (75.1)	99.8 (63.5)	99.9 (83.8)
Redundancy	12.48 (12.40)	6.81 (6.94)	10.34 (10.35)	13.06 (12.49)
Refinement				
Resolution [Å]	45.08—2.40	47.49—2.00	46.63—2.50	44.92—2.00
No. reflections	13417	74112	17435	38568
R_{work} / R_{free}	20.22 / 23.91 (28.26 / 32.26)	19.19 / 22.02 (30.74 / 31.35)	21.47 / 24.40 (30.68 / 32.63)	19.02 / 21.59 (28.57 / 33.23)
No. atoms				

Protein	2199	8114
		(chain A=2086;
		chain B=2026;
		chain C=2030;
		chain D=1972)
			2415	4189
				(chain A=2094;
				chain B=2095)

Ligand	35	43	43	66 chain A=33; chain B=33

	EGFR-T790M+V948R with LDC8201 PDB ID: 7A6I	**EGFR-T790M+V948R with TAK-788** PDB ID: 7A6K	**EGFR-wt with TAK-788** PDB ID: 7B85	**EGFR-T790M+V948R with poziotinib** PDB ID: 7A6J
Ion	20	35	-	20
Ligand 2 (EDO)	-	-	-	40
Ligand 3 (MES)	-	-	12	-
Water	21	137	6	142
B-factors				

Protein	58.19	51.82
		(chain A=49.19;
		chain B=50.08;
		chain C=50.19;
		chain D=57.81)
			82.61	48.73
				(chain A=45.99
				chain B=51.47)

Ligand	48.87	43.40
		(chain A=44.27;
		chain B=40.75;
		chain C=40.69;
		chain D=47.88)
			83.76	39.2
				(chain A=38.60;
				chain B=39.80)

Ion	112.49	71.23	-	55.58
Ligand 2 (EDO)	-	-	-	65.25
Ligand 3 (MES)	-	-	117.84	-
Water	56.22	46.65	86.24	46.80
R.m.s. deviations				
Bond lengths [Å]	0.003	0.002	0.002	0.005
Bond angles [°]	0.738	0.532	0.485	0.911

[a] Diffraction data from a single crystal was used to determine the complex structure. Values in parenthesis are referring to the highest resolution shell.

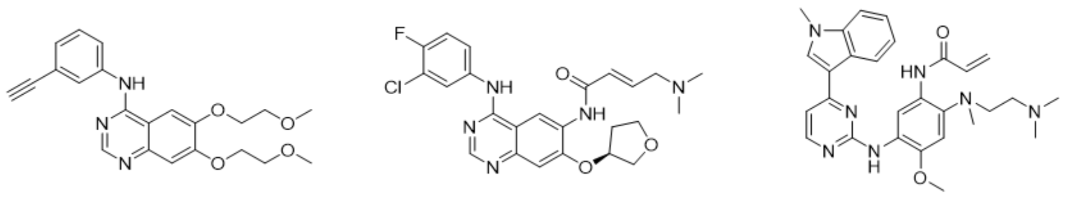

erlotinib **afatinib** **osimertinib**

Figure S1. Chemical structures of selected EGFR-targeted TKIs.

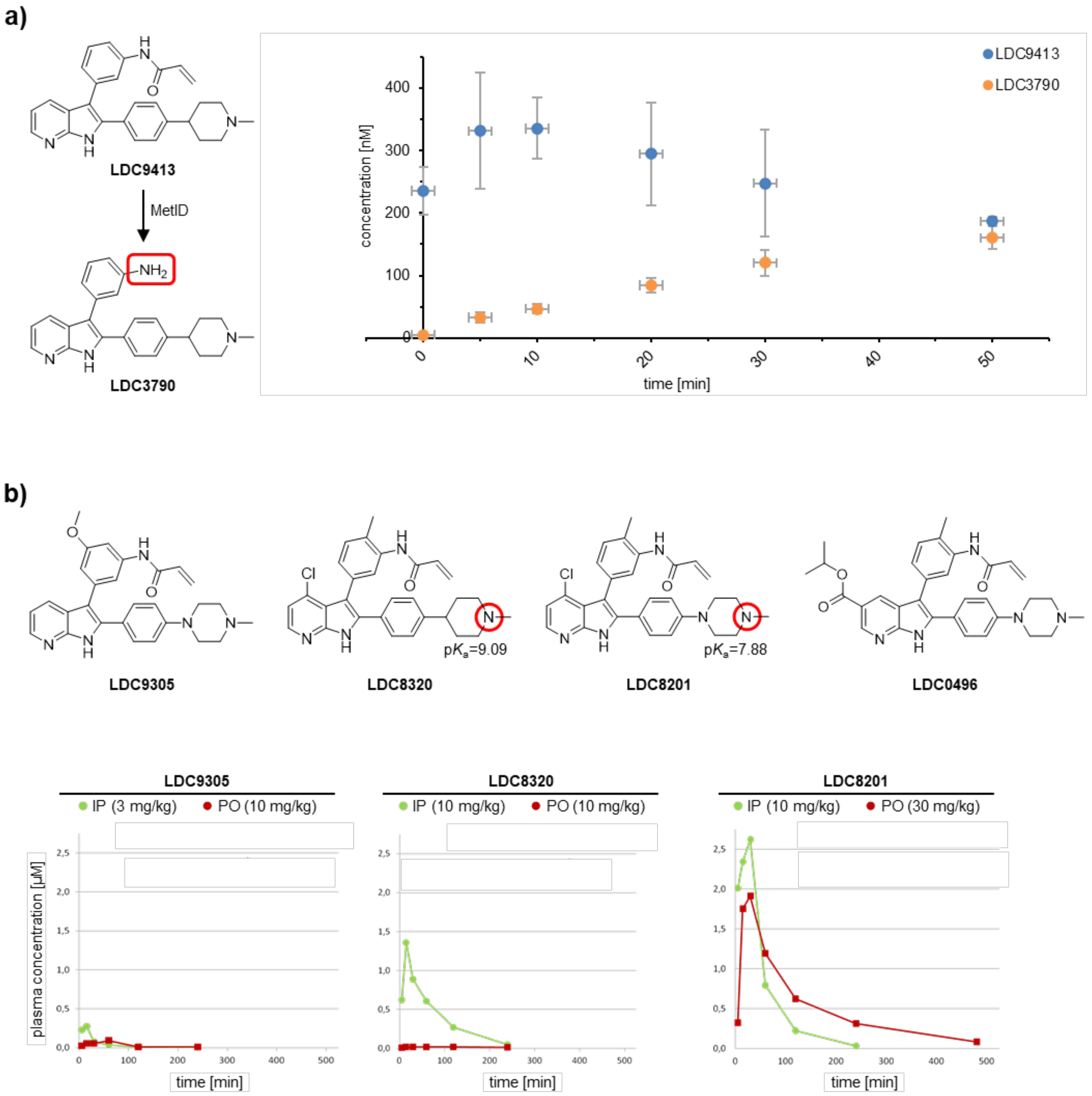

Figure S2. a) Quantification of the primary metabolite of LDC9413 *in vitro* in mouse liver microsomes. **b)** Chemical structures and calculated pK_a values of selected inhibitors, as well as corresponding *in vivo* plasma concentration–time profiles following intraperitoneal (IP), and oral (PO) administration in mice. The software ChemAxon was used for the calculation of pK_a values.

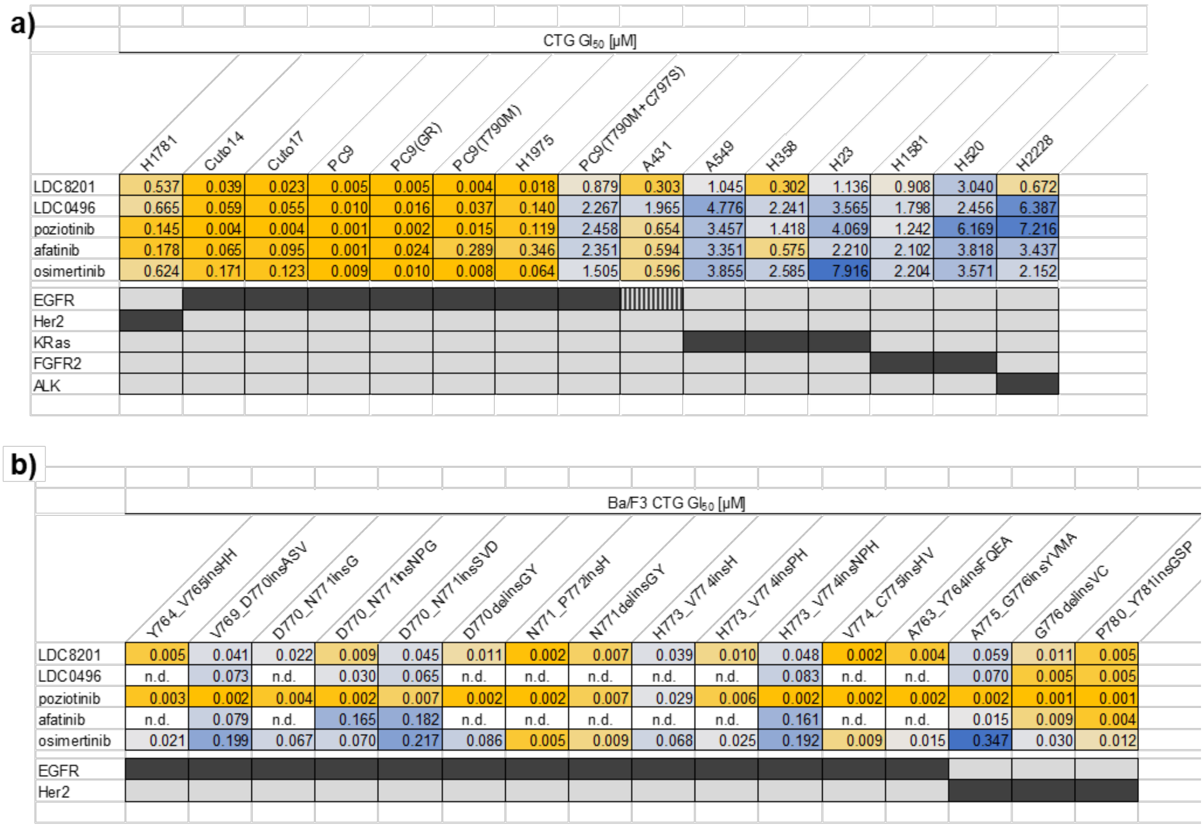

a)

	CTG GI$_{50}$ [µM]														
	H1781	Cuto14	Cuto17	PC9	PC9(GR)	PC9(T790M)	H1975	PC9(T790M+C797S)	A431	A549	H358	H23	H1581	H520	H2228
LDC8201	0.537	0.039	0.023	0.005	0.005	0.004	0.018	0.879	0.303	1.045	0.302	1.136	0.908	3.040	0.672
LDC0496	0.665	0.059	0.055	0.010	0.016	0.037	0.140	2.267	1.965	4.776	2.241	3.565	1.798	2.456	6.387
poziotinib	0.145	0.004	0.004	0.001	0.002	0.015	0.119	2.458	0.654	3.457	1.418	4.069	1.242	6.169	7.216
afatinib	0.178	0.065	0.095	0.001	0.024	0.289	0.346	2.351	0.594	3.351	0.575	2.210	2.102	3.818	3.437
osimertinib	0.624	0.171	0.123	0.009	0.010	0.008	0.064	1.505	0.596	3.855	2.585	7.916	2.204	3.571	2.152
EGFR	□	■	■	■	■	■	■	■	▥	□	□	□	□	□	□
Her2	■	□	□	□	□	□	□	□	□	□	□	□	□	□	□
KRas	□	□	□	□	□	□	□	□	□	■	■	■	□	□	□
FGFR2	□	□	□	□	□	□	□	□	□	□	□	□	■	■	□
ALK	□	□	□	□	□	□	□	□	□	□	□	□	□	□	■

b)

	Ba/F3 CTG GI$_{50}$ [µM]															
	Y764_V765insHH	V769_D770insASV	D770_N771insG	D770_N771insNPG	D770_N771insSVD	D770delinsGY	N771_P772insH	N771delinsGY	H773_V774insH	H773_V774insPH	H773_V774insNPH	V774_C775insHV	A763_Y764insFQEA	A775_G776insYVMA	G776delinsVC	P780_Y781insGSP
LDC8201	0.005	0.041	0.022	0.009	0.045	0.011	0.002	0.007	0.039	0.010	0.048	0.002	0.004	0.059	0.011	0.005
LDC0496	n.d.	0.073	n.d.	0.030	0.065	n.d.	n.d.	n.d.	n.d.	n.d.	0.083	n.d.	n.d.	0.070	0.005	0.005
poziotinib	0.003	0.002	0.004	0.002	0.007	0.002	0.002	0.007	0.029	0.006	0.002	0.002	0.002	0.002	0.001	0.001
afatinib	n.d.	0.079	n.d.	0.165	0.182	n.d.	n.d.	n.d.	n.d.	n.d.	0.161	n.d.	n.d.	0.015	0.009	0.004
osimertinib	0.021	0.199	0.067	0.070	0.217	0.086	0.005	0.009	0.068	0.025	0.192	0.009	0.015	0.347	0.030	0.012
EGFR	■	■	■	■	■	■	■	■	■	■	■	■	■	□	□	□
Her2	□	□	□	□	□	□	□	□	□	□	□	□	□	■	■	■

Figure S3. Cellular potency and selectivity. Values are the mean of a minimum of three independent measurements in triplicates. **a)** Potency and selectivity towards EGFR and Her2 mutant patient-derived cell lines as compared to KRas, FGFR2, and ALK related cell lines. **b)** Potency towards Ba/F3 transfected cell line models harbouring EGFR and Her2 exon20 insertion mutations.

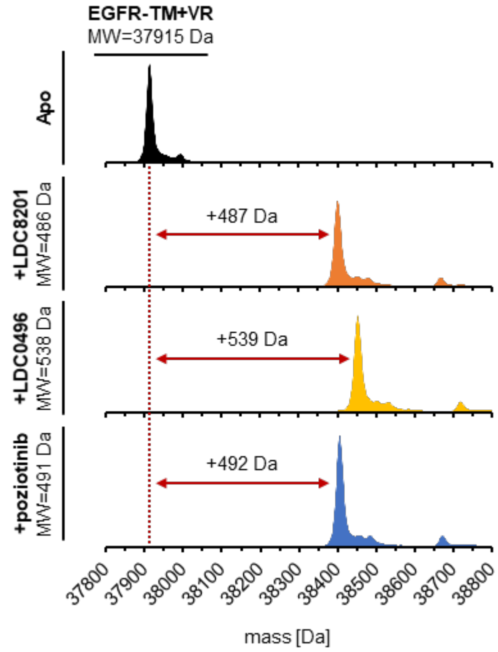

Figure S4. Mass spectrometry-based analysis of covalent bond formation of EGFR-T790M+V948R with selected inhibitors.

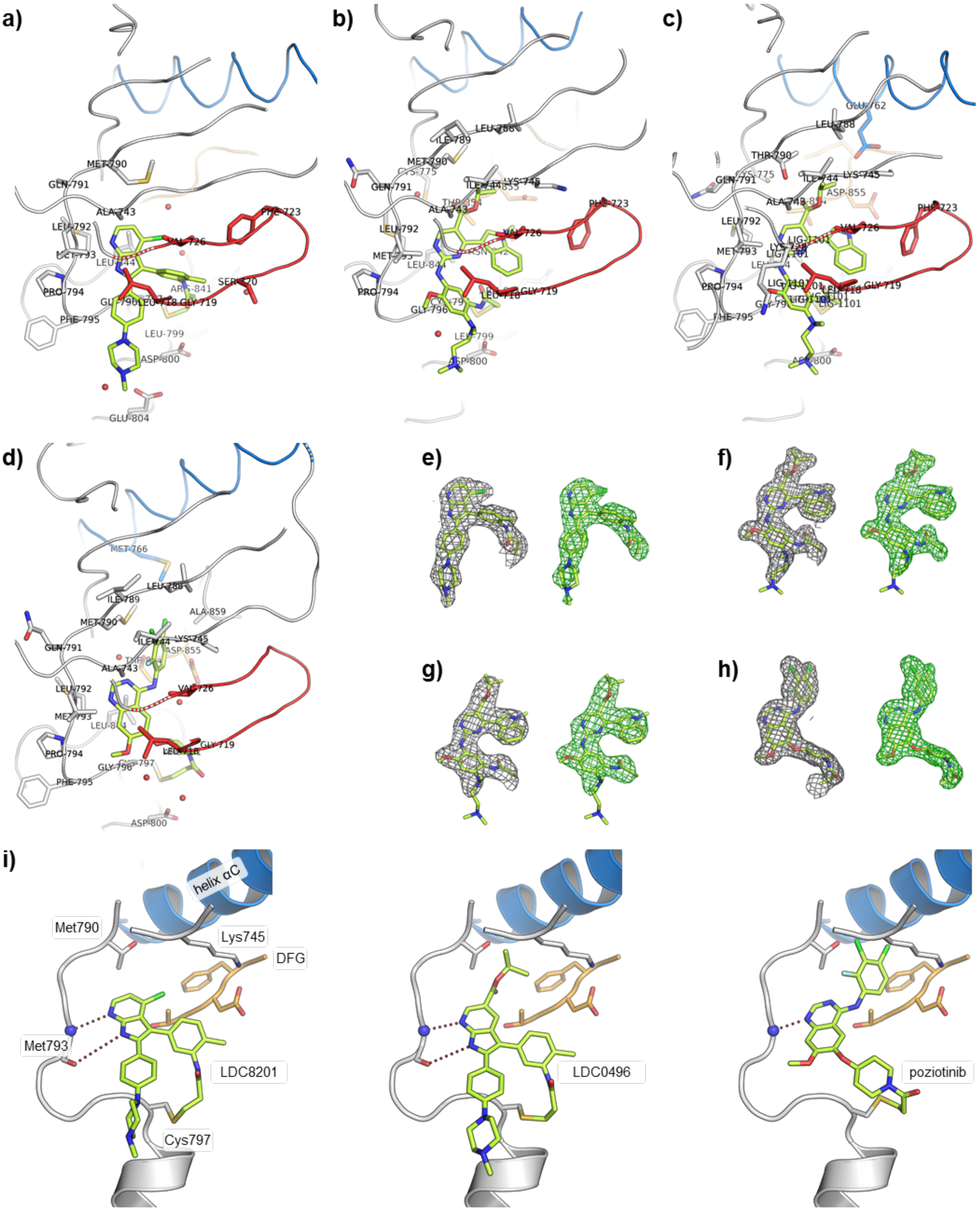

Figure S5. Co-crystal structures of inhibitors in complex with EGFR. **a)** LDC8201/EGFR-T790M+V948R at 2.4 Å (PDB ID: 7A6I), **b)** TAK-788/EGFR-T790M+V948R at 2.0 Å (PDB ID: 7A6K), **c)** TAK-788/EGFR-wt at 2.5 Å (PDB ID: 7B85) and **d)** poziotinib/EGFR-T790M+V948R at 2.0 Å resolution (PDB ID: 7A6J). The helix αC is shown in blue, DFG motif in orange and glycine-rich loop in red. Residues within 5 Å of the respective ligand were shown. **e)–h)** Electron density maps (2Fo-Fc) shown in gray (contoured at an r.m.s.d. of 1) and Fo-Fc simulated annealing omit maps shown in green (contoured at an r.m.s.d. of 2.8) of **e)** LDC8201/EGFR-T790M+V948R, **f)** TAK-788/EGFR-T790M+V948R, **g)** TAK-788/EGFR-wt and **h)** poziotinib/EGFR-T790M+V948R. **i)** Docking studies performed with LDC8201, LDC0496 and poziotinib in EGFR-D770_N771insNPG (PDB ID: 4LRM).

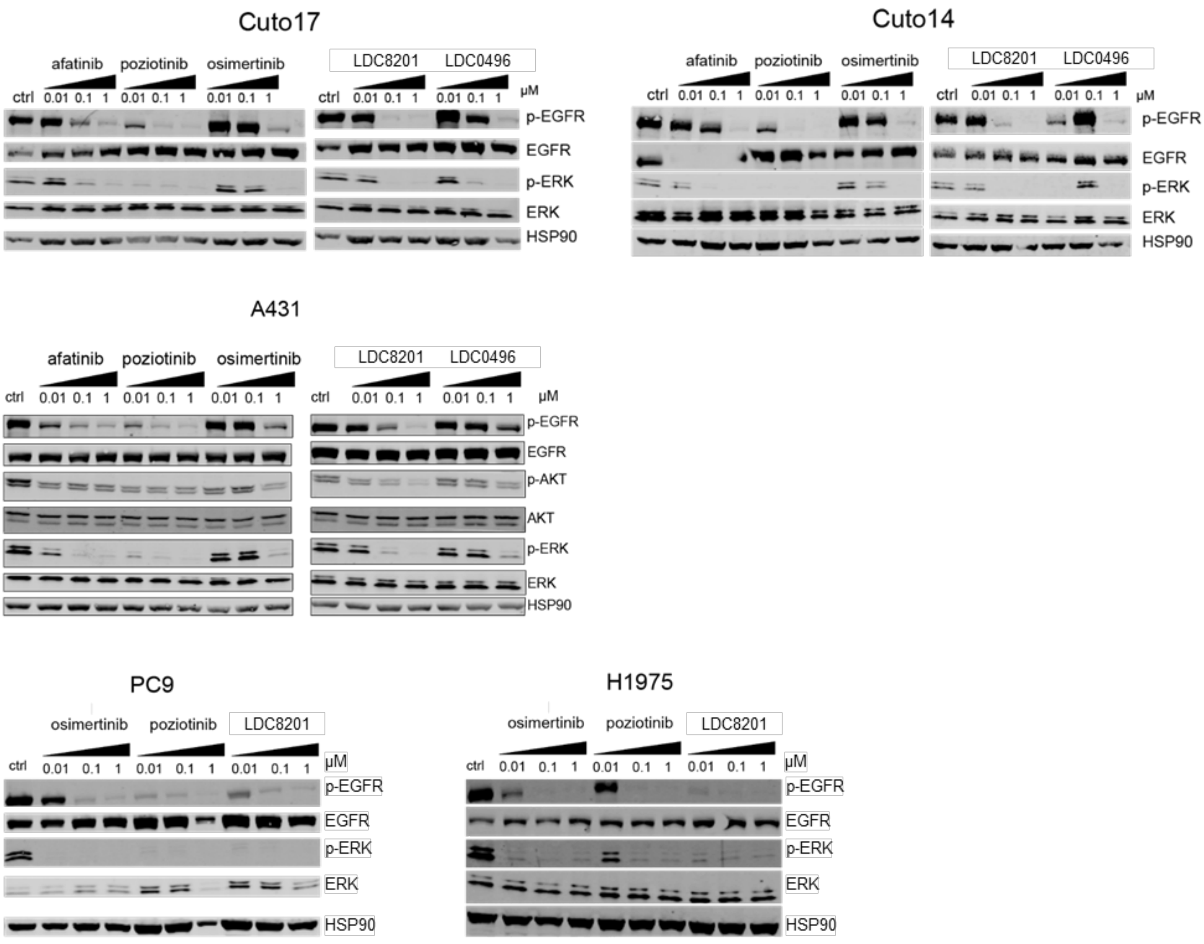

Figure S6. Western blot analysis of EGFR and downstream cascade phosphorylation inhibition in relevant cell lines.

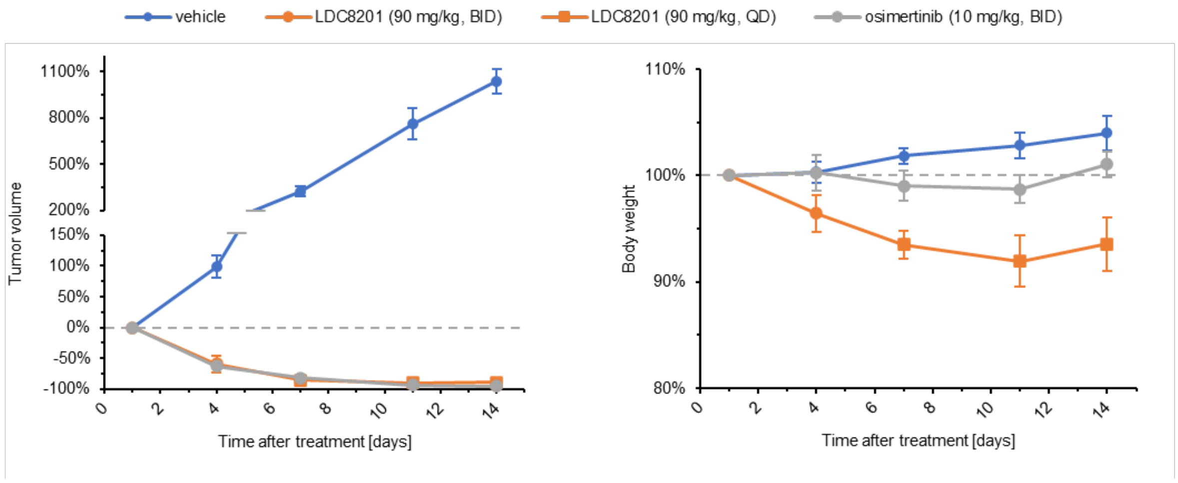

Figure S7. Tumor volume change (±SEM) and body weight change (±SEM) of mice injected with H1975 cells treated with LDC8201 (90 mg/kg, PO, twice daily→90 mg/kg, PO, once daily) and osimertinib (10 mg/kg, PO, twice daily).

Experimental Procedures

Synthetic procedures

LDC8201 (*N*-(5-(4-chloro-2-(4-(4-methylpiperazin-1-yl)phenyl)-1*H*-pyrrolo[2,3-*b*]pyridin-3-yl)-2-methylphenyl)acrylamide):

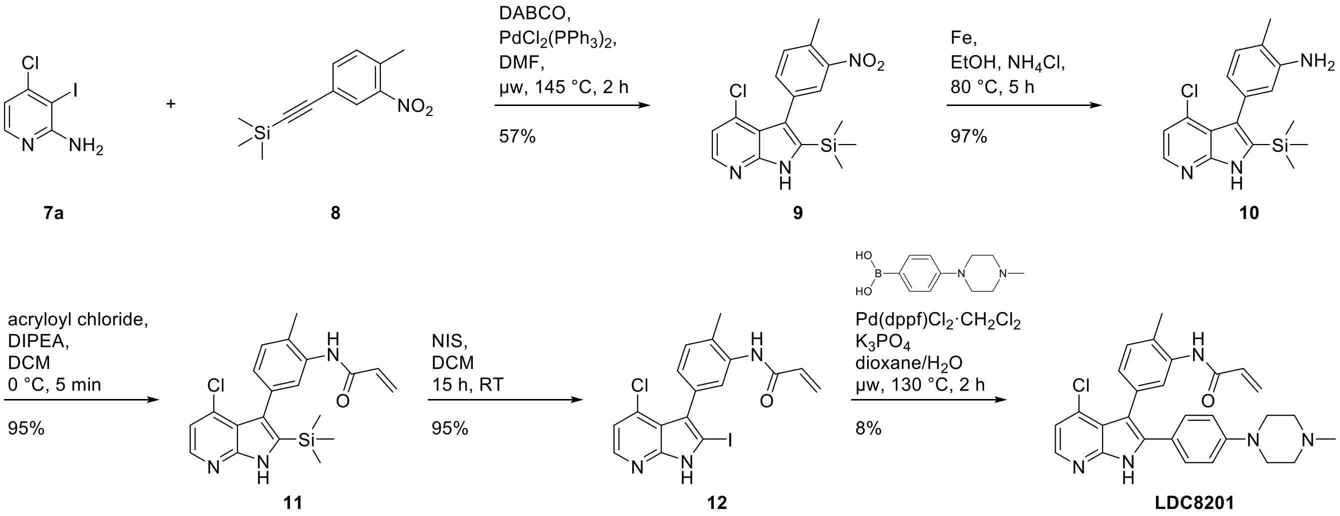

ESI-MS (m/z) calculated for $[C_{28}H_{28}ClN_5O+H]^+$ 486.21, found 486.20.

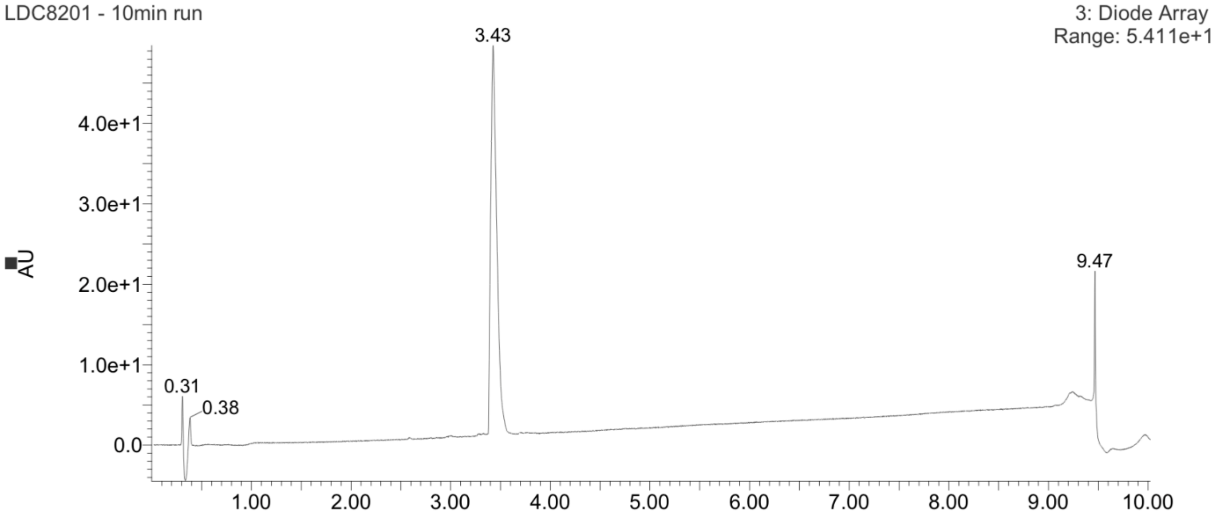

LDC0496 (Isopropyl 3-(3-acrylamido-4-methylphenyl)-2-(4-(4-methylpiperazin-1-yl)phenyl)-1*H*-pyrrolo[2,3-*b*]pyridine-5-carboxylate):

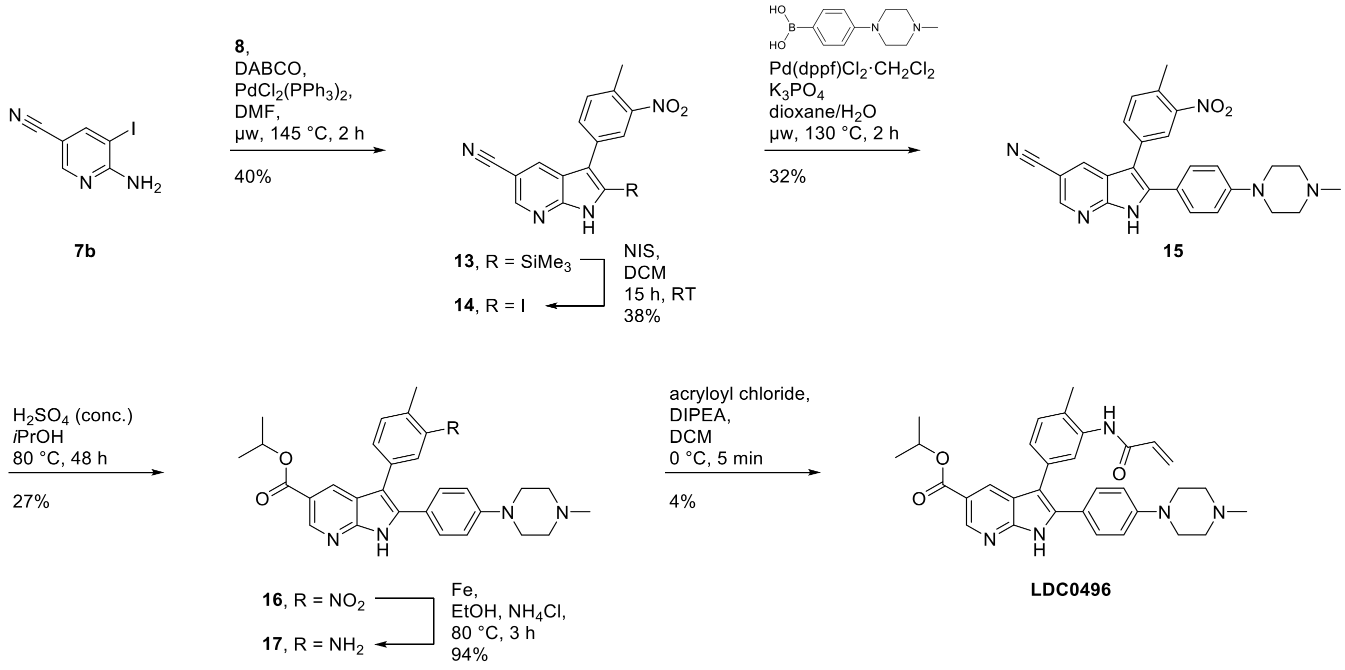

ESI-MS (m/z) calculated for $[C_{32}H_{35}N_5O_3+H]^+$ 538.28, found 538.28.

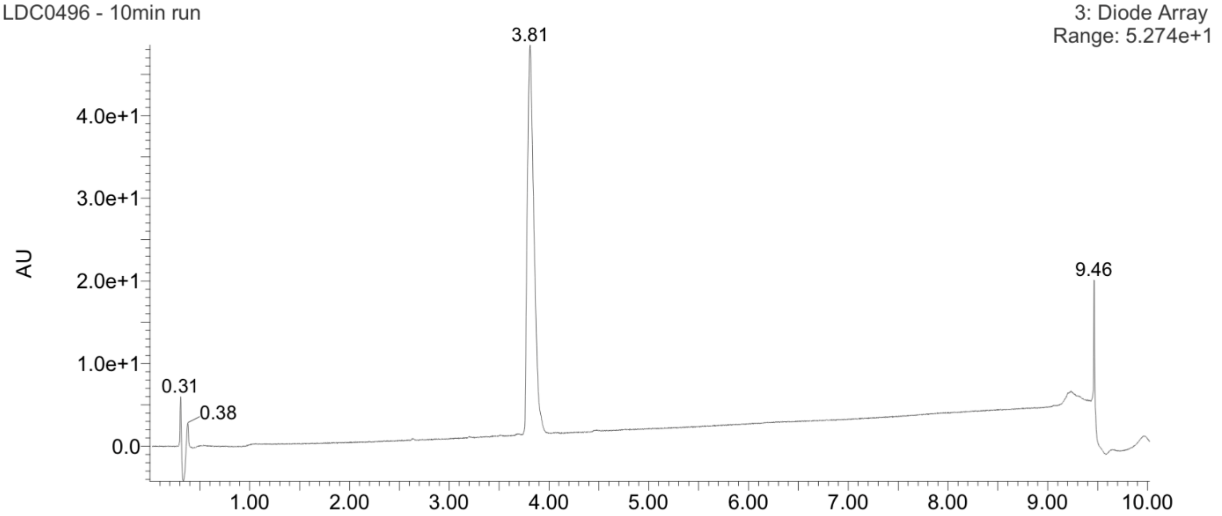

TAK-788 (Isopropyl 2-((5-acrylamido-4-((2-(dimethylamino)ethyl)(methyl)amino)-2-methoxyphenyl)amino)-4-(1-methyl-1*H*-indol-3-yl)pyrimidine-5-carboxylate):

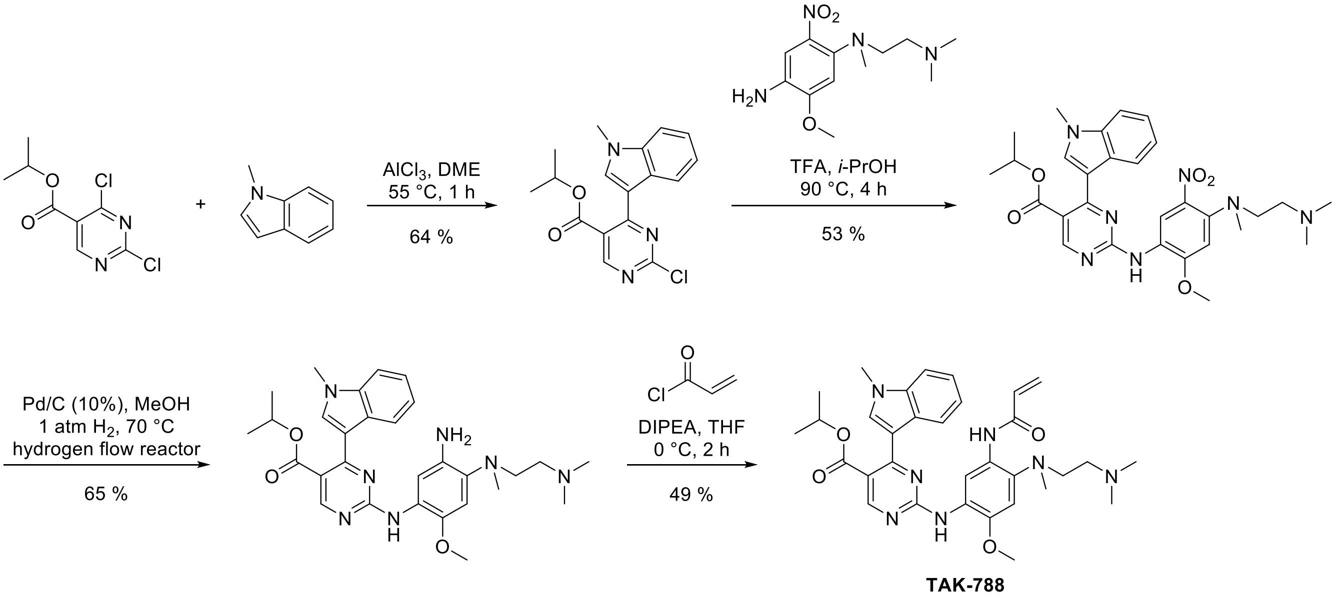

Supplement: Clonal dynamics of *BRAF*-driven drug resistance in *EGFR*-mutant lung cancer

Supplementary Material

Supplementary Table 1 (A-D)^{18}FDG-PET/CT assessment for monitoring of metabolic response during different lines of treatment of two patients with *EGFR*/*BRAF*-mutant lung adenocarcinoma. Table summarizes the standard uptake values (SUV). **(A)** P01, lesion 1; **(B)** P01, lesion 2; **(C)** P04, lesion 1; **(D)** P04, lesion 2. D+T, dabrafenib+trametinib; O+D(+T), osimertinib+dabrafenib(+trametinib);O(+CTX)+B,osimertinib(+chemotherapy)+bevacizumab; A+C, afatinib+crizotinib; O+TACE, osimertinib+transarterial chemoembolization; FU, Follow-up; PD, progressive disease.

A

Treatment	^{18}FDG-PET/CT assessments		Left upper lung lobe (initially hottest lesion) SUVmax
D+T	BASELINE	28.11.2018	11,64
D+T	2 WeFU	19.12.2018	9,49
D+T	6 WeFU	16.01.2019	10,64
D+T	10 WeFU	18.02.2019	11,89
O+D	2 WeFU	13.03.2019	14,46
A+C	2 WeFU	09.04.2019	8,12
A+C	6 WeFU	08.05.2019	10,91
O+D+T	3 WeFU	26.06.2019	9,83
O+D+T	7 WeFU	29.07.2019	11,89
O+D+T	12 WeFU	12.09.2019	7,74
O+D+T	20 WeFU	12.11.2019	8,07
O+D+T	32 WeFU	13.02.2020 (only CT)	Morphological PD
O+D+T	9 MoFU	20.03.2019	7,13
O+Beva (2x)	6 WeFU	06.05.2020	11,96
A+C	3 WeFU	09.06.2020	8,83
A+C	12 WeFU	18.08.2020	8,68 new PET positive retroperitoneal metastases
O+D+T	not done	not done	not done

B

Treatment	^{18}FDG-PET/CT assessments		Left lower lung lobe SUVmax
D+T	BASELINE	28.11.2018	10,36
D+T	2 WeFU	19.12.2018	6,29
D+T	6 WeFU	16.01.2019	8,20
D+T	10 WeFU	18.02.2019	8,24
O+D	2 WeFU	13.03.2019	11,01
A+C	2 WeFU	09.04.2019	6,24
A+C	6 WeFU	08.05.2019	10,84
O+D+T	3 WeFU	26.06.2019	9,39
O+D+T	7 WeFU	29.07.2019	7,74
O+D+T	12 WeFU	12.09.2019	5,24
O+D+T	20 WeFU	12.11.2019	6,95
O+D+T	32 WeFU	13.02.2020 (only CT)	Morphological PD
O+D+T	9 MoFU	20.03.2019	6,44
O+Beva (2x)	6 WeFU	06.05.2020	10,01
A+C	3 WeFU	09.06.2020	7,52
A+C	12 WeFU	18.08.2020	5,53 new PET positive retroperitoneal metastases
O+D+T	not done	not done	not done

C

Treatment	^{18}FDG-PET/CT assessments		Right upper lung lobe (hottest lesion) SUVmax
D+T	BASELINE	13.11.2018	8,41
D+T	2 WeFU	21.12.2018	12,25
D+T	6 WeFU	08.01.2019	10,99
O+D	2 WeFU	28.01.2019	9,05
O+D	6 WeFU	27.02.2019	10,89
O+D	12 WeFU	10.04.2019	10,56
O+D+T	2 WeFU	20.05.2019	5,91
O+D+T	6 WeFU	21.06.2019	10,46
O+CTX+B (2x)	4 WeFU	22.08.2019	6.37
O+TACE	not done	not done	not done

D

Treatment	^{18}FDG-PET/CT assessments		Right liver lobe metastasis SUVmax
D+T	BASELINE	13.11.2018	5,73
D+T	2 WeFU	21.12.2018	6,01
D+T	6 WeFU	08.01.2019	5,91
O+D	2 WeFU	28.01.2019	3,47
O+D	6 WeFU	27.02.2019	4,30
O+D	12 WeFU	10.04.2019	4,17
O+D+T	2 WeFU	20.05.2019	7,13
O+D+T	6 WeFU	21.06.2019	7,58
O+CTX+B (2x)	4 WeFU	22.08.2019	6,26
O+TACE	not done	not done	not done

Supplementary Table 2 **(A,B)** Treatment strategy, dose regimen and treatment-related adverse events according to Common Terminology Criteria for Adverse Events (CTCAE) Version 5.0. AEs of higher grade were mostly mixed disease- and treatment-related effects. **(A)** P01; **(B)** P04. D+T, dabrafenib+trametinib; O+D(+T), osimertinib+dabrafenib (+trametinib);O(+CTX)+B, osimertinib(+chemotherapy)+bevacizumab; A+C, afatinib+ crizotinib; O+TACE, osimertinib+transarterial chemo- embolization; TTD, time-to-treatment discontinuation; AE, adverse event.

A

Treatment	Start-Stop	Dose regimen	TTD (days)	AEs	Comments
D+T	06.12.2018-18.02.2019	dabrafenib 150mg 1-0-1 trametinib 2mg 0-0-1	74	Hyponatremia Grade II-III; GGT/AP increased Grade I-II; Fever Grade II-III; Nausea Grade I; Lipase/Amylase increased Grade I-II; Fatigue Grade I; Anorexia Grade I; Panniculitis Grade I-II; Anemia Grade I;	
O+D	22.02.2019-21.03.2019	osimertinib 80mg 0-0-1 dabrafenib 150mg 1-0-1	27	Lipase/Aamylase increased Grade II-III; GGT/AP increased Grad I; Anemia Grade I;	Intermittent interruption of O+D due to increase in amylase and lipase (no signs of pancreatitis);
A+C	24.03.2019-28.05.2019	afatinib 40mg 1-0-0 crizotinib 200mg 1-0-1	65	Rash maculo-papular Grade I-II; Diarrhea Grade I; Lipase/ Amylase increased Grade I-II; Nausea Grade I; Edema Grade I; Dry eyes Grade I; Anorexia Grade I; Paronychia Grade I-II; Anemia Grade I;	Intermittent interruption and/or dose reduction of A+C;
O+D+T	05.06.2019-19.03.2020	osimertinib 80mg 0-0-1 dabrafenib 150mg 1-0-1 trametinib 2mg 0-0-1	288	Lipase/Amylase increased Grade II-III; GGT/AP increased Grade I; Hyponatremia Grade II-III; Diarrhea Grade I; Fever Grade I-II; Nausea Grade I; Fatigue Grade I; Anorexia Grade I; Ascites Grade II; Anemia Grade II-III; Edema Grade I;	Intermittent interruption of O+D+T due to increase in amylase and lipase (no symptoms of pancreatitis); Ascites was associated to peritoneal carcinosis and cirrhosis (paracentesis); Tolvaptan treatment was administered for hyponatremia;
O+B	20.03.2020-12.05.2020	osimertinib 80mg 1-0-0 bevacizumab 15mg/kg Q3W (2x)	53	Ascites Grade II; Fatigue Grade II; Anorexia Grade II; Anemia Grade II; Edema Grade I-II; GGT increased Grade I;	Ascites/Edema/Fatigue/Anorexia were associated with tumor progression, pre-existing cirrhosis and hypoalbuminemia;
A+C	17.05.2020-30.08.2020	afatinib 30mg 1-0-0 crizotinib 250mg 1-0-1, later afatinib was reduced to 20 mg 1-0-0 and crizotinib to 200mg 1-0-1	105	Ascites Grade II-III; Fatigue Grade II; Anorexia Grade II; Anemia Grade II; Edema Grade I-II; Rash Grade I-II; GGT/AP increased Grade I-II; Diarrhea Grade I-II; Nausea Grade II;	Intermittent interruption and/or dose reduction of afatinib and crizotinib due to rash, edema, diarrhea or nausea;
O+D+T	02.09.2020-ongoing	osimertinib 80mg 0-0-1 dabrafenib 150mg 1-0-1 trametinib 2mg 0-0-1	na	Ascites Grade II-III; Fatigue Grade II; Anorexia Grade II; Anemia Grade II; Edema Grade I-II; GGT/AP increased Grade I-II; Diarrhea Grade I-II; Nausea Grade II;	

B

Treatment	Start-Stop	Dose regimen	TTD (days)	AEs	Comments
D+T	06.12.2018-13.01.2019	dabrafenib 150mg 1-0-1 trametinib 2mg 0-0-1	38	Nausea Grade I; Vomiting Grad I; GGT/AP increased Grade I; Fatigue Grade I; Fever Grade I; Dry mouth Grade I; Myalgia Grade I-II;	Increase in AP/GGT were associated with liver metastases;
O+D	14.01.2019-17.04.2019	osimertinib 80mg 0-0-1 dabrafenib 150mg 1-0-1	93	Nausea Grade I; Fatigue Grade I; GOT/GPT increased Grade I; GGT/AP increased Grade II-III; Cough Grade I; Lipase increased Grade I; Myalgia Grade I-II; Anorexia Grade I;	Increase in GOT/GPT can be related to treatment; Increase in AP/GGT can be associated with liver metastases; Cough was possibly associated with respiratory infection and resolved within a few days;
O+D+T	18.04.2019-04.07.2019	osimertinib 80mg 0-0-1 dabrafenib 150mg 1-0-1 trametinib 2mg 0-0-1, from 30.04.2019 trametinib was reduced to 1mg 0-0-1	77	Myalgia Grade II; Anorexia Grade I; GGT/AP increased Grade II; Fatigue Grade I; Fever Grade I;	Dose of trametinib was reduced which improved myalgia and fatigue symptoms;
O+CTX+B	05.07.2019-18.09.2019	osimertinib 80mg 1-0-0 carboplatin AUC 6 and pemetrexed 500 mg/m^2 (2x cycles; 2nd cycle: AUC 4 and 250/m^2) bevacizumab 15 mg/kg Q3W (2x cycles)	75	Fatigue Grade II; Anorexia II-III; GGT/AP increased Grade II-III; Fatigue Grade I;	Second cycle of chemotherapy was dose reduced due to clinical deterioration of the patient.
O+TACE	19.09.2019-Nk.09.2019	osimertinib 80mg 1-0-0	na	Ascites Grade II-III; Fatigue Grade II; Anorexia Grade II; Anemia Grade II; Edema Grade I-II; GGT/AP increased Grade I-II; Diarrhea Grade I-II; Nausea Grade II;	

Supplementary Table 3 Used Primers

Sequence	Purpose
CTAAGCCTCCGCCTCCTC	pBabe seq f
GACTAATTGAGATGCATG	pBabe seq r
TCCGCTGTCAAACATGTGGT	seq PBABE V600E inside Braf-casette
TCGTGGTGATGGAGGATCAAC	BRAF qPCR f
TCATCACTCGAGTCCCGTCT	BRAF qPCR r
CAGGTGGTGTTGGGAAAAGC	NRAS qPCR f
TCAACACCCTGTCTGGTCTT	NRAS qPCR r

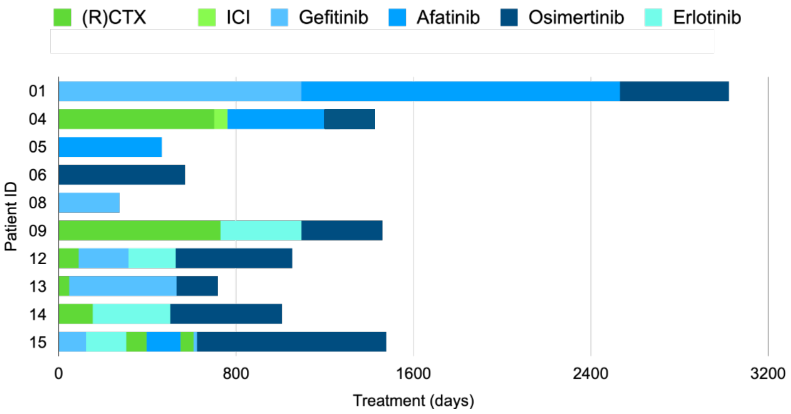

Supplementary Figure 1. Treatment history before the detection of acquired *BRAF* mutations in 10 patients evaluable for treatment history.

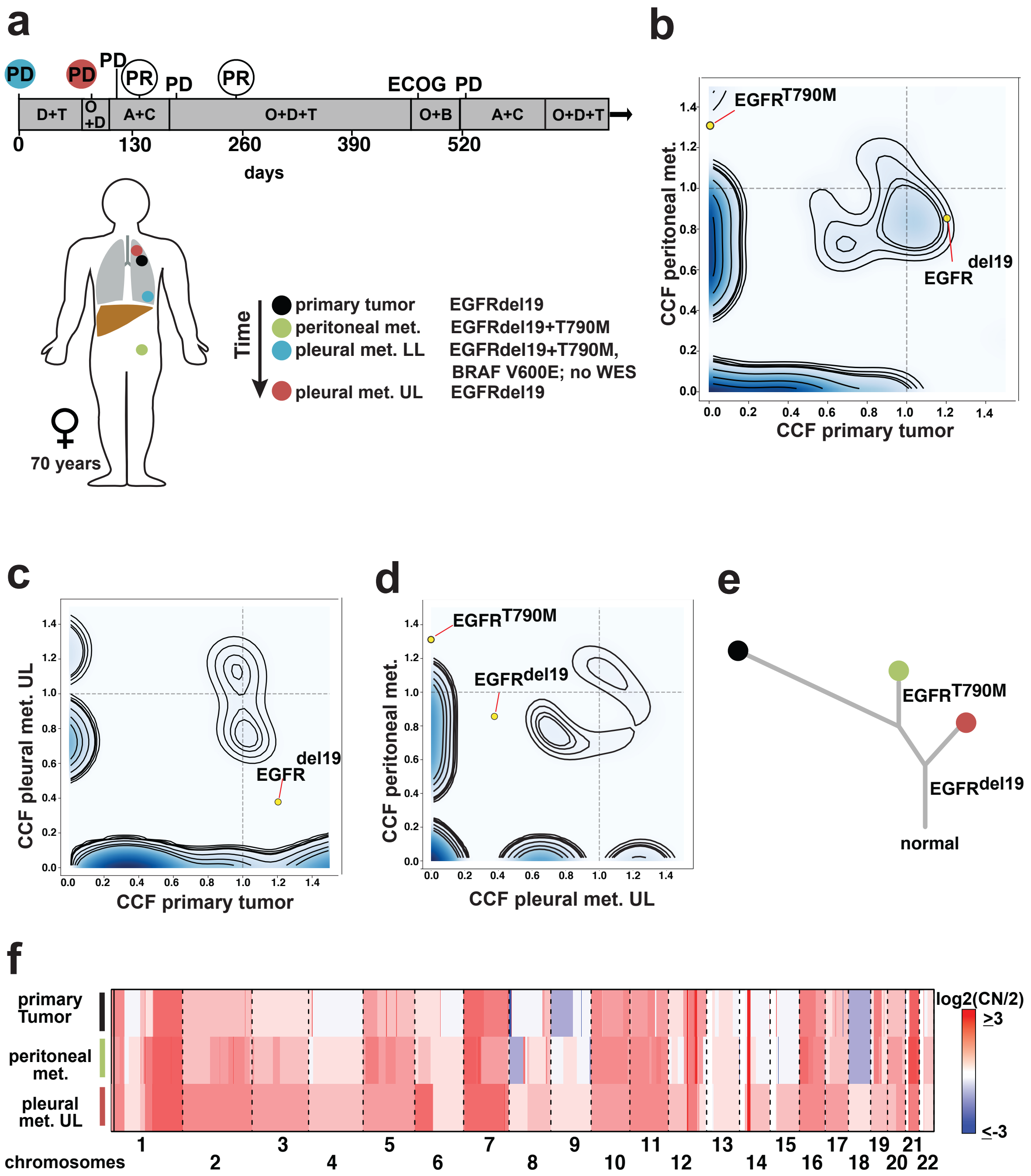

Supplementary Figure 2. (**a**) Overview of the biopsies and key molecular findings by targeted NGS for patient 01 and flow chart summarizing lines of therapy approaches over time after the acquisition of *BRAF*^{V600E} mutation following osimertinib. (**b-d**) Pairwise clustering of WES-derived mutations based on their CCFs between pairs of tumor biopsies. Large clusters of private mutations indicate a high degree of genetic dissimilarity between biopsies. Candidate mutations in *EGFR* are highlighted. (**e**) Visualization of genetic distances between normal tissue and longitudinal biopsies in a phylogenetic tree. Branching indicates that the metastases and the primary tumor derived from a shared common ancestor. (**f**) Profiles of purity and ploidy corrected copy number (CN) in the metastases. (red = CN gain, blue = CN loss). *EGFR*, epidermal growth factor receptor; *BRAF*, B-rapidly accelerated fibrosarcoma; WES, whole-exome sequencing; NGS, next-generation sequencing; PD, progressive disease; PR, partial response; D+T, dabrafenib+trametinib; O+D(+T), osimertinib+dabrafenib(+trametinib); A+C, afatinib+crizotinib; O+B, osimertinib+bevacizumab; ECOG, Eastern Cooperative Oncology Group; CCF, cancer cell fraction; LL, lower lobe; UL, upper lobe.

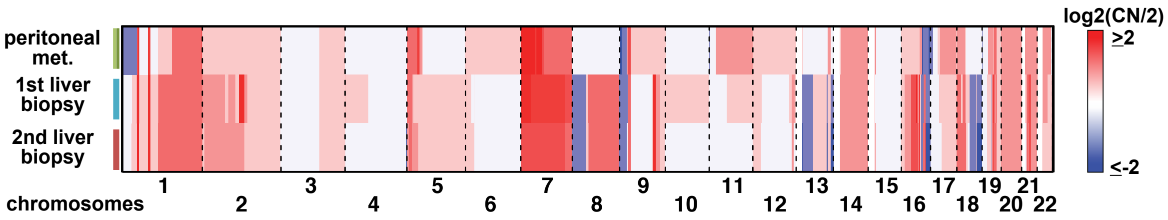

Supplementary Figure 3. Profiles of purity and ploidy corrected copy number (CN) in the metastases (red = CN gain, blue = CN loss) for patient P04.

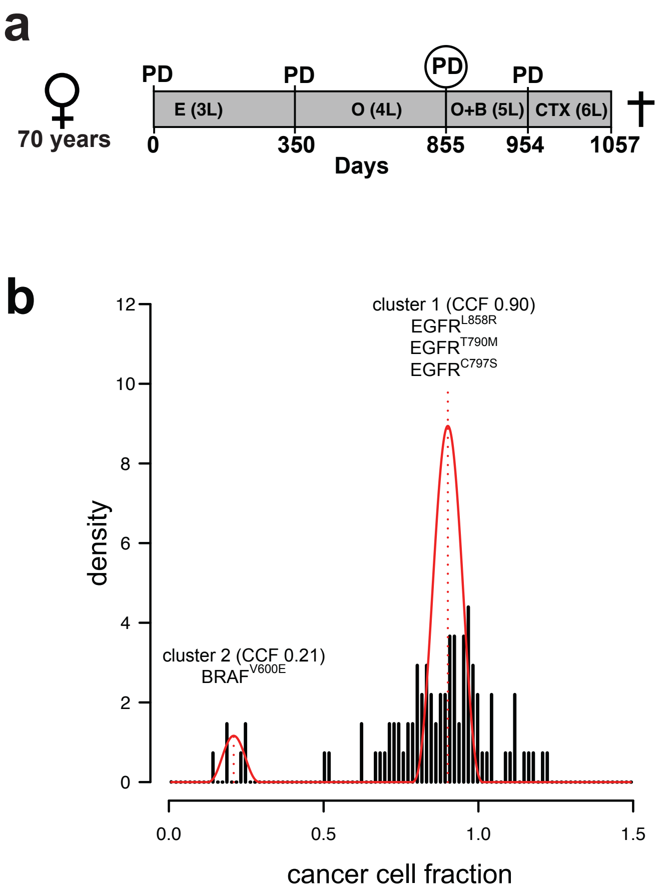

Supplementary Figure 4. (**a**) Overview of the treatment lines for patient P14 after erlotinib was started. Biopsy for WES obtained at the time of progression after osimertinib treatment was taken at day 855. (**b**) WES-based clonality analysis of the biopsy displayed two mutation clusters with corresponding cancer cell fractions (CCF). Relevant mutations are indicated above the corresponding clusters. *EGFR*, epidermal growth factor receptor; *BRAF*, B-rapidly accelerated fibrosarcoma; WES, whole-exome sequencing; PD, progressive disease; E, erlotinib; O, osimertinib; O+B, osimertinib+bevacizumab; CTX, chemotherapy. L, line of therapy.

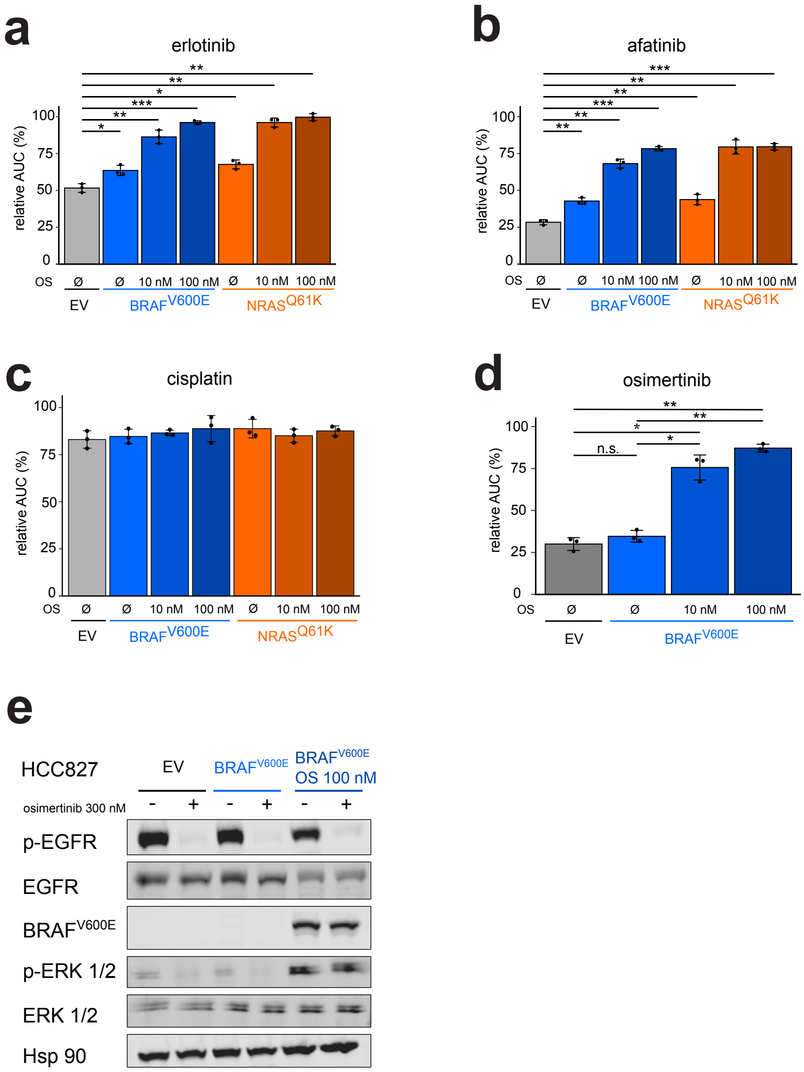

Supplementary Figure 5. (**a-c**) Viability assay of PC9 derived cell lines, treated for 72 hours with (**a**) erlotinib, (**b**) afatinib or (**c**) cisplatin. (**d**) Viability assay of HCC827 derived cell lines treated with osimertinib (72h) are shown. (**e**) Immunoblotting of HCC827 cells expressing the annotated constructs, treated with (+) or without (-) osimertinib (48h) and Hsp90 is used as loading control. The relative area under the curve (AUC) in % compared to a theoretical non-responding AUC. Error bars indicate mean ± SD. Two-tailed paired t-tests, $***p < 0.001$, $**p < 0.01$, $*p < 0.05$.

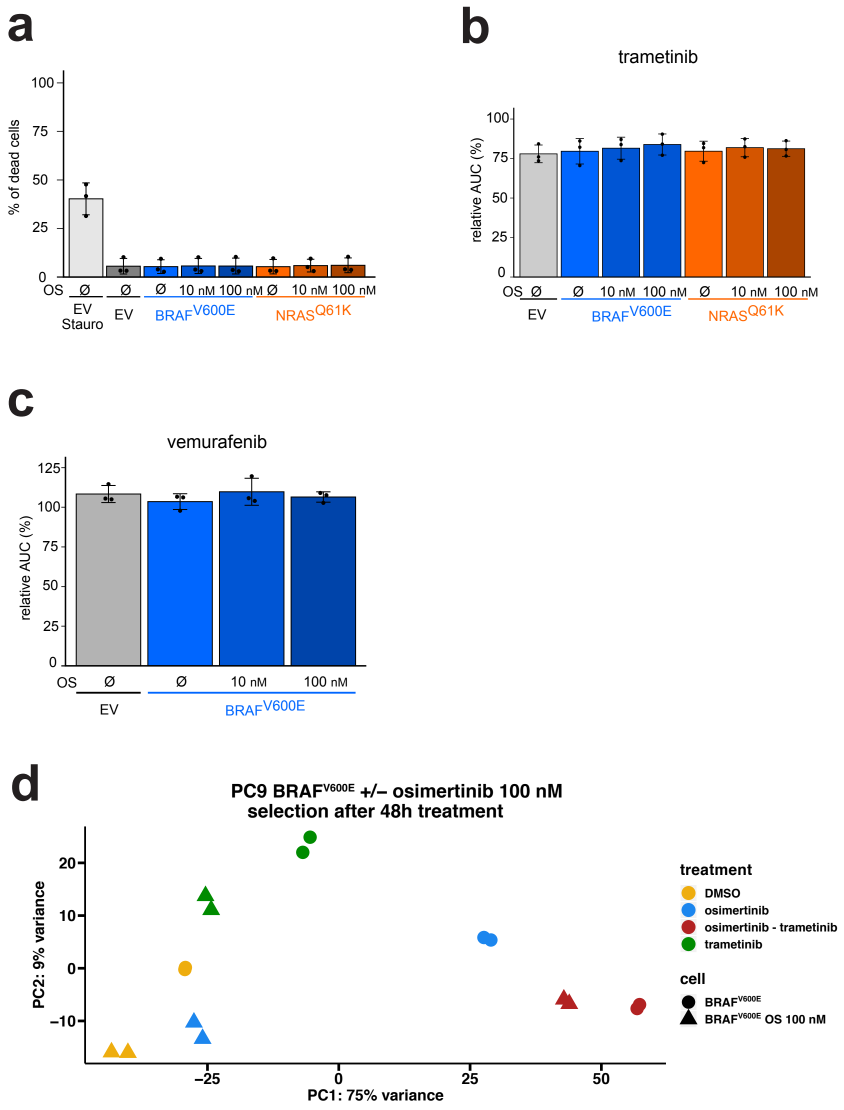

Supplementary Figure 6. (**a**) Percentage of dead cells measured by flow cytometry. Staurosporine control treated for 24 hours. (**b,c**) Viability assay of PC9 (EV) derived cell lines, treated for 72 hours with (**b**) trametinib or (**c**) vemurafenib. (**d**) Principal component analysis of 3'UTR-RNA-seq-samples in duplicates. The relative area under the curve (AUC) in % compared to a theoretical non-responding AUC. Error bars indicate mean ± SD. Two-tailed paired t-tests, *** $p < 0.001$, **$p < 0.01$, *$p < 0.05$.

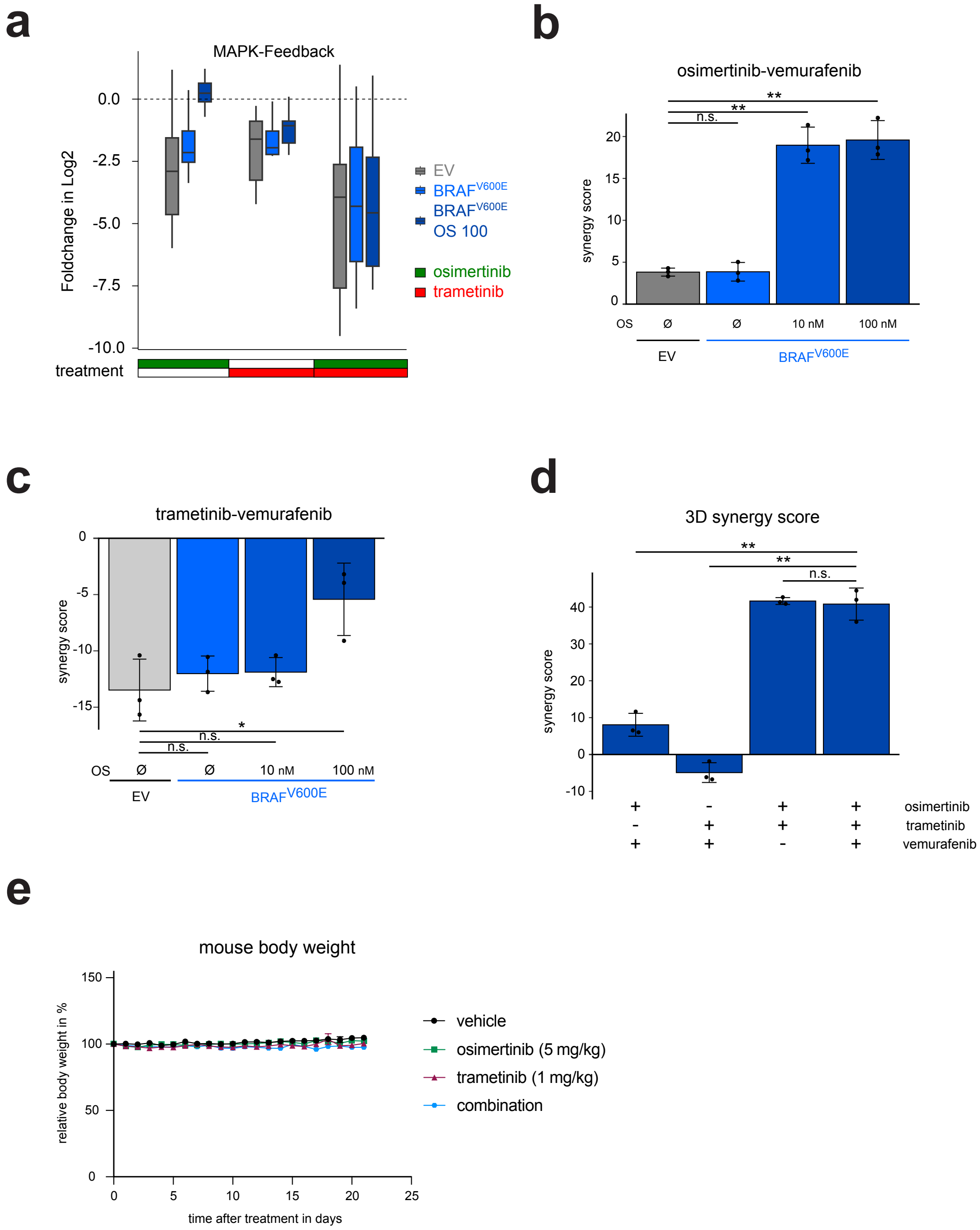

Supplementary Figure 7. (**a**) RNA-seq based log2 fold-changes of negative MAPK feedback genes (see methods) of PC9 derived cell lines after 48h treatment with indicated inhibitors compared to their respective DMSO controls. (**b**) Synergy screen of osimertinib and vemurafenib combination treatment in PC9 derived cell lines for 72 hours. (**c**) Synergy screen of trametinib and vemurafenib combination treatment in PC9 derived cell lines for 72 hours. (**d**) 3D Synergy screen of osimertinib, trametinib and vemurafenib combination treatment in PC9 pBABE BRAFV600E OS 100 cells for 72 hours. (**e**) Relative body weight of all mice in trial (see methods) in % compared to day 0. Error bars indicate mean ± SD. Two-tailed paired t-tests, *** $p < 0.001$, **$p < 0.01$, *$p < 0.05$.

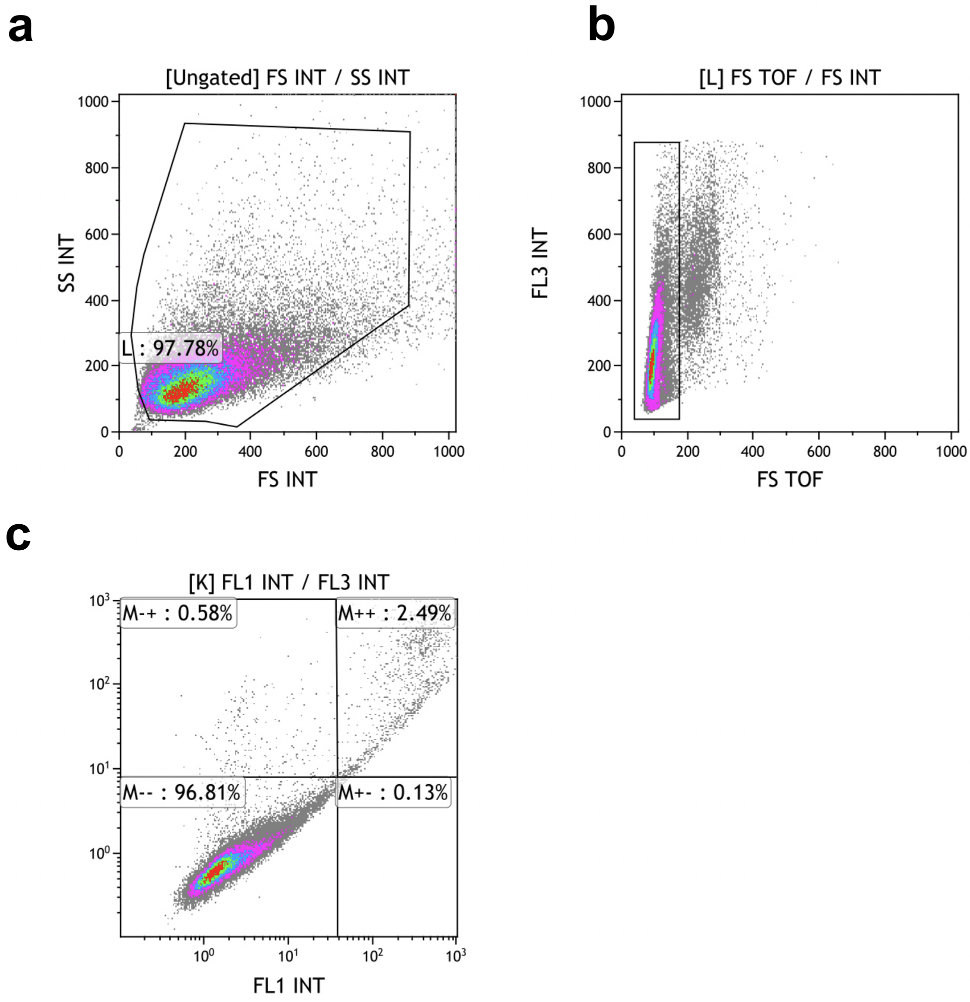

Supplementary Figure 8. Flow cytometry gating strategy. Apoptosis assay using flow cytometry after staining with annexin V-FITC/propidium iodide (PI). (**a**) Total cells were first gated on a forward scatter (FS)/side scatter (SS) for total counted events. (**b**) Cells were gated on a FS area versus FS width density plot to remove doublet cells. (**c**) Representative scatter plots of PI (y-axis) vs. annexin V (x-axis).

Supplement: MIZ1–ΔPOZ shapes treatment response in small cell lung cancer

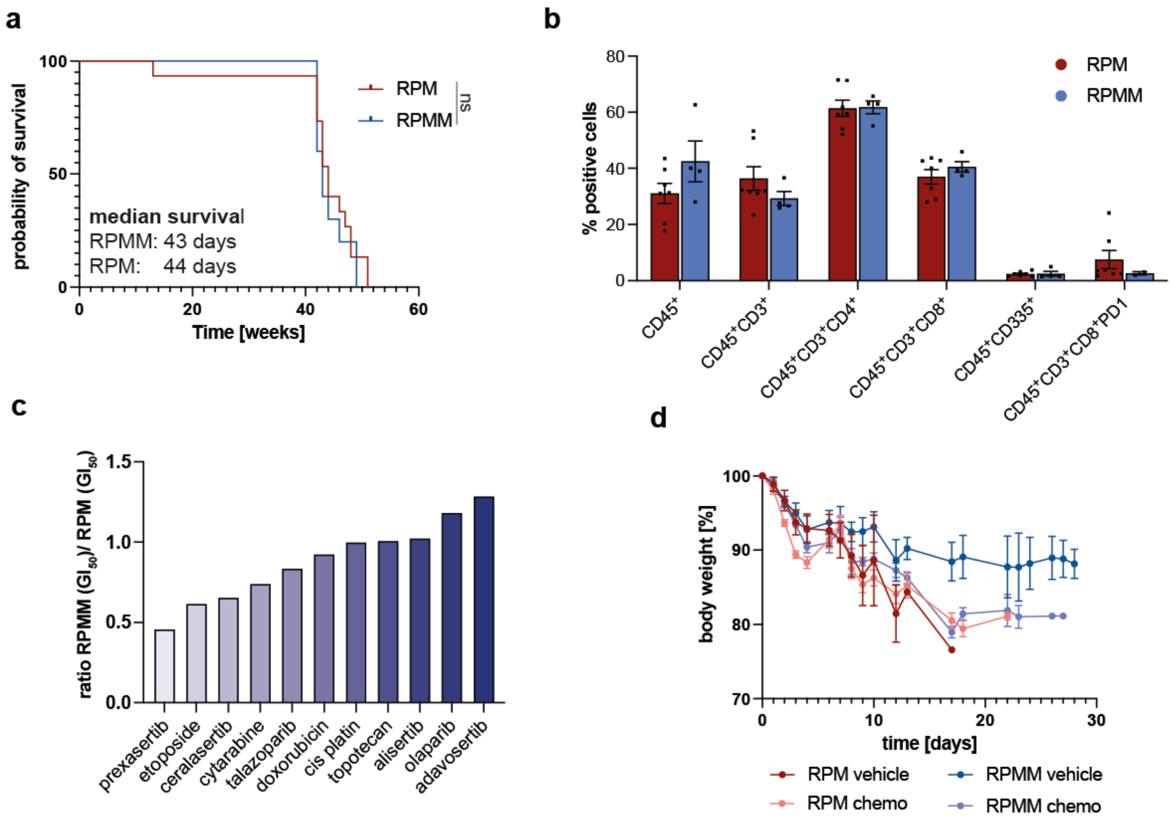

Supplementary Figure 11: (a) Kaplan-Meier survival of RPM and RPMM mice infected with Cmv-*Cre*. (b) FACS analysis of indicated immune markers. Gated on living, single cells. (c) GI_{50} values of RPMM cells normalized to the GI_{50} values of RPM cells. (d) Body weight changes of mice treated with chemotherapy (cisplatin and etoposide).

Erklärung zur Dissertation

gemäß der Promotionsordnung vom 12. März 2020

Diese Erklärung muss in der Dissertation enthalten sein.

„Hiermit versichere ich an Eides statt, dass ich die vorliegende Dissertation selbstständig und ohne die Benutzung anderer als der angegebenen Hilfsmittel und Literatur angefertigt habe. Alle Stellen, die wörtlich oder sinngemäß aus veröffentlichten und nicht veröffentlichten Werken dem Wortlaut oder dem Sinn nach entnommen wurden, sind als solche kenntlich gemacht. Ich versichere an Eides statt, dass diese Dissertation noch keiner anderen Fakultät oder Universität zur Prüfung vorgelegen hat; dass sie - abgesehen von unten angegebenen Teilpublikationen und eingebundenen Artikeln und Manuskripten - noch nicht veröffentlicht worden ist sowie, dass ich eine Veröffentlichung der Dissertation vor Abschluss der Promotion nicht ohne Genehmigung des Promotionsausschusses vornehmen werde. Die Bestimmungen dieser Ordnung sind mir bekannt. Darüber hinaus erkläre ich hiermit, dass ich die Ordnung zur Sicherung guter wissenschaftlicher Praxis und zum Umgang mit wissenschaftlichem Fehlverhalten der Universität zu Köln gelesen und sie bei der Durchführung der Dissertation zugrundeliegenden Arbeiten und der schriftlich verfassten Dissertation beachtet habe und verpflichte mich hiermit, die dort genannten Vorgaben bei allen wissenschaftlichen Tätigkeiten zu beachten und umzusetzen. Ich versichere, dass die eingereichte elektronische Fassung der eingereichten Druckfassung vollständig entspricht."

19.12.2022, Hannah Lea Tumbrink

Datum, Name und Unterschrift

Teilpublikationen

1. Resistance to MET inhibition in MET dependent NSCLC and therapeutic activity after switching from type I to type II MET inhibitors

   Richard R, Fassunke J, **Tumbrink, HL**, Scheel AH, Heydt C, Hieggelke L, Scheffler M, Heimsoeth A, Nogova L, Michels S, Weber JP,Fischer RN, Eisert A, Westphal T, Schaufler D, Siemanowski J, Ihle MA, Wagener-Ryczek S, Castiglione R, Pappesch R, Rehker J, Jürgens J, Stoelben E, Bunck A, Kobe C, Merkelbach-Bruse S, Sos ML, Büttner R, Wolf J,

   European Journal of Cancer; in Press. doi: 10.1016/j.ejca.2022.11.010
2. Insight into Targeting Exon20 Insertion Mutations of the Epidermal Growth Factor Receptor with Wild Type-Sparing Inhibitors.

   Lategahn J, **Tumbrink HL***, Schultz-Fademrecht C, Heimsoeth A, Werr L, Niggenaber J, Keul M, Parmaksiz F, Baumann M, Menninger S, Zent E, Landel I, Weisner J, Jeyakumar K, Heyden L, Russ N, Müller F, Lorenz C, Brägelmann J, Spille I, Grabe T, Müller MP, Heuckmann JM, Klebl BM, Nussbaumer P, Sos ML, Rauh D.

   J Med Chem. 2022 May 12;65. doi: 10.1021/acs.jmedchem.1c02080.
3. Clonal dynamics of BRAF-driven drug resistance in EGFR-mutant lung cancer.

   Schaufler D, Ast DF, **Tumbrink HL**, Abedpour N, Maas L, Schwäbe AE, Spille I, Lennartz S, Fassunke J, Aldea M, Besse B, Planchard D, Nogova L, Michels S, Kobe C, Persigehl T, Westphal T, Koleczko S, Fischer R, Weber JP, Altmüller J, Thomas RK, Merkelbach-Bruse S, Gautschi O, Mezquita L, Büttner R, Wolf J, Peifer M, Brägelmann J, Scheffler M, Sos ML.

   NPJ Precis Oncol. 2021 Dec 17;5. doi: 10.1038/s41698-021-00241-9.

4. Ferroptosis response segregates small cell lung cancer (SCLC) neuroendocrine subtypes.

   Bebber CM, Thomas ES, Stroh J, Chen Z, Androulidaki A, Schmitt A, Höhne MN, Stüker L, de Pádua Alves C, Khonsari A, Dammert MA, Parmaksiz F, **Tumbrink HL**, Beleggia F, Sos ML, Riemer J, George J, Brodesser S, Thomas RK, Reinhardt HC, von Karstedt S.

Nat Commun. 2021 Apr 6;12. doi: 10.1038/s41467-021-22336-4.

5. The next tier of EGFR resistance mutations in lung cancer.

   Tumbrink HL, Heimsoeth A, Sos ML.

   Oncogene. 2021 Jan;40. doi: 10.1038/s41388-020-01510-w.

6. Targeting Her2-insYVMA with Covalent Inhibitors-A Focused Compound Screening and Structure-Based Design Approach.

   Lategahn J, Hardick J, Grabe T, Niggenaber J, Jeyakumar K, Keul M, **Tumbrink HL**, Becker C, Hodson L, Kirschner T, Klövekorn P, Ketzer J, Baumann M, Terheyden S, Unger A, Weisner J, Müller MP, van Otterlo WAL, Bauer S, Rauh D.

   J Med Chem. 2020 Oct 22;63. doi: 10.1021/acs.jmedchem.0c00870.

7. Inhibition of osimertinib-resistant epidermal growth factor receptor EGFR-T790M/C797S.

   Lategahn J, Keul M, Klövekorn P, **Tumbrink HL**, Niggenaber J, Müller MP, Hodson L, Flaßhoff M, Hardick J, Grabe T, Engel J, Schultz-Fademrecht C, Baumann M, Ketzer J, Mühlenberg T, Hiller W, Günther G, Unger A, Müller H, Heimsoeth A, Golz C, Blank-Landeshammer B, Kollipara L, Zahedi RP, Strohmann C, Hengstler JG, van Otterlo WAL, Bauer S, Rauh D.

   Chem Sci. 2019 Oct 4;10. doi: 10.1039/c9sc03445e.

8. MYC paralog-dependent apoptotic priming orchestrates a spectrum of vulnerabilities in small cell lung cancer.

   Dammert MA, Brägelmann J, Olsen RR, Böhm S, Monhasery N, Whitney CP, Chalishazar MD, **Tumbrink HL**, Guthrie MR, Klein S, Ireland AS, Ryan J, Schmitt A, Marx A, Ozretić L, Castiglione R, Lorenz C, Jachimowicz RD, Wolf E, Thomas RK, Poirier JT, Büttner R, Sen T, Byers LA, Reinhardt HC, Letai A, Oliver TG, Sos ML.

   Nat Commun. 2019 Aug 2;10. doi: 10.1038/s41467-019-11371-x.

9. Overcoming EGFR^{G724S}-mediated osimertinib resistance through unique binding characteristics of second-generation EGFR inhibitors.

   Fassunke J, Müller F, Keul M, Michels S, Dammert MA, Schmitt A, Plenker D, Lategahn J, Heydt C, Brägelmann J, **Tumbrink HL**, Alber Y, Klein S, Heimsoeth A, Dahmen I, Fischer RN, Scheffler M, Ihle MA, Priesner V, Scheel AH, Wagener S, Kron A, Frank K, Garbert K, Persigehl T, Püsken M, Haneder S, Schaaf B, Rodermann E, Engel-Riedel W, Felip E, Smit EF, Merkelbach-Bruse S, Reinhardt HC, Kast SM, Wolf J, Rauh D, Büttner R, Sos ML.

Nat Commun. 2018 Nov 7;9. doi: 10.1038/s41467-018-07078-0.

* co-first author